# Development of an Acoustic Communication Link for Micro Underwater Vehicles


Geraint M. Goodfellow

School of Electrical and Electronic Engineering

Newcastle University

A thesis submitted for the degree of

*Doctor of Philosophy*

September 2013

To my family and close friends.

# Acknowledgements

The list of people to whom I owe thanks is extensive. My journey has taken many twists and turns since its original conception but having friends and colleagues prepared to offer guidance and support has been critical to the project's success. Firstly I would like to thank my primary supervisor Jeff Neasham. His support and enthusiasm has allowed me to achieve the original objectives of this project. I thank him for his continued patience and understanding. My thanks also go to my secondary supervisors, Bayan Sharif and Charalampos Tsimenidis.

Within the university I have been fortunate to have made several close friends, without whose help I am certain this thesis would not have come to fruition. Particularly I would like to thank Dave Graham, for both his technical insight and ability to see the lighter side of a difficult situation. Although the university has primarily been a place of learning, the friends I have met along the way have made this task far more enjoyable. I am also highly indebted to the universities technical support staff. This project has consisted of a significant amount of practical work and their ability to produce hardware prototypes, in many cases 'at last minute', has been critical to the success of this research.

Outside of the university walls I have received endless support and encouragement from my close family and friends, reminding me of the importance of spending time in the 'outside world'. Throughout my studies my Mum, Sister and Granny have offered continual support, seeing both the ups and downs and never ceasing to help me continue on. Each day I am reminded how lucky I am to have been born into such a fantastic family. I would also like to thank my 'extended family', Dave and Shona, for their support and encouragement the last few years.

Finally, I have reserved the biggest thanks to my fiancé Ailsa. The last year of finishing my PhD has felt very intense, having you by my side has made it all possible. Thankyou for sticking by me and for giving me the emotional support I have needed to see it through! There is no way I can ever thank you for all the help you have given.

# Abstract

In recent years there has been an increasing trend towards the use of Micro Remotely Operated Vehicles ($\mu$ROVs), such as the Videoray and Seabotix LBV products, for a range of subsea applications, including environmental monitoring, harbour security, military surveillance and offshore inspection. A major operational limitation is the umbilical cable, which is traditionally used to supply power and communications to the vehicle. This tether has often been found to significantly restrict the agility of the vehicle or in extreme cases, result in entanglement with subsea structures.

This thesis addresses the challenges associated with developing a reliable full-duplex wireless communications link aimed at tetherless operation of a $\mu$ROV. Previous research has demonstrated the ability to support highly compressed video transmissions over several kilometres through shallow water channels with large range-depth ratios. However, the physical constraints of these platforms paired with the system cost requirements pose significant additional challenges.

Firstly, the physical size/weight of transducers for the LF (8-16kHz) and MF (16-32kHz) bands would significantly affect the dynamics of the vehicle measuring less than 0.5m long. Therefore, this thesis explores the challenges associated with moving the operating frequency up to around 50kHz centre, along with the opportunities for increased data rate and tracking due to higher bandwidth.

The typical operating radius of $\mu$ROVs is less than 200m, in water $<$ 100m deep, which gives rise to multipath channels characterised by long timespread and relatively sparse arrivals. Hence, the system must be optimised for performance in these conditions. The hardware costs of large multi-element receiver arrays are prohibitive when compared to the cost of the $\mu$ROV platform. Additionally, the physical size of such arrays complicates deployment from small surface vessels. Although some recent developments in iterative equalisation and decoding structures have enhanced the performance of single element receivers, they are not found to be adequate in such channels. This work explores the optimum

cost/performance trade-off in a combination of a micro beamforming array using a Bit Interleaved Coded Modulation with Iterative Decoding (BICM-ID) receiver structure.

The highly dynamic nature of $\mu$ROVs, with rapid acceleration/deceleration and complex thruster/wake effects, are also a significant challenge to reliable continuous communications. The thesis also explores how these effects can best be mitigated via advanced Doppler correction techniques, and adaptive coding and modulation via a simultaneous frequency multiplexed down link. In order to fully explore continuous adaptation of the transmitted signals, a real-time full-duplex communication system was constructed in hardware, utilising low cost components and a highly optimised PC based receiver structure. Rigorous testing, both in laboratory conditions and through extensive field trials, have enabled the author to explore the performance of the communication link on a vehicle carrying out typical operations and presenting a wide range of channel, noise, Doppler and transmission latency conditions. This has led to a comprehensive set of design recommendations for a reliable and cost effective link capable of continuous throughputs of >30 kbits/s.

# Contents

**Nomenclature** **xv**

**1 Introduction** **1**
1.1 Contributions . . . 3
1.2 Publications . . . 3
1.3 Thesis Outline . . . 4

**2 Background and State-of-the-Art** **6**
2.1 Underwater Communication Mechanisms . . . 6
2.1.1 Magneto Inductive Communications . . . 8
2.1.2 Optical Communications . . . 9
2.1.3 Acoustic Communications . . . 10
2.1.4 Summary of Communication Mechanisms . . . 11
2.2 Physical Channel Characteristics . . . 12
2.2.1 Transmission Loss . . . 14
2.2.1.1 Spreading Loss . . . 14
2.2.1.2 Sound Absorption . . . 15
2.2.1.3 Total Transmission Loss . . . 16
2.2.2 Multipath . . . 16
2.2.2.1 Refraction . . . 19
2.2.3 Doppler Effect . . . 21
2.2.4 Noise and Interference . . . 22
2.2.4.1 Ambient Noise . . . 22
2.2.4.2 Application Induced Noise . . . 25
2.3 State of The Art: Acoustic Telemetry . . . 25
2.3.1 Historical Background . . . 25
2.3.2 Receiver Developments . . . 26
2.3.2.1 Channel Equalisation . . . 26
2.3.2.2 Spatial Diversity Processing . . . 27
2.3.2.3 Multi-Carrier Transmissions . . . 29
2.3.2.4 *'Turbo'* Decoding Techniques . . . 29
2.4 Summary . . . 30

**3 Underwater Acoustic Receiver Algorithms 32**
3.1 Signal Design . . . 32
3.1.1 Single Carrier Communication . . . 32
3.1.1.1 Amplitude Shift Keying (ASK) . . . 33
3.1.1.2 Phase Shift Keying (PSK) . . . 33
3.1.1.3 Differential Phase Shifted Keying (D-PSK) . . . 35
3.1.1.4 Quadrature Amplutude Modulation (QAM) . . . 35
3.1.1.5 Mapping Evaluation . . . 36
3.1.2 Spread Spectrum Communication . . . 37
3.1.3 Multi Carrier Communications . . . 39
3.2 Receiver Design . . . 41
3.2.1 Single Carrier Communication . . . 41
3.2.1.1 Synchronisation . . . 42
3.2.1.2 Channel Equalisation . . . 44
3.2.1.3 Coefficient Update Algorithms . . . 50
3.2.1.4 Array Receivers . . . 56
3.2.1.5 Doppler Estimation and Compensation . . . 58
3.2.1.6 Open-Loop Doppler Estimation . . . 59
3.2.1.7 Closed-Loop Doppler Estimation . . . 61
3.2.1.8 Doppler Correction . . . 62
3.2.2 Spread Spectrum Communication . . . 63
3.2.2.1 Chirp Spread Spectrum (CSS) . . . 63
3.2.2.2 CSS Transmitter Structure . . . 64
3.2.2.3 CSS Receiver Structure . . . 65
3.2.2.4 Multipath Tolerance . . . 66
3.2.2.5 Doppler Tolerance . . . 67
3.2.3 OFDM Communication . . . 67
3.2.3.1 Guard Period . . . 69
3.2.3.2 Pilot Tones . . . 69
3.2.3.3 Sub-carrier Bit Loading . . . 70
3.2.3.4 Peak to Average Power Ratio (PAPR) . . . 70
3.2.3.5 Frequency Offset Sensitivity . . . 71
3.3 Error Correction Coding . . . 71
3.3.1 Convolutional Coding . . . 72
3.3.2 Turbo Coding . . . 73
3.3.3 Combined Coding and Modulation . . . 74
3.3.3.1 Interleaving . . . 75
3.3.4 Turbo Equalisation . . . 76
3.4 Receiver Design Overview . . . 77

**4 Investigation of a High Data Rate Up-Link** **79**
4.1 Single Element Receivers . . . 79
4.1.1 Motivation . . . 79
4.1.1.1 Fundamental Transmission Parameters . . . 80
4.1.2 ROV Interference . . . 80
4.1.3 Equaliser Performance . . . 84
4.1.3.1 Linear Transversal Equaliser . . . 85
4.1.3.2 Decision Feedback Equaliser . . . 85
4.1.3.3 Sparse Equalisation . . . 91
4.1.3.4 BICM-ID Performance . . . 94
4.2 Multi Element Receivers Structures . . . 97
4.2.1 Array Construction . . . 100
4.2.1.1 Beam Pattern . . . 101
4.2.2 Receiver Validation and Field Results . . . 103
4.3 Doppler Estimation and Compensation . . . 106
4.3.1 Closed Loop Doppler Correction Gain . . . 109
4.4 Variable Code Rates and Modulation Schemes . . . 112
4.4.1 Variable Code Rates . . . 112
4.4.1.1 Code Puncturing . . . 112
4.4.1.2 Performance Evaluation . . . 112
4.4.2 High Order Modulation Schemes . . . 114
4.4.3 Performance Evaluation . . . 114
4.5 Design Rules for Optimum Performance . . . 117

**5 Receiver Design and Implementation** **119**
5.1 Receiver Considerations . . . 119
5.1.1 Synchronisation Techniques . . . 119
5.1.1.1 Normalised Cross-Correlation . . . 120
5.1.1.2 Hard Limited Cross-Correlation . . . 120
5.1.1.3 Summary . . . 121
5.1.2 Equalisation: Adaptive Algorithm Selection . . . 121
5.1.3 Soft Decoding . . . 122
5.1.3.1 Maximum a Posteriori Probability (MAP) Decoder . 123
5.1.3.2 Logarithmic Domain Representation . . . 124
5.1.3.3 Comparative Performance . . . 125
5.1.4 Receiver Structure . . . 126
5.1.5 Packet Structure . . . 126
5.2 Receiver Implementation . . . 129
5.2.1 Hardware Design . . . 129
5.2.1.1 Signal Processing Platform . . . 130
5.2.1.2 Data Acquisition and Conversion . . . 131

5.2.1.3 Buffered Operation . . . 132
5.2.1.4 Beamformer Construction . . . 133
5.2.1.5 Physical Constraints . . . 135
5.2.1.6 Pre-amplification and Filtering . . . 135
5.2.2 Software Considerations . . . 137
5.2.2.1 Coding Optimisation . . . 138
5.2.2.2 Intel® Integrated Performance Primitives (IPP) . . . 138
5.2.2.3 Multi-Threaded Implementation . . . 139
5.2.3 Receiver Benchmarking . . . 143
5.2.3.1 Benchmarked Receiver Performance: Single Packet Processing . . . 143
5.2.3.2 Benchmarked Receiver Performance: Packet Breakdown . . . 146
5.3 Transmitter Structure . . . 148
5.3.1 Hardware Description: PC Interface Unit . . . 148
5.3.2 Software Requirements . . . 151
5.3.2.1 Initialisation . . . 152
5.3.2.2 Thread 1: Signal Generation . . . 153
5.3.2.3 Thread 2: Signal Transmission . . . 154
5.3.2.4 Thread Execution . . . 154
5.4 Summary . . . 154

**6 Development of a Full Duplex Link 156**
6.1 Transmission Multiplexing . . . 156
6.1.1 Half Duplex Communications . . . 156
6.1.2 Full Duplex Communications . . . 157
6.1.3 Overview . . . 157
6.1.4 Full Duplex Message Analysis . . . 158
6.1.4.1 Downlink Transmissions . . . 158
6.1.4.2 Uplink Transmissions . . . 159
6.1.4.3 Overview . . . 160
6.2 The *'Near-Far'* Problem . . . 160
6.2.0.4 Physical Channel Evaluation . . . 161
6.2.1 Acoustic Solutions . . . 162
6.2.2 Passive Filtering . . . 163
6.2.2.1 Filter Shape . . . 164
6.2.2.2 Higher Order Filters . . . 164
6.2.3 Digital Filtering . . . 165
6.2.3.1 Finite Impulse Response (FIR) . . . 166
6.2.3.2 Adaptive Noise Cancellation . . . 166
6.3 Controlled Experimentation . . . 167

6.3.1 Channel Model . . . 169
6.3.2 Full Duplex Results . . . 169
6.3.3 Summary . . . 173

**7 Investigation of Adaptive Modulation and Coding (AMC) Techniques 174**
7.1 Benefits of Adaptive Techniques . . . 174
7.2 Past Research in the Field of Adaptive Subsea Communications . . . 175
7.3 Adaptive System Overview . . . 176
7.3.1 Channel Quality Indicators (CQI) . . . 177
7.3.2 Adaptive Parameters . . . 179
7.3.3 Summary of AMC Techniques . . . 180
7.4 Adaptive Protocol Structures . . . 180
7.4.1 Configuration 1: Linear Adaptation . . . 181
7.4.2 Configuration 2: Fall Back . . . 181
7.4.3 Configuration 3: Fully Adaptive . . . 182
7.4.4 Configuration 4: Gated Fully Adaptive . . . 183
7.5 Experimental Results . . . 184
7.5.1 Hardware Configuration . . . 184
7.5.2 Measured Experimental Delay . . . 184
7.5.2.1 Downlink Processing Delay . . . 186
7.5.2.2 Round Trip Transmission Delay . . . 186
7.5.3 Data Set A: Varying Noise Profiles and Transmission Delays . 187
7.5.3.1 Noise Profiles . . . 187
7.5.3.2 Hydrophone Configuration . . . 189
7.5.3.3 Profile 1: Slowly Varying (Sinusoidal) . . . 189
7.5.3.4 Profile 2: Stepped Response . . . 191
7.5.3.5 Profile 3: Impulsive Noise . . . 192
7.5.4 Data Set B: Varying Channel Conditions and Vehicle Motion . 193
7.5.4.1 Experimental Description . . . 193
7.5.4.2 Comparative Results . . . 194
7.5.5 Summary . . . 195

**8 Conclusion 198**
8.1 Future Work . . . 201

**A Sea Trials and Experimental Conditions 203**
A.1 Newcastle University Anechoic Tank . . . 203
A.2 Royal Quays Marina . . . 203
A.3 Windermere . . . 204
A.4 Summary of Supporting Trial Work . . . 206

**References** **207**

# List of Figures


1.1 Acoustically Controlled Tetherless Remotely Operated Vehicle . . . . 2

2.1 Shallow Water Channel Geometry . . . . . 20
2.2 Multipath Channel Model . . . . . 20
2.3 Wenz Curves of Background Ambient Noise . . . . . 23
2.4 Analysis of Self Induced $\mu$ROV Thruster Noise . . . . . 25

3.1 Signal Mapping of Different Modulation Schemes . . . . . 34
3.2 Power Spectral Density: Spread Spectrum Waveform . . . . . 38
3.3 Orthogonal Frequency Division Multiplexing (OFDM) . . . . . 40
3.4 Conventional Single Carrier Receiver Structure . . . . . 42
3.5 Ambiguity Function: LFM and PN Sequence . . . . . 43
3.6 Linear Transversal Equaliser (LTE) . . . . . 45
3.7 Decision Feedback Equaliser (DFE) . . . . . 46
3.8 Adaptive Beamformer . . . . . 57
3.9 Open Loop Doppler Estimation and Correction . . . . . 59
3.10 Open Loop Block Doppler Estimation . . . . . 60
3.11 Closed Loop Doppler Estimation and Correction . . . . . 62
3.12 Single Bit Chirp Spread Spectrum (CSS) Transmitter . . . . . 65
3.13 Chirp Spread Spectrum Transmission . . . . . 65
3.14 OFDM Communication Structures . . . . . 68
3.15 Recursive Systematic Convolutional (RSC) Encoder . . . . . 73
3.16 Turbo Coding Structures . . . . . 73
3.17 Turbo Equalisation Structures . . . . . 76

4.1 Single Carrier Demodulator Output: Thruster Gain 100% . . . . . 82
4.2 Single Carrier Demodulator Output: Thruster Gain 60% . . . . . 83
4.3 Single Carrier Demodulator Output: Thruster Gain 40% . . . . . 83
4.4 Single Element Equaliser Performance (Data Set 1) . . . . . 86
4.5 Single Element DFE Performance (Data Set 2) . . . . . 88
4.6 Comparison of Sparse and Non-Sparse Equalisation Performance . . . 89
4.7 Binary Representation of Sparse Underwater Channels . . . . . 92
4.8 Single Element Equaliser Performance (Data Set 2) . . . . . 93

4.9 Single Element Receiver Analysis: Sparse Equalisation . . . . . 94
4.10 Single Element Receiver Analysis: BICM-ID Performance . . . . . 95
4.11 Distribution of Log Likelihood Ratios . . . . . 96
4.12 Simplified Channel Model of a Shallow Water Acoustic Link . . . . . 97
4.13 Short Range Shallow Water Channel: Multipath Delay Spread and Angular Separation . . . . . 99
4.14 Coherent Cancellation Utilising a Beamform Array . . . . . 100
4.15 Un-steered Beam Pattern for an $N$ Element $\lambda$ Spaced Array . . . . . 102
4.16 $\mu$ROV Operational Setup: Multiple Reverberation Paths . . . . . 104
4.17 CIR Probe of Packets Exhibiting Multiple Reverberation Paths . . . 104
4.18 Detailed Evaluation of a Highly Reverberant Multipath Channel . . . 105
4.19 Time Varying Channel Impulse Response (CIR) . . . . . 107
4.20 Packet Error Distribution for Various Doppler Estimation Techniques 108
4.21 Tracking of Closed Loop Doppler Estimation: Without Initial Block Estimate . . . . . 110
4.22 Tracking of Closed Loop Doppler Estimation: With Initial Block Estimate . . . . . 111
4.23 System Performance for Variable Code Rates . . . . . 113
4.24 Packet Error Distribution for QPSK and QAM Transmissions . . . . 116

5.1 'Hard Limit' Synchronisation Technique . . . . . 121
5.2 Convergence Rate of LMS and RLS Update Algorithms . . . . . 122
5.3 Proposed Multi-Channel DFE-BICM-ID Receiver Structure . . . . . 127
5.4 Proposed Packet Structures . . . . . 128
5.5 Multi-Element Receiver Hardware Structure . . . . . 130
5.6 For Channel Data Acquisition Unit . . . . . 133
5.7 Cross Sectional Outline of a Four Element Beamform Array . . . . . 134
5.8 Four Element Prototype Array Construction . . . . . 136
5.9 Active Differential Bandpass Filter Schematic: Implemented on Each Beamforming Channel for Pre-Amplification and Filtering Purposes . 136
5.10 Receiver Front End Filter Frequency Response . . . . . 137
5.11 Receiver Software Structure . . . . . 140
5.12 PC Based Real-Time Receiver Software Outputs . . . . . 144
5.13 Mean Processing Duration of QPSK and QAM 1/2 Transmissions . . 146
5.14 QPSK 1/2, 3 Inner Iterations. Comparison Between Processing Time of Single Element and Multi Element Receivers . . . . . 147
5.15 Itemised Processing Duration: Multi-Channel Receiver Structure . . . 148
5.16 Hardware Block Diagram for Custom PC Transmission Interface Unit 149
5.17 Transmit Anti-Imaging Filter . . . . . 150
5.18 USB DAC Unit Hardware Construction . . . . . 151
5.19 Real-Time Transmitter Software Structure . . . . . 153

6.1 Comparison of TDMA and FDMA Communication Schemes . . . . . 157
6.2 Illustration of the *'Near-Far'* Problem . . . . . 161
6.3 Comparison of High Order LC Passive Filters . . . . . 165
6.4 Adaptive Noise Cancellation Structure . . . . . 166
6.5 Experimental Hardware Configuration for Uplink Receiver . . . . . 168
6.6 Single Carrier Demodulator Output for a Simulated 150m Channel . 171
6.7 Single Carrier Demodulator Output for a Simulated 250m Channel . 172

7.1 Multipath Response: Channel Quality Indicators . . . . . 177
7.2 Adaptive Protocol 1: Linear *'Step-by-Step'* Approach . . . . . 181
7.3 Adaptive Protocol 2: *'Step Up: Fall Back'* Approach . . . . . 182
7.4 Adaptive Protocol 3: Fully Adaptive Approach . . . . . 182
7.5 Adaptive Protocol 4: Gated Fully Adaptive Approach . . . . . 183
7.6 Adaptive Modulation and Coding: Experimental Setup . . . . . 185
7.7 Adaptive Modulation and Coding: Synthesised AWGN Noise Signals 188
7.8 AMC Performance: Sinusoidal Noise Profile . . . . . 190
7.9 AMC Performance: Stepped Noise Profile . . . . . 191
7.10 AMC Performance: Impulsive Noise Profile . . . . . 192
7.11 Comparative Performance of AMC and CCM Techniques . . . . . 194
7.12 Transmission Scheme Variation: An AMC 'Drop Back' Approach . . 196

A.1 SEA-Lab Anechoic Test Tank Facilities . . . . . 204
A.2 Royal Quays Marina Trials Site . . . . . 205
A.3 Windermere Trials Site . . . . . 206

# List of Tables


2.1 Skin Depth of RF Carrier Frequencies in Salt Water . . . . . 7
2.2 Comparison of Underwater Communication Mechanisms . . . . . 13
2.3 Summary of Single Carrier High Data Rate Communication Systems 28

3.1 Evaluation of Single Carrier Modulation Schemes . . . . . 36
3.2 Comparison of Equalisation Update Algorithms . . . . . 55
3.3 Computational Complexity of Equalisation Update Algorithms . . . . 55
3.4 Comparison of Single Carrier, OFDM and Spread Spectrum Schemes 77

4.1 Single Carrier Packet Parameters Used During Preliminary Trials . . 81
4.2 RSC Puncturing Matrices: Variable Code Rates . . . . . 113
4.3 Incurred Packet Errors: QPSK and 16-QAM . . . . . 115

5.1 Computational Complexity of MAP Algorithms . . . . . 125
5.2 Packet Configuration: Channel Efficiency and Total Throughput . . . 129
5.3 Laptop Specification . . . . . 131
5.4 Agilent U2531A Data AcQuisition (DAQ) Unit Configuration . . . . 132
5.5 Front End Pre-Amplifier Circuit Parameters . . . . . 137
5.6 Summary of Benchmarked Processing Stages, for a 3 Inner 2 Outer DFE-BICM-ID Four Element Beamformer Receiver . . . . . 147

6.1 Comparison of Uplink and Downlink Transmission Requirements . . . 160
6.2 Evaluation of Realistic $\mu$ROV Channel Separations . . . . . 162
6.3 High Frequency (Uplink) Receiver Characteristics . . . . . 168
6.4 Calculated Transmission Power for Simulated Communication Ranges 170

7.1 Estimated Round Trip Delay for Varying Transmission Ranges . . . . 187
7.2 Performance of Static Transmission Schemes: Sinusoidal Noise Profile 190
7.3 Performance of Static Transmission Schemes: Stepped Noise Profile . 192
7.4 Performance of Static Transmission Schemes: Impulsive Noise Profile 193

A.1 Summary Of Related Trials, Conducted Between 2010 and 2012 . . . 206

# Nomenclature

### Roman Symbols

| | |
|---|---|
| $A$ | Amplitude |
| $B$ | Magnetic Field |
| $C$ | Capacitance |
| $c$ | Speed of Sound ($\approx 1500 m/s$ in Sea Water) |
| $E$ | Expected Value |
| $e_n$ | Equaliser Error Signal |
| $E_t$ | Transducer Efficiency |
| $f$ | Frequency |
| $f_{3db}$ | Half Power Cutoff Frequency |
| $f_c$ | Centre Frequency |
| $f_s$ | Sampling Frequency |
| $h[n]$ | Matched Filter Coefficients |
| $I$ | Identity Matrix |
| $I_1$ | Sound Intensity at a Distant Point |
| $I_0$ | Sound Intensity at a 1m Reference Point |
| $J_{\text{MSE}}$ | Mean Square Error Performance Index |
| $\mathbf{K}_n$ | Kalman Gain Vector |
| $L$ | Inductance |
| $N$ | Number of Turns (Coil) |
| $\mathbf{P}_{n-1}$ | Inverse Correlation Matrix |

| | |
|---|---|
| $P_a$ | Acoustic Power |
| $P_e$ | Electrical Power |
| $n(t)$ | Noise Signal |
| $r(t)$ | Received Signal |
| $s(t)$ | Transmitted Signal |
| $r$ | Transmission Range |
| $R$ | Rayleigh Parameter |
| $\mathbf{R_x}$ | Cross Correlation of the Filter Input and Desired Output |
| $\mathbf{R_{xx}}$ | Autocorrelation of the Unequalised Filter Input |
| $\hat{s}_n$ | Equaliser Symbol Estimates |
| $SL$ | Source Level |
| $s_n$ | Transmitted Signal |
| $\tilde{s}_n$ | Quantised Equaliser Output |
| $T$ | Symbol Duration |
| $TL$ | Transmission Loss |
| U | Upper Triangular Matrix |
| $V$ | Voltage |
| $V_{rx}$ | Induced Voltage (Receiver) |
| $w_k$ | Equaliser Filter Coefficients |
| $\mathbf{w}_{\text{opt}}$ | Optimal Filter Coefficients |
| $\mathbf{x}$ | Unequalised Filter Input |
| $n_n$ | Channel Noise and Interference |
| $x_n$ | Unfiltered Equaliser Input |

**Greek Symbols**

| | |
|---|---|
| $\alpha$ | Absorption Coefficient |
| $\Delta$ | Induced Doppler Shift |
| $\delta$ | Initial Value of the RLS Inverse Correlation Matrix |

| | |
|---|---|
| $\delta$ | Skin Depth |
| $\gamma$ | Conductivity |
| $\Lambda$ | Diagonal Matrix |
| $\lambda$ | Wavelength |
| $\lambda_f$ | Recursive Least Square Forgetting Factor |
| $\alpha_k(s)$ | Forward Error State Probability |
| $\beta_{k-1}(\acute{s})$ | Backward Error State Probability |
| $\gamma_k(\acute{s}, s)$ | Transition Probability |
| $\mu$ | Least Mean Squares Update Step-Size |
| $\mu$ | Mean Signal Level |
| $\mu_r$ | Relative Permeability |
| $\omega$ | Angular Frequency |
| $\pi$ | Mathematical Constant ($\simeq 3.14\ldots$) |
| $\psi$ | Angle of Arrival |
| $\rho$ | Resistivity |
| $\sigma$ | Standard Deviation |
| $\tau$ | Delay |
| $\Theta$ | Induced Doppler Shift |
| $\Upsilon$ | Threshold Level |
| $\varphi$ | Grazing Angle of an Acoustic Ray |

**Superscripts**

| | |
|---|---|
| $^*$ | Complex Conjugate |
| $^T$ | Matrix Transpose |

**Subscripts**

| | |
|---|---|
| $_{\text{actual}}$ | Actual Value |
| $_{hp}$ | High Pass |
| $_{\text{in}}$ | Input |

$_{lp}$ Low Pass

$_{\text{mp}}$ Multipath

$_{n}$ Normalised Prototype Values

$_{\text{noise}}$ Noise Level

$_{\text{out}}$ Output

$_{\text{pkpk}}$ Peak to Peak

$_{\text{rms}}$ Root Mean Square

$_{\text{rx}}$ Receive

$_{\text{signal}}$ Signal Level

$_{\text{sim}}$ Simulated Value

**Acronyms**

AC Alternating Current

ACTROV Acoustically Controlled Tetherless ROV

ADC Analogue to Digital Converter

AM Amplitude Modulation

AMC Adaptive Modulation and Coding

ASK Amplitude Shift Keying

AUV Autonomous Underwater Vehicle

AWGN Additive White Gaussian Noise

BER Bit Error Rate

BICM Bit Interleaved Coding and Modulation

BICM-ID Bit Interleaved Coding and Modulation with Iterative Decoding

BOK Binary Orthogonal Keying

CCM Continuous Coding and Modulation

CIR Channel Impulse Response

CML Coded Modulation Libraries

CQI Channel Quality Indicator

CRC Cyclic Redundancy Check

CSS Chirp Spread Spectrum

DAC Digital to Analogue Converter

DFE Decision Feedback Equaliser

ELF Extremely Low Frequency

EM Electro Magnetic

TDMA Time Division Multiple Access

FDM Frequency Division Multiplexing

FIR Finite Impulse Response

FSK Frequency Shift Keying

HF High Frequency

IPP Intel Performance Primitives

ISI Inter-Symbol Interference

ISM Industrial, Scientific and Medical

JPEG Joint Photographics Expert Group

LC Inductance, Capacitance

LED Light Emitting Diode

LE Linear Equaliser

LFM Linear Frequency Modulation

LMS Least Mean Squares

LOS Line-Of-Sight

MI Magneto Inductive

MPEG Moving Pictures Expert Group

OFDM Orthogonal Frequency Division Multiplexing

PCB Printed Circuit Board

PC Personal Computer

PER Packet Error Rate

PMT Photo Multiplier Tubes

PSD Power Spectral Density

PSK Phase Shift Keying

QAM Quadrature Amplitude Modulation

QPSK Quadrature Phase Shift Keying

RF Radio Frequency

RLS Recursive Least Squares

RMS Root Mean Square

ROV Remotely Operated Vehicle

$\mu$ROV Micro Remotely Operated Vehicle

SINR Signal and Interference to Noise Ratio

SNR Signal to Noise Ratio

SONAR SOund Navigation And Ranging

TCP Transmission Control Protocol

TDL Tapped Delay Line

FDMA Frequency Division Multiple Access

TVR Transmit Voltage Response

UAC Underwater Acoustic Communications

UHF Ultra High Frequency

USB Universal Serial Bus

VLF Very Low Frequency

# Chapter 1

# Introduction

A diverse range of underwater remotely operated vehicles (ROVs) have been developed to date, ranging in size, power and manoeuvrability. More recently, there has been a trend towards much smaller, simpler and cheaper vehicles. Micro-ROVs ($\mu$ROVs) are becoming common in many applications, both military and civilian, such as environmental monitoring and harbour security. Due to their small size and minimal weight ($< 10$kg) they are easily deployed and far more cost and time effective than larger traditional systems.

The major operational limitation of such vehicles is the tether, which is traditionally used to supply power and communications. This connection restricts the agility of the vehicle in strong currents or tides, and may become entangled with subsea structures. Additionally, the limitations of a tethered vehicle, in terms of detection and environmental impact, make them unsuitable for a range of niche applications. Examples such as the filming of marine wildlife or the detection of mine countermeasures demonstrate the requirement for covert, unobtrusive operation.

The limitations of the tether promotes the use of Autonomous Underwater Vehicles (AUV), which operate independently of the surface platform. However, due to the limited data rate of suitable subsea communication technology, minimal feedback information is typically available at the surface and comprises of critical status updates, such as battery health, and real-time position information. This approach is often seen to be ineffective as it restricts the ability of the operator to intervene during deployment and requires accurate mission planning to ensure successful operation.

Previous work within the field of Underwater Acoustic Communications (UAC), has pushed the boundaries in terms of effective throughput and operational range. A variety of adaptive filtering techniques, combined with diversity array receivers, have been shown to successfully negate the effects of the highly time variable multipath channel. Despite these improvements, limited research has focussed on the

specific challenge of developing a reliable low-cost, high data rate modem suitable for deployment on a dynamic $\mu$ROV platform. Key limiting factors inhibiting the use of a conventional receiver structures within a $\mu$ROV scenario, are the physical dimensions and high costs of a large multi-channel receiver structure. However, recent developments in the field of iterative turbo coding has promoted research to re-evaluate the use of single element receivers.

Utilising a commercially available low data rate modem, an Acoustically Controlled Tetherless ROV (ACTROV) was developed during the early stages of this research. As shown in Fig. 1.1, adaptations were made to a Videoray Pro4 $\mu$ROV consisting of a closed loop depth and direction controller to replicate similar functionality to that of a tethered vehicle. Despite the additional hardware enabling the vehicle to operate successfully without a connecting tether, the limited feedback information supplied to the surface caused difficulty in manoeuvring the vehicle when out of sight.

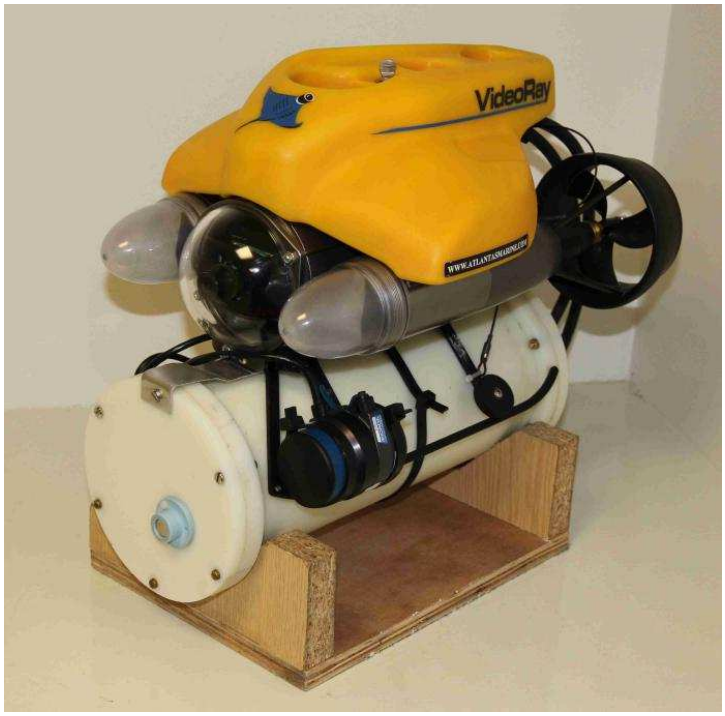


Figure 1.1: Acoustically Controlled Tetherless Remotely Operated Vehicle (ACTROV)

To facilitate true tetherless operation, a high data rate communication link is required, capable of streaming real time sensor information such as video or SONAR imagery to the surface. This research investigates the development of a bandwidth efficient communication scheme capable of overcoming the complexity of a shallow water, short range communication channel. A practical real-time receiver is developed, allowing a rigorous examination of the challenges faced in conducting reliable

communications within the operating environment of a $\mu$ROV. The thesis is believed to highlight a comprehensive set of recommendations for the production of a low-cost portable full-duplex communication link.

## 1.1 Contributions

The key areas of novelty can be attributed to the development of a reliable low-cost, high data communication scheme capable of supporting continuous video or SONAR transmissions from a dynamic $\mu$ROV platform. The research specifically focusses on the individual challenges relating to the operational environment of the vehicle and the complications in overcoming the sparse nature of the multipath channel. The following list summarises the key contributions that have been made within the scope of this research:

1. Rigorous investigation and analysis of the specific challenges relating to the development of a reliable, high data rate acoustic communication system for a $\mu$ROV platform.
2. Development and optimisation of a low-cost real-time multi-channel DFE-BICM-ID acoustic receiver, for underwater $\mu$ROV applications.
3. Demonstration of an asymmetric full-duplex communication system, capable of supporting bidirectional transmissions of reliable control information and continuous video imagery.
4. Development and practical implementation of an Adaptive Modulation and Coding (AMC) scheme, capable of improving the throughput and reliability of the proposed high data rate uplink.
5. Examination of the effect of feedback latency, in particular highlighting the reduction in throughput and increase in packet errors.
6. Production of a comprehensive set of design recommendations for the practical implementation of a reliable high data rate $\mu$ROV communication link.

## 1.2 Publications

The following papers have been published based on the research presented in this thesis:

[1] **G. M. Goodfellow**, J. A. Neasham, C. C. Tsimenidis, O. R. Hinton, B. S. Sharif, "Investigation of a Full Duplex Acoustic Link for a Tetherless Micro-ROV" *Proc. IEEE Oceans*, Santander, Spain, 6-9 June 2011.

[2] **G. M. Goodfellow**, J. A. Neasham, C. C. Tsimenidis, B. S. Sharif, "High Data Rate Acoustic Link for Micro-ROVs, Employing BICM-ID" *Proc. IEEE Oceans*, Yeosu, South Korea, 21-24 May 2012.

[3] **G. M. Goodfellow**, J. A. Neasham, B. S. Sharif, C. C. Tsimenidis, "Bit-Interleaved Coded Modulation with Iterative Decoding for Micro-ROV" *Proc. ECUA*, Edinburgh, United Kingdom, 2-6 July 2012.

## 1.3 Thesis Outline

The structure of this thesis is outlined in the following paragraphs.

*Chapter 2* investigates different mechanisms of communicating through the underwater channel and highlights the benefits of acoustics for mid-to-long range high data rate transmissions. An evaluation of the challenges presented by the shallow water channel and $\mu$ROV are emphasised including time variable multipath and highly dynamic Doppler shift.

*Chapter 3* provides an extensive evaluation of various signalling approaches and examines the pros and cons of single carrier, multi carrier and spread spectrum techniques. An in depth analysis of the required receiver structure is provided, with particular focus given to suitable equalisation techniques capable of overcoming the dynamic multipath channel.

*Chapter 4* presents the results collected during rigorous testing of the proposed receiver structure. Based on extensive experimentation, the performance of both single-element and multi-channel receivers are explored. Specifically, the complexities of ensuring reliable communications with a $\mu$ROV are discussed, emphasising the effects of self induced thruster noise and unpredictable Doppler shift. Variable coding rates and modulation schemes are explored, demonstrating data rates in excess of 30kbps.

*Chapter 5* discusses the implementation of a PC based real-time receiver structure and analyses the construction of a suitable low-cost solution tailored to the proposed $\mu$ROV application. A thorough analysis of the design methodology and software optimisation techniques used within this design are presented, which emphasise the importance of a multi-threaded architecture for real-time operation. Benchmarking results demonstrate the processing performance of the proposed multi-channel iterative decoding scheme and show that this is suitable for a modest PC specification.

*Chapter 6* investigates the construction of an asymmetric full-duplex bidirectional communication scheme, capable of supporting simultaneous transmissions of high data rate sensor readings and high integrity vehicle control packets. The use of frequency multiplexing is proposed to address the challenges related to the *'near-far'* problem. Practical experimentation is conducted in a controlled environment, to examine the performance of the system at simulated ranges of upto 250m.

*Chapter 7* examines the performance of an Adaptive Modulation and Coding (AMC) structure. In particular, the chapter explores the challenges and practicalities associated with ensuring accurate feedback information through a high latency communication channel. Adaptive structures are discussed in depth along with methods for selecting suitable Channel Quality Indicators (CQI) to ensure optimum operating performance. Results are presented demonstrating real-time testing of various AMC schemes in controlled conditions.

*Chapter 8* summarises the key contributions of the preceding chapters, highlighting the most notable findings and emphasises a set of design recommendations for the development of a low-cost real time communication scheme. Finally, the author highlights aspects of future work, indicating areas where further contributions to the academic field could be made.

# Chapter 2

# Background and State-of-the-Art

This chapter explores the background of underwater communications, examining different mechanisms suitable for reliable transmissions and highlights some of the complications faced in communicating sub-sea. Particular focus is given to the challenges relating to the operational environment of a small $\mu$ROV. A comprehensive literature review provides insight into the current state of the art and gives context to the proposed area of research.

## 2.1 Underwater Communication Mechanisms

Underwater acoustics have been utilised for decades for positioning, imaging and telemetry, for both military and commercial applications. Due to an increasing interest to explore the seabed and monitor subsea activities, the area of underwater communications and mapping continues to grow.

A variety of methods have been explored to enable reliable communications subsea. Typically, the majority of research in this field has focussed on three main transmission methods; optical, inductive and acoustic. Unlike the air channel, where electromagnetic (EM) communications, i.e. Radio Frequency (RF), is the dominant method of communication, the EM spectrum is rarely utilised subsea. The main limitation of radio transmissions underwater is the attenuation of such signals caused by the skin effect. The skin effect is a phenomenon whereby, in any conductor a current will tend to flow with higher density close to the surface, with the signal having increased attenuation at increased depths [1]. The skin depth, $\delta$, is defined as the depth where the signal is attenuated to $1/e$ of the original amplitude and can be calculated for a good conductor using (2.1), where, $\mu$ is the absolute magnetic permeability of the conductor, $\rho$ is the resistivity of the conductor and $\omega$ is the angular frequency. It should be noted that for a materials with a lower conductivity, such as fresh water, the effect of permittivity also needs to be considered.

$$\delta = \sqrt{\frac{2\rho}{(2\pi f)(\mu_0\mu_r)}} = \sqrt{\frac{2\rho}{\omega\mu}} \tag{2.1}$$

For salt water, with a salinity of 35 g/L and at a temperature of 10°C, the conductivity, $\gamma$, can be considered to be ≈3.808 S/m. The relative permeability of water can be considered to be approximately one, $\mu_r \approx 1$, indicating minimal influence on the magnetic field, i.e. $\mu \approx \mu_0$. The skin depth of salt water can therefore be calculated using (2.2).

$$\delta \approx \sqrt{\frac{2}{(2\pi f)\gamma\mu_0}} \approx \sqrt{\frac{2}{3.006 \times 10^{-5} f}} \tag{2.2}$$

Utilising (2.2) it can be shown that for an RF carrier frequency of 2.4 GHz the skin depth would be approximately 5.25mm, which is impractical for most applications. Table 2.1 presents the skin depth in salt water for a range of carrier frequencies.

| Band | Frequency ($f_c$) | Wavelength ($\lambda$) | Skin Depth ($\delta$) |
|---|---|---|---|
| UHF (ISM) | 2.4 GHz | 0.125m | 5.25mm |
| HF | 2 MHz | 150m | 18.23cm |
| VLF | 2 kHz | $150 \times 10^3$m | 5.76m |
| ELF | 2 Hz | $150 \times 10^5$m | 182.39m |

Table 2.1: Skin Depth and Wavelength for a Selection of RF Carrier Frequencies in Salt Water

Table 2.1 clearly demonstrates that at standard radio communication frequencies, minimal transmission distance through water is possible. Practical transmission distances are found to only be possible within the Extremely Low Frequency (ELF) band. The wavelength, $\lambda$, of the various carrier frequencies is also shown, calculated using (2.3). The speed, $c$, for RF transmissions is considered to be equal to the speed of light i.e. $3 \times 10^8$ m/s

$$\lambda = \frac{c}{f} \tag{2.3}$$

For efficient RF radiation the antennas are typically specified to be $\lambda/4$ in length. From Table 2.1, it can be seen that for ELF transmissions of 3Hz-3kHz, which would allow for a feasible transmission range, that the length of an efficient antenna would need to be impractically large. Such techniques have been used in the past for military applications, i.e. for communicating with submarines. However, they have been limited to one way transmissions (surface to subsea), utilising unrealistic

levels of transmission power, to overcome antenna inefficiencies, and a smaller receive antennas mounted on the submarine.

The limited range of EM communications has severely restricted research into its use in subsea applications. Instead, the majority of research can be split into three areas; *Inductive*, *Optical* and *Acoustic*. Each of these techniques are explored further, summarising their specific strengths and weaknesses.

### 2.1.1 Magneto Inductive Communications

Magneto Inductive (MI) communications differ from RF communications because the energy is confined into a non-propagating magnetic field rather than radiating into a far field electromagnetic signal. This technique is also know as *'near field'* communications. Magneto Inductive (MI) signals are an AC magnetic-dipole field with very little, if any, electric field. The electric field is suppressed due to the extremely low frequencies utilised, therefore, the multiple turn coil antennas have very low radiation resistance and generate minimal EM signal. Due to the lack of electric field produced by the coil, the magnetic signal can be seen to be non-propagating. In a conductive medium, such as salt water, this can be described as a diffusion field. [2]

A major advantage highlighted in many magneto-inductive applications, is the covertness or security of the communication link. The non-propagating nature of the magnetic field restricts the range of interrogation and thus reduces unwanted detection from outside the operational field. Another inherent property caused by the non-propagating nature of MI signals, is the lack of delayed multipath arrivals and consequent fading [3]. This ultimately simplifies the overall receiver design.

Inductive communication systems are composed of two coil antennas, the primary transmitter and the secondary receiver. A magnetic field, $B$, is generated at the transmitter due to the flow of current through the coil. A reduction in the magnetic field, $\Delta B$, occurs as a function of range from the transmit coil, $r$, in the form (2.4).

$$\Delta B \propto \frac{1}{r^3} \tag{2.4}$$

The RMS voltage induced by the receive coil, $V_{rx}$, can be related to the magnetic field using (2.5), where: $N$ is the number of turns on the coil; $A$ is the cross sectional area of the coil; $f_c$ is the carrier frequency of the signal; and $\mu_R$ is the relative magnetic permeability of the medium. [2].

$$V_{rx} = \mu_R 2\pi f_c BAN \tag{2.5}$$

For both the receiver and transmitter, it can be seen that by enlarging the dimensions of the coil, or increasing the number of turns, the generated magnetic field and the sensitivity of the receiver will grow thus enabling improved range. It should be noted that an optimum point is found in most applications, with increased turns not only causing copper losses and core losses, but equally having practical implications due to the increased mass from the copper windings. Additionally, at the transmitter, increasing the current flow through the coil can be seen to generate a greater magnetic field. However, both power losses and core losses will again have an effect, decreasing the efficiency of the overall system.

A trade-off in MI systems is apparent, between the size, weight and power requirement of the overall system. In the case of an implementation for a $\mu$ROV, the size and weight of the antenna required for sufficient operational range would heavily restrict movement of the vehicle. Additionally, for a completely tether free implementation, where all systems would be powered from portable power sources, a compromise would be made between deployment duration and transmit power. Consequently, such systems are typically seen to be impractical for mobile deployments on a $\mu$ROV platform.

A wide range of research has explored the use of inductive communication techniques for subsea applications. Specific focus has been for short range applications where, due to the physical characteristics of the channel, acoustic methods would struggle to operate effectively; such examples are very shallow water environments and areas of breaking water i.e. surf zones. The limited change in magnetic permeability between water, air and rock also makes MI techniques ideal for applications where cross boundary interaction is desirable [4]. For example Sojdehei *et al.* [2] demonstrated transmissions of 300bps at a combined range of upto 400m in a coastal, mixed media environment.

### 2.1.2 Optical Communications

Optical communications for subsea communication have seen extensive research over the last decade. Utilising the semi-transparent ocean water as an optical transmission medium, light can propagate from transmitter to receiver in a similar manner to a fixed fibre optic link.

The development of optical communications has seen a large growth in recent years due to the decreasing cost of components required for the construction of reliable receiver and transmitter pairs. To enable effective generation of narrow light beams, high quality Light Emitting Diodes (LED) or laser diodes are required. Similarly to ensure a good signal to noise ratio at the receiver, avalanche diodes or Photo Multiplier Tubes (PMT) are generally utilised.

Optical communication links are often limited in range due to the turbidity of the water. In deep water channels, where the water quality is good, scattering and diffusion of light caused by sediment is minimal, enabling operation over ranges of several hundred metres. However, in shallow water channels, where a greater content of suspended particles exist, extreme distortion of the transmitted beam occurs causing the operating range to reduce significantly [5].

Directional light sources and receivers cause difficulty in set up and operation of such systems. Misalignment can have catastrophic effects, hence, small movements can easily result in packet drop outs. The nature of the system, requires direct Line of Sight (LOS) for feasible operation, any shadowing or masking of the light will cause immediate disruption to communications [6]. Some initial research has been carried out exploring the reflection of light off the surface to enable communication over rock formations or other subsea obstacles [7] [8]. However, minimal results have been presented to date and the realistic practicality of such systems has yet to be proven.

Despite the limited transmission range of subsea optical systems, particularly in turbid water, benefits have been shown in applications requiring very short distance ($< 50$m) high data rate links. A typical example is the upload of sensor readings from an AUV / ROV without the requirement to surface or mechanically dock. In this application, high throughput links enable minimal down time of the vehicle. Due to the nature of the application, only a short transmission range is required and the vehicle must remain stationary at close proximity to the receiver.

### 2.1.3 Acoustic Communications

For several decades acoustic techniques have been selected to enable reliable transmission of information through the underwater channel. The ability for acoustic waves to propagate over long ranges in water make them ideal when compared to both optical and inductive techniques. A range of research has previously demonstrated the ability for acoustic techniques to be used for transmissions over several kilometres. It should, however, be noted that the absorption loss exhibited by the channel is a function of frequency [9]. Therefore, the available spectrum for long range acoustical communications is typically very low, in the order of 5 to 10kHz.

In contrast to optical techniques, acoustic transmissions incur minimal degradation due to the turbidity of the water. Such transmissions are not typically spread or scattered by suspended sediment or particles. Therefore, the results achieved in both turbid and clear water are comparable, making the technology suitable for use across a range of operating environments, whether deep sea or shallow water. Additionally, the omni-directional radiation of acoustic signals significantly reduces

the complexity required to configure and track a point-to-point link. Without the use of directional transducers, both ends of the communication link can be positioned freely within the water column. This attribute is of significant importance in the discussed application, where the dynamic motion of the vehicle would make the tracking and alignment of a very directional link practically impossible.

The severe difference in acoustic impedance between water and air, and for that matter water and rock, cause difficulty in transferring acoustic signals across channel boundaries without severe loss in signal power. Therefore, to ensure reliable underwater communications, the generation and detection of acoustic signals should occur below the surface, rather than outside the channel boundaries.

### 2.1.4 Summary of Communication Mechanisms

As discussed previously communication utilising RF poses inherent complications due to attenuation resulting from the skin effect. Even in fresh water, where the skin depth increases, penetration through water is still only possible at lower frequencies where the antenna size is impractical. Despite these limitations certain areas of niche research have been carried out into the use of RF subsea for short range applications such as pipeline or riser monitoring and non-contact subsea connectors [10].

An alternative method of communication is magneto-inductive, or 'near field' communications. This method demonstrates several key advantages in comparison to both acoustic and optical communications, such as: the feasibility to link across boundaries, i.e. air to water; inherently multipath tolerant; and immune to acoustic interference. An increasingly important aspect of inductive communications is the reduced environmental impact of such systems, with no known effect on subsea wildlife or their habitat. For both EM and MI communications there are practical limitations on the size of the antenna, severely restricting the effective transmission range.

Optical communication is a promising technology for subsea data transfer, in particular high data rate docking applications for AUV's, where a large amount of data is exchanged over a very short distance. The major drawback of such systems is the range limitation, particularly in shallow and turbid water. The use of highly directional light sources have improved the feasible range and increased the receiver SNR, however, within a highly dynamic application, such as communication with a $\mu$ROV, tracking and steering of the transmitter would be near impossible. Additionally, with the typical operation of such vehicles generally being in inshore, shallow water environments a high amount of suspended particles can generally be encountered. A summary of the advantages and disadvantages of the discussed communication techniques are presented in Table 2.2.

In recent years research has started to examine the combining of two, or more, of these mechanisms into a single platform. An example is the 'BlueComm' modem developed by Wood Hole Oceanography Institute (WHOI) in collaboration with Sonardyne Limited [11]. This modem combines the benefits of both optical and acoustic communications to establish a system capable of both short range, high data rate optical communications and reliable long range, low data rate acoustic communications. Results have been presented by Farr *et al.* [11], demonstrating video transmissions from a large work class ROV (*'Jason'*) using optical methods, while utilising acoustic communications for status updates while out of range.

To enable reliable communication over the required range and in the case of a highly dynamic platform, acoustic techniques have been highlighted as the most appropriate technology. Although acoustic systems suffer from degradation caused by channel reverberation and background ambient noise, their ability to operate over much greater ranges and the practical requirements in terms of size, weight and directionality make acoustic receivers ideal for mounting on a $\mu$ROV.

## 2.2 Physical Channel Characteristics

The physical configuration of the underwater channel presents a range of complications to reliable communication systems. Four, well documented, characteristics of the acoustic channel are considered in the development of any viable acoustic modem, these are [9]:

1. Transmission Loss
2. Time Varying Multipath
3. Time Varying Doppler Shift
4. Ambient Noise

| Characteristic | EM | MI | Optical | Acoustic |
|---|---|---|---|---|
| Effective Operational Range | $< 1$m | $\sim 10$m | $\sim$ 10-100m | $\sim$ km |
| Antenna Size | $> 1$m | $\sim 0.5$m | $\sim 0.1$m | $\sim 0.1$m |
| Wave Propagation Speed | $\sim 7.5 \times 10^4$ at 1kHz<br>$\sim 2.5 \times 10^6$ at 1MHz | $\sim 3 \times 10^8$m/s | $\sim 3 \times 10^8$m/s | $\sim 1500$m/s |
| Adversely Affected By: | | | | |
| *Turbidity* | No | No | Yes | No |
| *Marine Fouling (Transducers)* | No | No | Yes | Yes |
| *Ambient Acoustic Noise* | No | No | No | Yes |
| Restricted to 'Line-of-Sight' Operation | No | No | Yes | No |
| Reliable Cross Boundary Interface | No | Yes | No | No |
| Known Impact On Marine Life | No | No | No | Yes |
| Requires Tight Alignment | No | No | Yes | No |

Table 2.2: Comparison of Examined Underwater Communication Mechanisms
Nb. Wave Propagation Speeds of EM Transmissions Given for a Sea Water Channel [12] [13]

### 2.2.1 Transmission Loss

Acoustic signals transmitted through the underwater channel can be seen to exhibit severe variation, distortion and weakening due to the complex structure and variability in both density and temperature. The resultant reduction in magnitude is defined as Transmission Loss (TL) by the standard SONAR equations .

Transmission loss defines the reduction in sound energy as it propagates from transmitter to receiver. The loss can be defined as a ratio between the intensity at a reference point, $I_0$, typically 1m from the transmitter, and the intensity at a set point in the distance, $I_1$, given by (2.6).

$$\mathrm{TL} = 10 \log_{10} \frac{I_0}{I_1} \tag{2.6}$$

Transmission loss is typically seen to be the summation of two contributions, *Spreading Loss* and *Sound Absorption*.

#### 2.2.1.1 Spreading Loss

Spreading loss, is used to describe the signal weakening as it travels away from the transmitter. As a signal moves through the ocean it will continue to spread in a uniform manner, thus causing a reduction in the received sound intensity. Depending on the nature of the channel, two forms of spreading are typically used to define the loss between transmitter and receiver, these are, spherical spreading and cylindrical spreading [14].

Spherical spreading is typically used to describe the signal weakening in the majority of shallow underwater channels. As a sound wave is transmitted from an omnidirectional transducer into an unbound fluid, the signal will begin to propagate in a spherical manner, radiating uniform energy in all directions. Assuming no loss in the medium, the power at both the reference point and the distant point must be equal. This can be expressed using (2.7), where; $I_1$ and $I_2$ are the intensities at the reference and distance point respectively; and $r_1$ and $r_2$ are the ranges from the center point of transmission to the same positions.

$$P = 4\pi {r_1}^2 I_1 = 4\pi {r_2}^2 I_2 \tag{2.7}$$

Assuming the reference is positioned at 1m from the acoustic center, i.e. $r_1 = 1$, the spherical loss, at a distance of $r_2$, can be given by (2.8).

$$\begin{aligned} \mathrm{TL} &= 10 \log_{10}({r_2}^2) \\ &= 20 \log_{10}(r_2) \end{aligned} \tag{2.8}$$

From (2.8) it can be observed that the transmission loss increases, and thus the sound intensity decreases, by the square of the range. This form of loss is often known as *'Inverse-Square'* spreading.

A similar form of loss is cylindrical spreading, which applies when the transmitted sound is constrained within the medium by an upper and lower bound. Examples of this occur in long range transmissions, where the acoustic wave can become 'trapped' within a channel, giving a similar effect to a wave-guide or transmission line. Alternatively cylindrical spreading can occur in very shallow water, where the channel is constrained by both the surface and seabed.

In this case, due to the sound being bound within the channel, it can no longer be seen to be transmitted in a spherical manner. Instead, the wave propagation is modelled as a cylinder with the radius equating to the range of transmission and the height of the cylinder, $H$, representing the width of the channel guide.

As with spherical spreading the power is considered to be evenly spread across the whole surface of the cylinder. Therefore, assuming again that there is no loss in the medium, the power can be seen to be equal at both the reference point and the distant measurement point (2.9).

$$P = 2\pi r_1 H I_1 = 2\pi r_2 H I_2 \tag{2.9}$$

Given a reference point, positioned 1m from the acoustic centre (i.e. $r_1 = 1$), the cylindrical spreading loss can be calculated using (2.10).

$$\text{TL} = 10\log_{10}(r_2) \tag{2.10}$$

#### 2.2.1.2 Sound Absorption

Absorption loss represents the reduction in signal magnitude caused by the conversion of acoustic energy into heat. The absorption coefficient, $\alpha$, is typically shown to be the sum of several chemical relaxation processes, paired with the absorption observed in pure water. The two most significant chemical processes observed are: Magnesium Sulphate, $MgSO_4$, relaxation; and Boric Acid, $H_3BO_3$, relaxation. Absorption loss is often defined in the form (2.11), where: $P_1$, $P_2$ and $P_3$ represent the pressure dependencies; and $f_1$ and $f_2$ represent the relaxation frequencies [15] [16] [17].

$$\alpha = MgSO_4 \text{ Relaxation} + H_3BO_3 \text{ Relaxation} + H_2O \text{ Contribution}$$

$$\alpha = \frac{A_1 P_1 f_1 f^2}{{f_1}^2 + f^2} + \frac{A_2 P_2 f_2 f^2}{{f_2}^2 + f^2} + A_3 P_3 f^2 \tag{2.11}$$

Over the years, a range of algorithms have been developed to express the absorption loss observed in water. Various speculations have been made about the dominant causes of absorption, with a wide range of data collected to demonstrate the affects of different channel conditions, i.e. water temperature, salinity, etc. Despite the underlying theory becoming well defined, many of the developed algorithms still show variation from the collected data sets. This error relates to the difficulty in accurately measuring the observed loss, particularly at lower frequencies where many of the contributing processes have minimal impact compared with spreading losses.

Two models for absorption loss are generally considered, the first developed by Francois and Garrison in 1982 [16] [17] and the second by Ainslie and McColm in 1997 [18]. The model by Ailslie and McColm is seen to be considerably simpler while offering similar accuracy to the algorithm developed by Francois and Garrison, this model is therefore regularly referred to in UAC research.

Absorption loss is shown to be heavily frequency dependent, with greater losses being observed when operating in higher frequency bands. In contrast to spreading loss, absorption can be seen to have a significant effect on the available bandwidth, restricting operation at higher frequencies particularly when operating over longer ranges.

#### 2.2.1.3 Total Transmission Loss

A generic formula encompassing both forms of loss is expressed in (2.12), where: the expression to the left hand side relates to spreading losses; and the expression to the right combines any absorption losses caused by the channel. In this form: the absorption coefficient, $\alpha$, is expressed in dB/m; and $k$ is considered to be 10 for cylindrical spreading and 20 for spherical [14].

$$\mathrm{TL} = k \log_{10}(r) + \alpha(r) \tag{2.12}$$

### 2.2.2 Multipath

One of the most severe challenges in the UAC is the effect of multipath propagation. Because acoustic signals radiate in an omnidirectional fashion, the received signal is often composed of both the direct path and multiple reverberations. In many scenarios, the direct path or Line Of Sight (LOS) transmission can become heavily

corrupt by multipath arrivals causing both amplitude fluctuations and frequency distortion.

Reverberations occur when the transmitted signal reflects off a channel boundary, such as the surface, the seabed or any other subsea structure. Depending on the geometry of the channel and medium of the boundaries, the signal may then be reflected back towards the receiver or absorbed.

In deep water channels, where the water column is much deeper than the horizontal range of transmission, multipath signals will largely be attenuated by spreading and reflection losses caused by large grazing angles with the surface. With a clear distinction between the direction of arrivals, the remaining channel reverberation can often be minimised through the use of directional transducers or receivers.

For shallower channels this is not the case, due to reduced grazing angles; far less of the reflected signal is attenuated resulting in the received signal comprising additional multipath components. In cases where the difference between the direction of arrivals is insignificant, the use of spatial discrimination will be ineffective in isolating the direct arrival.

Examining the composition of the received signal, it can be seen that the delayed paths are heavily dependent on the interaction with the channel boundaries. The Rayleigh parameter, $R$, as defined in (2.13) is used to characterise the way the signal is reflected at the channel boundaries [19] [20] [21] [22]. Where; $f$ is the frequency of the signal; $c$ is the speed of sound; $\sigma$ is the RMS surface wave height, measured from trough to crest; and $\varphi$ is the grazing angle of the acoustic ray.

$$R = \left(\frac{2\pi f}{c}\right)\sigma sin(\varphi) \tag{2.13}$$

If $R \gg 1$ the boundary is typically found to act as a scatterer, spreading the signal energy in all directions. However, if $R \ll 1$ the boundary acts as a 'coherent specular reflector' [21] causing a reflection at the specular angle equal to the angle of incidence.

Several channel models have been developed for the UAC, and more specifically for a shallow water channel. In [23], Zielinski examines the effect the geometry of a shallow water channel has on the received acoustic signal. Fig. 2.1 presents the channel demonstrated by this model. Both the channel depth and the sound velocity within the medium are assumed to be constant.

The channel shown in Fig. 2.1 demonstrates five arrivals; the direct path, $DP$, and four multipath arrivals. The notation used can be broken down as: the first letter indicating the first reflective boundary; the second letter indicating the last reflective boundary and the subscript indicating the order of the arrival, $n$. The altitude of

the transmitter and receiver are represented by $d_1$ and $d_2$, where, in this model the height of the receiver is considered to be greater than that of the transmitter (i.e. $d_2 \gg d_1$).

For each of these arrivals the length of the path, $L_k$, can be calculated using (2.14). Where, $L$ is the horizontal transmit range and $A$ is the vertical transmit distance, given by (2.15).

$$L_k = \sqrt{L^2 + A^2} \tag{2.14}$$

$$A = \begin{cases} d_2 - d_1, & (k = -1) \quad \text{for } DP \\ 2(n-1)D + d_2 + d_1, & (k = -1) \quad \text{for } BB_n \\ 2nD - d_2 - d_1, & (k = 1) \quad \text{for } SS_n \\ 2nD + d_2 - d_1, & (k = 1) \quad \text{for } BS_n \\ 2nD - d_2 + d_1, & (k = -1) \quad \text{for } SB_n \end{cases} \tag{2.15}$$

The angle of arrival, $\psi$, for each of the acoustic paths can also be calculated using (2.16).

$$\psi = k \times tan^{-1}\left(\frac{A}{L}\right) \tag{2.16}$$

Therefore, the time delay from the arrival of the direct path, $DP$, to any of the multipath arrivals can be calculated using (2.17), in this example the delay between the direct path and the surface-surface arrival is shown.

$$\tau_{SS_n} = (t_{SS_n} - t_{DP}) = \left(\frac{SS_n - DP}{c}\right) \tag{2.17}$$

At a discrete period in time, $t$, the received signal, $r(t)$, can be presented as the summation of each of the multipath arrivals including the direct path arrival. As shown in (2.18), each arrival is scaled by an individual attenuation factor, $W_n$, dependent on the transmission and grazing losses. An additive noise signal, $n(t)$, is included to represent any additional background ambient noise present at the receiver.

$$r(t) = \sum_{n=1} W_n(t) s[t - \tau_n(t)] + n(t) \tag{2.18}$$

The multipath channel can successfully be modelled as a Tapped Delay Line (TDL), as shown in Fig. 2.2. Each of the delay blocks, $Z^{-1}$, are used to indicate the delays

between the direct arrival to each of the multipath arrivals. The scaling, by $W_n$, is used to demonstrate the amplitude fluctuation

In a multipath channel, any delayed arrivals present at the receiver can cause an effect known as Inter-Symbol Interference (ISI). This is caused by the delayed symbols arriving within the same period as a current symbol. Therefore, at a given time the received signal may be composed of both the wanted data symbol and echoes of several previous symbols.

Due to the time variability of the channel, resulting from changes in the sea state, the temperature gradients in the water and the changing profile of the sea floor, the induced ISI is unpredictable at any given period. Additionally due to the slow transmission velocity of sound waves, the length of time between the direct path and the last multipath arrival, known as the delay spread, can last tens of milliseconds. A method to both predict and suppress any delayed arrivals must be implemented to ensure the reliable demodulation of any received packets.

#### 2.2.2.1 Refraction

The sound velocity of an acoustic wave in water is highly affected by the variability in temperature and salinity. In a shallow water channel, i.e. $d < 50$m, the sound velocity can vary significantly at different times of year due to solar heating. The heating of the upper part of the water column can generate a severe thermocline causing a velocity gradient as the wave propagates to increased water depths [24]. At greater depths, the variation in sound velocity is less severe, due to the temperature and salinity remaining relatively stable throughout the season [20] [19].

As described by the Snell-Descartes law, the variation in sound velocity across different thermal layers can result in the acoustic wave becoming refracted. From (2.19), it can be shown that the acoustic wave is refracted by the interface between layers of water with different temperatures or salinity. Where: $c_1$ and $c_2$ represent the sound velocity within the first and second layers of water; and $\beta_1$ and $\beta_2$ express the angle of arrival and refraction from the normal of the boundary. If a low grazing angle is observed, i.e. $\beta$ is particularly small, total internal reflection will occur, resulting in the signal being unable to propagate into the second medium and being reflected back towards the surface / receiver.

$$\frac{\cos\beta_1}{c_1} = \frac{\cos\beta_2}{c_2} \tag{2.19}$$

Over longer transmission range a non-uniform sound velocity profile will result in severe bending or refraction of the generated sound waves. This complex form of sound propagation typically gives rise to a larger number of dispersed multipath

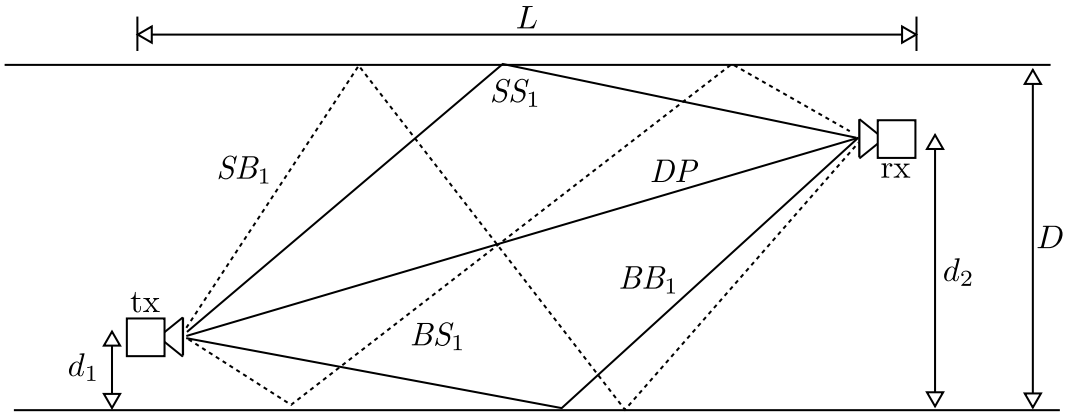


Figure 2.1: Shallow Water Channel Geometry

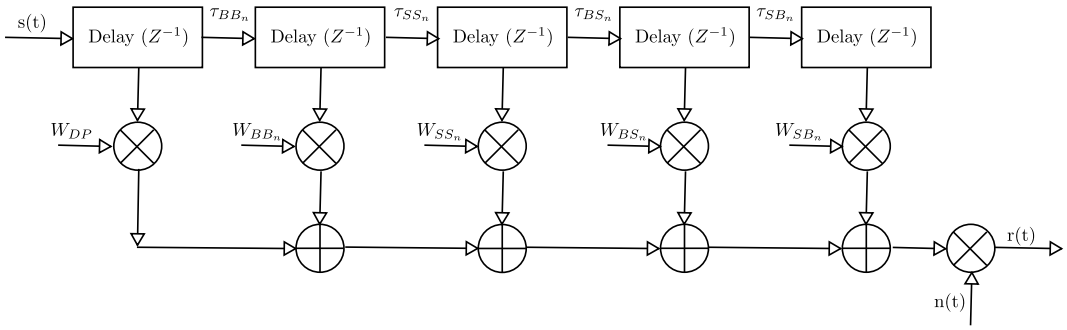


Figure 2.2: Multipath Channel Model: Tapped Delay Line (TDL)

arrivals. Over a shorter communication channel, such as that of a $\mu$ROV, total internal reflection will occur beyond the range between receiver and transmitter, allowing this effect to generally be neglected and significantly simplifying the transmission model to that of a uniform sound profile. Therefore, the distinguishing features of a short range channel can be primarily defined by its long time spread and sparse arrivals [25].

### 2.2.3 Doppler Effect

Due to the velocity of acoustic signals being much less than that of EM waves, the dynamic motion of the $\mu$ROV, may be seen to cause a severe Doppler shift to be induced onto the received waveform. If the transmitter moves towards or away from the receiver, the affect on the received signal can be expressed by (2.20), where, $f_c$ is the received carrier frequency, $f_o$ is the transmitted carrier frequency and $\Theta$ is the relative Doppler shift.

$$f_c = f_o(1 \pm \Theta) \tag{2.20}$$

As discussed by Kinsler *et al.* [26] (2.20) can be expressed in the form (2.21), where, $v_{rx}$ is the velocity of the receiver, $v_{tx}$ is the velocity of the transmitter and $c$ is the speed of sound in the medium.

$$f_c = f_o \left( \frac{c + v_{rx}}{c + v_{tx}} \right) \tag{2.21}$$

If the assumption is made that $v_{rx} \ll c$ and $v_{tx} \ll c$ then (2.21) can be simplified to (2.22), where, $\Delta f_c$ represents the change in frequency given as $\Delta f_c = f_c - f_o$.

$$\Delta f_c \approx \left( \frac{v_{rx} - v_{tx}}{c} \right) f_o \tag{2.22}$$

For the rest of this work, the numerator of the induced Doppler shift $(v_{rx} - v_{tx})$ will be referred to as the relative velocity, $v_r$. The induced Doppler shift can be either positive or negative, depending on whether the distance between transmitter and receiver has increased or decreased, which causes compression or dilation of the original signal.

In the case of a narrowband signal, where the bandwidth of the transmission is negligible in comparison to its centre frequency, the effect of Doppler shift can be approximated to that of a single frequency component (2.22). However in the case of a wideband signal, typical of those used for underwater acoustic communications, each of the individual frequency components are translated differently by

the incurred Doppler shift. In this case the Doppler shift may be more effectively modelled as a time dilation, i.e. an expansion or compression of the transmitted waveform, expressed by (2.23), where, $r(t)$ and $s(t)$ represent the transmitted and received signals respectively.

$$r(t) = s([1 \pm \Theta]t) \tag{2.23}$$

To highlight the severe nature of the underwater channel we assume a typical scenario, where a $\mu$ROV is moving at maximum speed ($\approx$ 2 m/s), away or towards a static surface vessel. In this case we calculate the fractional Doppler shift to be $\Theta = (2/1500) = 0.133\%$, for a sound velocity of $\approx$1500 m/s. This could be made worse by the addition of tidal flow moving the $\mu$ROV at an increased velocity, or movement of the surface vessel.

Comparing the induced Doppler shift in the underwater channel to a complex case in the RF channel, the increased severity can be observed. For a worst case example, take into account two jet planes travelling directly towards each other at a velocity of 1500mph ($\approx$670m/s). Assuming the speed of the transmissions to be that of the speed of light, the fractional Doppler shift can be calculated to be $\Theta = (1340/3 \times 10^8) \approx 4.5 \times 10^{-6}\%$

It is also important to consider the rate of change of velocity, or acceleration, of the vehicle. Due to the $\mu$ROV being a very dynamic vehicle, rapid changes in both direction and speed can occur over the length of a single packet. Therefore, a method of tracking and compensating for the instantaneous Doppler shift is essential to ensure error free demodulation and decoding.

### 2.2.4 Noise and Interference

A wide variety of underwater sources can cause both low frequency and high frequency noise and interference. Fig. 2.3 illustrates a range of typical ambient noise sources, highlighting their spectral contribution across a wide range of frequencies. Within the frequency band typically occupied by acoustic communication transmissions, i.e. 5kHz $< f_c <$ 60kHz, the sea state and heavy precipitation effects can be seen to be dominant over other sources of ambient noise.

#### 2.2.4.1 Ambient Noise

A wide range of research has been carried out to examine the sources of background ambient noise in the UAC. In general the three main contributing sources of ambient noise are identified as, water motion, man-made sources and marine life. Each of

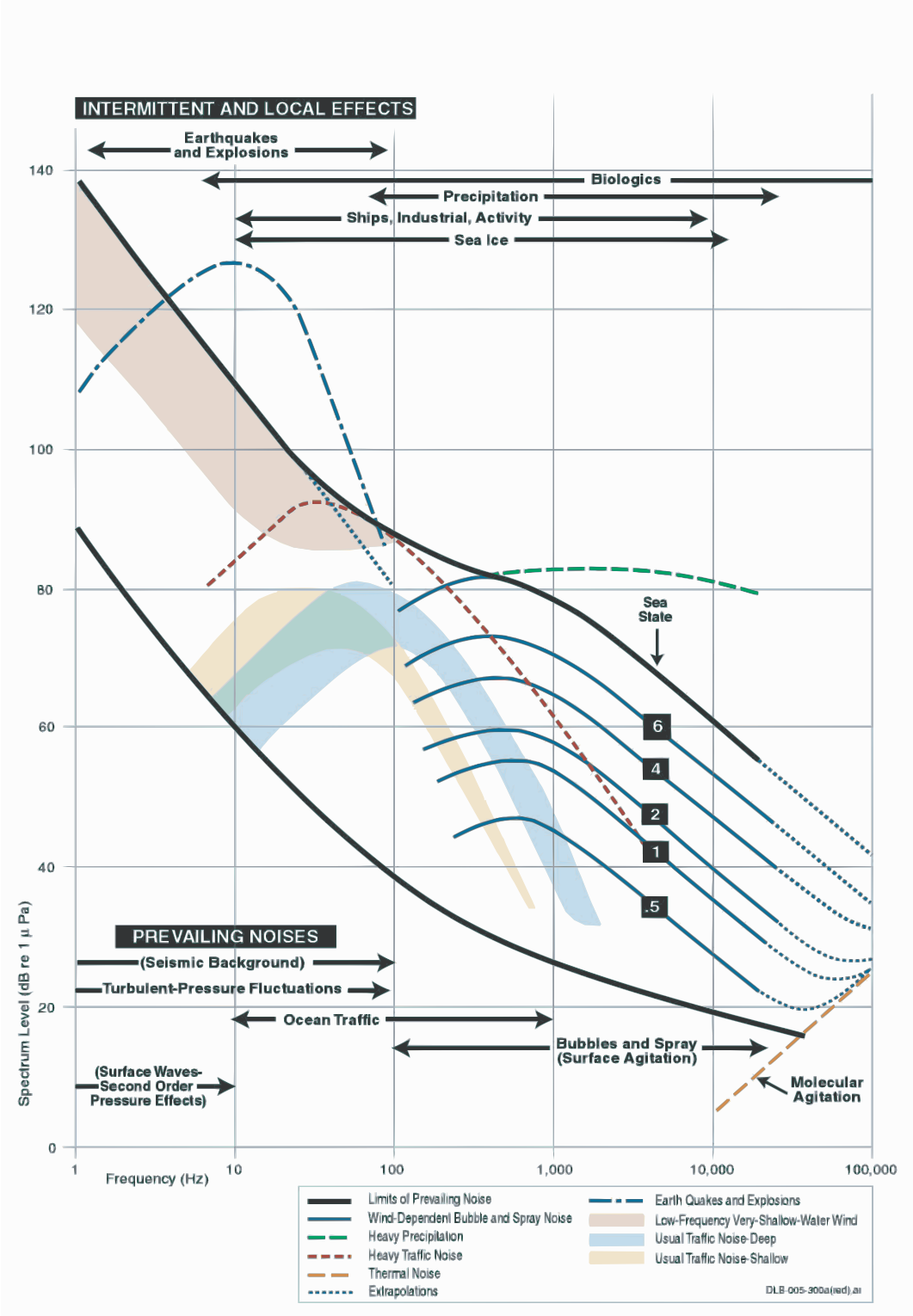


Figure 2.3: Wenz curves demonstrating the pressure spectral density levels of marine ambient noise caused by commercial shipping, geological activity, wind, weather and marine mammal activity. Original curves developed by Wenz [27], with additional overlays of marine mammal activity by David Bradley. Original source image from *"Ocean Noise and Marine Mammals"* [28]

these sources tend to have a varied response depending on the frequency band, repetition rate and magnitude of generated noise. Further details on these sources and the nature of the emitted signal is given below:

**Water Motion**

The various movement and flow of water can produce a wide range of interfering noise, across a wide frequency band. Water motion can include; the breaking of waves, both close to shore and mid ocean; the flow of water past the receive hydrophone, caused by tide and currents in harbour estuaries; and surface disruption caused by rainfall and wind causing the surface to become broken up and distorted. Ambient noise caused by water motion is heavily dependent on the environment of deployment, the proximity to areas of breaking water, strength of the tide, wind strength and rainfall all have a large effect on the magnitude of the background noise.

**Man-made Sources**

In both offshore and inshore harbour applications, a major source of man-made noise is caused by shipping movement. Commercial and leisure shipping is the cause of a large proportion of low frequency noise, mainly due to propeller movement and cavitation. Since the 1960's an increase in background noise has been observed and linked to higher numbers of large container ships [29]. In harbour and coastal environments, additional man-made noise is present due to industrial noise generated ashore and around dock areas. Examples of such disturbances are hammering, pile driving and noise related to the loading and unloading of vessels. These forms of noise can cause high magnitude, broadband interference.

**Biological Sources**

Marine life can be attributed to a wide range of interference within the UAC. Various species found subsea, can be seen to be responsible for the generation of different tones and noises across the acoustic spectrum. These noises include clicks, whistles, taps and cries which can occur in a repetitive or singular manner. Examples of such noises are the clicking caused by freshwater shrimp and higher pitched pulses linked to porpoises and whales.

It should be stressed that within the underwater channel some sources of noise are predictable and can be estimated, depending on the location of operation and time of year. However, other forms of ambient noise may be seen to be erratic and unpredictable in nature. Ambient noise is heavily time variant, particularly within the shallow water channel, and can be seen to be inversely proportional to the depth of the channel.

#### 2.2.4.2 Application Induced Noise

Along with the generic sources of noise discussed previously, a form of noise which is very application specific is the interference created by the $\mu$ROV itself. Wideband noise has been shown to be generated by the vehicles thrusters, as shown in Fig. 2.4. Due to the proximity to the transducers mounted on the vehicle this form of noise can have a heavily detrimental effect.

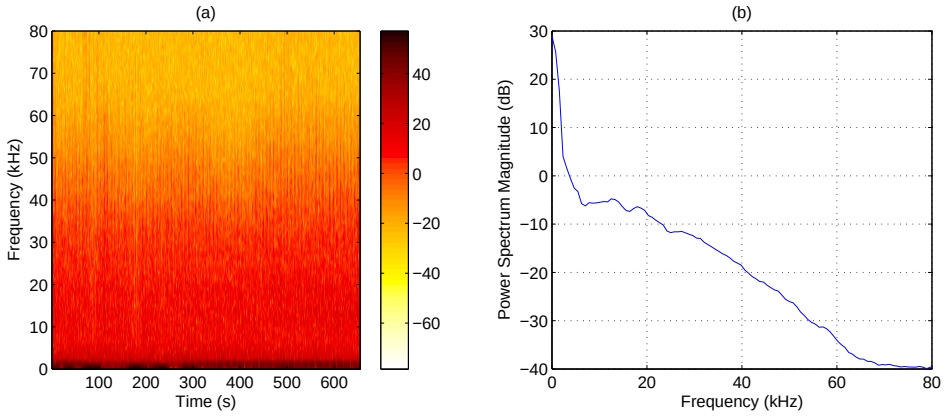


Figure 2.4: Analysis of Self Induced $\mu$ROV Thruster Noise:
(1) Spectrogram, (2) Power Spectrum Density (PSD)

An increase in noise has been found to be linked to the operation of the vehicle at shallower depths, where low pressure gives rise to the possibility of cavitation. Additionally, slow speed operation has been found to cause *'cogging'* of the thrusters, resulting in the emission of a high pitched sound. Further evaluation of the incurred thruster noise is conducted in Chapter 4.

## 2.3 State of The Art: Acoustic Telemetry

An initial review of relevant research is conducted, discussing the historical background of underwater acoustic communications and highlighting areas of recent developments. Various communication techniques are presented, examining their capability in terms of data rate, operational range and reliability.

### 2.3.1 Historical Background

Prior to the late 1970's the majority of published work, focused on the transmission of information utilising basic analogue techniques. The development of reliable digital modulation techniques was initially observed with the implementation of

incoherent Frequency Shift Keying (FSK), which had traditionally be utilised in terrestrial radio systems. FSK techniques were found to be naturally suited to operation in the UAC and demonstrated reliability in the presence of time and frequency spreading caused by the doubly selective nature of the channel.

However, the development of FSK techniques was seen to diminish during the late 80's to early 90's, with the only notable improvement being the use of larger signalling alphabets, made possible by the improved capability of modern processing architectures. The lack of research was largely provoked by FSK's inefficient use of bandwidth, causing research to instead focus on the development of coherent Phase Shift Keying (PSK) and Quadrature Amplitude Modulation (QAM) techniques [30].

### 2.3.2 Receiver Developments

Despite PSK offering better bandwidth efficiency, a considerable limitation of a coherent transmission scheme is the difficulty in suppressing the effects of a highly dynamic dispersive multipath channel. A wide variety of research has focussed on the development of suitable techniques to overcome the sparse channel conditions. These techniques have included: the development of adaptive equalisation structures; and the use of large multi-element array receivers.

To simplify the carrier recovery of the transmitted sequence differential-PSK was often preferred, encoding information in the relative change in phase from the previous symbol, rather than from a known reference signal. In the early stages of development, differential strategies were favoured due to the compromise between improved throughput and system complexity. Recent developments have tended to focus on fully-coherent communication schemes, and demonstrate a significant reduction in error probability [31].

#### 2.3.2.1 Channel Equalisation

Many early examples of coherent communication systems focused on transmissions through deep vertical channels, where minimal multipath arrivals were observed due to negligible surface and seabed reflections. In such cases, if a significant reflection path was evident, 'baffling' techniques were used to suppress the multipath arrival, thus negating the requirement for a complex equaliser structure. An early example of a coherent D-BPSK transmission, through a vertical channel, was presented in 1985 by Olson *et al.*. The proposed scheme demonstrated data rates of upto 2kbps across a deep vertical channel, at ranges of $\approx$ 6km [32].

A significant turning point in the use of coherent phase-based transmission schemes came with the development and application of adaptive equaliser structures, such as

the Linear Equaliser or the Decision Feedback Equaliser, which were employed to actively suppress any Inter-Symbol Interference (ISI). An early example of an adaptive equaliser structure was presented by Suzuki *et al.* in 1992. A communication link, utilising D-QPSK, was developed to transmit colour images from a deep sea submersible at a data rate of 16kbps. Successful transmissions were achieved through a vertical channel at a range of upto 6.5km. A combination of directional transducers, with an 80° beamwidth, and a fractionally spaced LE were shown to suppress any multipath arrivals [33]. A similar example, utilising a 16-QAM transmission scheme, was presented in 1989 by Kaya and Yauchi [34]. In this case, reliable transmissions were demonstrated across a short range, 60m, shallow water channel. Reliable data rate in the order of 500kbps, were shown to be possible, utilising steerable narrow beam transducers, 5°, and a symbol spaced DFE.

#### 2.3.2.2 Spatial Diversity Processing

Some of the first examples of coherent transmissions through long range horizontal communication channel were demonstrated by Stojanovic, Catipovic and Proakis during 1993 and 1994 [35] [36]. Two sets of practical results were examined: the first within a deep water channel, $500-1500$m, and at transmission ranges of 40-140 nautical miles; and the second within a shallow water channel, $\approx$50m, at transmission ranges of 15-65 nautical miles. In contrast to the previously discussed research, delay spreads of upto 100ms were exhibited by the long range horizontal channel.

In combination with a traditional DFE structure, the use of a multi-channel diversity array was recommended, enabling the exploitation of long delay spreads, through coherently combining the energy of each of the transmission paths. The research clearly indicated the benefits of a multi-channel DFE structure by demonstrating reliable data rates of upto 1.5kbps, at ranges of 48 nautical miles. The described array consisted of 20 elements spaced vertically over a depth of 15-35m. A comparison with a single element receiver was conducted, demonstrating an improvement in SNR of approximately 3dB and a significant reduction in symbol errors [35].

A range of publications have demonstrated similar structures, combining multi-channel arrays with adaptive equaliser structures to offer gains from either spatial diversity processing or adaptive beamforming. The benefits of such systems have supported transmissions across long range, shallow water channels at data rates of upto 20kbps [37]. A selection of published research, demonstrating various forms of coherent receiver structures, are presented in Table 2.3. The listed publications demonstrate systems operating across a wide variety of communication channels, utilising different combinations of: equaliser structures; multi-element arrays; and directional transducers.

| Research Group | Data Rate | Range | Channel | $f_c$ ($f_{band}$) | Receiver | Transmitter | Equaliser | Ref |
|---|---|---|---|---|---|---|---|---|
| Wood Hole (WHOI)<br>(Freitag *et al.*) | 1670bps<br>6700bps | 4km Horiz<br>2km Horiz | Shallow<br>(10 - 30m) | 3kHz (2kHz)<br>25kHz (10kHz) | 8 Element Towed<br>6 Element Vertical | Omnidirectional<br>Directional | xxx | [38] |
| Newcastle University<br>(Neasham *et al.*) | 20kbps | 2km<br>(Horizontal) | Shallow<br>(<100m) | 49kHz<br>(28kHz) | 7 Element<br>($\lambda$ spaced) | | DFE | [37] |
| Wood Hole (WHOI)<br>(Freitag *et al.*) | 5kbps<br>to 15kbps | 3000m<br>(Vertical) | Deep<br>(3100m) | 15kHz<br>(5kHz) | | | DFE | [39] |
| ENST-Bretagne<br>(Trubuil *et al.*) | 6.7kbps<br>to 40kbps | 500m - 2km | Mixed<br>(22 - 200m) | 20kHz or<br>35kHz | 4 Element Vertical<br>($5\lambda$ spaced $\approx$ 20cm) | Omnidirectional | DFE | [40] |
| KDD R&D Labs<br>(Kojima *et al.*) | 16kbps | >1200m<br>(Vertical) | Deep<br>($\leq$400m) | 55kHz<br>(10kHz) | Directional (45°) | Directional (45°) | LE | [41]<br>[42] |
| NEC Corporation<br>(Suzuki *et al.*) | 16kbps | >6500m<br>(Vertical) | Deep<br>(6500m) | 20kHz<br>(8kHz) | Directional (80°) | Directional (35°) | LE | [43] |
| MIT / WHOI<br>(Pelekanakis *et al.*) | upto<br>150kbps | 10m<br>(Vertical) | Shallow<br>(Dockside) | 75kHz<br>(30kHz) | Directional (6°) | Directional (6°) | LE<br>DFE | [44] |
| Oki Electric<br>(Kaya *et al.*) | 500kbps | 60m<br>(Horizontal) | Shallow<br>(2m) | 1MHz<br>(250kHz) | Directional (5°) | Directional (5°) | LE | [39] |

Table 2.3: Summary of Single Carrier High Data Rate Underwater Acoustic Communication Systems
($f_c$: Carrier Frequency, $f_{band}$: Bandwidth)

#### 2.3.2.3 Multi-Carrier Transmissions

In recent years, research has tended towards the development of Multi-Carrier Modulation (MCM) techniques for the UAC. Techniques, such as Orthogonal Frequency Division Multiplexing (OFDM), have been shown to offer inherent tolerance to multipath channels, through division of the available frequency band into multiple subcarriers, each exhibiting flat frequency fading [45]. A particular benefit of OFDM is the reduced complexity of the receiver structure, which negates the requirement for extensive equaliser structures. However, such systems still pose a range of challenges, including the reduction of Peak to Average Power (PAPR) and in the implementation of an accurate Doppler compensation technique.

Despite some of the complications experienced in developing practical OFDM systems, results are beginning to demonstrate the true performance of a multi-carrier system for underwater acoustic communications. In 2009, Li *et al.* demonstrated the ability to support data rates of upto 125kbps across ranges of several 100s of metres utilising a Multi-Input-Multi-Output (MIMO) OFDM structure [46]. A combination of a multi-element array and narrow sub-bands ensured successful operation through particularly hostile channel conditions. Further demonstration of the performance of OFDM have been presented by: Stojanovic in 2006, demonstrating data rates of upto 30kbps, across ranges of 2.5km through a shallow water channel [47]; and Huang *et al.* in 2011, achieving throughput in the region of 5-10kbps at a range of $\leq$1km [48].

Although the benefits of MCM schemes are clearly evident for static point to point links, the complexity in overcoming variations in Doppler shift restrict their use for a $\mu$ROV application. A wide range of research is currently being explored to compensate for varying Frequency Carrier Offset (FCO), however the ability to overcome the dynamic motion of the vehicle is still yet to be proven [49] [50].

#### 2.3.2.4 *'Turbo'* Decoding Techniques

Over the last decade, a wide range of research has explored the use of iterative receiver structures for transmission across the UAC. This development was heavily motivated by the *'Turbo'* concept published by Berrou, Glavieux and Thitimajshima at a conference in 1993. The presented coding scheme demonstrated the ability to deliver performance very close to the theoretical Shannon bound [51]. The benefit of the turbo principle was found to correspond with the use of an iterative decoding structure, exchanging soft decisions between 2 convolutional decoders to improve the certainty of the output sequence.

The key benefit of this approach comes from the successful use of soft decisions. In contrast to more traditional receiver structures, which truncate the decoder output

to hard limited binary values, the soft decoding structure is shown to supply more detailed information relating to the reliability of the decoded symbol. Two forms of soft output are typically utilised, these are: A Posteriori Probabilities (APP) and Log Likelihood Ratios (LLR). By exchanging such soft decisions between the two decoder blocks, and through performing multiple iterations, the performance of the receiver structure can become closer to that of the optimal solution. Based on this concept, the turbo equalisation structure was proposed by Douillard *et al.*, utilising the exchange of soft decisions between the channel equaliser and soft decoder to improve the performance of the receiver [52].

Since early 2000, several publications have demonstrated the successful application of turbo equalisation within the underwater acoustic channel. This has included: the work by Sifferlen *et al.* who demonstrated the performance of a multi-channel iterative receiver structure, through a 120m deep channel and at ranges of upto 10km [53]; an analysis of different turbo receiver structures by Sözer *et al.*, through shallow water channels, $<$ 15m and at ranges of upto 1.5km [54]; and the long term deployment of a turbo equalisation system conducted by Otnes and Eggen across an 850m shallow water channel [55]. Additionally, work conducted at Newcastle University in 2009, has examined the use of a more computationally efficient BICM-ID receiver structure, comprising a single convolutional encoder and decoder. Results demonstrated the ability to support data rate of 8kbps through a shallow water channel, $<$ 50m, at ranges of upto 1km utilising a single element receiver structure [56].

## 2.4 Summary

This chapter examines a selection of communication mechanisms suitable for the transmission of information through a shallow water channel. By exploring the benefits and limitations of each approach, acoustic signals are shown to best accommodate the requirements of the proposed $\mu$ROV application. A review of the physical characteristics of the shallow water channel highlight the four main challenges of reliable acoustic communications: transmission loss; time varying multipath; Doppler shift; and background ambient noise.

A concise review of the research conducted in the field of underwater acoustic telemetry is presented. The use of coherent communication techniques, combined with adaptive equaliser structures and multi-channel receiver arrays are shown to be capable of supporting reliable data rates in the order of 10-20kbps through shallow water channels [57]. Additionally, multi-carrier OFDM schemes are shown to offer an inherent tolerance to severe multipath channels and a significant reduction in computational complexity of the receiver structure [30]. Finally, iterative decoding

and demodulation techniques are presented, highlighting the benefits of a 'turbo' equalisation structure in offering increased reliability for a single element receiver.

Future chapters examine the development of a suitable communication scheme and receiver structure, capable of suppressing the detrimental time varying effects of the shallow water channel. Specific focus is placed on the challenges of supporting reliable communications from a dynamic $\mu$ROV, at data rates suitable for the continuous streaming of video or sonar data.

# Chapter 3

# Underwater Acoustic Receiver Algorithms

This chapter presents three different signalling approaches utilised in subsea communications: single carrier modulation; spread spectrum techniques; and multi-carrier modulation. Initially an overview of the different signalling approaches is presented, followed by a more detailed examination of the specific receiver requirements. Analysis of a variety of different receiver structures will be conducted, highlighting the theoretical performance of each and discussing their suitability in the discussed application.

An evaluation of previous research is intended to enable discussion of the different transmission schemes, highlighting their advantages and limitations relating to the proposed application. Additionally, the theoretical background presented within this chapter should allow the reader to give context to the research presented and enable an understanding of the developments required to produce a reliable communication scheme.

## 3.1 Signal Design

### 3.1.1 Single Carrier Communication

To enable data to be sent through the UAC a method of reliably conveying information as an analogue waveform is required. Typically, in the case of single carrier modulation, a sinusoidal carrier wave occupying the entire channel bandwidth is digitally modulated through adjustments to its phase and amplitude [31]. Three linear single carrier modulation schemes are discussed in this work: Amplitude Shift Keying (ASK); Phase Shift Keying (PSK); and Quadrature Amplitude Modulation (QAM).

#### 3.1.1.1 Amplitude Shift Keying (ASK)

Utilising Amplitude Shift Keying (ASK) data is conveyed on a constant phase carrier signal, using $M$ different signal amplitudes. Each amplitude level is used to represent a symbol of $k$-bits, where the number of bits per symbol can be calculated as $k = \log_2(M)$. The output signal of an M-ASK modulated signal, $s_m(t)$, is given as (3.2), where $g(t)$ defines the pulse shape of the transmitted signal; $f_c$ is the centre frequency of the carrier signal; and $A_m$ is the amplitude used to represent each symbol, chosen from the alphabet expressed by (3.3).

$$s_m(t) = Re\left[A_m g(t) e^{j2\pi f_c t}\right] \qquad m = 1, 2, ..., M \tag{3.1}$$

$$= A_m g(t) \cos(2\pi f_c t) \tag{3.2}$$

$$A_m = 2m - 1 - M \qquad m = 1, 2, ..., M \tag{3.3}$$

Fig. 3.1a, presents the signal space diagram for 4-ASK.

#### 3.1.1.2 Phase Shift Keying (PSK)

Alternatively, in the case of Phase Shift Keying, data is represented by changes in the phase of the waveform rather than the amplitude. Similarly to ASK, $M$ states are used to convey the required data at a rate of $k$ bits per symbol. The carrier phases, $\theta_m$, utilised by an M-PSK system can be described by (3.4) with the resulting output waveform, $s_m(t)$, expressed as (3.6).

$$\theta_m = \frac{2\pi(m-1)}{M} \qquad m = 1, 2, ..., M \tag{3.4}$$

$$s_m(t) = Re\left[e^{j\theta_m} g(t) e^{j2\pi f_c t}\right] \qquad m = 1, 2, ..., M \tag{3.5}$$

$$= \cos(\theta_m) g(t) \cos(2\pi f_c t) - \sin(\theta_m) g(t) \sin(2\pi f_c t) \tag{3.6}$$

The signal space diagram for QPSK and 8-PSK are shown in Fig. 3.1b, and Fig. 3.1c respectively. As a consequence of the carrier signal having a constant amplitude, the constellation points of both QPSK and 8-PSK can be seen to lie on a unit circle.

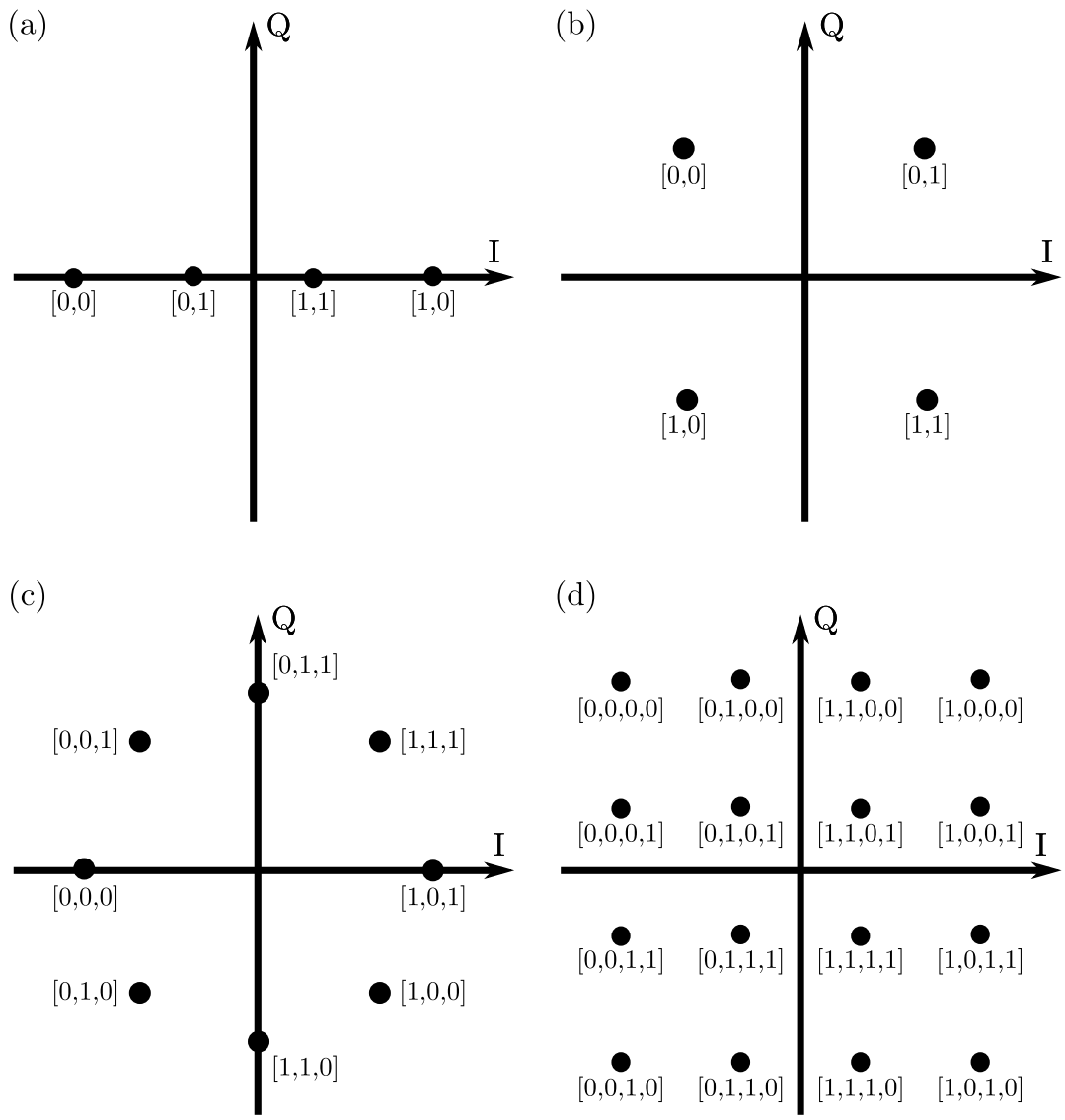


Figure 3.1: Signal Mapping of Different Modulation Schemes, Utilising Gray Coding: (a) 4-ASK, (b) QPSK, (c) 8-PSK and (d) 16-QAM

#### 3.1.1.3 Differential Phase Shifted Keying (D-PSK)

An alternative representation of M-PSK, is Differential Phase Shift Keying (D-PSK). In the case of D-PSK symbol information is represented by a change in the relative phase between the current and previous symbol. Such transmissions are regularly referred to as non-coherent modulation schemes,due to the removal of the local carrier waveform. This approach can be seen to significantly reduce the complexity of the receiver structure, removing the need to generate a synchronised local carrier waveform and simplifying the symbol recovery process. The carrier phases, $\theta_m$, utilised in a M-DPSK system are described by (3.7), where, $\theta_m(t)$ represents the current carrier phase and $\theta_m(t-1)$ represents the phase of the previous symbol.

$$\theta_m(t) = \begin{cases} \theta_m(t-1) + \left(\dfrac{2\pi(m-1)}{M}\right) & \text{where, } t > 0 \\ \pi & \text{where, } t = 0 \end{cases} \tag{3.7}$$

Although D-PSK mappings offer a reduction in receiver complexity, the simplified mapping process can be seen to result in a degradation in the BER performance when compared with a perfectly synchronised M-PSK transmission. If the computational requirements allow, and if an alternative method of symbol synchronisation is available a coherent scheme is always preferable [58].

#### 3.1.1.4 Quadrature Amplutude Modulation (QAM)

In the case of Quadrature Amplitude Modulation (QAM), the generated output signal can be seen to be a combination of both ASK and PSK, with differing phases and amplitude levels used to convey the binary data stream. To generate a QAM symbol, two quadrature carrier signals are used, $\cos(2\pi f_c)$ and $\sin(2\pi f_c)$. The two carriers are modulated simultaneously, where $A_{mi}$ and $A_{mq}$ express the magnitudes of the inphase and quadrature carriers respectively. The modulated output signal $s_m(t)$ is expressed by (3.9).

$$s_m(t) = Re\left[\left(A_{mi} + jA_{mq}\right) g(t) e^{j2\pi f_c t}\right] \qquad m = 1, 2, ..., M \tag{3.8}$$

$$= A_{mi} g(t) \cos(2\pi f_c t) - A_{mq} g(t) \sin(2\pi f_c t) \tag{3.9}$$

The signal space representation for rectangular 16-QAM is shown in Fig. 3.1d, the affect of both phase and amplitude modulation can be seen through the grid like positioning of the constellation points.

#### 3.1.1.5 Mapping Evaluation

Three different mapping schemes have been presented to enable a binary data sequence to be represented on a single carrier waveform. Through changes in amplitude, phase, or a combination of the two, a range of symbols can be generated to allow data to be effectively conveyed through the underwater channel. Each of these schemes demonstrate a range of advantages and disadvantages when utilised for communication across the UAC.

A method often used of evaluate the performance of a specific modulation scheme is the minimum euclidean distance, $d_{\min}$. The euclidean distance measurement expresses the spacing between two neighbouring points when represented in an IQ signal space plot. Higher order modulation schemes, will typically exhibit closer constellation points, resulting in a reduced minimum euclidean distance. Increased separation can be seen to enable clearer estimation of the received symbol, with less opportunity to wrongly predict an incorrect symbol value. Therefore reduced spacing between neighbouring symbols can be seen to result in a system struggling to overcome severe channel conditions. Table 3.1 evaluates the minimum euclidean distance for each of the discussed schemes, with varying modulation depths between 2 and 32.

| Scheme | $d_{\min}$ | M=2 | M=4 | M=8 | M=16 | M=32 |
|---|---|---|---|---|---|---|
| M-ASK | $\sqrt{\frac{12\log_2(M)}{M^2-1}\varepsilon_{\text{bavg}}}$ | 2 | 1.26 | 0.75 | 0.43 | 0.24 |
| M-PSK | $2\sqrt{\log_2(M)\sin^2\left(\frac{\pi}{M}\right)\varepsilon_{\text{bavg}}}$ | 2 | 2 | 1.32 | 0.78 | 0.44 |
| M-QAM | $\sqrt{\frac{6\log_2(M)}{M-1}\varepsilon_{\text{bavg}}}$ | N/A. | 2 | N/A. | 1.26 | 0.98 |

Table 3.1: Evaluation of Suitable Modulation Schemes for High Data Rate Single Carrier Communications. Comparison of Minimum Euclidian Distance, $d_{\min}$, for M-ASK, M-PSK and M-QAM Schemes.

In each of the equations shown in column 2, $M$ expresses the modulation order and $\varepsilon_{\text{bavg}}$ is the average energy per bit. Therefore, the total energy per symbol, $\varepsilon_{\text{savg}}$, can be calculated using (3.10). It should also be noted that each of the values expressed for row 3, are based on rectangular QAM. Therefore, the calculated values for $M = 2$ and $M = 8$ are not included as they are considered invalid states.

$$\varepsilon_{\text{bavg}} = \frac{\varepsilon_{\text{savg}}}{\log_2(M)} \tag{3.10}$$

From the results presented, there are several points to note. Examining the various PSK mappings, the use of a two state, Binary PSK (BPSK) scheme is typically an inefficient use of the available bandwidth. The constellation spacing can be seen to be comparable with Quadrature PSK (QPSK), i.e. M=4, where double the number of bits can be represented over the same symbol duration and with the same minimum euclidean distance. Additionally, in most realistic scenarios the small increase in separation of 8-PSK over 16-QAM will have a minimal affect on the performance of the receiver structure. Therefore, most applications will typically select the latter of the two schemes due to the improved throughput offered.

A considerable restriction on schemes utilising variable amplitude levels, i.e. QAM or ASK, is the requirement for a linear transmit amplifier and linear signal processing stages. Any none linear effects performed on the generated waveform will cause symbol distortion and result in a significant loss in performance. In the case of PSK, where a constant amplitude carrier wave is utilised, a simpler non-linear amplifier can be utilised. Where possible the use of linear amplifiers is avoided, due to the complex design requirements and additional expense incurred, for this reason the use of QAM and ASK are often ignored.

### 3.1.2 Spread Spectrum Communication

An alternative technique suitable for use in the UAC is Spread Spectrum (SS) communications. The underlying principle behind these systems is to intentionally spread the generated infomation signal across the frequency domain, resulting in a generated wide band transmission. In comparison to the single carrier techniques disccused previously, spread spectrum signalling incurs a penalty in bandwidth efficiency in order to operate at very low SNR levels.

Spread spectrum signalling can be summarised using the definition made by Haykin, in his book *Communication Systems*, [59] as:

1. *A means of transmitting a sequence of data, where the bandwidth utilised significantly exceeds the minimum bandwidth required.*

2. *The spreading occurs prior to transmission, through the use of a code independent of the data sequence. The same code is used at the receiver to despread the received signal and allow the original data sequence to be recovered.*

Spread spectrum typically uses a noise-like sequence to spread a narrowband infomation signal over a relatively wide bandwidth. Fig. 3.2 demonstrates the spectrum of a narrowband infomation signal (a), with bandwidth $f_{\min}$, and the spectrum of a transmitted waveform post spreading (b), of bandwidth $f_{\text{ss}}$.

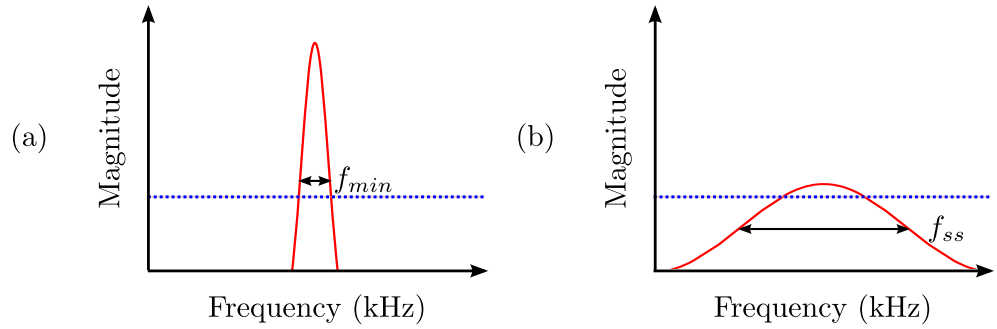


Figure 3.2: Representation of the Power Spectral Density for: (a) A Narrow Band Information Signal, (b) Wide Band Transmission Post Spreading

The benefits of spread spectrum communication can be explored by referring back to the Shannon Hartley theorem, for theoretical bandwidth capacity [31]. In any given channel, the theoretical capacity, $C$, can be seen to be a function of the available bandwidth, $B$, the signal level, $S$, and the noise level, $N$ (3.11).

$$\frac{C}{B} = \log_2\left(1 + \frac{S}{N}\right) \tag{3.11}$$

Through logarithmic expansion, [60], it can be shown that by utilising a wider bandwidth it is possible for successful error-free transmissions in a channel where the signal level is comparable to the background noise level (i.e. $S/N \leq 1$) (3.12).

$$B \approx \frac{NC}{S} \tag{3.12}$$

A range of further benfits can be observed in the case of spread spectrum systems:

**Ability to Operate in Low SNR Conditions** : By correlating the received waveform with a local version of the spreading code, the desired information can be reduced back to its original bandwidth. Any additional interference or noise will be spread out of band, allowing additional filtering to be used to significantly suppress its effects. This effect can be referred to as the processing gain of the spread spectrum system and is expressed as (3.13), where, $G_p$ is the processing gain, $B$ is the transmission bandwidth and $R_{\text{info}}$ is the information rate.

$$G_p = \frac{B}{R_{\text{info}}} \tag{3.13}$$

**Multipath Tolerant** : By spreading the signal energy across a bandwidth much wider than the information rate, spread spectrum signals can be seen to naturally suppress the effects of frequency selective fading. An example is the fading caused by the channel reverberation effects observed in a shallow water environment. Such fading will cause minimal system outages as only a small proportion of the bandwidth will be affected.

**Difficult to Unintentionally Detect** : If the same energy per bit prior to spreading is used as is with a narrow band single carrier system, a very low Power Spectral Density (PSD) is observed. In some cases the PSD may appear lower than the noise floor of the channel inhibiting unintentional detection. Additionally, if the spreading code is unknown by the recipient, the transmitted signal can become very difficult to decode.

**Resistant to Jamming** : By spreading the signal over a wide bandwidth, the system can easily overcome jamming by narrow band signals. Such interference will only affect a small percentage of the utilised bandwidth, resulting in minimal degradation of the transmitted waveform. Alternatively, in the case of wideband jamming, the processing gain of spread spectrum signals allows for operation down to a very low SNR. This causes rejection of such artificial interference and ensures continuous error free transmission.

**Capable of Unsynchronised Multiple Access** : By using different spreading codes per user, multiple transmissions can occur simultaneously in the same time and frequency slot. This technique is referred to as Code Division Multiple Access (CDMA).

Spread spectrum techniques are presented as a method of ensuring increased reliability, at a cost to the required bandwidth and feasible data rate. Typical applications therefore focus on the transmission of low data rate information, such as status updates or sensor readings, through channels which exhibit complex multipath arrivals or high levels of background noise. Spread spectrum techniques are generally not suited to higher data rate transmissions due to their inefficient use of the available bandwidth.

### 3.1.3 Multi Carrier Communications

In recent years, the focus of research in both terrestrial and subsea communications has been on the use of multi-carrier modulation schemes. Initially systems focused on the use of Frequency Division Multiplexing (FDM), which utilised non-overlapping sub-bands. This technique minimised any inter-channel interference

through minimising the spectral overlap of neighbouring bands, however, a considerable drawback of the scheme was the inefficient use of the available bandwidth, due to large proportions of the spectrum being utilised as guard intervals between consecutive bands. Additionally, demanding hardware design was required to optimise the performance of narrow band filters, ensuring the maximum suppression of any remaining inter-channel interference.

The initial concept of overlapping sub-carrier bands was first presented in the mid-1960s by Burton Saltzberg of Bell Laboratories. The scheme now referred to as Orthogonal Frequency Division Multiplexing (OFDM), utilises overlapping sub-carriers to maximise bandwidth utilisation. To minimise the interference between carriers, the frequency of the carrier signals are carefully selected to be linearly independent. To ensure carriers are orthogonal, the spacing between consecutive carriers must be selected as a multiple of $\frac{1}{T_o}$, where, $T_o$ refers to the duration of a single OFDM symbol.

Fig. 3.3 demonstrates how the available spectrum is utilised by OFDM schemes. The available bandwidth, $\Delta f$, can be seen to be divided into $N$ narrow sub-bands, each occupying an equal bandwidth of $\Delta f_{sb}$ (3.14).

$$\Delta f_{sb} = \frac{\Delta f}{N} \tag{3.14}$$

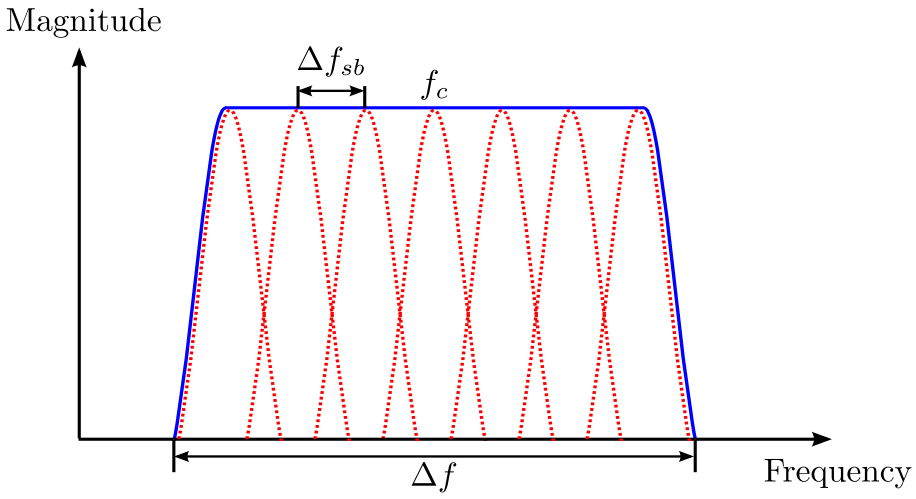


Figure 3.3: Orthogonal Frequency Division Multiplexing: Division Of Available Bandwidth Into Multiple Subcarriers

Based on this description, the output modulated OFDM signal, $s(t)$, can be expressed in the form of $N$ parallel carrier signals (3.15), where, $d_k$ is the constellation symbol modulated onto the $k$th sub-carrier, and $g(t)$ is the pulse shape of each sub-band.

$$s(t) = Re\left[\sum_{k=0}^{N-1} d_k e^{j2\pi f_k t} g(t)\right] \tag{3.15}$$

We can therefore define the centre frequency of $k$th sub-carrier, $f_k$, using (3.16), where, $f_0$ represents the frequency of the first sub-carrier.

$$f_k = f_0 + k\left(\frac{B}{N}\right) \qquad 0 < k < N \tag{3.16}$$

If the number of sub-carriers selected, $N$, is sufficiently large, the bandwidth of each sub-band, $\Delta f_{sb}$, can be considered narrow enough such that the frequency response remains flat during transmission. This therefore allows the frequency selective fading channel to be observed as a series of flat fading channels, minimising the effects of ISI and removing the requirement for complex receiver structures.

In the presence of severe narrow band interference, some individual sub carriers may become distorted and faded, however, unlike in the case of single carrier structures, the data transmitted by the remaining sub-carriers can still be successfully demodulated. This property highlights the power of the scheme when used in conjunction with modern Forward Error Correction Codes (FEC), where data sent through affected sub-bands can be corrected ensuring reliable communications through severe time varying channels.

## 3.2 Receiver Design

### 3.2.1 Single Carrier Communication

This section explores the development of a single carrier receiver structure, examining the design requirements of a system capable of combating the complex nature of the underwater channel. In order to minimise the decremental channel effects discussed previously, a receiver will typically utilise a chain of signal processing blocks in order to equalise the received signal and enable successful demodulation. A typical receiver structure is shown in Fig. 3.4.

The presented single carrier receiver structure can be seen to comprise four elements:

1. **Synchronisation:** A suitable method to detect the start of a new packet and to ensure accurate time synchronisation between the transmitter and receiver.
2. **Doppler Estimation:** Estimate and compensate for packet compression and expansion caused by the induced Doppler shift.

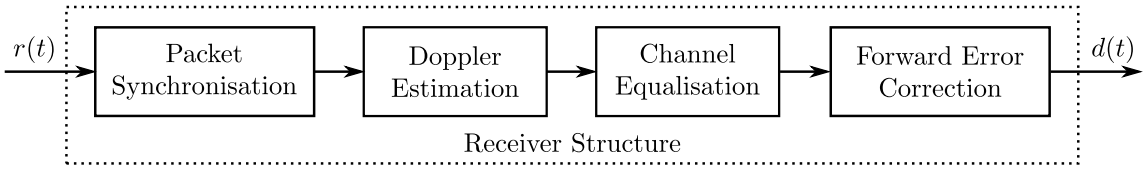


Figure 3.4: Conventional Single Carrier Receiver Structure

3. **Equalisation:** Estimate the channel reverberation and suppress the effects of highly time varying, frequency selective fading.

4. **Forward Error Correction (FEC):** Correct for errors caused by channel interference and propagation of incorrect decisions through the equaliser structure.

Further investigation into the design of each processing block is carried out, highlighting their importance in ensuring reliable demodulation. Discussion will focus on the development of a receiver structure suitable for use in a shallow water channel, drawing attention to areas of previous work.

#### 3.2.1.1 Synchronisation

To enable reliable communications, it is essential that a method of ensuring synchronisation between the transmitter and receiver is achieved. Loss of timing synchronisation can regularly occur in the UAC due to the time and frequency variations incurred by the channel, alongside the packet dilation caused by the observed Doppler shift. A technique often utilised in the recovery of packet synchronisation is the detection of a known sequence inserted within each transmission. The most typical approach is to appended a preamble to the start of each data packet, which through *a priori* knowledge at the receiver can be used to identify the start of a new packet and resynchronise the receiver. This structure is effectively implemented through the pairing of a basic correlator bank with a normalised detector circuit.

In most underwater modems, the synchronisation preamble will either be a dedicated sequence such as a Linear Frequency Modulated (LFM) 'Chirp' or a Pseudo-Noise (PN) sequence modulated using a PSK mapping scheme. Irrespective of synchronisation, the second of these two sequences are often observed at the start of a single-carrier transmission for the purpose of training the equaliser structure. Therefore, to reduce packet overhead and maximise throughput, several groups have suggested the use of the same B-PSK sequence for both training and synchronisation purposes.

The limitations of utilising a PSK training sequence for synchronisation purposes is apparent from Fig. 3.5. This plot demonstrates the effects of the induced Doppler

shift on the cross correlation output, typically referred to as the ambiguity function. The first sub-plot shows the advantages of a spread spectrum LFM transmission, demonstrating a continued cross correlation peak across a very wide range of Doppler shifts. In contrast, the output from a BPSK modulated PN sequence is limited in the Doppler direction, generating a peak response across a very narrow range of Doppler frequencies, i.e. -1m/s $\leq v \leq$ 1m/s.

Although, a reduced overhead is typically achieved through use of a PSK training sequence, a dedicated LFM preambles is shown to be significantly more reliable in scenarios where a Doppler induced frequency shift is observed. Therefore, in the context of this research, a dedicated LFM preamble will be utilised for synchronisation purposes. Further information about the benefits of spread spectrum LFM 'Chirp' signals is given in Section 3.2.2.

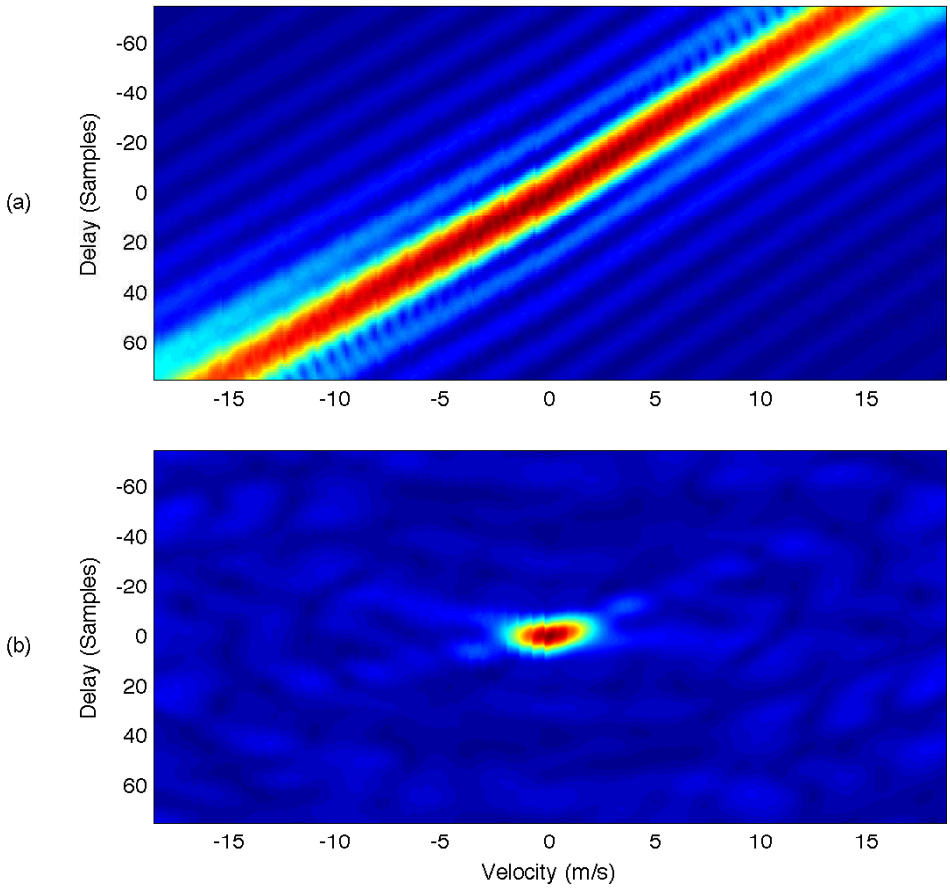


Figure 3.5: Ambiguity Function for:
(a) Linear Frequency Modulated (LFM) 20ms 'Chirp' Signal
(b) Pseudo-Noise (PN) Binary Phase Shift Keyed (BPSK) Signal (500 Symbols)

#### 3.2.1.2 Channel Equalisation

As discussed in Section 2.2.2, channel reverberation can cause severe distortion of the received signal due to the inter-symbol interference (ISI). Therefore a method of compensating for the induced fluctuations in both phase and amplitude is required. The use of a suitable equaliser structure to suppress the effects of channel reverberation is proposed. Because of the highly dynamic time varying nature of the underwater channel, static equaliser structures are on the whole unsuitable, therefore the use of an adaptive equaliser is examined. This section will discuss the use of both the Linear Transversal Equaliser (LTE) and the Decision Feedback Equaliser (DFE) to overcome any channel interference.

**Adaptive Filtering**

Most forms of channel equalisation are based around the technique of adaptive filtering. Utilising an adaptive filter, any interference, noise or detrimental channel effects are removed from the signal by applying a digital filter to the input signal. In comparison to static filtering techniques, the coefficients of the filter are adapted in real time based on feedback from a selected algorithm. Therefore, in its simplest form an adaptive equaliser structure can be observed as two objects: a linear temporal filter; and a coefficient update algorithm.

The received signal, and input to the filter, $x_n$, can be observed to be a combination of both the transmitted signal, $s_n$, and any noise or interference caused by the channel, $n_n$. It should be noted that the transmitted signal and the observed background noise can be shown to be uncorrelated.

$$x_n = s_n + n_n \tag{3.17}$$

A typical adaptive algorithm will try to adjust the tap coefficients of the filter such that the error, $e_n$, between the original transmitted sequence, $s_n$, and the output of the filter, $\tilde{s}_n$, can be minimised [61]. In an ideal scenario, the coefficients of the filter will be calculated such that the filter output directly corresponds to the original transmission prior to any undesirable channel distortion, i.e. $s_n = \tilde{s}_n$.

**Linear Transversal Equaliser (LTE)**

One of the simplest methods of removing ISI from a received data set is through the use of a Linear Equaliser (LE). A linear equaliser attempts to remove any unwanted components from the incoming data stream through convolution with a linear filter. A typical implementation of a LE can be constructed from a Transversal or Finite Impulse Response (FIR) filter. The tapped delay line structure, utilised as the basis

for both of these filters, is shown in Fig. 3.6. The structure can be seen to consist of: multiple unit delay elements, $Z^{-1}$; their corresponding multipliers; and a single adder stage, denoted by $\Sigma$.

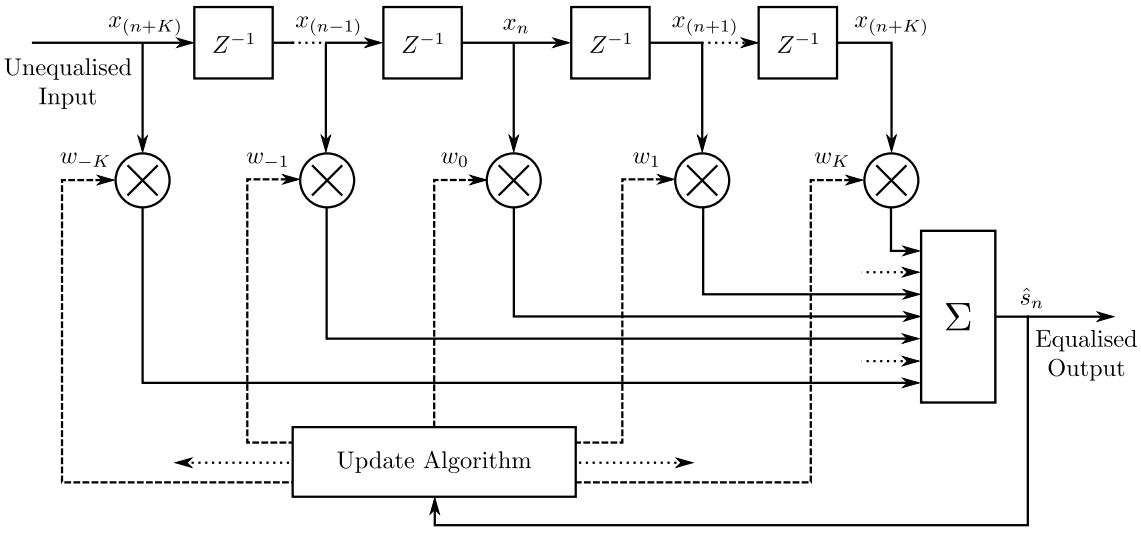


Figure 3.6: Linear Transversal Equaliser Structure: Utilising a $(2K+1)$th Order Transversal Filter

Using a linear equaliser structure an estimate of the $n$th data symbol, $s_n$, can be calculated as the convolutional sum of the $2K+1$ filter coefficients, $w$, with the unequalised input sequence, $x$. The output of the filter can therefore be expressed in the form (3.18), where, the $k$th filter coefficient is represented by $w_k$ and the $n$th unequalised input sample is given as $x_n$.

$$\hat{s}_n = \sum_{k=-K}^{K} w_k x_{n-k} \tag{3.18}$$

The output estimates, $\hat{s}_n$, are individually hard limited to the nearest valid information symbol, generating a sequence of quantised decisions, $\tilde{s}_n$. If the filter has successfully removed the ISI generated by the channel, then the symbol decisions should be equal to the original transmission sequence, $s_n = \tilde{s}_n$. To accurately compensate for the incurred ISI, the temporal length of the delay line must be seen to span the overall duration of the channel delay spread. Because of the additional number of delay elements, multiplier blocks and the processing of the update algorithm, the computational complexity of the filter is found to increase in proportion to the temporal length of the multipath delay spread.

**Limitations of Linear Equalisers**

A Linear Equaliser structure has been shown to be a very effective means of de-

modulation for channels where ISI is not perceived to be severe. The finite length of a LE structure can be seen to significantly restrict its ability to combat longer durations of ISI. Anything falling outside the predetermined span of the filter will continue to cause degradation at the output. More importantly, the discussed structure struggles to combat deep nulls in the frequency spectrum. If a channel exhibits such fades, the transmitted waveform can become attenuated far below the noise floor of the system. In this scenario, the use of a LE will result in a significant enhancement of the background noise. [62]

**Decision Feedback Equaliser (DFE)**

An alternative suboptimal equaliser structure to the LE, is the Decision Feedback Equaliser (DFE). In the presence of severe frequency selective fading, the DFE structure will typically offer superior performance. The DFE can be described as a non-linear equaliser structure, due to its use of a feedback loop to supply knowledge about symbols that have been received previously. Knowledge of previous decisions made by the receiver can be used to suppress the ISI observed on the current symbol. This structure can be seen to significantly improve the ability for the equaliser to overcome longer periods of ISI and deeper spectral fades.

As shown in Fig. 3.7 the DFE structure can be seen to consist of: a feed-forward transversal filter, with coefficient weights $w$; a feed-back transversal filter, with coefficient weights $fw$; and a decision device used to quantise the output sequence.

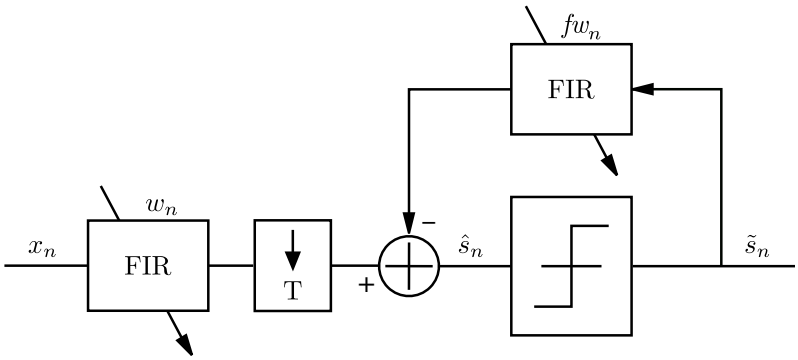


Figure 3.7: Decision Feedback Equaliser (DFE) Structure

The $n$th symbol estimate made by the DFE, $\hat{s}_n$, can be calculated utilising (3.19), where, $x_n$ defines the $n$th unequalised input to the DFE and $\tilde{s}_{n-j}$ is a previous quantised symbol decision. In this example, the feedforward and feedback filters utilise $N$ and $M$ filter coefficients respectively.

$$\hat{s}_n = \sum_{i=-N}^{0} w_i x_{n-i} - \sum_{j=1}^{M} fw_j \tilde{s}_{n-j} \tag{3.19}$$

As the input vector to the feedback filter is constructed from the quantised decisions of previous symbols, it can be considered to be free of any received channel noise. Assuming the correct detection of all previous symbols, $\tilde{s}_n = s_n$, the input to the feedback filter can be considered 'ideal', enabling significant removal of ISI from the symbol currently being processed by the DFE structure.

A key benefit of the DFE structure is its ability to cancel out any post-cursor ISI, through matching the feedback taps, *fw*, to the received channel response. Additionally, the forward filter ensures fine time synchronisation of the received packet on a symbol by symbol basis. The expansion or compression of the packet in time domain, along with any inaccuracy in the reference clock frequencies, can cause a significant drift in symbol synchronisation. The forward filter can accurately compensate for such mis-alignment, continuously resynchronising throughout the duration of the packet.

**Limitations of Decision Feedback Equalisers (DFE)**

A significant limitation of the DFE structure is the generation of burst errors due to the propagation of incorrect decision through the feedback filter. Up until now we have assumed that the decisions supplied to the feedback filter are correct. If this assumption is invalid, i.e. $\tilde{s}_n \neq s_n$ , incorrect symbol estimates will be transferred back into the feedback loop and allowed to propagate into the feedback filter. Future decisions are therefore made based on an inaccurate convolution of the feedback filter, typically resulting in further 'bursts' of errors.

The propagation effect can be seen to become further exaggerated if a increased number of filter taps are required to span the multipath spread. The additional latency required for the initial error to fully propagate out of the feedback filter can often result in longer 'bursts' of errors and in severe cases cause the equaliser to become unstable.

**Tap Spacing**

As presented by Ungerboeck, in 1976, [63] symbol spaced equaliser filters can be seen to be extremely sensitive to any form of drift in symbol clock frequency. Through utilising a $T$ spaced filter, a deviation in sample timing has been shown to cause serious degradation to the receivers performance. A fractionally spaced filter, with taps spaced at Nyquist divisions (i.e. $\frac{T}{2}$ spacings) have been shown to significantly reduce the receivers sensitivity to timing offset. The benefits of utilising a $\frac{T}{2}$ spaced

filter is further compounded by the minimal affect observed on the convergence rate of the equaliser.

When examining a DFE structure, the feedforward filter, in the same way as a simple LE, demonstrates the improvement in performance, through utilising a fractionally spaced equaliser. However, in the case of the feedback filter, no gain is observed when tap spacings of less than the symbol rate, i.e. $< T$ are implemented. It should also be noted that if the feedback filter does utilise fractionally spaced taps, the number of filter coefficients required to fully span the multipath delay spread will increase significantly.

### Calculation of Filter Weights

To maximise the performance of an adaptive filter, a measurement criteria that indicates the receivers instantaneous performance is selected. Based on this measurement a suitable algorithm is used to estimate future coefficient values which should further improve the receivers ability to suppress any non-ideal channel effects.

An ideal metric to assess the performance of a communication system is the average probability of error. A considerable limitation of this metric is the non-linear response generated, requiring an exceedingly complex algorithm to be used to calculate optimal coefficient values [31]. Therefore, one of the most popular alternatives for generating filter coefficients in a practical system, is the Mean-Square-Error (MSE) criteria. Utilising this technique, the coefficient weights are selected such that the performance index, $J_{\text{MSE}}$, is minimised. In a complex equaliser structure this index can be calculated using (3.20), where $E$ denotes the expected value.

$$J_{\text{MSE}} = E|\varepsilon_n|^2 = E|s_n - \hat{s}_n|^2 \tag{3.20}$$

The Wiener-Hopf equations can be used to define the optimal filter weights, $\mathbf{w}_{\text{opt}}$, for an adaptive filter when utilising the minimal mean square error criteria. For ease of presentation, the Wiener-Hopf equations may also be expressed in the matrix form given by (3.21).

$$\mathbf{w}_{\text{opt}} = \mathbf{R}_{\mathbf{xx}}^{-1}\mathbf{R}_{\tilde{\mathbf{s}}\mathbf{x}} \tag{3.21}$$

In this format, $\mathbf{R}_{\mathbf{xx}}$ is used to denote the autocorrelation of the unequalised filter input sequence, $\mathbf{x}$, and $\mathbf{R}_{\tilde{\mathbf{s}}\mathbf{x}}$ is used to define the cross correlation between the filter input and the desired output, $\tilde{s}_n$.

In general, due to the computational complexity, the matrix form of the Wiener-Hopf equation is not used to directly calculate future filter tap weights. The process of calculating a $N \times N$ matrix inversion, where $N = 2K + 1$, comes at a high

computational load, making it highly ineffective for calculating regular coefficient updates [62]. In the case of a semi-static channel, where updates are required at reduced regularity, the idealised Weiner filter equations may be suitable. However, for a highly time varying channel, such as the UAC, a more efficient solution is required.

**Modes of Operation**

During the reception of an individual packet an adaptive filter will typically operate in two different modes. These are, the training mode and the decision directed mode. The training mode is typically used at the beginning of each packet to initialise the weights of the equaliser taps to a state replicating the channel characteristics. Once trained the filter will switch modes and begin operating in a decision directed mode, enabling the detection and demodulation of real data.

**Training Mode:**

During the training period a known pattern, such as a Pseudo-Random Noise (PN) sequence, is transmitted. This signal is correlated with a time synchronised version of the sequence at the receiver, allowing an accurate measure of the error signal to be calculated. Use of a training sequence allows the filter tap weights to converge to near optimal values, ensuring ideal operation once running in a decision directed mode. Once the filter coefficients have converged to suitable values, the system can change modes and begin decoding actual data sequences.

**Decision Directed Mode:**

This is the typical mode of operation once the filter coefficients have been trained and during the periods of standard data transmission. In this mode the taps are updated based on the estimation of previously received symbols. As the error signal is calculated based on the hard limited symbol estimates, rather than from a predefined sequence, this mode presents the possibility for error propagation through the feedback filter and thus the generation of 'burst' errors.

Without the use of a dedicated training sequence an initial estimate of the channel conditions, and thus the relevant tap weights, would become complex. Various 'blind' equalisation techniques have been proposed, whereby the filter coefficients can be initialised without the need for a known sequence to be transmitted [64]. Such techniques give a significant reduction in packet overhead and thus an improvement in data throughput. However, 'blind' equalisation typically comes at a cost in terms of increased computational complexity and inability to operate at very low SNR's.

#### 3.2.1.3 Coefficient Update Algorithms

To ensure successful channel equalisation, a suitable coefficient update algorithm should be selected. In the case of both the LE and the DFE, the selection of inaccurate tap weights will significantly degrade the performance of the equaliser structure. Although the Wiener-Hopf filter equations offers an idealised solution for calculating the filter tap weights, their computational complexity make them inherently impractical for real-time implementation.

Additionally, it should be noted that the generated filter coefficients are only considered valid for a period where the channel conditions remain static. As discussed previously, a combination of the vehicles movement, the variable channel geometry and the uncertain boundary conditions, contribute to a highly dynamic multipath response. These effects can therefore be seen to cause variation in both the phase and position of the arrivals observed across the length of a single packet.

To overcome the variability in the channel response, it is essential that the filter coefficients are regularly re-evaluated at periodic intervals across the packet. Without this form of processing the coefficients can quickly become dated, resulting in the current channel conditions being unsuccessfully equalised.

**Least Mean Squares (LMS)**

The Least Mean Squares (LMS) algorithm, proposed by Bernard Widrow and Marcian Hoff in 1960 [65] [66], utilises an iterative process to estimate the optimum Wiener-Hopf solution. This form of algorithm, is typically referred to as a stochastic steepest descent solution, where the optimum filter tap weights are selected through an iterative process of estimation and improvement.

The iterative process adjusts the filter coefficients such that the tap weights minimise the Mean Square Error (MSE) of the output signal. Since this criteria is a second order function of the filter weights, a paraboloid error-performance surface is observed with a minimum point signifying the optimum filter solution [62]. By calculating the polarity of the gradient vector, at a given instant in time, the algorithm can estimate the direction of the future filter coefficients, such that the output error is reduced.

The LMS algorithm typically consists of three processing stages: the calculation of the filter output; an estimate of the error signal; and an update of the filter coefficients. To explain this procedure, we examine the $n^{\text{th}}$ output of a basic filter, calculated through convolution of the input sequence, $x$, with a set of $N$ filter coefficients, $w_i$, (3.22).

$$\hat{s}_n = \sum_{i=0}^{N-1} w_i x_{n-i} \tag{3.22}$$

$$= \mathbf{w}_n^T \mathbf{x}_n \tag{3.23}$$

The error signal, between the filter output, $\hat{s}_n$, and the desired response, $s_n$, can then be calculated utilising (3.24). As discussed in Section 3.2.1.2, the equaliser utilises two different operational modes: training; and decision directed. In training mode, the desired response is known *a priori*, whereas in decision directed mode the desired response is estimated by hard limiting the output symbol.

$$e_n = s_n - \hat{s}_n \tag{3.24}$$

Utilising the LMS tap update equation, (3.25), a new set of filter coefficients, $\underline{\mathrm{w}}(n+1)$ are generated based on the calculated error. Where, $\mu$ denotes the step-size value, typically selected as a small positive value between 0 and 1.

$$\mathbf{w}_{n+1} = \mathbf{w}_n + 2\mu e_n^* \mathbf{x}_n \tag{3.25}$$

**Step Size Selection**

The selection of a suitable step-size, $\mu$, is critical to the optimal performance and reliable operation of the equaliser structure. The magnitude of the step-size parameter effectively specifies the amount of change in the filter coefficients from one iteration to the next. Therefore, adjustments to the step-size parameter can be seen to have a direct impact on the convergence rate of the filter, with a larger value offering faster converge and improved tracking of the channel conditions.

However, the magnitude of the step-size parameter can also be seen to have an effect on the steady state error. Smaller step-size values enable the equaliser to converge to a point closer to the ideal solution, offering a reduced MSE during steady state conditions. Therefore a trade-off is evident, between the steady state error and the convergence rate of the algorithm, typically requiring a trial and error process to be used to select the optimum value for the given conditions.

**Normalised Least Mean Squares (N-LMS)**

A noticeable limitation of conventional LMS, is its sensitivity to variations in magnitude of the input vector, $\mathbf{x}_n$. The selection of a suitable step-size, $\mu$, is heavily dependent on the power of the equaliser input, with any scaling or fluctuations of the input signal seen to directly impact on the performance of the receiver structure, occasionally resulting in a loss of stability [62].

Therefore, a modified update equation is proposed, performing power normalisation on the input signal during the calculation of new coefficient weights (3.26). In many applications this derivative of traditional LMS is preferred, enabling simplified selection of the optimal step-size parameter.

$$\mathbf{w}_{n+1} = \mathbf{w}_n + \frac{2\mu e_n^* \mathbf{x}_n}{\mathbf{x}_n^T \mathbf{x}_n} \tag{3.26}$$

**Recursive Least Square (RLS)**

Although the LMS algorithm is shown to be a highly efficient method of adjusting the equalizer filter coefficients, a considerable limitation is the slow convergence rate of the system. The additional time taken to adapt the filter weights to the optimal solution, can be shown to directly effect the length of the training sequence and the ability to track rapid changes in the channel impulse response.

In order to improve the convergence rate of the equaliser an alternative update algorithm is proposed, namely the Recursive Least Square (RLS) approach. In comparison to LMS, where a single global parameter, $\mu$, is used to control the convergence rate of the system, RLS utilises an array of parameters to update each filter weight independently [31].

In a similar way to the LMS algorithm, the first stage of the update process is to calculate the filter output, $\hat{s}(t)$, given by (3.27). Where, $\mathbf{x}$ is the input vector, and $\mathbf{w}$ is the set of filter coefficients. In the case of the first iteration, i.e. $n = 1$, $\mathbf{w}_{n-1}$ is initialised to all zeros.

$$\hat{s}_n = \mathbf{x}_n^T \mathbf{w}_{n-1} \tag{3.27}$$

Based on the filter output the error signal, $\mathrm{e}_n$, can be calculated as the difference from the desired symbol value, $s_n$ (3.28).

$$\mathrm{e}_n = s_n - \hat{s}_n \tag{3.28}$$

The Kalman gain vector, $\mathbf{K}_n$, can then be calculated using (3.29), where, $\mathbf{P}_{n-1}$ is the inverse of the correlation matrix and $\lambda_f$ is a forgetting factor, between 0 and 1. The forgetting factor is used to exponentially weight the previous data, giving less weight to older data and increased impact to the more recent samples. This process is essential when the channel conditions are variable with time [31].

$$\mathbf{K}_n = \frac{\mathbf{P}_{n-1} \mathbf{x}_n^T}{\lambda_f + \mathbf{x}_n^T \mathbf{P}_{n-1} \mathbf{x}_n^*} \tag{3.29}$$

Once the Kalman gain vector has been calculated, the inverse correlation matrix can be updated using (3.30). It should be noted that to ensure successful operation, the inverse correlation matrix is initialised such that $\mathbf{P}_0 = \delta I$, where, $I$ is an identity matrix and $\delta$ is a small constant value.

$$\mathbf{P}_n = \lambda_f^{-1}\mathbf{P}_{n-1} - \lambda_f^{-1}\mathbf{K}_n\mathbf{x}_n^T\mathbf{P}_{n-1} \tag{3.30}$$

Finally, a new set of filter coefficients are generated using (3.31).

$$\mathbf{w}_n = \mathbf{w}_{n-1} + \mathbf{K}_n\mathrm{e}_n^* \tag{3.31}$$

The improved convergence rate of the RLS algorithm, is highly beneficial in the discussed application. The ability to train to the optimum solution in fewer iterations enables a shorter training sequence to be utilised, significantly reducing the packet overhead and improving the average throughput of the system. However, an important consideration is the increased computational complexity required in updating the inverse correlation matrix, $\mathbf{P}_n$. Where, the conventional RLS algorithm has been shown to require in the order of $N^2$ operations per iteration.

The interested reader can find further information relating to the operation of the RLS algorithm in a selection of the referenced literature [31] [62] [61] [67].

**RLS Derivatives**

A range of alternative RLS based algorithms have been developed, offering a reduction in computational complexity, or an improvement in mathematical stability. The two most common approaches are the 'Fast' family of algorithms, and the Square Root approximation technique. A brief overview of each is given below:

**Square Root Decomposition**

A significant complication with conventional RLS, is the numerical instability caused by the rounding errors from the finite precision of the utilised storage vectors. The majority of these errors can typically be observed during the calculation of the covariance matrix, $\mathbf{P}$. Therefore, to improve the numerical stability of the algorithm various decomposition techniques have been presented, such as the square root factorisation.

To simplify the covariance matrix, we can consider it in the factorised form shown in (3.32), where: U is the upper triangular matrix with unity diagonal elements and non equal off-diagonal elements; and $\Lambda$, is a diagonal matrix. This form of decomposition is typically referred to as square root factorisation, [31].

$$\mathbf{P}_n = \mathrm{U}_n^T \Lambda_n \mathrm{U}_n \tag{3.32}$$

Although this approach still exhibits an exceedingly high computational complexity, in the order of $1.5N^2 + 6.5N$ operations, a proposed technique is to reduce the duty cycle between coefficient updates, calculating tap weights at a periodic interval rather than on a symbol-by-symbol basis. A suitable update interval can be selected based on the measurement of the Mean Square Error (MSE), with an increase in MSE indicating the need for more regular RLS updates to be performed. [68]

**Fast-RLS**

Derived from the conventional RLS approach, the 'fast'-RLS family of equations offer significantly reduced computational complexity. In comparison to the traditional RLS approach, which requires $O(N^2)$ per iteration, the fast techniques complexity grows linearly with the number of filter coefficients, i.e. $O(N)$. Although this approach comes with a slight trade off in terms of convergence time, the algorithm can still be seen to significantly outperform the capability of LMS.

It should be noted that a limitation of fast-RLS techniques is the observed mathematical instability, whereby a reduction in the complexity of the algorithm typically corresponds to an increase in the systems sensitivity to rounding and accumulation errors [69]. Further information relating to the construction of the fast-RLS algorithm can be found in the works by Halkias *et al.* [70], Falconer and Ljung [71] and Carayannis *et al.* [72]

**Algorithm Comparison**

Historically, the Least Mean Squares (LMS) family of update algorithms have been highly favoured, offering a suitable iterative approach to the Wiener-Hopf solution. Although the approach does not offer a fast convergence rate, typically taking a high number of iterations to produce the optimum coefficient weights, the low computational complexity makes it an ideal solution for real-time practical implementations.

The development of the Recursive Least Square (RLS) collection of adaptive algorithms have enabled faster convergence rates to be demonstrated. Enabling shorter training sequences to be utilised, reducing the packet overhead and achieving higher data rate transmissions. Additionally, the convergence rate is found to directly effect the systems capability to track rapid changes in the channel conditions.

A comparison of the discussed algorithms is compiled in Table 3.2, highlighting the benefits and limitations of each.

| Algorithm | Pros | Cons |
|---|---|---|
| LMS | • Lowest Complexity: $O(N)$<br>• Numerically Stable | • Convergence Time (Long)<br>• Step Size Sensitive to Input |
| N-LMS | • Normalised Magnitude<br>• Numerically Stable | • Convergence Time (Long) |
| RLS | • Fastest Convergence Time | • High Complexity: $O(N^2)$<br>• Sensitive to Rounding Errors |
| Fast RLS | • Reduced Complexity<br>• Convergence Time (Short) | • Numerically Unstable |
| $\sqrt{\text{RLS}}$ | • Numerically Stable<br>• Convergence Time (Short) | • Increased Complexity |

Table 3.2: Comparison of Equalisation Update Algorithms

This evaluation has highlighted the trade-off between the convergence time and the computational complexity of current filter coefficient update algorithms. Given unlimited computational resource the reduced convergence time of the RLS algorithm can be seen to be highly desirable, making it the obvious selection for updating the DFE filter coefficients. However, for a realistic practical implementation, further consideration must be given regarding the constraints of the receiver hardware.

Table 3.3 summarises the computational cost per iteration for each of the discussed algorithms. In each case, the values are given for complex data sets, evaluating the number of real multiplications, real additions and real divisions performed.

| *Algorithm* | *Computational Cost* | | | *Ref* |
|---|---|---|---|---|
| | $\times$ | $+$ and $-$ | $\div$ | |
| LMS | $8N+2$ | $8N$ | 0 | [61] |
| N-LMS | $10N+2$ | $10N$ | 1 | [61] |
| RLS | $4N^2+16N+1$ | $4N^2+12N-1$ | 1 | [61] |
| Fast RLS | $11N+3$ | $10N+2$ | 2 | [73] |
| $\sqrt{\text{RLS}}$ | $6N^2+11N$ | $6N^2+6N$ | $N$ | [74] |

Table 3.3: Computational Complexity of Equalisation Update Algorithms

Based on these analytical values, it is evident that the complexity of the RLS algorithms is considerably higher than the conventional LMS approach. Since the difference in complexity becomes increasing evident with higher numbers of coefficients, filter lengths suitable of overcoming the underwater channel conditions, i.e. $50 < N < 120$, are shown to be highly impractical to construct. Although

*'fast'*-RLS algorithms have demonstrated reduced complexity, the inherent numerical instability makes them unsuitable for implementations with finite resolution. Further discussion on the selection of a suitable adaptive update algorithm is given in Section 5.1.2.

#### 3.2.1.4 Array Receivers

Array receivers have been demonstrated to dramatically improve system performance through their ability to suppress long channel delays, that exhibit significant angular separation from the direct path. Circular planar arrays are typically well suited to deep water channels, enabling a conical beam to be focused in the horizontal axis. Alternatively, vertical arrays have been used in shallow water channels to allow a beam to be steered in the vertical axis, minimising the effects of surface and sea floor reflections.

An array is typically constructed from multiple piezoelectric transducer elements, evenly distributed in a linear or horizontal pattern. A vertical array typically exhibits a torus, or 'doughnut', beam shape, while a horizontal planar array can be seen to produce more of a searchlight beam. When unsteered the direction of maximum sensitivity, also known as the *'acoustic axis'*, can be seen to lie at right angles to the orientation of the array.

The directivity of an array receiver comes from the phase summation of each of the received channels. For a basic sinusoidal wave, when generated at right angles to the array, the signal received by all of the elements will arrive in-phase, resulting in maximum correlation and thus constructive summation. This is the point of maximum sensitivity defined as the *'acoustic axis'*. A gain in signal to noise (SNR), will also be observed due to the correlated nature of the transmitted broadband signal, compared with the uncorrelated background noise.

To enable maximum receiver performance, arrays are typically steered, to focus the *'acoustic axis'* towards the direction of transmission. Arrays can be rotated either physically, mechanically or through electrical beam steering. To electronically steer the beam, delays are inserted between the elements such that the response appears as a transmission from an alternative direction. This technique minimises the requirement for complex hardware to steer the array, reducing the possibility of component failure and thus system downtime.

**Adaptive Beamforming**

The beam pattern of a linearly spaced vertical array can be adapted using a sequence of basic delay blocks, placed in a manner to manipulate the 'acoustic axis' towards the direction of the observed transmission source. In the case of a receiver utilising

a DFE structure a forward filter may be assigned to each individual channel of the array, as demonstrated in Fig. 3.8. By calculating each of the filter coefficients independently, the update algorithm will automatically apply suitable delays in a manner that will minimise the mean-square error of the output signal.

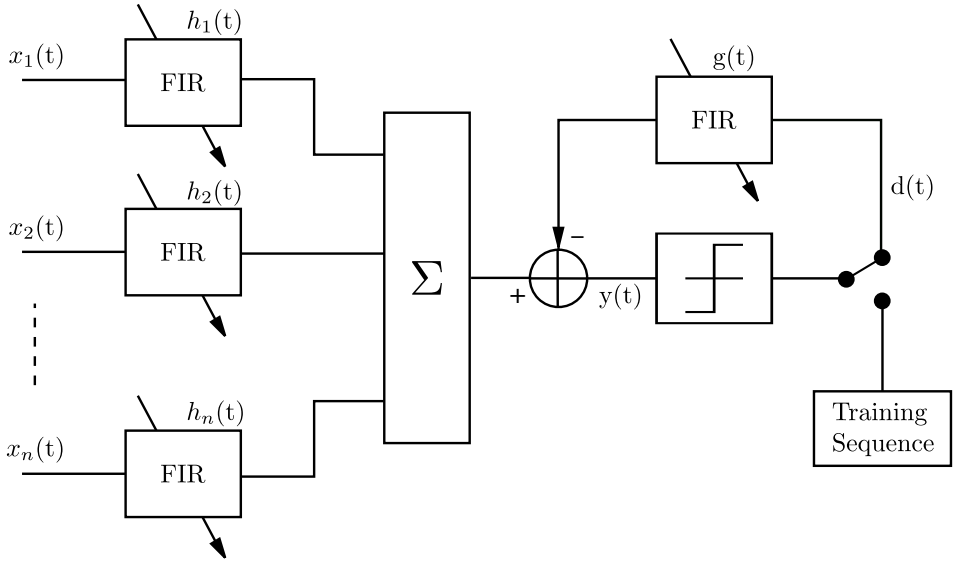


Figure 3.8: Adaptive Beamformer Combined with a Decision Feedback Equaliser Structure

As presented by Neasham *et al.* [75], a combination of equalisation and spatial beamforming can be used to supply near optimum receiver performance. Along with the default benefits shown by temporal equalisation, an adaptive beamformer can be seen to demonstrate two characteristics that further reduce the effect of any multipath arrivals:

**Spatial Equalisation**

Resolve the direction of each individual multipath component and adjust the filter weights to enable the coherent combination of all arrivals. This technique ensures the amplification of the total 'wanted' signal level.

**Coherent Cancellation**

To reduce the MSE of the output signal the beamformer can be forced to place nulls, of the receiver beam pattern, in the direction of any significant sources of ISI or uncorrelated noise, including shipping noise, surface wave noise and thruster interference.

The output of the equaliser structure can therefore be calculated as the summmation of each of the individual feedforward filters, $w_0$ - $w_N$, with removal of any remaining ISI through the implementation of a single feedback filter, $fw$ (3.33).

$$y(t) = \sum_{n=1}^{N} x_n(t) w_n(t) - d(t) f w(t) \tag{3.33}$$

Each of the feedforward filter taps, $w_n(t)$, are independently calculated using a standard update algorithm, such as the Least Mean Square (LMS) algorithm demonstrated in (3.34). Where, $\mu$ is the gradient step-size and $e(t)$ is the estimated error signal.

$$w_n(t+1) = w_n(t) + 2\mu e(t) x_n(t) \tag{3.34}$$

Beamforming arrays have been shown to provide an optimum method of resolving any complex multipath arrivals, such as those observed in the shallow water channel [75]. The use of a steerable array ensures suppression of any indirect arrivals, while amplifying the contributions made be the direct transmission. Array receivers can be seen to vastly improve the receivers performance without the need to permanently constrain the field of 'vision' by physically masking the receive transducer.

A considerable limitation of multi-element receivers is the complexity involved in manoeuvring a physically large array. The wide spacing between elements, along with the amount of transducers required to ensure accurate spatial isolation, gives rise to the difficulty in deploying from small vessels or in situations where manpower is severely limited. Additionally, in the case of large adaptive beamformers, the duplication of the forward filter structure can result in a significant increase in the computational complexity. of the system.

#### 3.2.1.5 Doppler Estimation and Compensation

As highlighted in Section 2.2.3, the relative movement between the transmitter and receiver can cause serious degradation of the received signal, often resulting in a catastrophic number of bit errors post demodulation. In the case of a narrow-band system we can model the effect of Doppler in a similar way to that of an individual frequency component, $\omega_n$. In this scenario the induced Doppler shift can be seen to result in a scaling of frequency (3.35), where, $\dot{\omega_n}$ is the scaled frequency component and $\Theta$ is the fractional Doppler shift.

$$\dot{\omega_n} = \omega_n(1 \pm \Theta) \tag{3.35}$$

Typically, the removal of such distortion has been achieved utilising carrier synchronisation techniques. Several papers have previously demonstrated the use of a Phase Locked Loop (PLL) for this purpose, dynamically adjusting the local carrier frequency to compensate for any deviation caused by Doppler shift [36] [76].

However, in the case of broadband transmissions we must also take into account the time-scaling of the received signal, $r(t)$, expressed by (3.36), where, $s(t)$ is the time domain transmit waveform. This effect can be seen to result in considerable temporal dilation or compression of the original waveform, requiring re-sampling of the analog waveform to successfully recover the modulated binary data stream.

$$r(t) = s([1 + \Theta]t) \tag{3.36}$$

Two Doppler estimation and compensation structures are presented: a single block estimate approach; and a continuous closed loop update technique. The first system utilises a single estimate, assuming continuous Doppler shift across the duration of a single packet. On the other hand a closed loop technique allows updates to be calculated on a symbol by symbol basis, enabling the system to track changes in signal dilation over the course of an individual packet.

#### 3.2.1.6 Open-Loop Doppler Estimation

A range of literature has previously demonstrated computationally efficient methods of calculating a block Doppler estimate. Such techniques have proved to be suitable for overcoming the distortion caused by a slowly varying relative motion between the receiver and transmitter [77] [76]. Previous trials have indicated the ability for such techniques to compensate for high levels of movement, often in excess of 5m/s.

Once per packet, a single Doppler estimate is calculated based on observations of the incoming data stream, $r(t)$. The estimate of the fractional Doppler shift,$\hat{\Theta}$, is then used to linearly interpolate the entire data set, as shown in Fig. 3.9. If the Doppler estimation and compensation processes are successful, and assuming no other channel affects, the re-sampled signal, $\acute{s}(t)$, should be equal to the modulated waveform transmitted from the vehicle, i.e. $s(t) = \acute{s}(t)$.

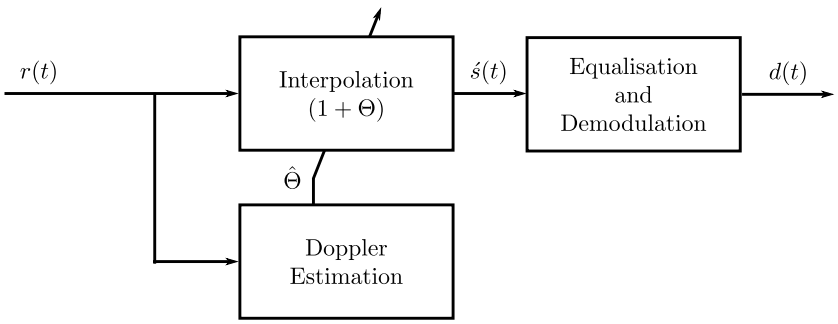


Figure 3.9: Open Loop Doppler Estimation and Correction Structure

Typically, an estimation of the induced Doppler scaling is calculated based on observations of a known data set, such as the training or synchronisation sequence which are known *a priori* by the receiver. Two open-loop Doppler estimation techniques have previously been presented, these are: a multi correlator, ambiguity function approach; and a block Doppler estimation technique.

*a) Ambiguity Function:*

An estimate is achieved through conducting a search of the cross-ambiguity function for a maximum response in the $\Theta$ direction. As demonstrated by Johnson *et al.*, this approach can be practically realised through the use of a bank of discrete correlator blocks [76]. Each of these matched filters are a replica of the transmitted waveform, offset by an incremental Doppler shift in either the positive or negative direction. The required number of correlators can be seen to be directly related to: the anticipated range of the Doppler shift; and the precision of the generated estimate. In applications where a high level of Doppler shift, or increased resolution, is required the number of individual correlator blocks can become excessive for realistic practical implementation.

*b) Block Estimation*

As discussed previously, the relative movement between the two platforms can be shown to correspond in a temporal dilation of the transmitted packet. Therefore, by examining the length of the received packet, and observing the incurred expansion or compression, an accurate estimate of the induced Doppler shift can be achieved. A suitable technique for measuring the length of the received packet, $T_{rp}$, is through the insertion of a Doppler tolerant preamble to the start of each packet. At the receiver this known sequence can be detected utilising a single cross correlator, as demonstrated in Fig. 3.10. To ensure optimum performance, a preamble with a very wide ambiguity function is typically utilised. In general, an LFM 'chirp' signal is selected due to its high degree of Doppler tolerance.

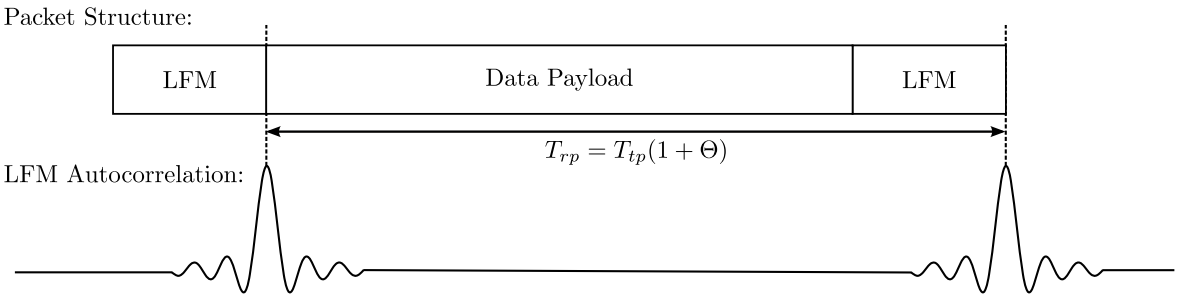


Figure 3.10: Open Loop Block Doppler Estimation (LFM Matched Filter)

Once the length of the received packet, $T_{rp}$, has been calculated, and if the length of the transmitted packet, $T_{tp}$, is known by the receiver *a priori*, an accurate estimation of the induced Doppler shift, $\hat{\Theta}$ can be calculated utilising (3.37).

$$\hat{\Theta} = \frac{T_{rp}}{T_{tp}} - 1 \tag{3.37}$$

This approach was originally presented in early 2000 by Sharif *et al.*, highlighting its benefits in terms of efficient implementation [77]. In comparison to the ambiguity function approach previously discussed, this technique only requires a single correlator block, ensuring a significant reduction in the overall computational complexity of the receiver structure. A significant limitation of an open-loop 'block' estimation technique is the inability to track rapid variations in acceleration and velocity. Therefore, if a block estimate approach is used in isolation packet durations must be kept short, to ensure constant velocity across the length of the packet. Additionally, a block estimation approach typically offers finite resolution, measuring the expansion of the packet in terms of discrete samples and therefore exhibiting reduced accuracy over shorter packet lengths.

#### 3.2.1.7 Closed-Loop Doppler Estimation

Whether utilised independently or to further compensate for any residual Doppler shift, a closed-loop estimation approach offers increased accuracy and higher levels of Doppler tracking. Traditionally a Phase Locked Loop (PLL) has been utilised to offer local carrier recovery, through the removal of any frequency shift caused by the discussed Doppler effect [76]. When combined with an adaptive equaliser structure, the PLL enables continuous tracking of any phase distortion in a closed-loop fashion.

Certain publications have commented on the complications faced in utilising a PLL structure in the UAC, most noticeably citing unreliability issues due to the severe multipath distortion and related channel fading [75]. Additionally, the practical complexity of implementing a PLL with a loop filter bandwidth capable of tracking the incurred highly variable Doppler shift, limits its suitability in a real-time system [77].

An alternative closed-loop approach was suggested by Sharif *et al.* in late 2000 [77] [78]. The proposed scheme utilises a maximum likelihood cost function, calculated from the output from the adaptive equaliser structure, to estimate the induced Doppler shift. This structure tracks the vehicles velocity, on a symbol by symbol basis, ensuring the receiver can compensate for any significant accelerations or decelerations encountered within a single packet. A block diagram demonstrating the structure of a closed loop estimation scheme is shown in Fig. 3.11

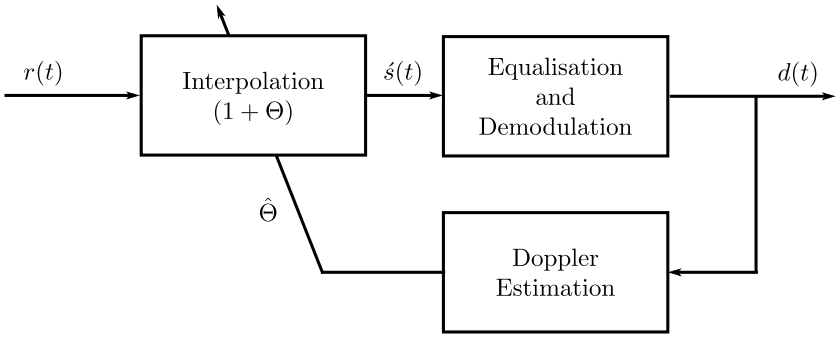


Figure 3.11: Closed Loop Doppler Estimation and Correction Block Diagram

A suitable indicator of the induced Doppler shift can be calculated as the phase error, $\phi_e[i]$, between the DFE output and the estimated symbol value (3.38). This cost function can be seen to linearly rise with an increase in relative velocity, with a positive phase shift corresponding to a positive Doppler shift, and vice versa.

$$\phi_e[i] = \arg\lfloor y[i].\overline{d}[i]\rfloor \tag{3.38}$$

The calculated phase error can be used within a closed loop control system to recursively estimate the induced Doppler shift of the incoming data set. For each iteration an approximation of the re-sampling interval, required to reverse the incurred packet dilation, is calculated. This value is referred to as the interpolation factor, $I$, where, $I = (1 + \Theta)$. Utilising a simple proportional controller, with gain $k_p$, the interpolation factor at a time $i + 1$, can be calculated using (3.39), where $I[0] = 1$.

$$I[i + 1] = I[i] + k_p.\phi_e[i] \tag{3.39}$$

#### 3.2.1.8 Doppler Correction

Once an estimate of the relative Doppler shift has been calculated, a compensation process is utilised to reverse the incurred time and frequency scaling. Through evaluating the temporal dilation incurred on a discrete set of samples, $s[nT_s]$, we can observe that the induced Doppler shift results in a scaling of the sample period, $T_s$, (3.40) [77].

$$r[nT_s] = s[n(1 + \Theta)T_s] \tag{3.40}$$

An interpolation process can therefore be used to reverse the time scaling of the received data set. This re-sampling process can be mathematically described using (3.41), where the received signal is interpolated by a factor of $(1 + \Theta)$.

$$s[nT_s] = r\left[\left(\frac{n}{1+\Theta}\right)T_s\right] \tag{3.41}$$

To overcome small Doppler shifts i.e. $\pm 0.1\%$, it is essential that highly accurate re-sampling techniques are utilised. Typically, the most effective method of sample rate conversion is through poly-phase filtering. However, as highlighted by Sharif *et al.* in practical implementations this approach is avoided due to its high computational complexity, instead favouring the use of linear interpolation [77].

### 3.2.2 Spread Spectrum Communication

This section focusses on the design of a spread spectrum communication scheme suitable for reliable subsea transmissions. Discussion will be made about the benefits of such structures, highlighting their ability to overcome severe channel conditions through under-use of the available bandwidth. Despite the majority of spread spectrum schemes having been utilised in one way or another for UAC transmissions, Chirp Spread Spectrum (CSS) transmissions will be primarily discussed due to its increased tolerance to both multipath and induced Doppler shift. The design of a practical transmitter and receiver platform for a CSS scheme will also be discussed, indicating the simplicity of both structures.

#### 3.2.2.1 Chirp Spread Spectrum (CSS)

In comparison to many other spread spectrum techniques, such as FHSS or DSSS, Chirp transmissions do not utilise a pseudo random noise sequence to spread the data sequence across the available signal bandwidth. In contrast, CSS increases or decreases the modulation frequency, in a linear manner, such that the transmitted signal occupies the entire bandwidth, $B$. For this reason the scheme is often referred to as Linear Frequency Modulation (LFM). The generated wideband LFM Chirp sequence can be expressed by (3.42), where, $f_o$ is the initial frequency; $T$ is the duration of the chirp; and $\mu$ is the rate of change in frequency. [60].

$$s(t) = \alpha(t)\cos(2\pi f_o t + \pi\mu t^2) \qquad 0 \leq t \leq T \tag{3.42}$$

The rate of change, $\mu$, is often referred to as the slope rate of the signal and is defined by (3.43), where, $\Delta f$ is the change in frequency across the duration of the

chirp, given as $\Delta f = f_{\max} - f_o$. From this equation we can see that if $\mu > 0$, the frequency increases with time, thus we define it as an *'Up' Chirp*. Similarly if $\mu < 0$ the frequency decreases and we define it as a *'Down' Chirp*.

$$\mu = \frac{\Delta f}{T} = \frac{B}{T} \tag{3.43}$$

For a linearly swept chirp, the instantaneous frequency, $f_i$, at a given time period, $t$, can therefore be calculated as:

$$f_i = \frac{1}{2\pi}\frac{d}{dt}\cos(2\pi f_o t + \pi\mu t^2) \tag{3.44}$$

$$= f_o + \mu t \tag{3.45}$$

The processing gain, $G_p$, of a CSS system is used to numerically indicate the benefit observed through the spreading process. Typically this value expresses the ratio between the SNRs before and after spreading, and therefore highlights the improvement made through utilising a spread spectrum system. This value is often also referred to as the time bandwidth product or the compression ratio and can be calculated for a CSS system using (3.46).

$$G_p = 10\log_{10}(BT) \tag{3.46}$$

#### 3.2.2.2 CSS Transmitter Structure

A typical CSS transmission scheme uses up or down chirps to convey the state of the incoming binary data sequence. If the input bit is a '1' the transmit waveform is encoded as an up chirp and a '0' represented by a down chirp. This form of signalling can be generated using very basic hardware, with a typical CSS transmitter constructed from two matched filter blocks and a data multiplexer or switch. A block diagram of the transmit structure is shown in Fig. 3.12, the binary input steam, $u(t)$, is fed through a basic switch block, which selects the relevant up or down chirp filter, $g_u(t)$ or $g_d(t)$ respectively.

For a linear chirp transmission, the two modulating waveforms used are given by: (3.47) for the up chirp; and (3.48) for the down chirp. An example of an LFM transmission sequence is shown in Fig. 3.13. The binary data set [1 1 0 0 1] is modulated using linear chirp sequences, exhibiting a start frequency $f_L$ and end frequency $f_H$. The duration $T$ indicates the length of an individual chirp transmission, and is often referred to as the chirp rate.

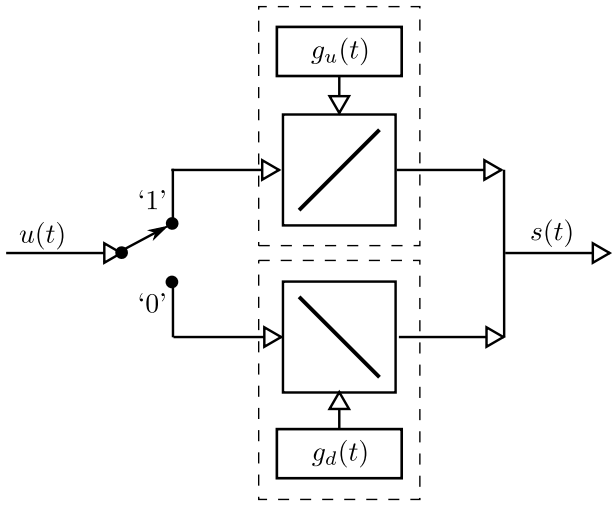


Figure 3.12: Single Bit Chirp Spread Spectrum (CSS) Transmitter

$$g_u(t) = \alpha(t)\cos(2\pi f_o t + \pi\mu t^2) \tag{3.47}$$

$$g_d(t) = \alpha(t)\cos(2\pi f_o t - \pi\mu t^2) \tag{3.48}$$

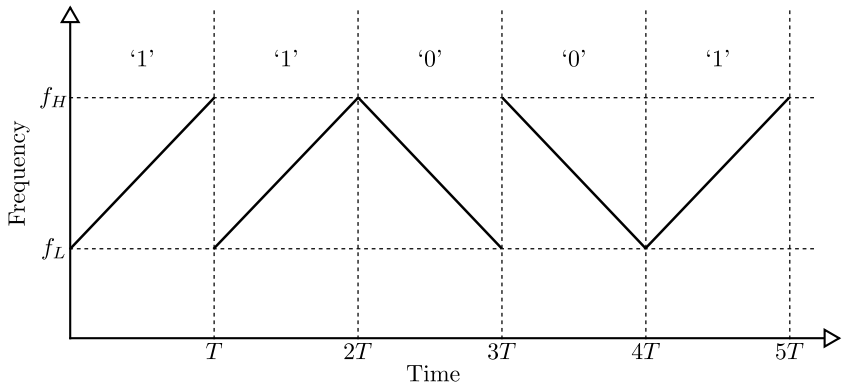


Figure 3.13: Chirp Spread Spectrum Transmission:
Sequence '1 1 0 0 1' [Up Chirp ($\mu > 0$) = 1, Down Chirp ($\mu < 0$) = 0]

#### 3.2.2.3 CSS Receiver Structure

The detection of the transmitted binary sequence can be achieved through simultaneous cross correlation with the matched filters $h_u(t)$ and $h_d(t)$, for the respective up and down chirps. The output from each of the parallel filters are tested against a threshold value and the filter with the highest correlator output across a set window is selected as the correct binary value. The matched filters are generated such that

the chirp rate is the inverse of the corresponding waveform, as demonstrated for the up chirp in (3.49).

$$h_u(t) = k(t)\cos(2\pi f_o t - \pi\mu t^2) \tag{3.49}$$

Given a perfect up chirp, $g_u(t)$, at the input to the matched filter, the output can be expressed as (3.50). This process is often described as the autocorrelation of the sequence.

$$z_u(t) = g_u(t) * h_u(t) \tag{3.50}$$

Through further expansion the output can be presented in the form (3.51). From this expression we can observe that the autocorrelation of a chirp waveform is a narrow impulse, with a sinc-like response. The central peak of this function can be observed at $t = 0$, with the first zeros at $t = \pm\frac{1}{B}$. The 3dB, half power temporal bandwidth of the autocorrelation output is therefore seen to be approximately $\frac{1}{\Delta f}$.

$$z_u(t) = \sqrt{BT}\frac{\sin\left[\pi Bt\left(1 - \frac{|t|}{T}\right)\right]}{\pi Bt}\cos\left[2\pi f_o t\right] \tag{3.51}$$

The principle of generating a very narrow autocorrelation response from a waveform of suitable temporal length and bandwidth, is referred to as pulse compression. An LFM signal is generally shown to have a far more concentrated autocorrelation response than alternative transmissions of similar length. The high pulse compression ratio of LFM waveforms is what makes them increasingly popular in both RADAR and SONAR technology, offering noticeable improvements in range resolution.

#### 3.2.2.4 Multipath Tolerance

The inherent multipath tolerance of the Chirp signal comes from the wideband nature of the transmitted signal. The occurrence of narrow band fading, caused by channel reverberation, can be seen to only affect a small interval of the overall transmission. Additionally, given a long enough chirp duration the delayed arrivals from previous symbols will have subsided, resulting in a minimal effect on the current symbol and thus reduced Inter-Symbol Interference (ISI).

Therefore, the duration of the chirp must be carefully selected to ensure it exceeds the maximum delay spread. In the case of a shallow water channel, each chirp must have a duration of at least 10ms to ensure it fully spans the worst case channel

conditions. If this condition is not met then the system will have difficulty overcoming the incurred frequency selective fading and can no longer be assumed to be multipath tolerant.

#### 3.2.2.5 Doppler Tolerance

A significant advantage of LFM waveforms are their inherent immunity to Doppler shift. If we perform the same matched filter process, as discussed previously, on a signal which has been distorted by a Doppler shift of $f_d$, we derive the correlator output as (3.52).

$$z_u(t) = \sqrt{\frac{2\mu}{\pi}} \cos\left[\left(\omega_o + \frac{\omega_d}{2}\right) t\right] \frac{\sin\left[\frac{\omega_d + \mu t}{2}\left(\frac{T}{2} - |t|\right)\right]}{\omega_d + \mu t} \tag{3.52}$$

Through further examination of this expression, we can observe that the location of the correlation peak will now occur at a time, $t$, given by (3.53). Apart from this shift in position, and a slight widening of the correlator output, minimal deterioration is observed.

$$t = -\frac{f_d}{B} T \tag{3.53}$$

### 3.2.3 OFDM Communication

In 1971, Weinstein and Ebert proposed the use of the *Discrete Fourier Transform* (DFT) to perform baseband OFDM modulation and demodulation [79]. This was the first demonstration of an efficient way of producing an OFDM data symbol, eliminating the need for banks of sub-carrier oscillators and minimising the affect of oscillator drift. The digital implementation of the OFDM structure is often believed to have been critical in the development of low-cost OFDM modems [80].

Through use of the discrete Fourier transform, each sub-carrier is shaped as a *Sinc* function, of spacing $T_s$. When combined the peak of a specific sub-carrier occurs at the same period as the first zero of its neighbour. This characteristic ensures orthogonality between individual carriers, while enabling an overlap of the spectrum. Further improvement is achieved through the use of the Fast Fourier Transform (FFT) and Inverse Fast Fourier Transform (IFFT). These algorithms can be seen to reduce the computational complexity symbol from the order of $(N^2)$ operations to $(N \log_2 N)$, through use of the *Radix-2* Cooley-Tukey algorithm.

An example of a basic OFDM transmitter and receiver structure, utilising the IFFT and FFT algorithms, are shown in Fig. 3.14. At the transmitter, the incoming

serial binary sequence is buffered into a parallel block and converted into the frequency domain utilising the IFFT operation. A cyclic prefix is then appended to the sequence prior to being output by a Digital to Analog Converter (DAC). At the receiver this operation is effectively reversed, utilising an FFT operation to convert between frequency and time domain.

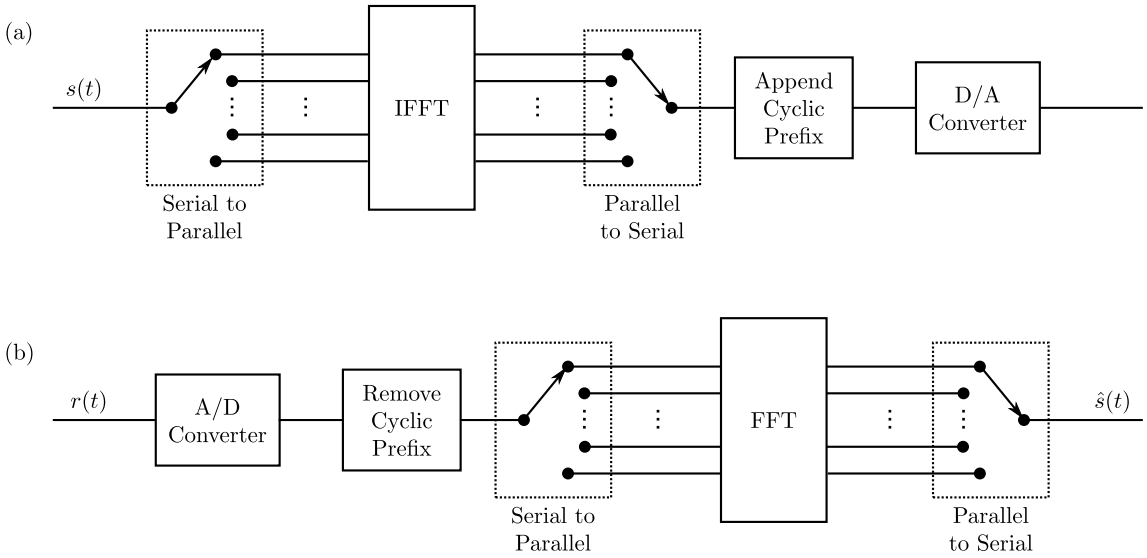


Figure 3.14: OFDM Communication Structures: (a) Transmitter, (b) Receiver

The baseband output from the IFFT operation, $s(t)$, can be expressed mathematically in the form (3.55). Where: $X_k$ expresses the $k$th data symbol; $T$ represents the duration of the OFDM symbol; and $N$ is the number of independent sub-carriers. To ensure orthogonality, each of the sub-carriers are spaced at intervals of $\frac{1}{T}$.

$$s(t) = \sum_{k=0}^{N-1} X_k e^{j2\pi \frac{kt}{T}} \qquad 0 \leq t < T \tag{3.54}$$

$$= \sum_{k=0}^{N-1} X_k \left( \cos\left(2\pi \frac{kt}{T}\right) + j \sin\left(2\pi \frac{kt}{T}\right) \right) \tag{3.55}$$

To reverse this process and recover the original binary sequence the FFT operation, described in (3.57), can be utilised.

$$\hat{X_k} = \frac{1}{T} \sum_{t=0}^{T-1} x(t) e^{-j2\pi \frac{kt}{T}} \qquad 0 \leq k < N \tag{3.56}$$

$$= \frac{1}{T} \sum_{n=0}^{T-1} x(t) \left( \cos\left(2\pi \frac{kt}{T}\right) - j \sin\left(2\pi \frac{kt}{T}\right) \right) \tag{3.57}$$

As emphasised previously, the effect of multipath can be seen to result in specific frequencies becoming attenuated. If narrow enough sub-bands are utilised then the amplitude across each can be considered constant i.e. the fading is linear across each narrow band. It is therefore essential to select a suitable number of sub-carriers such that the bandwidth of each is significantly less than the width of the frequency selective fades. In the case of the underwater channel a minimum of 1024 sub-carriers are typically selected, across an 8kHz bandwidth.

Although OFDM transmissions offer simplicity in the receiver structure and the ability to overcome severe multipath channels, several limitations are observed. The following sections highlight some of the difficulties faced in implementing a practical OFDM system.

#### 3.2.3.1 Guard Period

Although the use of narrow sub-carriers ensure that frequency selective fades have minimal effect within an individual symbol, the long delay spread observed in the UAC can be seen to result in continued interference between neighbouring symbols. A suitable technique to reduce the degradation caused by ISI, is the insertion of a time-domain guard period prior to the transmission of the consecutive symbol [45]. Two different guard sequences are typically proposed, Zero Padding (ZP-OFDM) or Cyclic Prefix (CP-OFDM).

In the case of CP-OFDM, an extension of the last $N$ samples of the OFDM symbol are appended to the start of the transmission. The use of a segment of the generated symbol, results in the channel performing cyclic convolution and thus ensures orthogonality between individual carriers [81]. Despite the transmission of a cyclic prefix requiring additional energy, the ability to reduce Inter-Carrier Interference (ICI) is typically believed to warrant its use.

#### 3.2.3.2 Pilot Tones

A method of estimating the instantaneous CIR is essential in compensating for the time-varying frequency selectivity of the channel. By interspersing known tones at points across the bandwidth of the transmission, estimates of both magnitude and phase fluctuations can be achieved [82]. Since pilot tones are used solely for the estimation of the channel conditions, and hence do not represent any actual data, their insertion can be seen to come at a cost in terms of overall system throughput.

#### 3.2.3.3 Sub-carrier Bit Loading

Based on accurate knowledge of the spectrum, gained via a suitable channel probe, sub-carriers which exhibit minimal interference can be modulated utilising higher order communication schemes. Unlike single carrier techniques, where a single modulation scheme and code rate are utilised for the entire packet transmission, in the case of multi-carrier schemes individual sub-carriers can use independent parameters based on their ability to successfully relay error free data through a frequency selective channel.

#### 3.2.3.4 Peak to Average Power Ratio (PAPR)

Although OFDM transmissions offer significant benefits in terms of receiver complexity and multipath tolerance, the transmitted waveform can regularly be found to exhibit periods of very high peak amplitudes, caused by the summation of independent sub-carrier phases. If a large number of sub-carriers are found to combine constructively in a given period, high peaks in the transmitted signal will occur.

The constructive generation of such peaks occur rarely in comparison to the length of the overall symbol. However, the variance from the average signal level is considerable, causing a significant dynamic range between the average output level and the peak levels. A method of measuring the variability between the peak amplitude and the mean level is known as the Peak to Average Power Ratio (PAPR) or the *crest factor*. The PAPR is defined by (3.59), where, $x(t)$ is the generated transmission, and $T_o$ is the period of the OFDM symbol.

$$\text{PAPR} = \frac{{|x|_{\text{peak}}}^2}{{x_{\text{rms}}}^2} \tag{3.58}$$

$$= \frac{\max|x(t)|^2}{1/T_o \int_0^{T_o} |x(t)|^2 dt} \tag{3.59}$$

In practical terms, the high PAPR of the OFDM signals cause a range of limitations in the design and implementation of a suitable hardware platform. The variation in the generated waveform requires the use of high resolution Digital to Analog Converters (DAC) and Analog to Digital Converters (ADC), with a wide dynamic range, to avoid digitisation or clipping. Additionally, linear amplifiers must be utilised at the transmitter to avoid distortion of the original signal. Such hardware requirements are typically shown to have a considerable effect on the cost and complexity of the system.

A variety of techniques have been presented to facilitate the reduction of PAPR, including: amplitude clipping and filtering; coding ; selected mapping; use of partial

transmit sequences (PTS); and signal interleaving. However, It should be noted, that these techniques come at a trade off in terms of computational complexity, Bit Error Rate (BER), data throughput or the requirement for additional transmit power. For the interested reader, additional information about the different approaches, and their performance, can be found in the referenced literature [83], [84].

#### 3.2.3.5 Frequency Offset Sensitivity

A considerable limitation of any OFDM transmissions is its sensitivity to frequency offsets. Considering the frequency domain representation of an OFDM signal, incorrect sampling of the received waveform can result in loss of orthogonality between adjacent sub-carriers and the generation of Inter-Carrier Interference (ICI) [85]. To ensure orthogonality, each carrier must be shown to have an integer number of cycles within the FFT window. In the case of a frequency offset, this assumption is found to be invalid resulting in the signal being down converted to the incorrect baseband frequency.

The two most significant sources of Frequency Carrier Offset (FCO), within an OFDM symbol, are: the mismatch of local oscillators; and the effect of any induced Doppler shift. The difficulty in producing accurate hardware oscillators is often shown to a misalignment of sub-carriers. Additionally, as with a single carrier system, the induced Doppler shift, due to the movement of the vehicle, results in a considerable frequency scaling of the transmitted waveform. Various estimation and compensation techniques have been proposed, demonstrating variable performance in the UAC [49] [50] [86], however a suitable compensation technique, capable of overcoming the highly variable motion of the $\mu$ROV, has yet to be practically demonstrated.

## 3.3 Error Correction Coding

In its simplest form, error correction coding exists to protect digital data as it propagates through a non-ideal communication channel [87]. The majority of modern communication systems employ a method of detecting and removing an incorrect sequence of data. The process of channel coding involves the insertion of redundant information into the binary data stream, such that the receiver can mitigate the effects of noise, and other forms of signal disturbance.

This section gives a concise overview of suitable error correction schemes, firstly examining the benefits of conventional convolutional codes, before discussing the merits of various iterative decoding techniques. It should be noted that the scope of this research is not focussed on the development or improvement of error correction

coding schemes. On the contrary, the main objective of this work is to examine the real-time implementation of a previously developed decoding strategy, for $\mu$ROV applications. Therefore, this section is solely included to give a description of suitable schemes, and provide theoretical background. For more in depth analysis and examination of the discussed coding techniques the reader is directed towards the literature referenced throughout.

### 3.3.1 Convolutional Coding

For many years convoltional codes have been utilised across a range of applications, both terrestrial and subsea. A convolutional code is typically generated utilising a binary shift register which stores the previous $N$ symbols. As new data enters the shift register, the output of the filter is calculated based on the current input value summed with a selection of the previous inputs stored in the shift register. The generator polynomial, $G = \{g_1, g_2, ..., g_n\}$, indicates the position of the taps used to calculate the output stream. The number of generator polynomials, $n$, indicates the number of output streams generated by the encoder and thus the overall code rate, $1/n$. The length of each polynomial, $k$, is known as the constraint length and reflects the number of previous symbols stored in the shift register.

Two forms of convolutional code are typically utilised: 1. 'non-systematic' encoder, where, the output is based solely on the values calculated by the shift register taps, i.e. the input does not appear explicitly in the output; 2. 'systematic' encoder, where, the input sequence is included in the output. In many systems a set of tap outputs are used to generate a feedback path, which is added to the new input value prior to being inserted into the shift register. This form of encoder is classed as *'recursive'*, and in many cases is used alongside a systematic output, i.e. a Recursive Systematic Convolutional (RSC) code. An example illustrating a 1/2 rate RSC encoder, utilising a constraint length of 3, is presented in Fig. 3.15.

To further improve the performance of the transmission, a technique of combining multiple coding stages has been successfully demonstrated [88], this technique is typically referred to as a serial concatenated codes. These codes are shown to significantly reduce the probability of an error, while simplifying the complexity of the required receiver structure. A typical example of a serial concatenated code, is the combination of a convolutional code with a Reed Solomon (RS) block code. This structure is typically referred to as a Reed Solomon Viterbi (RSV) code.

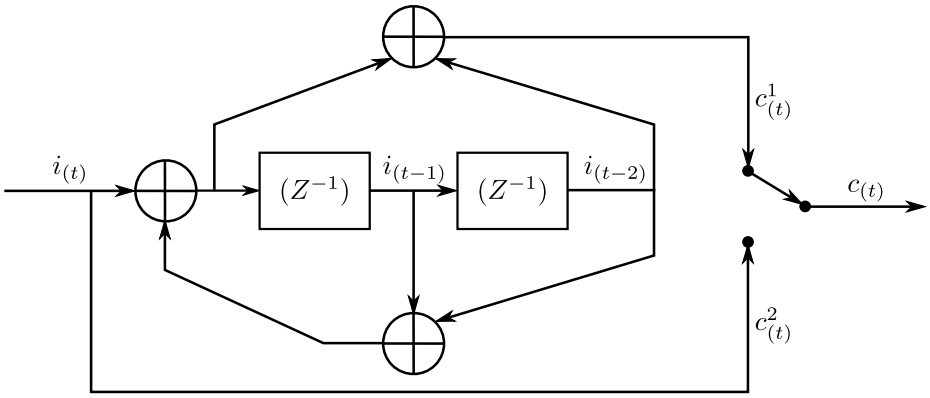


Figure 3.15: Recursive Systematic Convolutional Encoder of Rate, $R_c = 1/2$, with Constraint Length, $k = 3$, and Generator Polynomials, $g_1 = \{1, 0, 1\}$, $g_2 = \{0, 1, 1\}$

### 3.3.2 Turbo Coding

A significant development in error correction coding, was the introduction of turbo codes in 1993 by Berrou, Glavieus and Thitimajshima [51]. In its simplest form, a turbo code is shown to be constructed from a serial concatenation of two RSC codes, each of which is separated by a random interleaver, where the interleaver is included in the structure to ensure randomness between the two generated codewords. A block diagram of a turbo encoder is shown in Fig. 3.16a, where: $i(t)$ is the binary input sequence; $s(t)$ is the encoded output; and $c_1$ and $c_2$ are the two codewords generated by the RSC encoders.

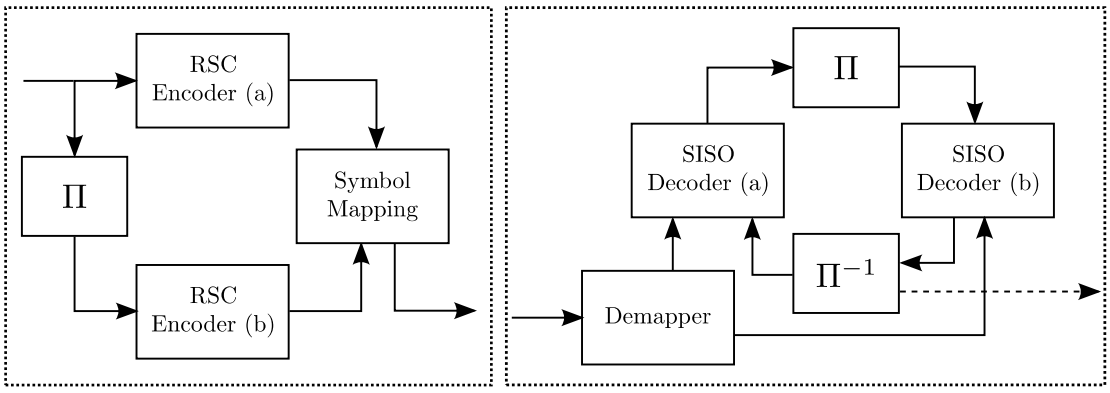


(a) Turbo Encoder / Transmit Structure

(b) Turbo Decoder / Receive Structure

Figure 3.16: Turbo Coding Structures: a) Encoder, b) Decoder

The turbo decoder, shown in Fig. 3.16b, consists of a similar structure to that of the encoder, incorporating a pair of Soft-Input Soft-Output(SISO) decoders each separated by an interleaver block. The improved performance of the turbo concept

is shown to correspond with the successful exchange of soft information between each of the decoding blocks. Each SISO decoder is shown to generate two output sequences: the first corresponding to the decoded information sequence; and the second representing the soft probabilities of the encoded bits. These soft decisions are typically expressed in the form of Log Likelihood Ratios (LLR) given by (3.60), where, $P(u_k = -1)$ is the probability that the decoded bit is negative and $P(u_k = +1)$ is the probability that the decoded bit is positive. The selection of a suitable SISO decoder algorithm is discussed in more depth in Section 5.1.3.

$$L(u_k) = \ln \left[ \frac{P(u_k = +1)}{P(u_k = -1)} \right] \tag{3.60}$$

The turbo decoder is shown to utilise an iterative feedback loop to supply extrinsic soft information about the coded input sequence to the next decoder block. In the first iteration, the primary decoder operates solely on the received input symbols, generating a set of LLRs relating to the encoded data bits. This soft information is interleaved and utilised as *a priori* information by the second decoder to further improve the estimate of the original input sequence. By exploiting these soft decisions, the performance of the decoding structure is found to significantly improve, resulting in a reduction in BER. This recursive cycle of exchanging soft information between the two decoders continues until acceptable performance is achieved or until a set stop criteria is met.

### 3.3.3 Combined Coding and Modulation

Despite conventional coding techniques offering a reduced probability of packet errors, the benefits of such schemes come at a considerable cost in terms of system throughput or operational bandwidth. If we consider a system which generates $n$ coded bits for every $k$ uncoded input bits, the data rate of the encoded transmission, $R_c$, can be given by (3.61), where, $R_u$ expresses the data rate of the original input sequence.

$$R_c = \frac{k}{n} R_u \tag{3.61}$$

Therefore, for a communication channel with a fixed bandwidth, the throughput of the system can be seen to reduce by $k/n$. Alternatively, to achieve the same data rate, and utilising the same level of coding redundancy, the bandwidth of the transmission signal would need to expand by $n/k$.

In 1982, Ungerboeck demonstrated that by combining the coding and modulation operations into a single process, a significant improvement in the spectral efficiency

of the generated waveform could be observed [89]. Trellis Coded Modulation (TCM) utilises signal-set expansion to maximise the minimum euclidean distance or *'free space'* between consecutive coded sequences. This process ensures that the modulated code offers a greater free distance than the uncoded transmission, whilst operating at a comparable information rate and occupying the same bandwidth [90] [91]. TCM is therefore shown to offer a significant coding gain whilst avoiding expansion of the signal bandwidth or loss in throughput.

#### 3.3.3.1 Interleaving

A notable limitation of most Forward Error Correction (FEC) schemes is their inability to combat long bursts of errors. The majority of codes in mainstream use are developed to correct for errors that are randomly distributed across the length of the codeword, making them ideally suited to transmission through an AWGN channel. However, the effect of a fading channel is shown to result in bursts of errors during periods in the transmission which correspond with the occurrence of deep fades. Therefore, an interleaver is utilised to disperse the resulting burst across many codewords, such that they can be represented as a randomised pattern and corrected by a typical FEC scheme.

Previous research has demonstrated two forms of combined interleaving, these are: Symbol-Interleaved Coded Modulation (SICM); and Bit-Interleaved Coded Modulation (BICM). In the first case, the modulation and coding processes are performed jointly, as in TCM, with the generated symbols being interleaved prior to transmission. Alternatively, in the case of BICM, the encoded bits are interleaved before being mapped onto a modulated symbol. In both cases, the reverse process is utilised at the receiver to deinterleave the original transmissions sequence, where the interleaving pattern is known *a priori* by both the transmitter and receiver.

Initially SICM transmissions were believed to offer a considerable improvement in performance, due to the preservation of the joint coding and modulation strategy. However, in the case of a fading channel, the performance of the system is shown to depend on the Hamming distance of the signal rather than the Euclidean Distance. Therefore, due to the reduction in code diversity of SICM transmissions, its performance is found to be ineffective [92]. In contrast, the performance of BICM is shown to demonstrate a significant improvement in performance, where the bit interleaving process ensures the coding diversity of the sequence is maximised and becomes equal to the smallest number of distinct bits [93]. While the placement of a bitwise interleaver breaks away from the traditional joint coding and modulation structure, the BICM structure is shown to offer a significant improvement in performance across a fading channel.

Based on these variations, it has been found that BICM is shown to offer a significant improvement in performance over TCM in an uncorrelated fading channel. However, TCM is still shown to have an advantage in a Gaussian channel due to an increase in Euclidean distance.

### 3.3.4 Turbo Equalisation

Based on the turbo coding principle, Douillard *et al.* demonstrated an iterative equalisation structure, often referred to as turbo equalisation [52]. In contrast to conventional receiver structures, which operate in a linear manner, a turbo equalisation structure utilises an iterative loop to supply soft extrinsic information between the SISO equaliser and SISO channel decoder. In a similar manner to the turbo coding principle, the supply of *a priori* information between each of the iterative blocks is shown to improve the reliability of the receiver structure [94]. The iterative feedback process is performed recursively until suitable performance is achieved, or until a pre-defined stop criteria is met. A block diagram of an iterative receiver structure is presented in Fig. 3.17. A variety of published work has demonstrated the use of a turbo equalisation structure but typically requires perfect prior knowledge of the channel state to ensure successful operation [95] [96].

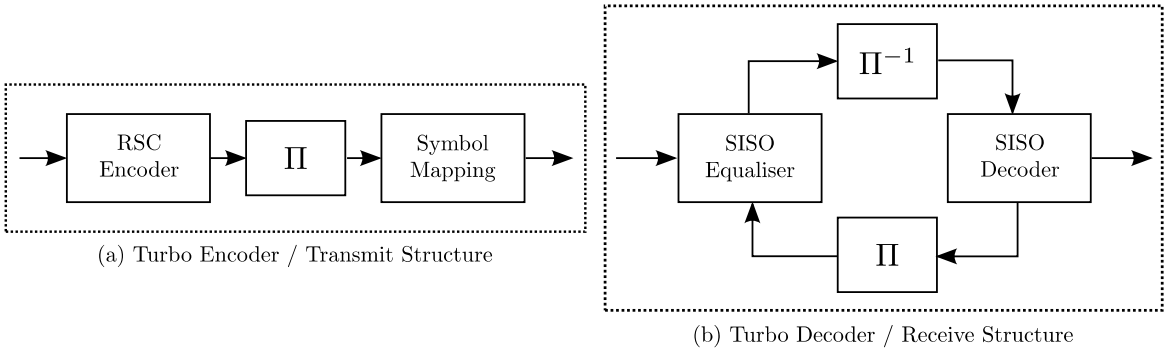


(a) Turbo Encoder / Transmit Structure

(b) Turbo Decoder / Receive Structure

Figure 3.17: Turbo Equalisation Structures: a) Encoder, b) Decoder

Iterative decoding is often combined with BICM, to increase the Euclidean distance of the generated codes, whilst continuing to exploit the benefits of bit interleaving. This approach is often termed Bit Interleaved Coded Modulation with Iterative Decoding (BICM-ID) and is typically shown to offer better performance than TCM and BICM in both Rayleigh fading and AWGN channels [97]. For the remainder of this work, while referring to BICM-ID, the iterative process performed between the soft demapper and the soft decoder will be termed as an inner iteration and the exchange of information with the equaliser structure as an outer iteration.

It should be noted that in a conventional communication scheme a Gray mapping scheme is favoured over natural mapping due to the reduced variation in the binary pattern of neighbouring constellation points. However, in the case of BICM-ID where iterations are performed between the soft demapper and soft decoder, the receiver is found to perform better with natural binary coding. Extensive research has demonstrated that when utilising Gray mapping, the number of distances at minimum Euclidean distance are not reduced through the exchange of *a priori* information. Therefore a limited improvement in performance is experienced from performing additional iterations [98].

## 3.4 Receiver Design Overview

This chapter has presented three different communication systems, Single Carrier; OFDM; and Spread Spectrum. Each has been rigorously reviewed, evaluating the benefits and limitations of each, in developing a high data rate communication link for a $\mu$ROV. Detail has been given relating to the design of a suitable receiver structure, focusing on techniques that overcome the severe multipath channel and the frequency and time dilation caused by the highly dynamic Doppler effect. Table 3.4 summarises the strengths and weaknesses of each signalling technique, in terms of: data rate; practical implementation; and reliability.

| System | Benefits | Limitations |
|---|---|---|
| Single Carrier | • High Data Rate<br>• Doppler Compensation | • Complex Equaliser Structure |
| OFDM | • Simple Structure<br>• Multipath Tolerant<br>• Ability to 'Load' Subcarriers | • High PAPR<br>• Frequency Offset Sensitivity<br>• Increased Overheads |
| Spread Spectrum | • Operational at Low SNRs<br>• Multipath Tolerant<br>• Simple Receiver Structure | • Low Data Rate |

Table 3.4: Comparison of Underwater Communication Schemes: Single Carrier, OFDM and Spread Spectrum

It can be seen from Table 3.4 that spread spectrum techniques offer a significant advantage in their ability to operate in low SNR conditions and environments exhibiting very long delay spread. The considerable limitation in spread spectrum techniques is the reduced data rate caused by the inefficient use of bandwidth ($\ll$ 0.5bit/s/Hz). This is compounded by the bandwidth limitations of the underwater acoustic channel, caused by severe signal attenuation at higher frequencies. Therefore, Spread Spectrum techniques are typically shown to be ideal for low data rate transmissions, but ineffective in the design of a high data rate acoustic modem.

When initially presented, the benefits of OFDM transmissions are thought to be conclusive, offering improved tolerance to the multipath channel and simplicity of the receiver implementation. However, on more detailed examination the challenges of the high PAPR and frequency offset sensitivity make the receiver more complex to implement than initially perceived. Of specific note is the effect of highly variable Doppler shift, which contributes to a severe mismatch in sub-carrier frequencies and overall degradation in performance. Although several block Doppler compensation techniques have been successfully demonstrated, a method of tracking rapid accelerations and decelerations within the length of a single OFDM symbol has yet to be demonstrated. The effective frequency sensitivity is further emphasised by the requirement for a high number of very narrow frequency bands to ensure flat fading in a very hostile underwater channel.

The author therefore recommend the use of a single carrier communication technique, in order to support reliable high data rate transmissions from a $\mu$ROV platform. Despite the increased complexity in receiver design, a non-linear equaliser structure combined with high level error correction codes have previously been shown to offer good performance through a long range, shallow water acoustic channel. Additionally, the use of a combination of open loop Doppler estimation and closed loop tracking are believed to be capable of overcoming the complex motion of such a small dynamic vehicle. The following chapters therefore examine the specific challenges in developing a high data rate single-carrier transmission system suitable for a $\mu$ROV.

# Chapter 4

# Investigation of a High Data Rate Up-Link

This chapter explores the complexities in developing a high data rate communication link for a $\mu$ROV application. Based on the evaluation of the various signalling techniques presented in Chapter 3, the author proposes the use of a single carrier communication scheme. Although such techniques have previously been researched for the underwater channel, limited research has addressed the specific challenges relating to the discussed application. In order to test and validate the performance of the proposed receiver structure, a range of realistic practical tests have been conducted utilising a Seabotix $LBV200^2$ $\mu$ROV platform. The trials comprehensively examine the challenges imposed by the specific operating environment, and show the route to a low-cost receiver structure capable of supporting high data transmissions with consistent performance. Further information relating to the location and conditions of the experimental work conducted in support of this research can be found in Appendix A.

## 4.1 Single Element Receivers

### 4.1.1 Motivation

Based on recent developments in iterative decoding structures and turbo equalisation techniques, research at Newcastle University has investigated the capability of single element BICM-ID receivers in overcoming severe multipath channels and low SNR conditions [56]. The ability to demonstrate near-Shannon performance, has encouraged the use of such 'turbo' decoding structures in the field of underwater acoustics. The use of soft decisions, and multiple decoding iterations, has

been found to significantly improve the performance of the receiver in particularly in hostile channel conditions.

In the proposed $\mu$ROV application the performance of a iterative single element receiver is shown to have merit in terms of both cost and ease of deployment. Therefore, this work initially focusses on the use of low-cost single element equaliser structure, utilising iterative decoding and equalisation, in the form of BICM-ID, to overcome the complications relating to the highly dynamic, short range - shallow water channel.

#### 4.1.1.1 Fundamental Transmission Parameters

.

Due to the considerable limitations of the vehicles size and payload capacity, the use of low frequency transducers is actively discouraged. Since the size of the transducer is typically inversely proportional to its resonant frequency, the use of transducers in the 8-16kHz band are deemed unsuitable due to their physical size and weight, i.e. ≈20-30cm and 4kg mass in water. The use of a higher frequency band is therefore deemed more suitable, with minimal absorption loss at such short ranges, <1km. Throughout this study the use of a 50kHz centre frequency is utilised, operating with a 20kHz bandwidth and a symbol rate of 20kSym/s, i.e. 1sym/Hz.

### 4.1.2 ROV Interference

Prior to evaluating the performance of the iterative receiver structure, preliminary field trials were conducted at Royal Quays Marina to examine the effect of any interference created by the vehicles thrusters. A simple transmitter structure was developed, whereby a single carrier, QPSK packet was generated in Matlab and repeatedly output from a Tektronix AFG3021B arbitrary signal generator. The parameters of the generated waveforms are given in Table 4.1. It should be noted that no error correction coding was utilised during these initial tests.

The output of the arbitrary signal generator was fed into a wideband amplifier prior to transmission from a single element transducer mounted on the Seabotix LBV200[2] vehicle. The transducer used for these preliminary tests was a 50kHz piston element, offering a flat transmit response (< 3dB down) across the 40-60kHz band. The beam pattern of the unit is approximately conical with an observed beam angle of $\approx 40^{\circ}$. The transducer was mounted such that beam pattern was angled horizontally across the transmission channel. In this configuration, the directional transducer can be seen to successfully minimise the generation of any multipath arrivals through shading of the transmit beam pattern, such that the amount of energy projected towards

| Parameter | Value |
|---|---|
| Sample Frequency ($f_s$) | 200kHz |
| Centre Frequency ($f_c$) | 50kHz |
| Bandwidth ($f_B$) | 20kHz |
| Total Packet Duration ($T_p$) | ≈146ms |
| Packet Modulation | QPSK (4064 Bits) |
| Training Sequence | BPSK (500 Bits) |
| Synchronisation | LFM (20ms) |
| Source Level (SL) | 170dB (≈ 1W) |

Table 4.1: Single Carrier Packet Parameters Used During Preliminary Trials

the surface or the seabed is reduced. This enables mitigation of the multipath effect, allowing focus to be initially placed on studying the receiver performance with respect to the induced thruster noise and Doppler shift. It should be noted that an acoustic Source Level (SL) of approximately 170dB, or 1W of acoustic power, was utilised throughout these experiments. This corresponds with an electrical power consumption of roughly 2W, which when compared with the draw of the vehicles thrusters is considered negligible.

At the receive end, signals were captured using an Agilent U2541A data acquisition unit via a Reson TC4032 omnidirectional wideband hydrophone. A pre-amplifier and filter unit were used to band-limit the received signals to between 10kHz and 100kHz and apply a gain of 30dB. Each data set was then post-processed offline using Matlab. For the purposes of these initial experiments, a simple DFE structure was constructed, utilising a Least Means Square (LMS) algorithm to update both the feed-forward and feed-back equaliser tap coefficients, this structure is shown in Fig. 3.7 (Section 3.2.1.2). Both a block estimate and a closed loop Doppler estimation scheme were implemented to attempt to remove any carrier phase and symbol timing errors caused by the motion of the vehicle.

The primary objective of the first set of trials, was to characterise the effect of the vehicle on the performance of a basic single carrier system. To allow for a fair comparison of the effect of thrusters on the performance of the system, the following procedure was repeated for each of the captures:

1. At the start of each capture, the vehicle was positioned approximately 1m away from the receive hydrophone.

2. The $\mu$ROV would accelerate with full available thrust from a static start until maximum velocity is achieved.

3. The vehicle would continue at full speed for the remainder of the tether, a distance of between 20-25m.

4. The speed was then reduced until the vehicle returned to a stop.

Throughout each capture, both the $\mu$ROV and the receive hydrophone were positioned at mid water column depth of approximately 5-6m. The receive hydrophone was mounted in a static position for the duration of all captures, hung from a moored surface pontoon. For each repeat of the described procedure the vehicle would be driven at a perpendicular angle to the receive hydrophone, which would ensure maximal Doppler shift was achieved. Several captures were recorded utilising different thruster gains. By controlling the gain, the amount of available power to each thruster could be restricted, causing a reduction in both the maximum speed and the acceleration of the vehicle. Fig. 4.1, 4.2 and 4.3, present three captured data sets for thruster gains of 100%, 60% and 40% respectively.

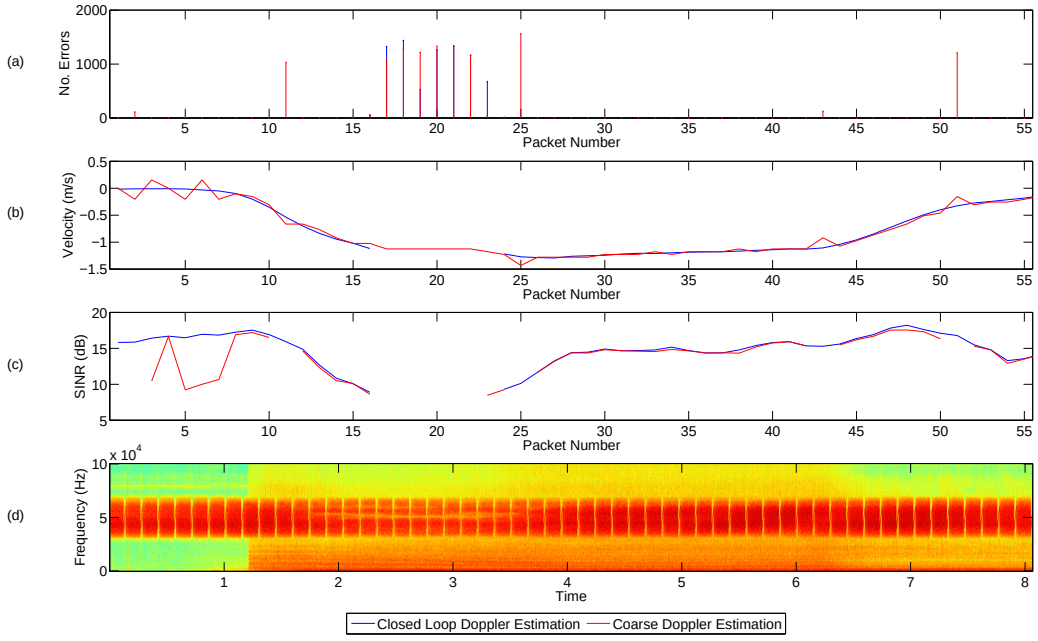


Figure 4.1: Single Carrier Demodulator Output (Thruster Gain = 100%): (a) Bit Errors Per Packet [Closed Loop = 7783 / 223520 Bit Errors, Open Loop = 11587 / 223520 Bit Errors], (b) Velocity Estimation, (c) SINR, (d) Spectrogram Of Received Signal

Examination of the spectrograms demonstrate that an increase in thruster gain results in, not only low frequency interference, but also a much more wide band effect. This is reflected in the SINR plot, where movement away from the receiver causes reduction in the power of the received signal, due to transmission loss, as well as additional noise from the thrusters causing an increase in wideband interference. When operating at low thruster gains, i.e. 40%, the interference is far less severe,

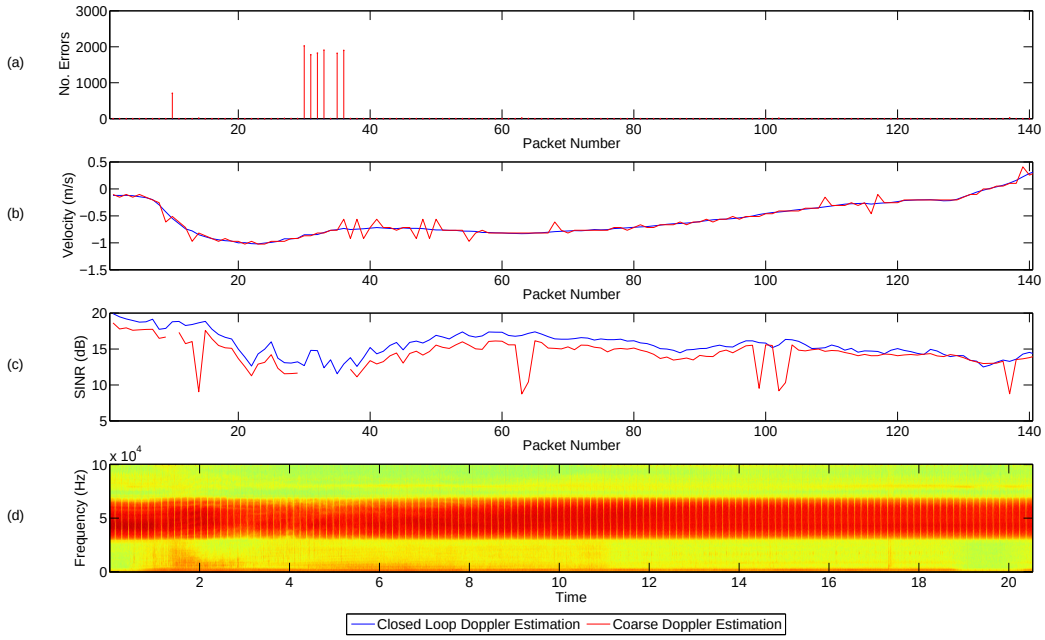


Figure 4.2: Single Carrier Demodulator Output (Thruster Gain = 60%): (a) Bit Errors Per Packet [Closed Loop = 2 / 568960 Bit Errors, Open Loop = 12062 / 568960 Bit Errors], (b) Velocity Estimation, (c) SINR, (d) Spectrogram Of Received Signal

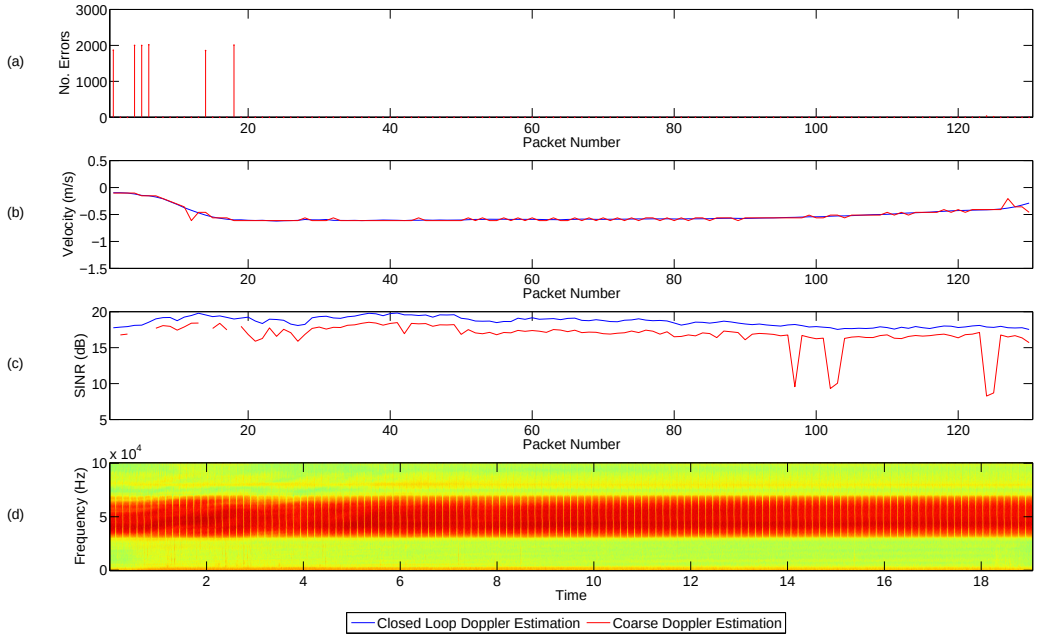


Figure 4.3: Single Carrier Demodulator Output (Thruster Gain = 40%): (a) Bit Errors Per Packet [Closed Loop = 0 / 528320 Bit Errors, Open Loop = 11820 / 528320 Bit Errors], (b) Velocity Estimation, (c) SINR, (d) Spectrogram Of Received Signal

with negligible low frequency noise and minimal fading across the transmission band. This is clearly represented in the other plots where minimal packet errors, and an insignificant reduction in SINR, are observed. In this scenario, when utilising a closed loop Doppler estimation technique, 0 bit errors are observed across the duration of the capture.

When operating with maximum thruster gain, clear nulls become apparent in the signal spectrum across the 40 to 60kHz transmission band, as shown in Fig. 4.1. These nulls were associated with the observed formation of '*bubble clouds*', due to propeller cavitation, resulting in a dramatic reduction in signal to noise ratio. Such bubble plumes can result in both the attenuation of the signal and the generation of high frequency interference caused by the collapsing of the bubbles. Higher gains are believed to clearly demonstrate a dramatic loss in thruster efficiency, with air pockets causing loss of torque. Therefore, lower gains are believed to offer higher practicality by minimising the formation of low pressure regions and, thus, reducing the probability of cavitation. The velocity estimations for gains of 100% and 60% show limited difference in both acceleration and top speed, however, for a higher gain, a dramatic increase in noise and interference is apparent.

Although a slight amount of low frequency noise is observed in the 60% case, the fading previously observed in the transmission band is far less apparent. This is therefore reflected by a reduced number of packet errors. It is believed that the incurred propeller cavitation is heavily affected by the shallow water environment. At greater depths, and with increased water pressure, it is believed that the possibility of the propeller slipping and forming air voids will be significantly reduced.

### 4.1.3 Equaliser Performance

This section explores the performance of the various adaptive equaliser structures discussed in Section 3.2.1.2. As highlighted, the UAC presents a highly time variable multipath response, which results in severe ISI. An adaptive equaliser structure can be utilised to suppress the incurred interference and to improve the time and phase synchronisation of the received packet. Both a Linear Transversal Equaliser (LTE) and Decision Feedback Equaliser (DFE) are examined below, discussing their performance in the presence of data recorded during trials.

For all results presented in this section, a 40-60kHz QPSK signal was generated using a bespoke software transmitter. The sequence was output from a custom-made Digital to Analogue Converter (DAC) unit prior to being amplified by a wideband amplifier and emitted from a omni-directional ball transducer mounted on a Seabotix LBV-200[2]. Further details of the transmitter structure and the packet format can be found in Chapter 5. A single element Reson TC4032 hydrophone was utilised

throughout this set of trials, with the data captured by an Agilent U2541A DAQ unit and processed by a real-time receiver application, developed in C++. All packets shown utilise a QPSK modulation scheme, with 1/2 rate RSC code, generated with the polynomial: $G_{1/2} = [23, 35]_8$.

#### 4.1.3.1 Linear Transversal Equaliser

A Linear Equaliser (LE) is initially proposed as a method of compensating for the multipath delay spread. A $\frac{T}{2}$-spaced LE utilising an LMS update algorithm, of length, $L_{\text{lte}}$, and step-size, $\mu$, is examined. Adjustments to both of these parameters have a significant effect on the performance of the equaliser, affecting both the convergence rate and the length of delay spread the filter can successfully compensate for.

For a $\frac{T}{N}$ fractionally spaced linear equaliser, which is assumed to be correctly synchronised, i.e. the current symbol is positioned in the centre of the tapped delay line, the filter can be assumed to span $S_{\text{ISI}}$ precursor symbols (4.1).

$$S_{\text{ISI}} = \frac{L_{\text{lte}} - 1}{2N} \tag{4.1}$$

Examining the requirements for the proposed system, a delay spread exceeding 5-6ms is often exhibited in a typical shallow water channel. Therefore, assuming a symbol rate of 20kS/s, i.e 1 Sym/Hz, a LE of 25 taps is only capable of spanning 6 post-cursor symbols (0.3ms), making it highly unsuitable for supporting realistic underwater channels. Fig. 4.4c demonstrates the limitations of a 25 tap LE structure when processing a data set captured during trials on Windermere in March 2012.

From the presented results it is immediately evident that during periods where significant arrivals are observed outside the 0.3ms span, the equaliser is unable to compensate for the incurred ISI. Assuming the maximum delay shown by the impulse response in Fig. 4.4, i.e. 4-5ms, an equaliser of over 400 taps would be required to successfully overcome the significant delay spread. Such a filter is immediately dismissed due to the poor convergence properties of such a long adaptive filter.

#### 4.1.3.2 Decision Feedback Equaliser

In the case of long delay spreads, or where severe spectral fades are exhibited, a DFE has been found in previous research to significantly outperform the performance of a typical LE structure. A DFE structure is presented utilising a $\frac{T}{2}$-spaced forward filter and a $T$-spaced feedback filter. Each filter requires an independent set of update equations to calculate its proceeding filter weights, where the overall convergence

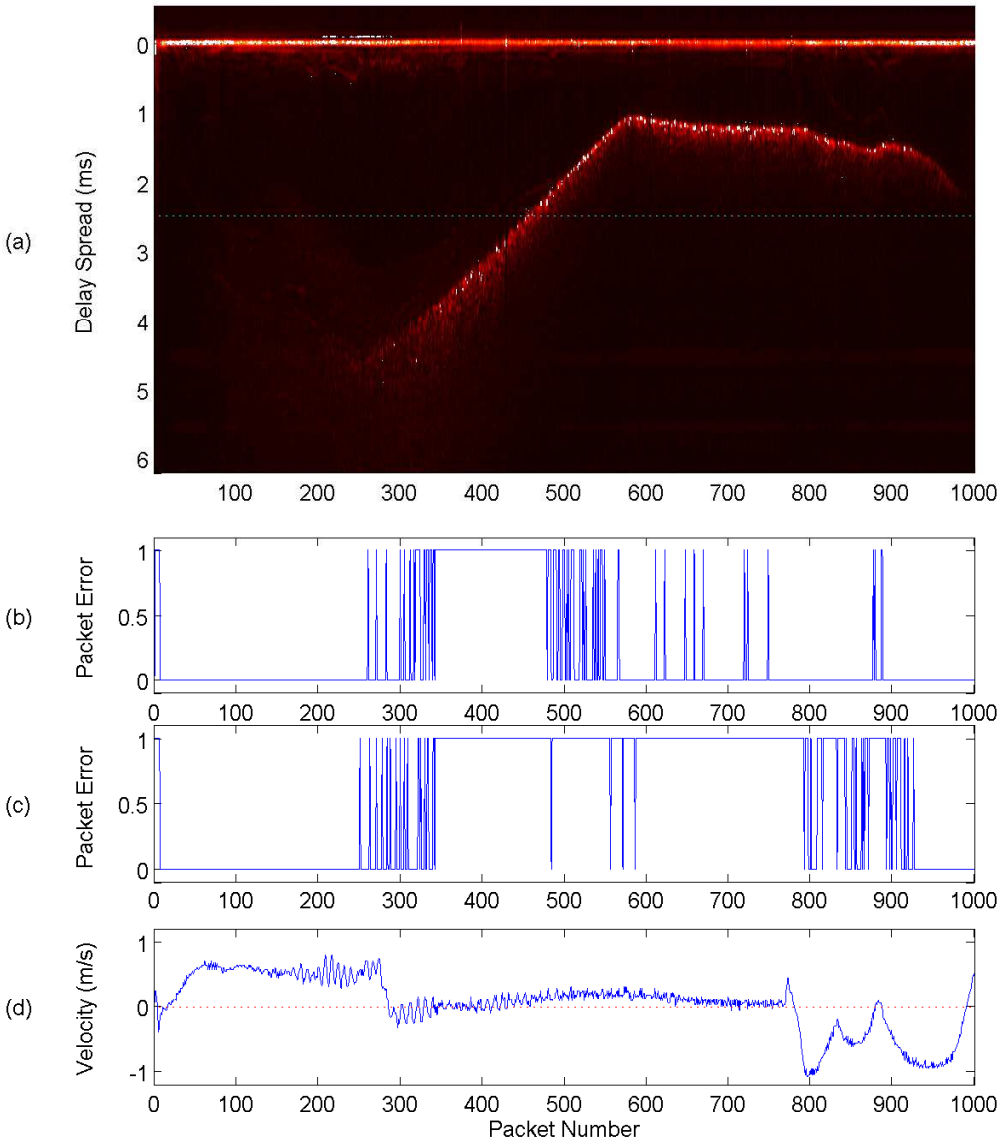


Figure 4.4: Single Element Equaliser Performance [Data Set 1]:
(a) Time Varying Channel Impulse Response (CIR),
(b) Decision Feedback Equaliser [$L_{\text{ff}} = 25$, $L_{\text{fb}} = 50$, $\mu_{\text{ff}} = 0.012$, $\mu_{\text{fb}} = 0.010$],
(c) Linear Transversal Equaliser [$\text{L}_{\text{LE}} = 25$, $\mu = 0.012$]
(d) Velocity Estimate (Based on Doppler Block Estimate) - $c \approx 1500$ m/s

and steady state performance is highly dependent on both the feed-forward, $\mu_{\text{ff}}$, and feed-back, $\mu_{\text{fb}}$, step-size.

The proposed transmission scheme is encoded using a RSC 1/2 rate code. To further improve the performance of the receiver, a Bit Interleaved Coding and Modulation with Iterative Decoding structure is utilised. Based on the findings of previous studies, a maximum length interleaver is used to distribute consecutive symbols across the duration of the packet. This technique is believed to significantly improve the ability of the system to overcome burst errors caused by the propagation of incorrect decisions through the DFE structure. During these trials, the receiver is configured to perform a maximum of 3 inner and 2 outer iterations.

Fig. 4.4b and Fig. 4.4c demonstrate the comparative performance of the DFE structure and the LE structure. The discussed receiver structure utilises 25 feed-forward taps and 50 feed-back taps, with step sizes of 0.012 and 0.010 respectively. To improve the convergence rate, and reduce the period of the required training sequence, an RLS algorithm is utilised during training. The data payload is composed of 4096 symbols, resulting in a packet duration of approximately 250ms including synchronisation, training and header overheads. The equaliser output for a single packet is shown in Fig. 4.5. Subplot c demonstrates the ability for the feedback filter coefficients to adapt and track the instantaneous channel response, shown in subplot e. The convergence rate of the proposed receiver is clearly demonstrated by the MSE plot, shown in subplot d. The use of the RLS update algorithm enables the filter coefficients to converge within the length of the training sequence (500 symbols), ensuring successful demodulation of the selected packet.

The performance of the DFE, with the described configuration, is clearly limited during periods of long delay spreads. Despite fewer errors being observed when compared with the LE approach, a DFE with just 50 feedback taps is shown to be unable to suppress the full delay spread experienced. Despite the feedback filter being symbol spaced, a 50 tap equaliser is still shown to be unable to overcome delay spreads much greater than 2.5ms. This is demonstrated in Fig. 4.4, where the system is only capable of overcoming shorter delay spreads, $<$ 2ms, observed during the latter stages of the capture, i.e. packets 600 - 900.

Fig. 4.6, demonstrates the performance of the receiver structure for a range of feedback filter lengths, ranging from 65-120 (3.25ms - 6ms). The performance of the receiver is tested using a data set of $\approx$ 3030 packets, collected during trials on lake Windermere in March 2012. Delay spreads ranging from 1-5ms are exhibited across the duration of the packet. For all filter lengths an LMS step size, $\mu_{\text{fb}}$, of 0.010 is utilised. This value was found through trial and improvement to offer optimum receiver performance. Alongside the performance of a conventional receiver structure,

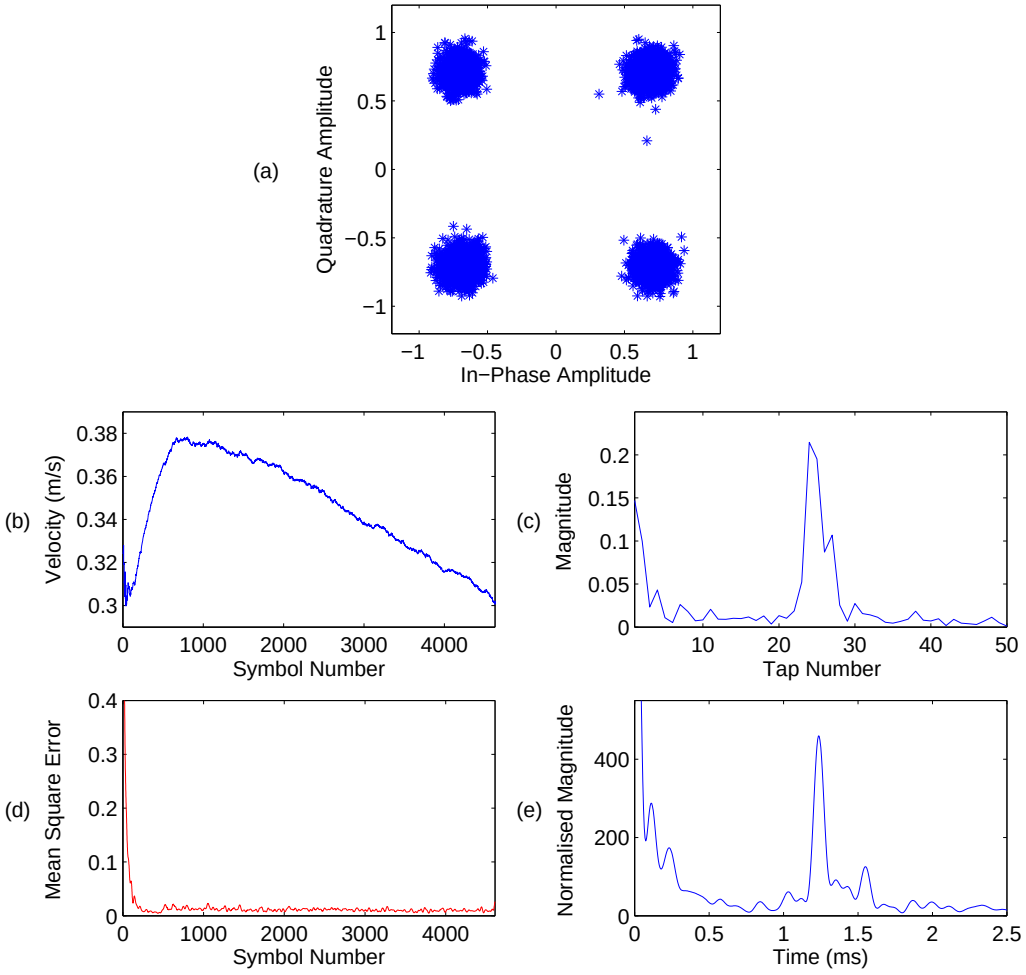


Figure 4.5: Single Element DFE Operation [Data Set 2 - Individual Packet Analysis]:
(a) IQ Plot, (b) Closed Loop Doppler Estimate,
(c) Feedback Filter Coefficients, (d) Mean Square Error (MSE),
(e) Estimated Channel Impulse Response (CIR)

the figure also presents the number of incurred packet errors for a 'sparse' receiver structure. Further discussion on sparse equalisers is given in Section 4.1.3.3.

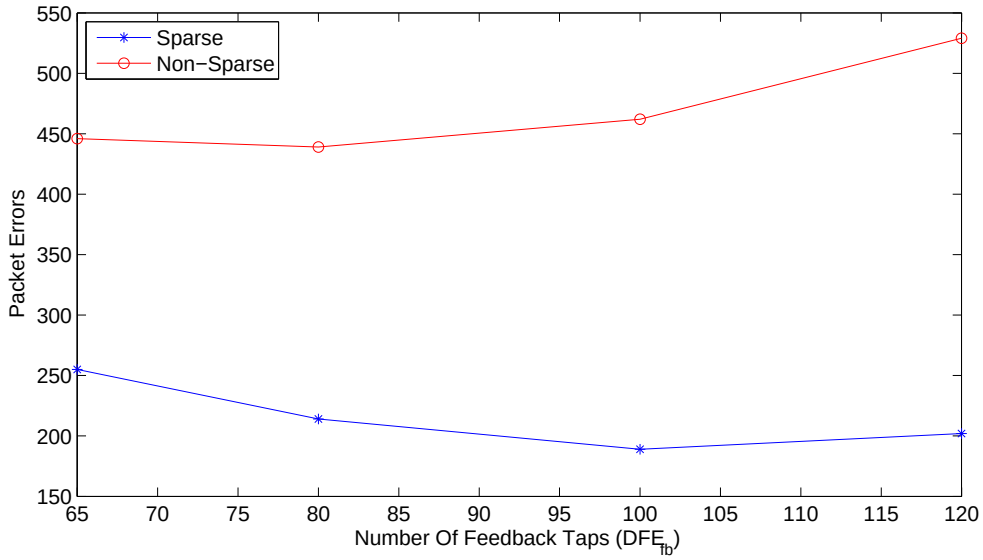


Figure 4.6: Comparison of Sparse and Non-Sparse Equalisation Performance, [Sparse $\mu_b = 0.010$, Non-Sparse $\mu_b = 0.005$]

Despite the use of longer feedback filters, the performance of the DFE structure is still severely limited during periods of long delay spread. The lowest number of observed packet errors was, in fact, observed when utilising a reduced number of filter coefficients. Despite longer filters offering greater coverage, an increase in packet errors was observed when greater than 100 filter taps were utilised. This is believed to be attributed to a combination of: 1. error propagation and 2. noise enhancement.

1. **Error Propagation:**
   If a 'wrong' or incorrect decision is made by the equaliser structure, the feedback path ensures the error propagates back into the filter. This process is shown to result in the generation, rather than the removal, of ISI, causing a detrimental effect on future symbol estimates. This process typically results in a *'burst'* of errors, which is commonly overcome with a combination of interleavers and high order error correction codes. This effect is further emphasised when utilising an increased number of filter coefficients. Longer filters can be seen to increase the time taken for an incorrect decision to propagate out of the delay line, causing an incorrect decision to have an effect on an increased number of consecutive symbols. If a significant sized *'burst'* of errors is observed, the DFE can become unstable and diverge away from the optimum solution. Since error correction codes have a limitation in the number of errors they are able to correct, long bursts of errors can be difficult to overcome.

2. **Noise Enhancement:**
   Examining the channel geometry of the proposed application, the ratio between range, $R$, and depth, $D$, can be seen to be approximately unity, i.e. $R/D \approx 1$. The CIR can therefore be seen to exhibit long delay spreads with distinct 'sparse' reverberation paths. This effect is further compounded by the insignificant temperature gradient observed across the depth of the shallow water channel, resulting in minimal signal refraction. In contrast, channels with a high range to depth ratio, i.e. $R \gg D$, will typically exhibit a more even distribution of multipath arrivals across the length of the delay spread. A limitation of the sparse channel relates to the long periods of negligible distortion between each of the significant arrivals. In order to compensate for the incurred ISI the feedback filter must be shown to span the entire duration of the multipath spread, with many of the coefficients representing minimal channel effects. Since the lowest value of an equaliser tap directly relates to the value of the step-size parameter, $\mu$, when the filter length increases the output becomes dominated by coefficients which represent minimal, if any, channel distortion. This effect is further exaggerated during periods of low SNR, where the 'null' coefficients will cause an increase in the noise floor of the filtered output.

A combination of noise enhancement and error propagation can be seen to cause a limitation in the functionality of long feedback filters. In the proposed shallow water channel a trade-off is observed between: utilising long enough feedback coefficients to span the full delay spread; and the occurrence of errors due to high numbers of coefficients which represent insignificant channel information. In the majority of previous research reduced symbol rates have been utilised, typically in the order of 4kSym/s. At these symbol rates the performance of a similar $T$-spaced equaliser structure is significantly improved, offering the ability to track delay spreads of upto 20ms with an 80 coefficient feedback filter. The use of higher symbol rates can therefore be seen to constrain the operation of the DFE structure, limiting the ability to overcome realistic delay spreads.

To improve the stability of the equaliser structure, and reduce the effect of noise enhancement, when utilising longer feedback filters the value of the step-size coefficient, $\mu$, can be reduced. However, the step-size is also found to significantly effect the convergence rate of the filter, causing difficulty when trying to track rapid changes in the channel conditions. When operating in a shallow water channel, at short ranges, the movement of the vehicle is shown to cause an exaggerated change in the multipath response. The coherence time of the channel is therefore very short, requiring continuous updates to the filter coefficients in order to track the ISI. Therefore, a reduction in step-size is seen to be a compromise, reducing the

enhancement of 'null' filter weights but in doing so affecting the tracking ability of the receiver structure.

#### 4.1.3.3 Sparse Equalisation

*'Sparse'* equalisation utilises a reduced set of filter coefficients to suppress the effects of long delay spreads. Through identification of the most significant multipath arrivals, filter coefficients which represent minimal channel contribution can be isolated, restricting the number of filter coefficients used and making the receiver less susceptible to error propagation and noise enhancement.

In order to identify the most significant multipath arrivals, the instantaneous CIR can be estimated using one of following techniques:

- Utilise the normalised cross correlation of a chirp waveform, typically appended to the start of each packet for synchronisation purposes. Given enough bandwidth and a suitable chirp duration an accurate probe of the channel conditions can be achieved.
- Examination of the feedback filter weights at the end of the training period. If the DFE has successfully converged during the training sequence, and the length of the filter is adequate to span the full delay spread, the taps will give an accurate representation of the individual multipath arrivals.

The output from either of these approaches is typically hard limited against a predetermined threshold level, $\Upsilon$. This process generates a binary representation of the channel, $b_{\text{mp}}$, which can later be used to identify which filter weights should be used during the equalisation process. Due to the dynamic nature of the shallow water channel, the filter coefficients cannot be considered static across consecutive packets. Therefore this process must be repeated on a packet by packet basis.

An example of two sparse underwater channels estimates are shown in Fig. 4.7. Both estimates were generated from the output of the chirp correlation process, using the autocorrelation of a 20ms LFM synchronisation sequence. A binary representation for each of the channels was produced utilising the hard limiting process. The threshold level, $\Upsilon$, was set as a fractional value of the maximum correlation peak, in this case 15%. With the exception of a non-minimum phase channel, this maximum correlation value will typically occur at the point of first arrival, i.e. the direct path. The binary representation of the multipath response is overlaid on the plot, by a dashed red line.

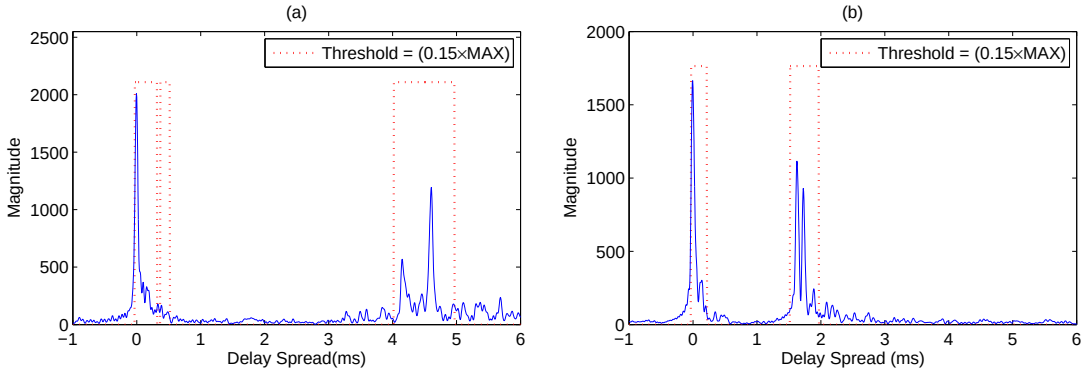


Figure 4.7: Binary Representation of Two Sparse Underwater Channels

The improved performance of the sparse equalisation structure is evident from Fig. 4.6, where, approximately half the number of packet errors are incurred when utilising the optimum sparse configuration. In the case of sparse equalisation, the span of the feedback taps, $\text{DFE}_{\text{fb}}$, refers to the maximum length covered by the available taps. Due to the nature of the sparse selection criteria, the actual number of taps calculated per symbol iteration is significantly less.

Additionally, by increasing the maximum number of coefficients available, the two systems can be found to differ greatly. In contrast to a traditional DFE structure, the increased temporal span of the 'sparse' feedback filter enables the equaliser to overcome longer delay spreads, with reduced degradation caused by noise enhancement and error propagation. Therefore, to an extent increased filter lengths are shown to further improve the performance of the equaliser structure when utilising a 'sparse' construction. The second data set, shown in Fig. 4.8, demonstrates a comparison of the error distribution for an optimum sparse and non-sparse receiver structure. During the 1000 packet capture, a reduction in the number of packet errors can be observed when utilising a sparse receiver structure, including periods of long delay spread.

Fig. 4.9a demonstrates the relationship between the number of packet errors and the selected threshold level. The lowest point in the curve, at approximately 15%, can be seen to represent the optimum threshold value. By utilising an increased threshold level, some of the significant filter coefficients are neglected, causing inaccuracy during equalisation. On the contrary, a lower threshold level can be seen to result in an rise in the number of insignificant filter weights used, leading to the possibility of increased noise enhancement.

An additional benefit of sparse equalisation is the reduced computational requirements of the receiver structure. As shown in Fig. 4.9b, the number of filter coefficients required considerably drops when utilising a sparse approach. For the optimum threshold level of 15%, or 0.15, on average approximately 25 filter taps are

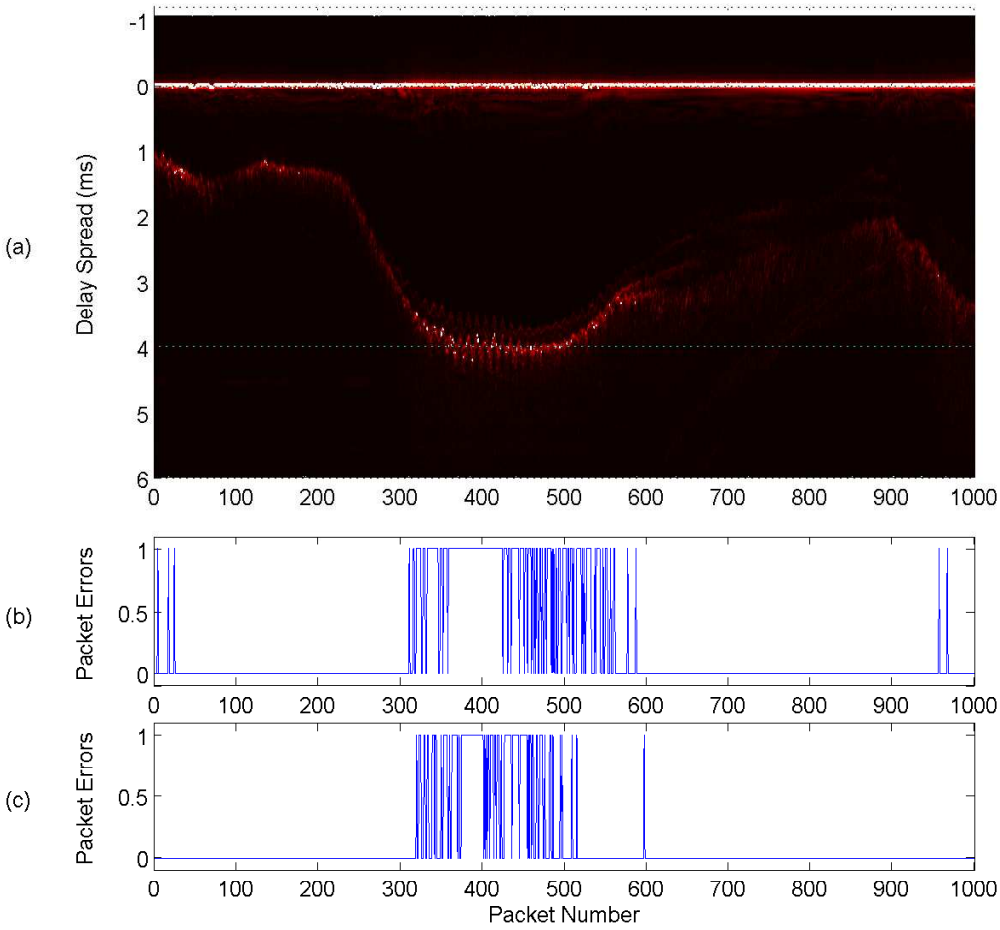


Figure 4.8: Single Element Equaliser Performance [Data Set 2]:
(a) Time Varying Channel Impulse Response (CIR),
(b) Traditional DFE Structure [$L_{\text{ff}} = 25$, $L_{\text{fb}} = 80$, $\mu_{\text{ff}} = 0.012$, $\mu_{\text{fb}} = 0.010$]
(c) DFE Structure with Sparse Equalisation

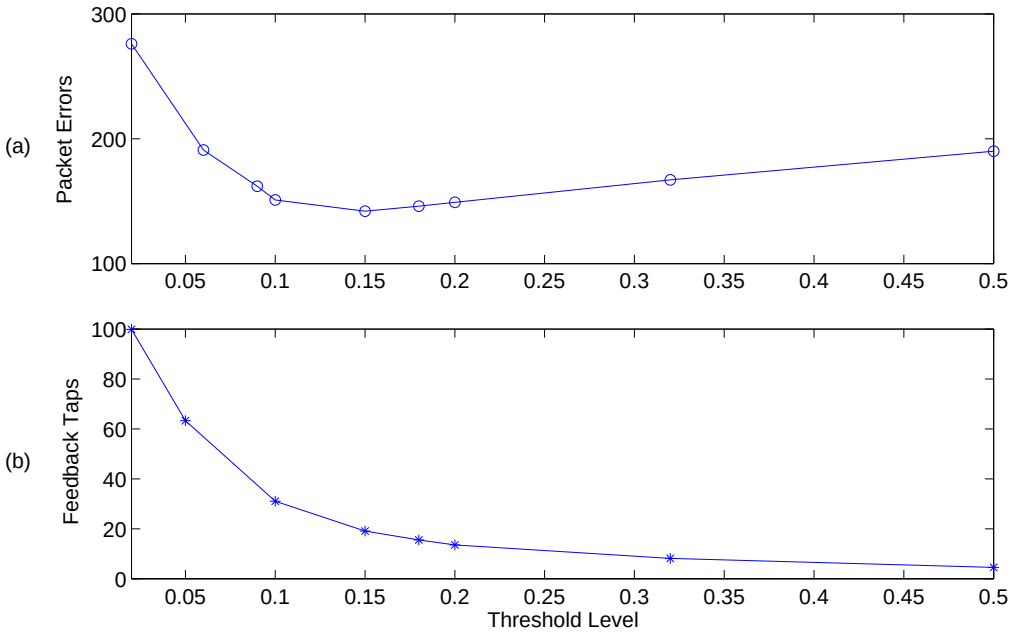


Figure 4.9: Comparison of Required Number of Feedback Taps and Observed Packet Errors for Varying 'Sparse' Threshold Levels ($\mu_b = 0.010$)
(a) Incurred Packet Errors,
(b) Number of Feedback Taps Computed at Different Threshold Levels.

used out of the maximum 100 available. The symbol-by-symbol computation of the filter output and consecutive filter weights is therefore made considerably simpler, occupying a fraction of the processing resource.

The time variability of the channel can be found to severely limit the performance of the sparse equalisation structure. Since the binary CIR estimate is generated at the start of the packet, a significant variation in the channel can result in aspects of the multipath response being neglected. A possible solution is to form the channel mask as a summation of two channel probes: one at the beginning of the packet; and one at the end. However, this technique is still limited by the assumption that the change is linear across the duration of the packet.

#### 4.1.3.4 BICM-ID Performance

Up until now the performance of the BICM-ID structure has been neglected, focusing attention solely on the capability of the various equaliser structure. Utilising the same extended data set shown in Fig. 4.6, the performance of the iterative receiver structure is discussed. The 3030 packet data set is evaluated for a varying number of inner and outer iterations, from 1 inner : 1 outer (i.e. a non-iterative receiver) through to 4 inner : 3 outer. The number of incurred packet errors for each configuration are shown in Fig. 4.10.

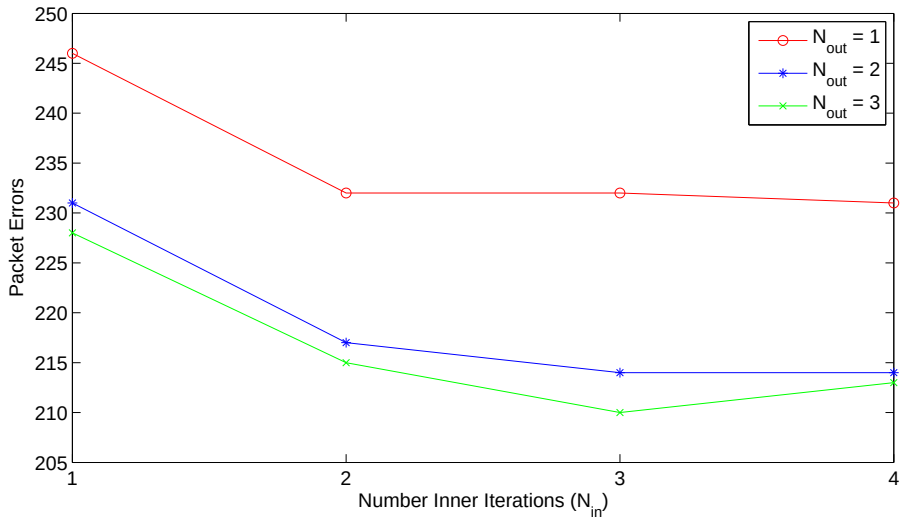


Figure 4.10: Single Element Receiver Analysis: BICM-ID Performance, Comparing Varying Numbers of Maximum Inner and Outer Iterations

Despite the structure being more than capable of maintaining reliable communications at low SNR levels, a limiting factor in the performance of the BICM-ID receiver structure is its inability to compensate for long delay spreads. Although the structure is capable of overcoming bursts of errors, or conditions where the symbol decision has a low level of certainty, when delay spreads are observed outside of the span of the equaliser the receiver will tend to diverge or fail to train at all. In these situations the quality of the extrinsic LLRs, supplied *a priori* by the previous receiver block, is shown to offer minimal certainty, resulting in negligible improvement through performing additional processing iterations.

As previously highlighted, the benefit of an iterative *'turbo'* receiver is the ability to transfer soft decisions between the various receiver blocks. If the structure has diverged, causing the equaliser to become unstable, then the quality of the soft decisions are limited, restricting the performance of further de-mapping and decoding stages. The uncertainty in the soft decisions effectively causes the iterative receiver to guess at optimal solution with minimal confidence or chance of selecting the correct symbol values.

Despite the limitations of the BICM-ID structure in severe channel conditions, the results shown in Fig. 4.10 demonstrates a reduction in the number of packet errors through both inner and outer iterations. Utilising a structure of 3 inner and 3 outer iterations the receiver is shown to correct for approximately 35 packet errors, reducing the effect of burst errors and overcoming periods of low SNR. The improved certainty of soft decisions in a single packet is shown in Fig. 4.11. This plot demonstrates the distribution of Log Likelihood Ratios (LLR) for various numbers of iterations, indicating an improvement from the initial estimate, exhibiting 476 bit

errors, to the successful demodulation after a second outer iteration and a further inner iteration.

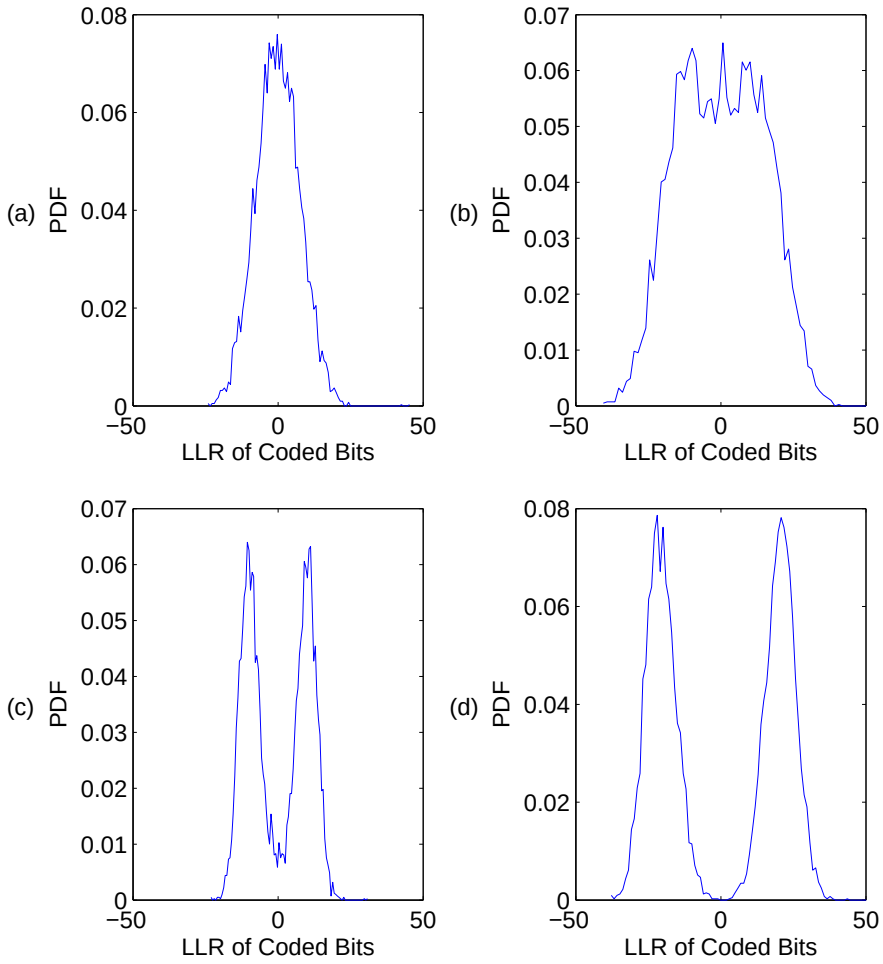


Figure 4.11: Distribution of Log Likelihood Ratios (LLRs): [Outer : Inner]
(a) [1 : 1] - 476 Bit Errors, (b) [1 : 3] - 304 Bit Errors,
(c) [2 : 1] - 183 Bit Errors, (d) [2 : 2] - 0 Bit Errors,

## 4.2 Multi Element Receivers Structures

The results presented in the previous section highlight the limitations of a single element receiver in overcoming the multipath interference typically observed in a short range shallow water channel. As discussed the highly reverberant nature of such channels often result in a significantly hostile Channel Impulse Response (CIR), in terms of the length of the delay spread and the magnitude of any secondary arrivals.

In most $\mu$ROV applications deployments, occurring in depths of less than 50m, transmissions are shown to propagate in straight lines, due to minimal deviation in both temperature and sound velocity across the cross section of the channel. Based on this assumption, and from the generation of a simplified channel model, shown in Fig. 4.12, the following equations have been developed to estimate the length of delay spread, (4.2), and angular separation of arrivals (4.3). Where: $R$ is used to identify the transmission range; and $h_1$ and $h_2$ represent the depths of the receiver and transmitter.

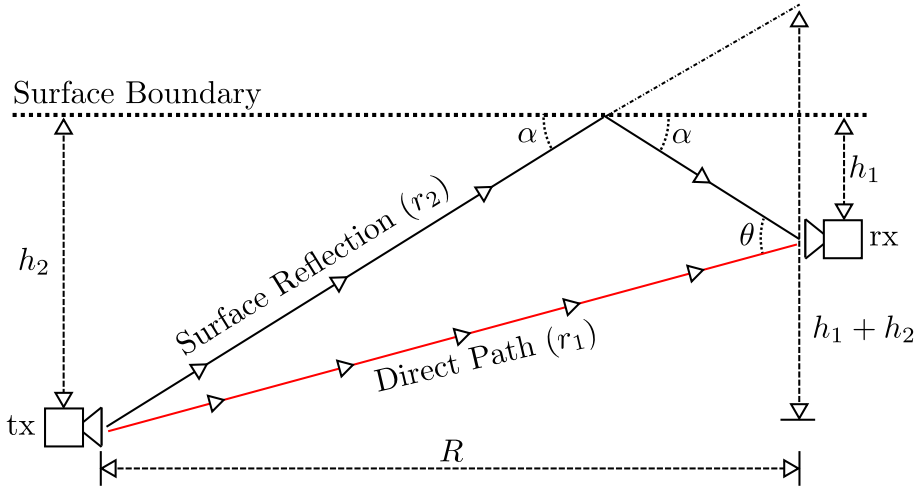


Figure 4.12: Simplified Channel Model of a Shallow Water Point-to-Point Communication Link

$$\tau = \frac{\Delta_r}{c} = \frac{(r_2 - r_1)}{c} \tag{4.2}$$

$$\theta = \tan^{-1}\left[\frac{h_1 + h_2}{R}\right] + \tan^{-1}\left[\frac{h_2 - h_1}{R}\right] \tag{4.3}$$

Where, the spatial length of the direct path, $r_2$, and surface reflection, $r_1$, can be calculated using (4.4) and (4.5) respectively.

$$r_1 = \sqrt{R^2 + (h_2 - h_1)^2} \tag{4.4}$$

$$r_2 = \sqrt{R^2 + (h_2 + h_1)^2} \tag{4.5}$$

For small angles of arrival, $\theta < 25°$, the delay spread can be approximated utilising (4.6). This approximation is therefore generally considered valid in scenarios where the transmission range is significantly greater than the depth between the transmitter and receiver, i.e. $R \gg (h_2 - h_1)$.

$$\tau \approx \frac{2h_1h_2}{R.c} \qquad \text{for:} \quad \theta < 25° \tag{4.6}$$

These equations can be used to analyse the observed channel response and express the severe nature of the shallow water channel. Fig. 4.13 presents the variation in delay spread and angular separation for two simulated shallow water channels. The first simulation, shown in 4.13a and 4.13c, utilises three set depths and multiple transmission ranges, while the second set, shown in 4.13b and 4.13d, considers four static ranges and variable depths. For both simulations, the resulting data set is calculated based on the surface receiver being deployed at a depth of 1m and a sound velocity of 1500m/s.

Examining firstly the extent of the multipath spread, it can be clearly seen that delays in excess of 5ms are possible during short range transmissions, i.e. when operating within a 1:1, depth to range ratio. Over longer ranges, the time span can be seen to reduce, highlighting the severe nature of working at such short ranges within a shallow water channel. At the symbol rate discussed, 20ksym/s, such delays can be seen to have an effect on the following 120 to 150 symbols. Therefore, the required equaliser can be seen to become unfeasible both in terms of computational complexity and mathematical stability.

The benefit of a multi-element beamforming structure becomes evident when examining the angular separation between the direct arrival and the surface reflection. During transmissions at shorter ranges, when long delay spreads are apparent, the angular separation between arrivals are significantly large, $> 100°$. Alternatively, when the angle of the two arrivals become comparable, i.e. both the multipath and the direct path appear from a similar direction, the delay spread can be seen to be significantly shorter, $\tau \ll 4ms$.

As indicated by Neasham *et al.* [75] this form of channel configuration lends itself well to a combined equalisation and beamforming approach. During long range transmissions where the angular separation is small, and an unrealistically high resolution beamformer would be required, a suitable equaliser structure is capable of

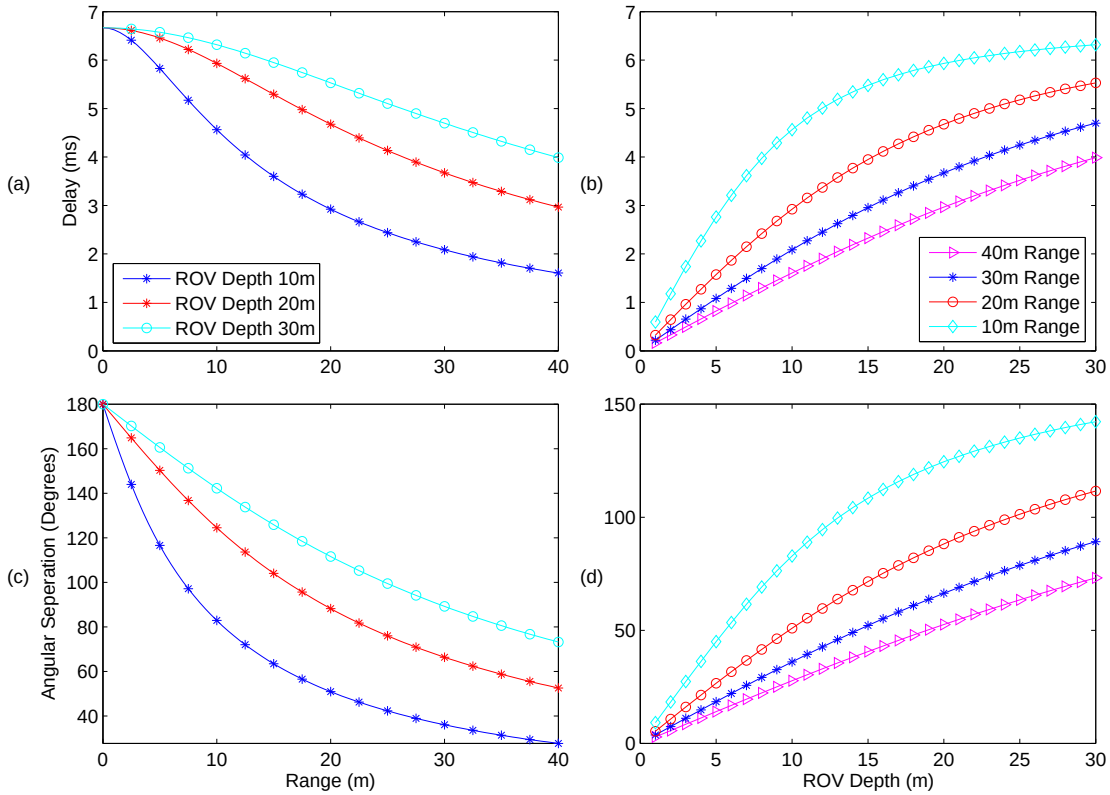


Figure 4.13: Variation Of Multipath Delay Spread and Angular Separation, In A Simplified Short Range Shallow Water Channel, For A Range Of ROV Depths And Ranges. [Static Receiver Depth, $h_1$, Of 5m and VOS, $c$, Of 1500m/s]

overcoming the short delay spreads incurred. Equally during shorter range transmissions, where the delay spread would be excessive for an equaliser to mitigate, a low resolution beamformer will be more than capable at isolating the arrivals due to their wide angular separation.

As discussed in Section 3.2.1.4, the combination of a multi-channel receiver and an adaptive equaliser structure can be shown to adapt the beam pattern of the receiver to reduce the Mean Squared Error (MSE) of the demodulated signal. In doing so the receiver is shown to utilise three mechanisms of operation: 1. temporal equalisation; 2. spatial equalisation; and 3. coherent cancellation.

It is important to note that the adaptive equaliser structure will not always try to aim the *acoustic axis* towards the direction of the main arrival. Instead the adaptive structure will typically try to ensure maximal separation between the direct arrival and any reverberation paths, steering a null in the direction of the multipath arrival. The beam pattern shown in Fig. 4.14, demonstrates the use of coherent cancellation to suppress the effects of a single multipath arrival. In this simulation the main arrival was shown to arrive from an angle of $\approx 0°$ and the reverberation path from

an angle of $\approx 11°$.

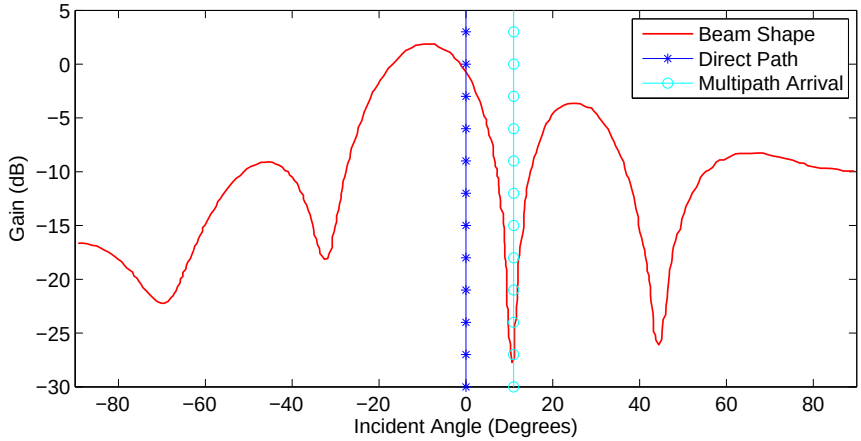


Figure 4.14: Demonstration of Coherent Cancellation Utilising a Beamform Array: (Simulated Channel with a Direct Arrival at 0° and a Multipath Arrival at 11°)

### 4.2.1 Array Construction

Based on the direction of separation between the multipath arrivals, the use of a linear vertical array is proposed. In contrast to a planar array, which is more suitable in deep water channels due to its vertical searchlight pattern, the linear array is shown to generate a horizontal toroid shaped beam, ideal for isolating surface and seabed reflections. During the design process, the number of elements and the spacing between consecutive elements must be considered. An overview of these two parameters is given below, indicating how the beam shape is affected.

- **Element Spacing:**
  By increasing the spacing between consecutive elements the 3dB beam-width of the main directional lobe can be seen to reduce, resulting in a tighter beam pattern and offering higher degrees of angular separation. A limitation when utilising increased element spacings, i.e. significantly greater than $\frac{\lambda}{2}$ ,is the severity of the generated grating lobes. As the spacing increases the magnitude of the side-lobes begin to rise, reducing the effectiveness of the resulting beam pattern.

- **Number of Elements:**
  An increase in the number of elements is found to reduce both the beam-width of the main lobe and the severity of the grating lobes. By increasing the number of elements, improved directionality is possible, with reduced degradation caused by the generated side lobes.

Therefore, the optimum multi-element receiver can be seen to consist of a large number of elements, with a wide physical separation. However, since the design is constrained in both size and cost, such an array is unrealistic for practical construction requiring a compromise to be considered. Despite improved directionality being demonstrated from sparse diversity arrays, where $d \gg \lambda$, the dimensions of the array become unrealistic for simple deployment and transportation from a small vessel or confined surface platform. To ensure the portability of the unit, this research therefore considers the development of a $\lambda$-spaced array.

#### 4.2.1.1 Beam Pattern

To examine the number of elements required to ensure suitable performance, the generated beam pattern must be considered. For an unsteered, $d$-spaced, $N$ element linear array the theoretical beam shape, $b$, can be calculated using (4.7) [14].

$$b(\theta) = \left[\frac{\sin(N\pi d \sin(\theta)/\lambda)}{N \sin(\pi d \sin(\theta)/\lambda)}\right]^2 \tag{4.7}$$

Fig. 4.15 demonstrates the theoretical beam pattern for three different $\lambda$ spaced array configurations, of 2, 4 or 8 elements with a corresponding array length of approximately 30mm, 90mm and 150mm respectively. The direction of maximum response, i.e. $\theta = 0°$, is classed as the *'acoustic axis'* of the array, offering optimal sensitivity to the incoming acoustic signal.

Due to a considerable separation between the direct arrival and the multipath arrivals, $> 20°$, the use of an array consisting of 4 elements can be seen offer a sufficiently tight enough main beam to isolate the independent arrivals. Additional elements can be seen to increase the directionality of the beam at a trade-off in terms of the physical size of the array. Additionally, the increased cost imposed by the transducer ceramic, analogue front-end hardware and sampling hardware can be seen to favour the selection of a reduced number of elements.

A significant benefit of the increased centre frequency is the reduction in $\lambda$. Arrays previously discussed in literature have been shown to typically operate at much lower centre frequencies, e.g. 11-12kHz, requiring much greater separation for comparable performance. Due to the reduction in element spacing at higher frequencies, a suitable array can be constructed at a fraction of the physical size. Further information relating to the physical construction of the prototype 4 element $\lambda$-spaced array can be found in Section 5.2.1.4.

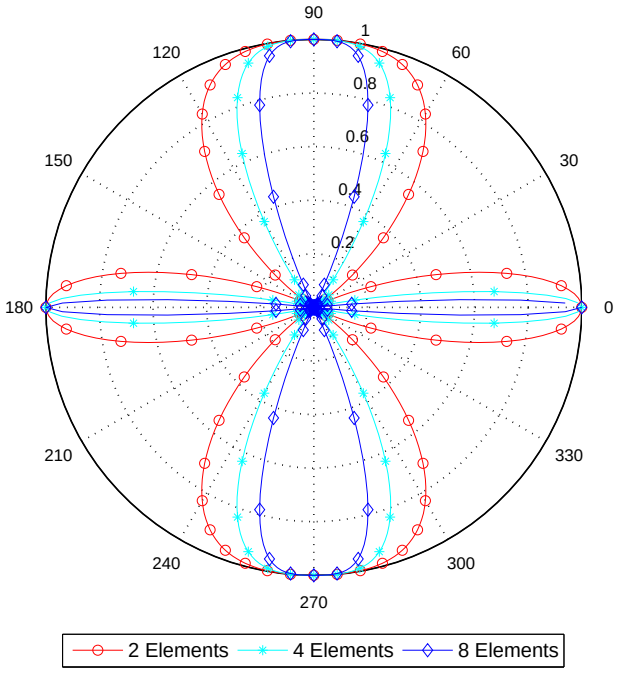


Figure 4.15: Un-steered Beam Pattern for an $N$ Element $\lambda$ Spaced Array, Demonstrating the Normalised Magnitude of the Received Signal for Varying Directions of Arrival ($\theta$)

### 4.2.2 Receiver Validation and Field Results

Results are presented from trials demonstrating the performance of a 4 element $\lambda$ spaced beamforming array. The included data set represents an exaggerated transmission channel, where the alignment of the ROV, receive transducer and pontoon support piles, shown in Fig. 4.16, result in the generation of additional multipath arrivals. The 3 main arrivals, $R_a$-$R_c$, are seen to occur due to reflections with the surface, the pontoon support piles and a combination of both.

Fig. 4.17 presents two isolated channel impulse probes, acquired at the start of the $80^{\text{th}}$ and $200^{\text{th}}$ packets respectively. Both captures are taken when the vehicle is positioned at a depth of 6-7m, with the first taken at a distance of 5-10m and the second at an increased range of $\approx$40m. In both cases four significant arrivals are observed, the first relating to the direct path and the other three labelled to correspond with the paths shown in Fig. 4.16.

This scenario tests the capability of a multi-element beamform array for resolving multiple reverberation paths. Through spatial isolation the effects of the three multipath arrivals can be shown to be significantly suppressed. Fig. 4.18a highlights the degree of channel variability caused by the movement of the $\mu$ROV. The significant change in all four paths as the vehicle drives away from the pontoon reiterates the importance for the receiver to track changes in the channel condition over the course of a single packet. Without the use of an adaptive structure the channel variability would result in a considerable degradation in receiver performance.

The results shown in Fig. 4.18d, demonstrate the receivers ability to operate successfully with a reduced set of filter coefficients. The least number of packet errors are encountered when operating with a particularly short feedback filter i.e. $<$24 weights. The performance of the receiver when operating with a suboptimal number of filter coefficients again highlights the benefits of a beam forming array, predominately utilising spatial equalisation and coherent cancellation to isolate interference paths which exhibit a large angular separation. In reality, a slightly longer feedback filter (60-80 taps) would be proposed, ensuring suppression of shorter delay spreads when the angular separation may be too small for the array to distinguish. Across a range of filter lengths, less than 15 packet errors were observed across a 1600 data set, including the occurrence of synchronisation and header payload errors.

The ability to overcome such exaggerated geometries highlights the capability of the receiver in even the most severe channel conditions. Although the majority of $\mu$ROV applications do not present such highly reverberant channels, the use of such vehicles in heavily industrialised environments, such as tank inspections, gives rise to interference caused by reflections off hard artificial surfaces. Additionally, through

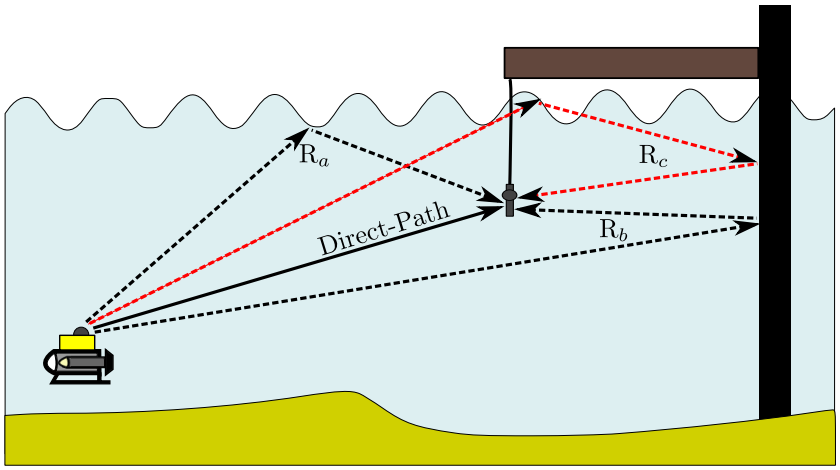


Figure 4.16: Illustration of the Operational Setup Resulting in Multiple Reverberation Paths

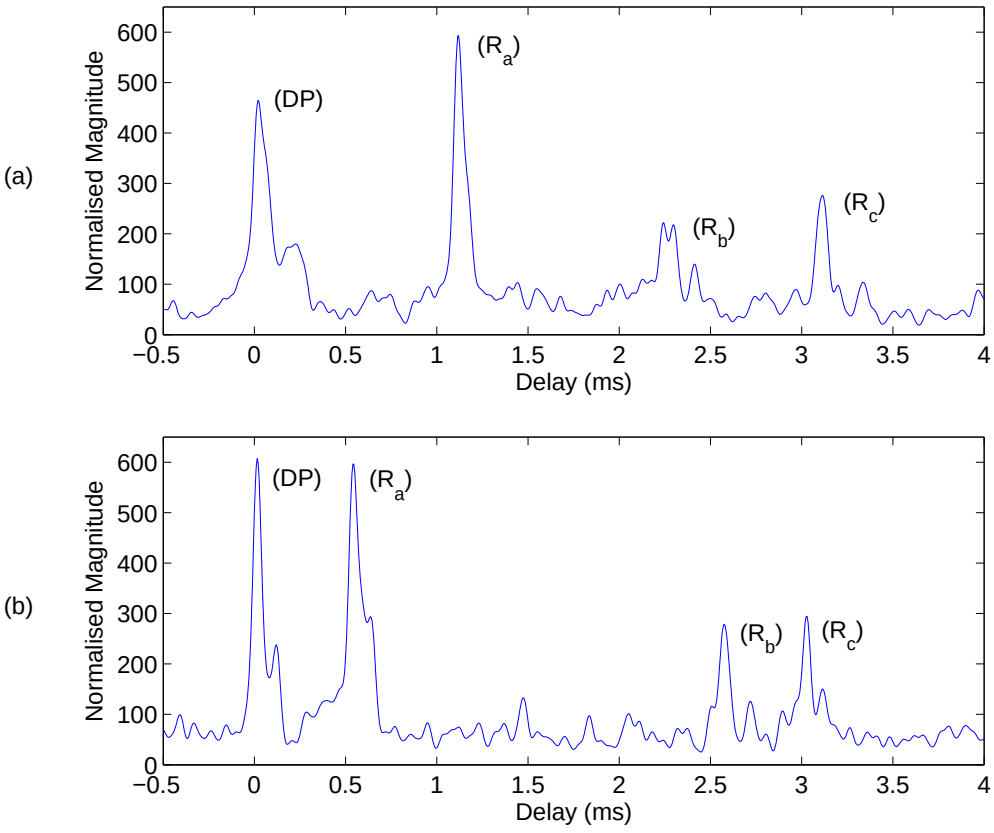


Figure 4.17: Spot CIR Probes of Packets Exhibiting Multipath Reflections from the Surface and Structural Support Piles
(a) Packet Number 80: ROV Depth 6 - 7m, Range 5 - 10m,
(b) Packet Number 200: ROV Depth 6 - 7m, Range ≈ 40m

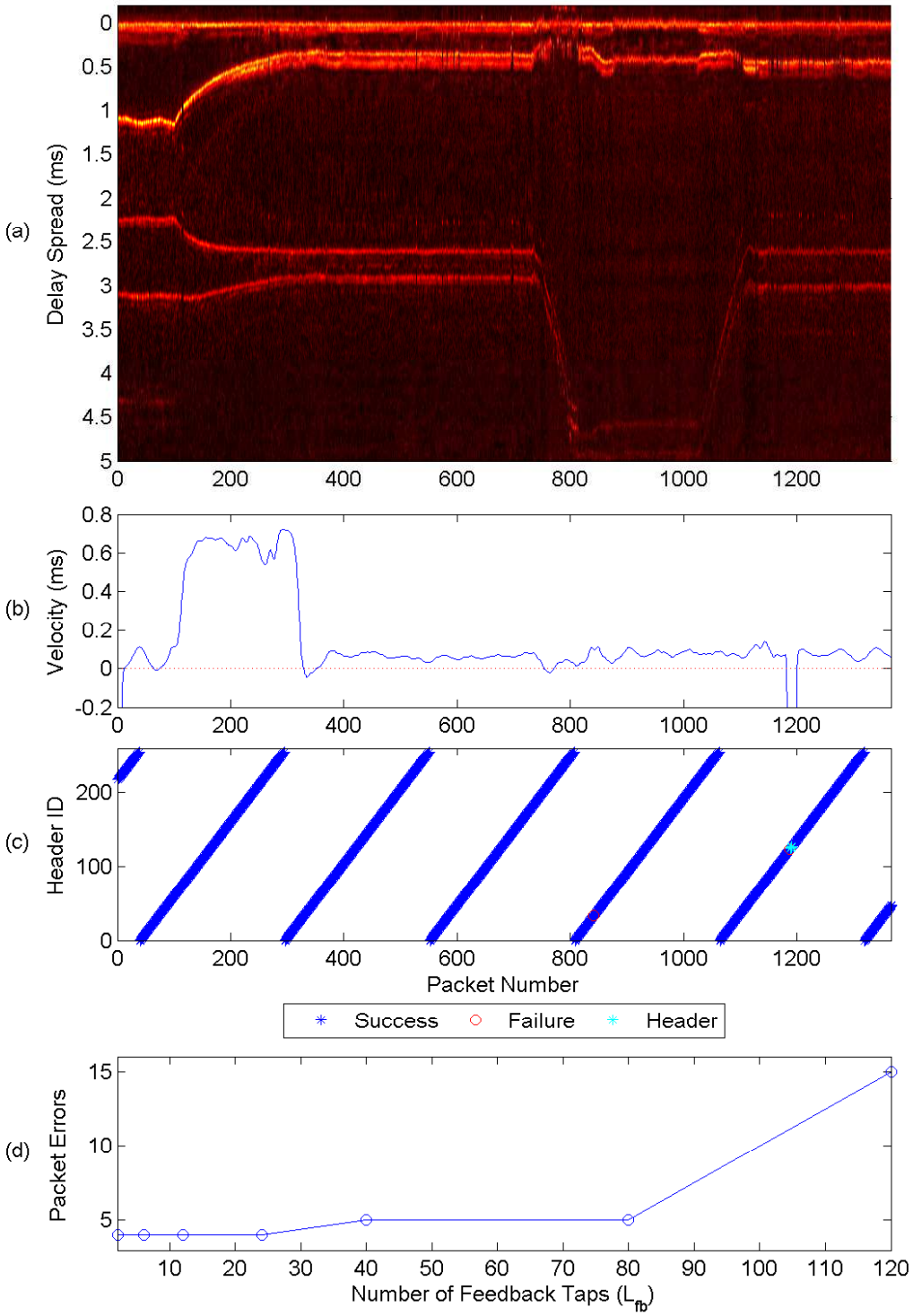


Figure 4.18: Detailed Evaluation of a Highly Reverberant Multipath Channel (a) Time Varying Channel Impulse Response, (b) Relative Velocity (Gained From Block Estimation Techniques), (c) Error Distribution Plot, (d) Number of Packet Errors for Varying Lengths of Feedback Filter

testing suitable acoustic links in such realistic scenarios enables full clarification of the overall system performance.

## 4.3 Doppler Estimation and Compensation

Another important aspect of the developed receiver structure is its ability to overcome periods of rapid acceleration or deceleration. As discussed in Section 3.2.1.5, the relative movement between the transmitter and receiver can result in distortion of the acoustic waveform in terms of both frequency scaling and time dilation. Unlike the majority of previously presented work, where experimental trials have been conducted from static platforms, less dynamic surface vessels or much larger submersible vehicles, one of the most significant challenges faced in this application is the rate of acceleration of the $\mu$ROV. The lightweight construction, paired with the use of direct electric drives, enable the vehicle to change speed and direction over a very short period of time.

A set of results are presented demonstrating the performance of the discussed estimation techniques. The data set was recorded during trials on Windermere in late September 2012. The vehicle was deployed from an anchored surface vessel on a 55m control tether. The anchorage offered a maximum depth of approximately 50m and the receive hydrophone array was deployed at a depth of 3-4m. During the data capture the vehicle was operated at depths ranging from 6m to full channel depth, additionally a variety of different motion is exhibited, with peak velocities of $\pm$1.2m/s.

Fig. 4.19 demonstrates the time varying CIR, estimated from the output of the chirp matched filter. The variation in CIR was greatly affected by the depth and range of the $\mu$ROV. The delay spread was seen to extend during periods where the vehicle was operated at an increased depth, with the longest delay spread encountered when the $\mu$ROV was located at an approximate depth to range ratio of 1:1. A selection of severe interference paths are observed throughout the capture and are believed to be related to the surface exhibiting minimal disruption. Such conditions are typically found to cause the boundary to act as an ideal acoustic reflector, with increased disturbance found to spread and distort the multipath reflection.

The recorded data set, of 2438 packets, was analysed utilising various combinations of closed loop and open loop compensation techniques. Fig. 4.20, demonstrates the errors incurred when utilising either technique. Additionally a structure utilising neither compensation technique is presented, enabling the benefits of each approach to be highlighted. The error distribution plots demonstrate the location of any incurred packet failures, where, red, cyan and green tick marks are shown to indicate failures caused by either synchronisation, payload or header faults.

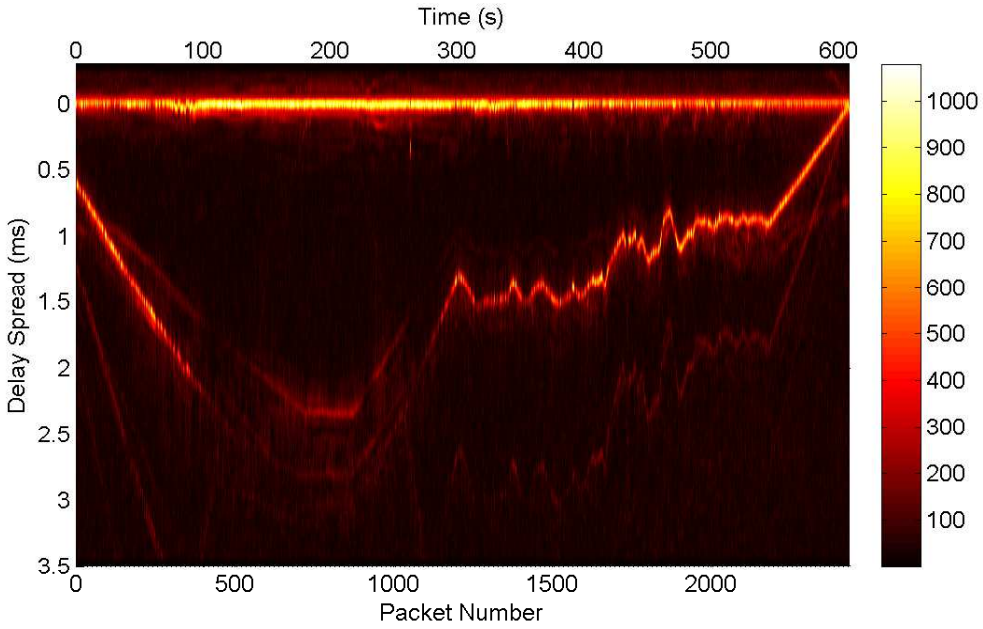


Figure 4.19: Time Varying Channel Impulse Response (CIR) for the Results Shown in Fig. 4.20

During the first half of the capture minimal Doppler shift is portrayed, exhibiting a gradual increase and decrease in velocity between ±0.2m/s. During this period the depth of the vehicle was adjusted, implying that this variation in Doppler shift corresponded to a slow movement in the vertical plane. However, the latter half of the transmission is found to exhibit more hostile variations in velocity, incurring significant acceleration and deceleration and peak velocities of >1m/s. Throughout the capture the receiver structure utilising both closed loop and open loop estimation, subplot a, is shown to incur minimal packet errors, i.e. $< 0.5\%$.

The limitations of both the closed loop and the open loop estimation techniques are evident when tested independently. Despite the closed loop approach offering reliable performance throughout the first 2/3rds of the capture, during periods of higher velocity and increased variation the system was shown to struggle. In each case the errors are are shown to correspond with the receiver failing to train, generally being caused by the closed loop estimate being unable to converge.

In contrast, the block estimation approach is found to demonstrate a range of errors across the duration of the capture period. These errors are typically accredited to two effects: 1. the variability in the velocity across the duration of the packet; and 2. the residual Doppler shift caused by inaccuracies in the block estimate. Since the estimate assumes a constant Doppler shift across the duration of the packet, any severe changes in velocity result in a degradation in performance. This is predominantly demonstrated in the latter stages of the capture. Additionally, in channels

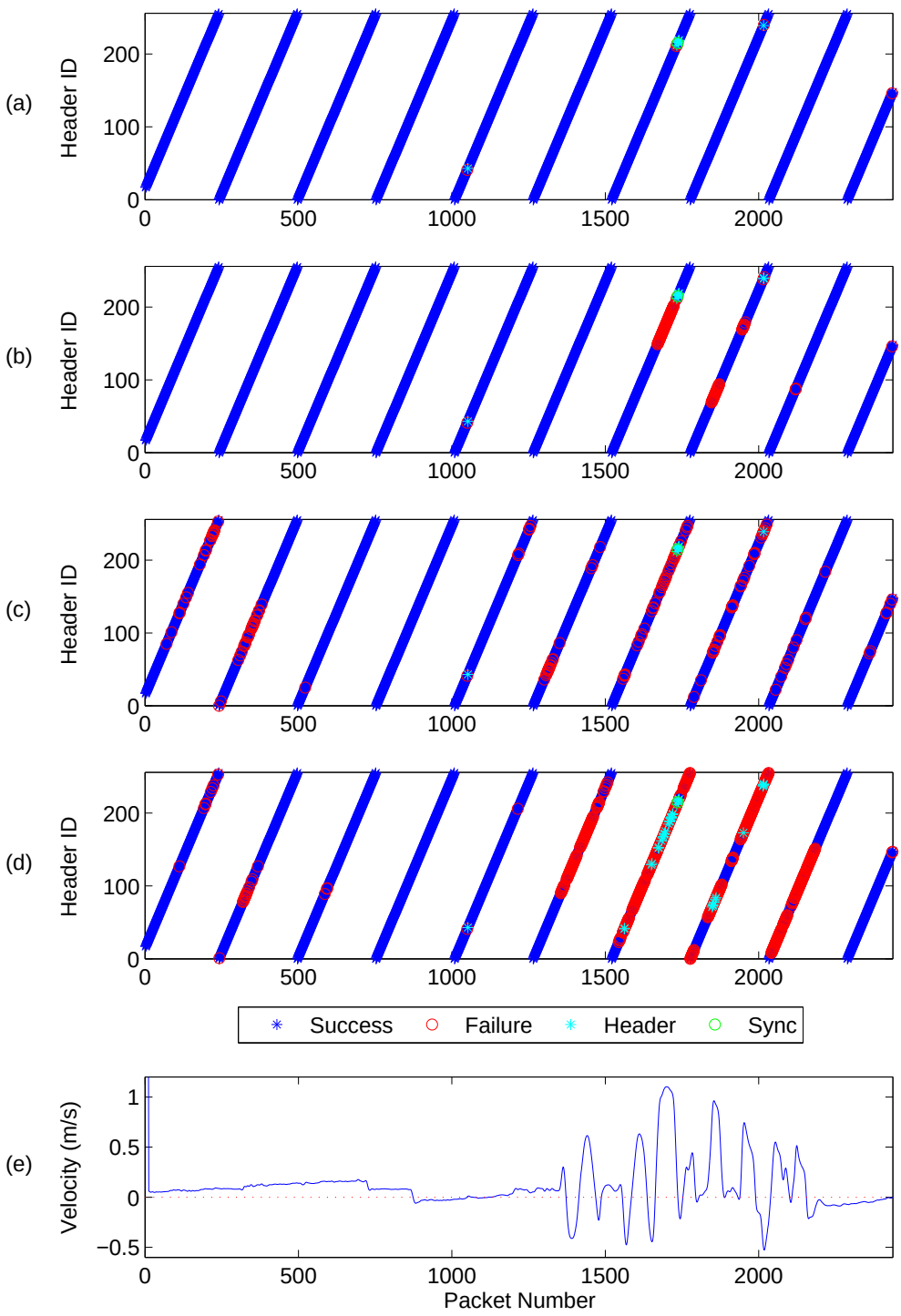


Figure 4.20: Packet Error Distribution for Various Doppler Estimation Techniques: (a) Initial Estimation With Closed Loop Gain (Kp) = $0.2 \times 10^{-5}$ (2423 Successful) (b) No Initial Estimation, Closed Loop Gain (Kp) = $0.2 \times 10^{-5}$ (2330 Successful) (c) Block Doppler Correction, No Closed Loop Gain (Kp) = 0 (2268 Successful) (d) No Doppler Compensation (1826 Successful) (e) Relative Velocity (Calculated From Block Doppler Estimation)

where low SNR and severe multipath is exhibited the accuracy of the synchronisation process can suffer. This can have a significant effect on the estimation of the packet length, resulting in ineffective re-sampling of the received data set.

### 4.3.1 Closed Loop Doppler Correction Gain

Further results are presented, examining the variation in performance when utilising varying levels of closed loop correction gain within the Doppler estimation structure. Background information relating to the operation of a closed loop structure may be found in Section 3.2.1.5. Two individual packets are selected for comparison with different levels of proportional gain, $K_p$, and for both with and without an initial block estimate. In the case of a closed loop approach, a proportional loop gain is selected to control the variation in the Doppler estimate from one iteration to the next. To ensure receiver stability and optimal performance, the value of $K_p$ must be carefully selected.

Fig. 4.21 presents an analysis of different proportional gain values, where an initial block estimate is not used. The two examined packets where captured when the vehicle was travelling at a velocity of 0.4m/s and -0.8m/s respectively. Minimal variation in velocity is observed across the duration of each packet.

As with any closed loop control system, the magnitude of the proportional gain is shown to significantly effect the ability for the system to converge within a specific period of time. In the first example, exhibiting a positive Doppler shift, the system is shown to be ineffective with a proportional gain of $< 0.2 \times 10^{-5}$. When operating with lower gain settings the closed loop Doppler estimate is shown to be unable to converge within the given training sequence of 500 symbols. In this case the receiver is unable to effectively operate and exhibits a large number of bit errors at the output, $> 2000$ bits. This effect is replicated with the second packet, where a proportional gain of $< 0.4 \times 10^{-5}$ is shown to be insufficient.

In contrast an increased proportional gain can result in the system becoming unstable. In the first example, a gain of $0.8 \times 10^{-5}$ is found to result in an under-damped response, demonstrating a significant overshoot while training and continued oscillations in the estimate across the remainder of the packet. An optimal solution is therefore found when the system offers a critically damped response, incurring minimal error between the estimated and actual interpolation factor.

Without the use of an initial block estimate, the proportional loop gain is found to be highly dependent on the magnitude of the incurred Doppler shift. The comparison between the two subplots demonstrates that with an increase in velocity, a larger gain setting is required to ensure the system converges within the given training period. To ensure the system converges when utilising lower gain settings, an increased

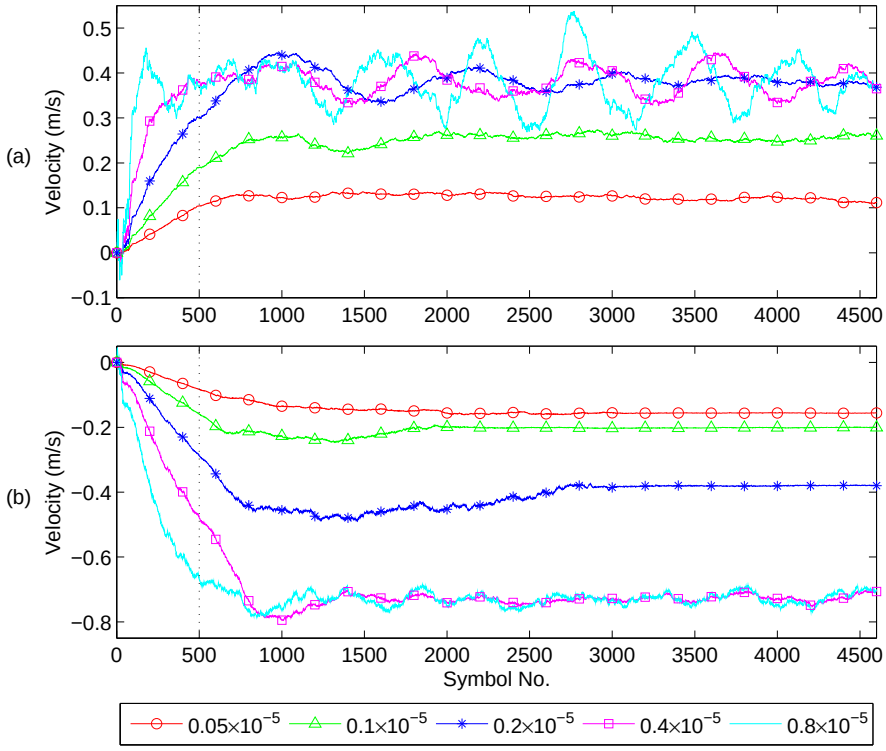


Figure 4.21: Tracking of Symbol by Symbol Doppler Estimation for Varying Levels of Closed Loop Proportional Gain ($K_p$): Without Block Estimate Initialisation

training sequence could be used. However, the additional overhead has a significant effect on the overall throughput, reducing the efficiency of the proposed system. Alternatively, to reduce the initial error, and minimise the convergence range, a block approach may be used to initialise the interpolation factor prior to training. Fig. 4.22 demonstrates the performance of the system when utilising an initial block estimation technique.

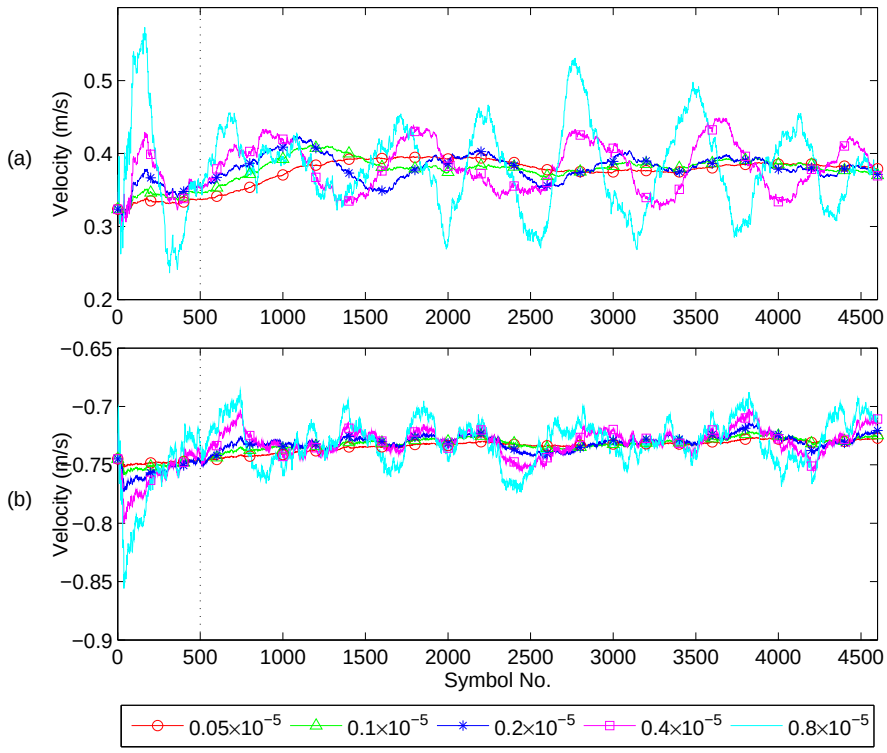


Figure 4.22: Tracking of Symbol by Symbol Doppler Estimation for Varying Levels of Closed Loop Proportional Gain ($K_p$): With Block Estimate Initialisation

The benefits of the initial block estimate are immediately evident, enabling the system to converge within a very short period. Additionally, through pre-determining an approximate interpolation rate, the proportional gain can be normalised across a range of Doppler shifts, enabling the same gain to be used at both high and low velocities. When utilising an initial open loop estimate, the system can be found to successfully operate with a very low proportional gain, only having to converge to the inaccuracy between the block estimate and the instantaneous velocity. In the examples shown in Fig. 4.22 low values of $K_p$ are shown to offer acceptable performance, with higher values demonstrating an under-damped response. In practice, a gain of $\approx 0.2 \times 10^{-5}$ is selected, ensuring adequate tracking if: 1. a particularly inaccurate block estimate is incurred; or 2. if a significant variation in velocity is observed across the length of the packet.

## 4.4 Variable Code Rates and Modulation Schemes

Through a reduction in coding redundancy and the use of more complex modulation schemes an increase in the overall system throughput can be realistically achieved. Both of these metrics come at a cost in terms of the schemes ability to combat severe multipath arrivals and overcome phase distortion, caused by incorrect synchronisation or residual Doppler shift. Testing of various code rates and modulation schemes are performed, with the results highlighting the suitability of each structure within the context of the proposed application.

### 4.4.1 Variable Code Rates

Initial testing was carried out utilising 1/2 rate convolutional coding scheme, utilising a generator polynomial of $G_{1/2} = [23, 35]_8$ and a constraint length, $k$, of 5. This value was selected from a table of optimum polynomials, chosen for exhibiting the largest minimum free distance, $d_{\min}$. Further testing is conducted utilising three punctured code rates of 2/3, 5/6 and 9/10.

#### 4.4.1.1 Code Puncturing

Rather than using dedicated generator polynomials for each individual coding level, a puncturing operation is used to derive reduced levels of redundancy from a single *'mother'* code. The puncturing operation removes sections of the code to reduce the amount of redundancy included in the output sequence. A puncturing matrix is used to indicate which aspects of the original mother code are removed. At the receiver a de-puncturing operation is performed to reverse the process, re-inserting null values into the positions where the original bits were removed. Once de-punctured the data sequence can be decoded using the *'mother'* decoder. The ability to generate various coding levels from a single encoder and decoder is shown to significantly reduce the complexity of both the receiver and transmitter structures.

Table 4.2 presents the puncturing matrices used to generate $R_p = \{\frac{2}{3}, \frac{5}{6}, \frac{9}{10}\}$ codes from a single $R_m = 1/2$ mother code. Where, a '1' indicates inclusion in the output sequence and '0' indicates removal or puncturing of the relevant binary value.

#### 4.4.1.2 Performance Evaluation

A comparison of four different coding schemes are presented in Fig. 4.23. The results were collated from a selection of experiments conducted in the anechoic test tank at Newcastle University. For each coding level a number of captures were recorded, each with a different level of artificial background noise interjected into

| $R_p$ | Puncture Matrix |
|---|---|
| 2/3 | $\left[\begin{array}{cc} 1 & 0 \\ 1 & 1 \end{array}\right]$ |
| 5/6 | $\left[\begin{array}{ccccc} 1 & 0 & 1 & 0 & 1 \\ 1 & 1 & 0 & 1 & 0 \end{array}\right]$ |
| 9/10 | $\left[\begin{array}{cccccccccc} 1 & 0 & 1 & 0 & 1 & 0 & 1 & 0 & 1 & \\ 1 & 1 & 0 & 1 & 0 & 1 & 0 & 1 & 0 & \end{array}\right]$ |

Table 4.2: Puncturing Matrices Used to Produce Code Rates of 2/3, 5/6 and 9/10 from a 1/2 Rate Mother Code

the channel. It should be noted that these results solely examine the performance of each transmission, for varying levels of background noise and do not examine the effects of Doppler or multipath interference.

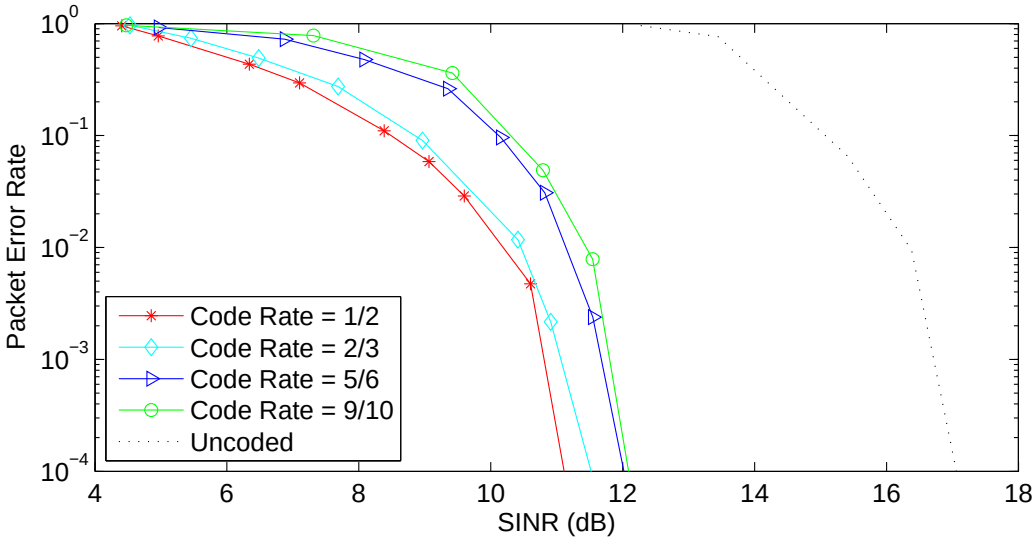


Figure 4.23: System Performance for Variable Code Rates, Utilising a Real Time QPSK Modulated BICM-ID system

For each set of results a DFE-BICM-ID receiver structure, combined with a four element micro beamformer array, was utilised. The maximum number of iterations performed by the decoding structure was limited to three inner and two outer iterations. In order to benchmark the coding gain of each scheme, the results from an uncoded transmission are also presented. In all cases the SINR value refers to the post equalisation SNR, calculated from the error variance of the DFE output signal.

From the presented results, the coding gain is immediately apparent: offering an increase in performance of approximately 6dBs between an uncoded and a 1/2 rate QPSK transmission. However, the comparable variation between the four different coding levels is found to be negligible, offering a maximum of 1dB improvement between the lowest level of redundancy, 9/10, and the highest, 1/2. A 9/10 code rate is therefore believed to offer the best compromise in performance, demonstrating a significant improvement in throughput and incurring a minimal loss in coding gain. In the case of a static transmission scheme, i.e. Continuous Coding and Modulation (CCM), the use of a 9/10 code rate would typically be advised.

Alternatively, if utilising an adaptive protocol, i.e. Adaptive Modulation and Coding (AMC), the variation in processing gain of the 2/3 and 5/6 code rates would make it very difficult to select the optimum coding scheme at any given time period, particularly in a highly time variable communication channel. For an AMC strategy the author would therefore limit the selected code rates to 9/10 and 1/2, each demonstrating a variation in coding gain and throughput. Further discussion on the development of an AMC structure can be found in Chapter 7.

### 4.4.2 High Order Modulation Schemes

An alternative technique to further improve the throughput of the system, is the use of higher order modulation schemes. Up until now this work has focussed on the use of QPSK transmissions, enabling data to be transferred at 2 bits/symbol. As highlighted in Section 3.1.1, a range of alternative modulation schemes could be utilised to further improve the throughput of the system, including 8-PSK and 16-QAM which would offer 3 bits/symbol and 4 bits/symbol respectively

Within the scope of this work, 8-PSK is not considered due to the inefficient use of the available bandwidth, offering a comparable euclidean distance to 16-QAM. Therefore, 16-QAM is preferred as a more efficient transmission scheme, offering a significant increase in throughput. This section will explore the comparable performance of 16-QAM and QPSK, evaluating the ability of the higher order scheme to operate in channels with variable SINR.

### 4.4.3 Performance Evaluation

During trials on Windermere in 2012, a data set was recorded featuring sequential transmission blocks of QPSK and 16-QAM packets. In both cases the data was encoded utilising a 1/2 rate RSC code. Fig. 4.24 presents the distribution of errors for both QPSK and QAM transmissions. Due to the vehicle being operated in a constant position in the water column, the channel conditions were found to be

comparable during both QPSK and 16-QAM segments. A variety of movement was observed throughout the capture, including a section of acceleration and deceleration during the 16-QAM transmission.

Throughout this capture minimal packet errors, $< 5$, were observed while utilising a QPSK transmission scheme. However, a more varied response was found while operating with 16-QAM, incurring $> 150$ errors across the length of the capture. Despite a large number of errors being shown, it should be noted that the majority were observed in a single block, roughly 2/3rds of the way through the capture. This block is shown to correspond with a reduction in SINR, where the majority of packets were successfully demodulated when the SINR>16dB. A dashed red line is marked on the SINR plot, subplot b, at a 16dB point, emphasising the relationship with the block of packet errors.

Through further testing in a tank environment, a 16-QAM scheme was found to successfully operate when the SINR was $> 15 - 16$dB. As shown in Table 4.3, ignoring any received packets with an SINR of $< 15.5$dB, very few errors are incurred while utilising 16-QAM. In the majority of cases these errors all fall within the same isolated block, i.e. packets $1300 - 1450$, with a select few corresponding to periods with a considerable change in velocity.

| Scheme | Packets | Errors | PER | Comment |
|---|---|---|---|---|
| QPSK | 811 | 2 | $2.5 \times 10^{-3}$ | |
| QAM | 1188 | 167 | 0.140 | Full Capture |
| QAM | 312 | 166 | 0.5321 | (SINR $< 15.5$dB) |
| QAM | 877 | 1 | $1.1 \times 10^{-3}$ | (SINR $\geq 15.5$dB) |

Table 4.3: Comparison of Packet Errors Incurred During Combined QPSK and 16-QAM Capture

Although the higher modulation scheme is generally found to operate successfully while the vehicle is in motion, in certain cases the residual Doppler shift is shown to cause an increase in the number of packet errors. Since the remaining phase distortion causes a rotation of the symbol positions in the complex state space, the reduced euclidean distance results in an increased possibility of a symbol being misinterpreted as one of the adjacent constellation points. Therefore, 16-QAM is typically found to be less tolerant of any residual phase distortion and require improved tracking of the incurred Doppler shift.

The results shown in this section clearly demonstrate the ability for the structure to support high order modulation schemes, i.e. 16-QAM. The recorded data set indicates a mixed performance, highlighting the need for increased SINR for the scheme

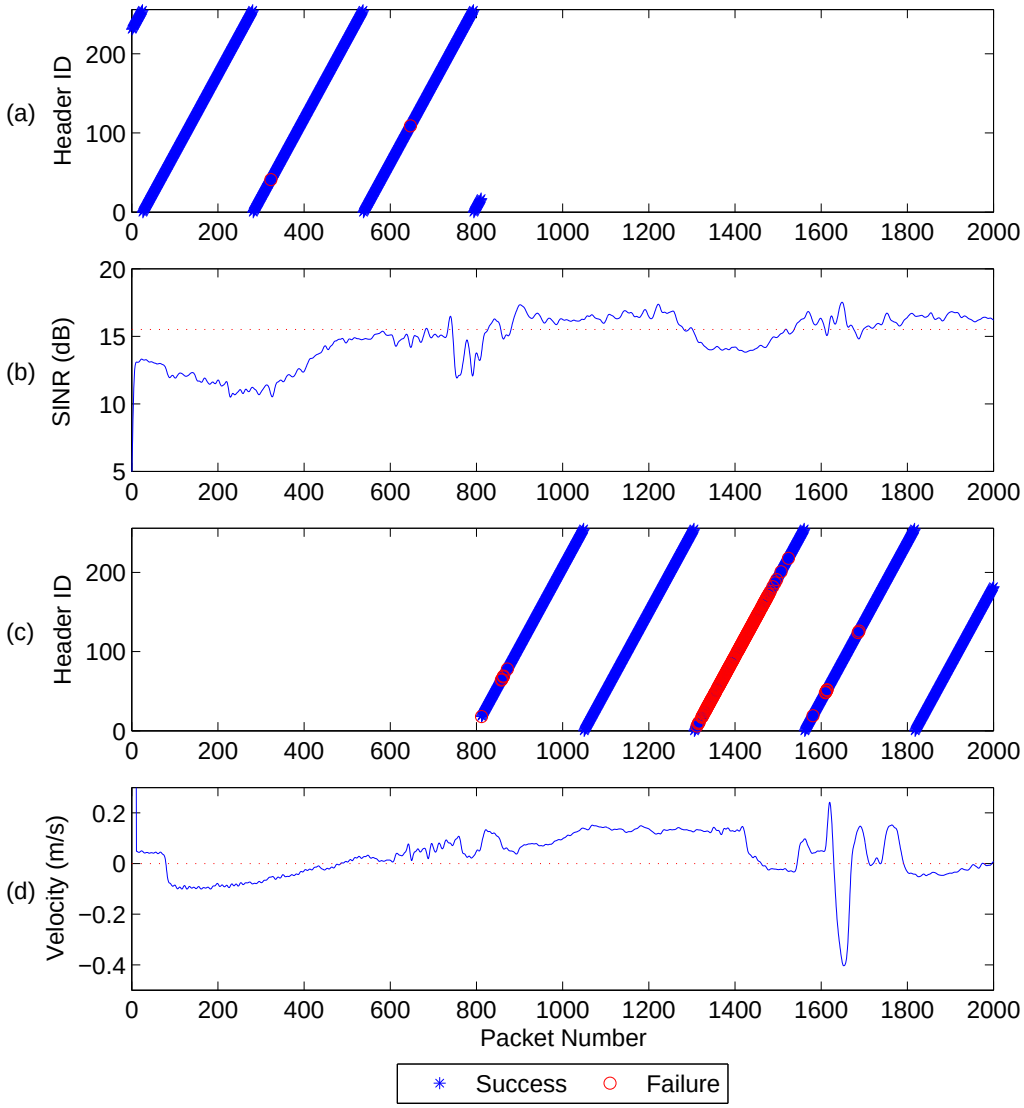


Figure 4.24: Packet Error Distribution for Comparative QPSK and QAM Transmissions:
(a) Quadrature Phase Shift Keying (QPSK) Error Distribution
(b) Signal and Interference to Noise Ration (SINR)
(c) Quadrature Amplitude Modulation (QAM) Error Distibution
(d) Relative Velocity (Calculated From Block Doppler Estimation)

to operate successfully. Although 16-QAM is shown to offer a significant increase in throughput, the unreliable performance when operating at low SNRs discourages the structure from being used within a static transmission scheme. However, if an adaptive AMC approach was to be implemented, a 16-QAM scheme would complement the use of a QPSK well, offering improved throughput during periods of favourable channel conditions.

## 4.5 Design Rules for Optimum Performance

The rigorous testing and evaluation presented in this chapter have enabled the author to examine the challenges faced in developing a high data rate communication link for a tetherless $\mu$ROV. An understanding of the complications of a highly dynamic shallow water channel, have led to the development of a small multi-element receiver. The results shown have clearly indicated the limitations of a single element receiver, even when utilising a high complexity iterative equaliser structure. An iterative receiver has in certain scenarios demonstrated the ability to overcome the hostile channel conditions. However, the limitation of the structure is observed when the signal space 'eye' is closed and minimal certainty of the symbol value is available. This scenario was typically observed when the equaliser was unable to overcome periods of long delay ISI, resulting in minimal improvement in performance through further inner and outer iterations.

Due to the specific channel conditions, a significant improvement in receiver performance was evident through the use of sparse equalisation techniques. Unlike many previously examined channels, which exhibit high range to depth ratios, the short range shallow water channel of the $\mu$ROV was shown to exaggerate the generation of widely spaced distinct multipath arrivals. Despite the sparse structure being unable to completely remove all errors, when compared with a conventional receiver a noticeable reduction of packet failures was observed, i.e. $\approx 50\%$.

The development of a combined micro-beamformer and complex iterative receiver structure, has demonstrated reliable transmissions across a wide range of realistic channel conditions. The use of a small 4-element $\lambda$ spaced array, enables isolation of the direct path and any surface reflections given adequate angular separation. Significant improvements have been demonstrated, offering improved SINR and the ability to operate in severely reverberant channel conditions. The operation of the proposed structure has been conducted across channels exhibiting long delay spreads, and multiple reflection paths. The use of a micro-array also supports the use of a wider operating bandwidth and symbol rate, with less restrictions caused by the span of the feedback filter. Given a lower Q transmit transducer it is believed that the developed system would be capable of operating across double the bandwidth,

e.g. 40-80kHz, with minimal degradation in system performance, and the ability to support significantly higher throughputs.

The extent of the testing is considered to be exhaustive, testing the suitability of the system across a range of realistic environments. Through the processing of several hundreds of gigabytes of data, the development of an effective receiver structure has been possible. The finalised structure has demonstrated the ability to offer reliable data rates of $\approx$ 30kbps post coding, utilising QPSK 9/10. Additionally, examination of higher order modulation schemes, 16-QAM, has indicated the feasibility to offer much higher data rates during periods of improved channel conditions. The varied performance of the two transmission schemes, QPSK and 16-QAM, have clearly indicated the benefits of an adaptive transmission structure, offering optimum performance for a given set of channel conditions.

# Chapter 5

# Receiver Design and Implementation

This chapter describes the implementation of an experimental high data rate uplink system for a $\mu$ROV. The proposed solution offers the optimum trade-off between system performance and implementation cost, taking into account the size and comparable price of the $\mu$ROV. This chapter initially focuses on the selection of suitable processing algorithms, taking into account the specific operating conditions and the limited processing power. Further evaluation of the hardware design is carried out, prior to a discussion on the software infrastructure, and the use of specific optimisation techniques to ensure real-time operation of the proposed system.

## 5.1 Receiver Considerations

Initially, the requirements of the receiver structure are considered, examining a range of suitable synchronisation, equalisation and decoding algorithms.

### 5.1.1 Synchronisation Techniques

In the majority of academic studies, the importance of a suitable synchronisation technique is often overlooked, presuming perfect packet synchronisation and focusing on the development of an idealised receiver structure. However, in reality, the effect of synchronisation inaccuracy and failure to detect the start of a new packet can have a catastrophic effect on the overall performance of the receiver. This is particularly evident in channels which exhibit low SNR levels, or highly dynamic multipath profiles. In such cases, the ability to normalise the signal and determine a suitable threshold level is essential in order to identify the start of a new transmission. An ineffective synchronisation scheme can also be found to result in the system falsely

detecting a new packet, due to: a rise in background noise; impulsive interference; or multipath reverberation.

As discussed in Section 3.2.1.1, a known sequence is typically used to mark the start of a new transmission. In the majority of cases this waveform is either: a PN-sequence, used for training; or a dedicated LFM chirp, appended to the start of the packet. The later is often favoured due to its high pulse compression ratio and its highly Doppler tolerant characteristics. In either case a matched filter is typically applied to the received data sequence, and the output is compared to a predetermined threshold level in order to indicate the starting position of a new packet. The selection of a suitable threshold level is often challenging, with intermittent fluctuations in background noise and loss in signal power, due to fading, causing the magnitude of the cross correlation output to vary with time.

#### 5.1.1.1 Normalised Cross-Correlation

In order to ensure successful synchronisation, across a range of operating conditions, it is important that the peak magnitude of the cross correlator output is kept constant. A variation in magnitude is typically caused by fluctuations in SNR, with increased noise levels causing the certainty of the chirp detection to diminish significantly. By normalising the matched filter output with the RMS voltage of the input signal, the proposed system can be seen to significantly reduce the effect of variations in SNR. This form of normalisation technique can be mathematically described by (5.1), where, $h[n]$ represents the matched filter coefficients, $y$ expresses the sampled input signal and $\mu$ defines the mean value of the input sequence. The numerator of this equation is shown to correspond with the cross correlation output, and the denominator as the standard deviation of the $L$ input samples currently found within the input delay line of the matched filter.

$$c(t) = \frac{\sum_{n=0}^{L-1} h[n]y[n+t]}{\sqrt{\frac{1}{L}\sum_{n=0}^{L-1}(y[n]-\mu)^2}} \tag{5.1}$$

Through utilising this form of normalisation, fluctuations in the input signal are shown to have a reduced effect on the matched filter output, enabling a suitable threshold level to be derived.

#### 5.1.1.2 Hard Limited Cross-Correlation

An alternative, more computationally efficient method of normalisation is to hard limit the input signal prior to the matched filter operation. Utilising this approach the input sequence is normalised to a magnitude of $\pm 1$, suppressing the effect of

any signal fluctuations. A block diagram of the proposed synchronisation technique is shown in Fig. 5.1. This technique is often preferred on embedded platforms due to its simple implementation and reduced computational complexity. By restricting the input of the matched filter to a boolean value, the computational load of the correlation operation is significantly reduced.

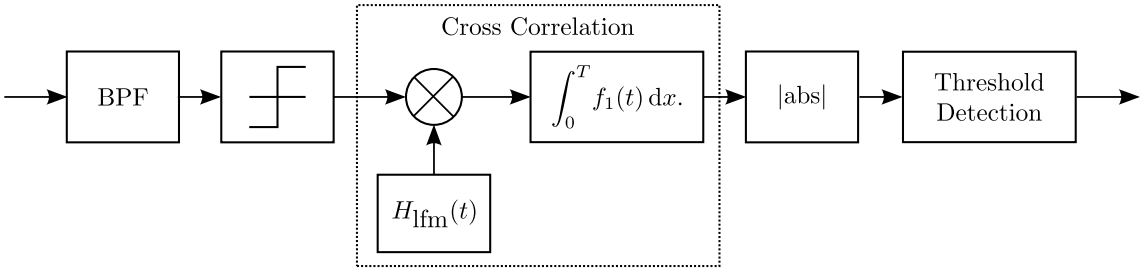


Figure 5.1: Block Diagram of a 'Single Bit' Hard Limited Synchronisation Technique

While operating at high SNRs, this technique is typically shown to offer similar performance to the idealised normalised cross correlation. However, the limitations of this approach are evident during periods of reduced SNR, where the hard limiting process can become dominated by background noise. In certain scenarios, this form of cross-correlation has been shown to be insufficient when utilising a multi-channel receiver structure, where the synchronisation process is performed based on a single element. Since a processing gain is observed due to the coherent summation and interference cancellation of the array, in many cases the hard-limited cross-correlation technique is found to fail in advance of the remaining equalisation and demodulation process.

#### 5.1.1.3 Summary

Within the context of this work a normalised cross correlation technique is utilised to ensure accurate synchronisation in a time varying channel. A hard limited matched filtering technique was shown to be unfavourable, due to its unreliability during periods of low SNR. The presented receiver structure therefore utilises a combination of a traditional normalised cross correlation technique and an adaptive threshold level to ensure successful synchronisation.

### 5.1.2 Equalisation: Adaptive Algorithm Selection

Despite the fast convergence rate of an Recursive Least Square (RLS) update, a considerable limitation is found in the ability to practicality implement the algorithm in real-time. This is further emphasised when utilising feedback filters with

a temporal length of over 100 symbols. In contrast, the complexity of the Least Mean Square (LMS) algorithm is shown to be highly suited to that of a real-time implementation, but offers a significant limitation in its convergence rate.

In order to ensure higher throughputs, a low packet overhead is typically preferred, favouring a training sequence of $\approx 500$ symbols. The comparable convergence rate of an LMS and RLS algorithm are demonstrated in Fig. 5.2. In both cases a BPSK training sequence of 500 symbols is utilised.

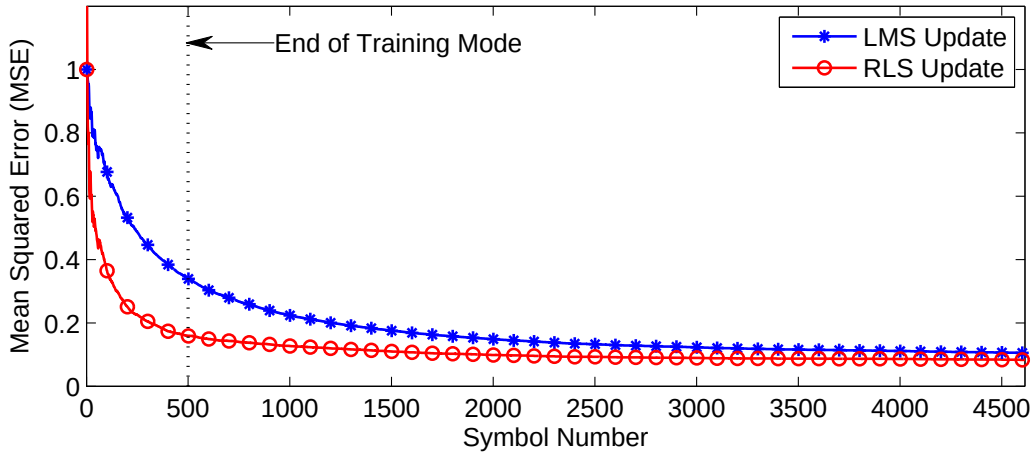


Figure 5.2: Convergence Rate of LMS and RLS Update Algorithms

The RLS algorithm demonstrates rapid convergence to an acceptable mean squared error (MSE). However, the LMS algorithm is shown to require an extended time period in order to converge on the same point, utilising additional iterations and failing to train within the allocated period. Despite both schemes demonstrating minimal bit errors for this packet, in cases where reduced SNR or increased interference are evident, the failure to train would have a catastrophic effect on the performance of the receiver. The RLS approach is therefore favoured when utilising a shorter training sequence.

To ensure successful convergence, while reducing the computational load of the system, a combination of the two algorithms is proposed. The hybrid strategy utilises an RLS algorithm while operating in training mode, i.e. for the first 500 symbols, and a lower complexity LMS algorithm for the remainder of the packet. Since the duration of the payload is significantly greater than that of the initial training period, the computational load is acceptable to ensure real-time operation.

### 5.1.3 Soft Decoding

An important aspect of the proposed iterative decoder, is the implementation of an efficient Soft-Input Soft-Output (SISO) decoding algorithm. Across the majority

of presented work, two forms of decoding algorithm have been shown to be most effective, these are: the Soft-Output-Viterbi Algorithm (SOVA); and the Maximum A posteriori Probability (MAP) or Bahl Cocke Jelinek and Raviv (BCJR) algorithm [99] [100]. Although the SOVA algorithm has a lower computational complexity and demonstrates comparable performance at high SNR levels, the MAP algorithm is typically shown to offer a significant benefit at lower SNRs. This improvement in performance encourages the investigation of the MAP algorithm.

#### 5.1.3.1 Maximum a Posteriori Probability (MAP) Decoder

For each decoded information bit, $u_k$, the MAP decoder is utilised to calculate the probability that the bit is either a '+1' or '−1', based on the received input sequence, $y$. This form of soft output, referred to as the Log-Likelihood Ratio, is typically expressed in the form of (5.2) [99].

$$L(u_k) = \ln\left[\frac{P(u_k = +1)}{P(u_k = -1)}\right] \tag{5.2}$$

Utilising the MAP algorithm, the calculation of the bit LLRs is typically broken down into three independent probabilities, these are: The forward error state probability, $\alpha_k(s)$; The reverse error state probability, $\beta_{k-1}(\acute{s})$; and the transition or branch state probability $\gamma_k(\acute{s}, s)$. Utilising these three probabilities, the LLR calculation, given by (5.2), is often expressed in the form of (5.3).

$$L(u_k) = \ln\left[\frac{\sum_{(\acute{s},s)\Rightarrow u_k=+1}\alpha_{k-1}(\acute{s})\gamma_k(\acute{s},s)\beta_k(s)}{\sum_{(\acute{s},s)\Rightarrow u_k=-1}\alpha_{k-1}(\acute{s})\gamma_k(\acute{s},s)\beta_k(s)}\right] \tag{5.3}$$

The forward error state probability, $\alpha_k(s)$, can be calculated utilising (5.4), where the value of $\gamma_k(\acute{s}, s)$ is known prior to the recursive calculation of $\alpha_k(s)$.

$$\alpha_k(s) = \sum_{\acute{s}\in\sigma_{k-1}} \alpha_{k-1}(\acute{s})\,\gamma_k(\acute{s}, s) \tag{5.4}$$

A similar form of this equation is utilised to calculate the backward error probability, $\beta_{k-1}(\acute{s})$, given by (5.5).

$$\beta_{k-1}(\acute{s}) = \sum_{s\in\sigma_k} \beta_k(s)\,\gamma_k(\acute{s}, s) \tag{5.5}$$

Finally, transition probability $\gamma_k(\acute{s}, s)$ is utilised to express the probability that for a received channel sequence, $y_k$, the trellis moves from a state $\acute{s}$ at a time $[k-1]$, to a state $s$ at time $[k]$. The transition probability can therefore be calculated using

(5.6), where, $P(u_k)$ expresses the *a priori* probability of the information bit and $x_k$ represents the transmitted codeword associated with the described transition.

$$\gamma_k(\acute{s}, s) = P(y_k|x_k)P(u_k) \tag{5.6}$$

For the interested reader, a more comprehensive description of the MAP decoding algorithm can be found in the original paper, presented by Bahl *et al.* [99].

#### 5.1.3.2 Logarithmic Domain Representation

Although the direct form of the MAP decoding algorithm is found to offer optimal performance, in the majority of real-time implementations, the computational complexity of the system makes it inherently impractical. Additionally, due to the dynamic range of the values utilised by the MAP algorithm, larger variable sizes are required, impacting on the processing and storage requirements. To overcome these limitations, the MAP algorithm is often calculated in the logarithmic domain, restricting the size of the calculated values and reducing the computational requirements by translating multiplications into simple additions.

**Max-Log-MAP Algorithm**

A simple approximation to the logarithm of a sum of numbers, can be calculated as the logarithm of the maximum value (5.7) [101].

$$\ln(A + B + C + ...) \simeq \ln(\max(A, B, C, ...)) \tag{5.7}$$

Therefore, the soft LLR output of the decoded data, shown in (5.3), can be approximated to (5.9)

$$L(u_k) \simeq \max_{(\acute{s},s)\Rightarrow u_k=+1} (\gamma_k(\acute{s}, s) + \alpha_{k-1}(\acute{s}) + \beta_k(s)) \tag{5.8}$$

$$- \max_{(\acute{s},s)\Rightarrow u_k=-1} (\gamma_k(\acute{s}, s) + \alpha_{k-1}(\acute{s}) + \beta_k(s)) \tag{5.9}$$

An approximation error is often observed in the calculation of the forward and backward error probabilities, $\alpha_k(s)$ and $\beta_k(s)$, caused by the inaccuracy between the maximisation operation and the ideal scenario. Since these values are calculated recursively, this approximation error is shown to propagate across the duration of the entire block and in the case of low SNR conditions result in a significant loss in performance.

**Log-MAP Algorithm**

Despite the Max-Log-MAP algorithm offering a significant reduction in computational complexity, when compared with the direct MAP algorithm, a reduction in the performance of the decoder is observed. An alternative technique is therefore proposed, utilising a correction function, $f_c(|x_1 - x_2|)$, to reduce the error between the approximation and the ideal form (5.11). This form is often referred to as the Jacobian Logarithm [102].

$$\ln\left(e^{x_1} + e^{x_2}\right) = \max\left(x_1, x_2\right) + \ln\left(1 + e^{-|x_1 - x_2|}\right) \tag{5.10}$$

$$= \max\left(x_1, x_2\right) + f_c\left(|x_1 - x_2|\right) \tag{5.11}$$

In this case, the correction function can be pre-calculated and stored in local look-up tables, or computed in real-time utilising a threshold detector. Both techniques have been demonstrated extensively, indicating near optimal performance with a reduction in computational complexity [101] [103] [104]. The benefits of utilising a Log-MAP algorithm has regularly been demonstrated across a range of literature, offering coding gains of within 0.1dB of the ideal MAP decoder.

#### 5.1.3.3 Comparative Performance

The analysis shown in Table 5.2 compares the computational complexity of the three discussed MAP algorithms: MAP, Log-MAP and Max-Log-MAP. The comparative complexity, given in terms of MOPS, is taken from the work presented by Hamid Sadjapour [105]. These supplied values are for a single iteration of a turbo decoder, where in each case the memory length of the RSC encoder is $v = 3$, creating a total of $M = 8$ decoder states, given that $M = 2^v$.

| | MAP | Log-MAP | Max-Log-MAP |
|---|---|---|---|
| Addition | 4M | 14M-4 | 10M-2 |
| Multiplication | 10M | 0 | 0 |
| Maximisation | 2M-1 | 4M-4 | 5M-2 |
| Table Lookup | 0 | 4M-2 | 0 |
| Total MOPS | 345.86 | 333.5 | 240.86 |

Table 5.1: Computational Complexity of Different MAP Algorithms
Originally Presented by H.R.Sadjadpour [105]

Despite, the slight degradation in performance demonstrated by the Max-Log-MAP algorithm, the significant reduction in computational complexity is shown to be

of considerable benefit in developing a real-time system. Therefore, the proposed implementation focusses on the adaptation and optimisation of the Max-Log-MAP SISO decoder originally implemented as part of the Coded Modulation Libraries (CML) [106].

### 5.1.4 Receiver Structure

A block diagram of the proposed receiver structure is presented in Fig. 5.3. The implemented system can be shown to comprise: 1. A multi-channel mixer and demodulator, with individual forward filters; 2. A DFE feedback filter; 3. A iterative BICM-ID decoder; and 4. A closed loop Doppler estimator.

### 5.1.5 Packet Structure

As part of the proposed real-time system, a suitable packet structure is defined, enabling flexible use of multi-level coding rates and variable modulation schemes. At the transmitter, the incoming data stream is divided into multiple packets each with a preamble appended to the start to assist with detection and demodulation. Fig. 5.4 illustrates both the packet and header structures used within the proposed real-time system.

Each packet transmission, as shown in Fig. 5.4a, is composed of four elements: a 20ms LFM 'chirp' used for synchronisation purposes; a 500 symbol BPSK training sequence for the initialisation of the equaliser coefficients; a short header, indicating the parameters of the data payload transmission; and the main data payload, which has a fixed length of 4096 symbols. Although a range of modulation schemes and code rates are used to represent the enclosed data, the fixed symbol length results in a constant packet duration of 251.6ms, enabling approximately four packets to be transmitted per second.

The header data, which is demodulated immediately after the equaliser coefficients have been trained, is used to supply the receiver with information relating to the coding and modulation of the data payload. The header, as shown in Fig. 5.4b, is made up of the following fields:

- Code Rate [3 Bits]:
  *The first three bits of the header are used to indicate the ratio between payload and data redundancy. It is possible to represent 8 different states, however in the current protocol only five are assigned: Uncoded, 1/2, 2/3, 5/6 and 9/10*

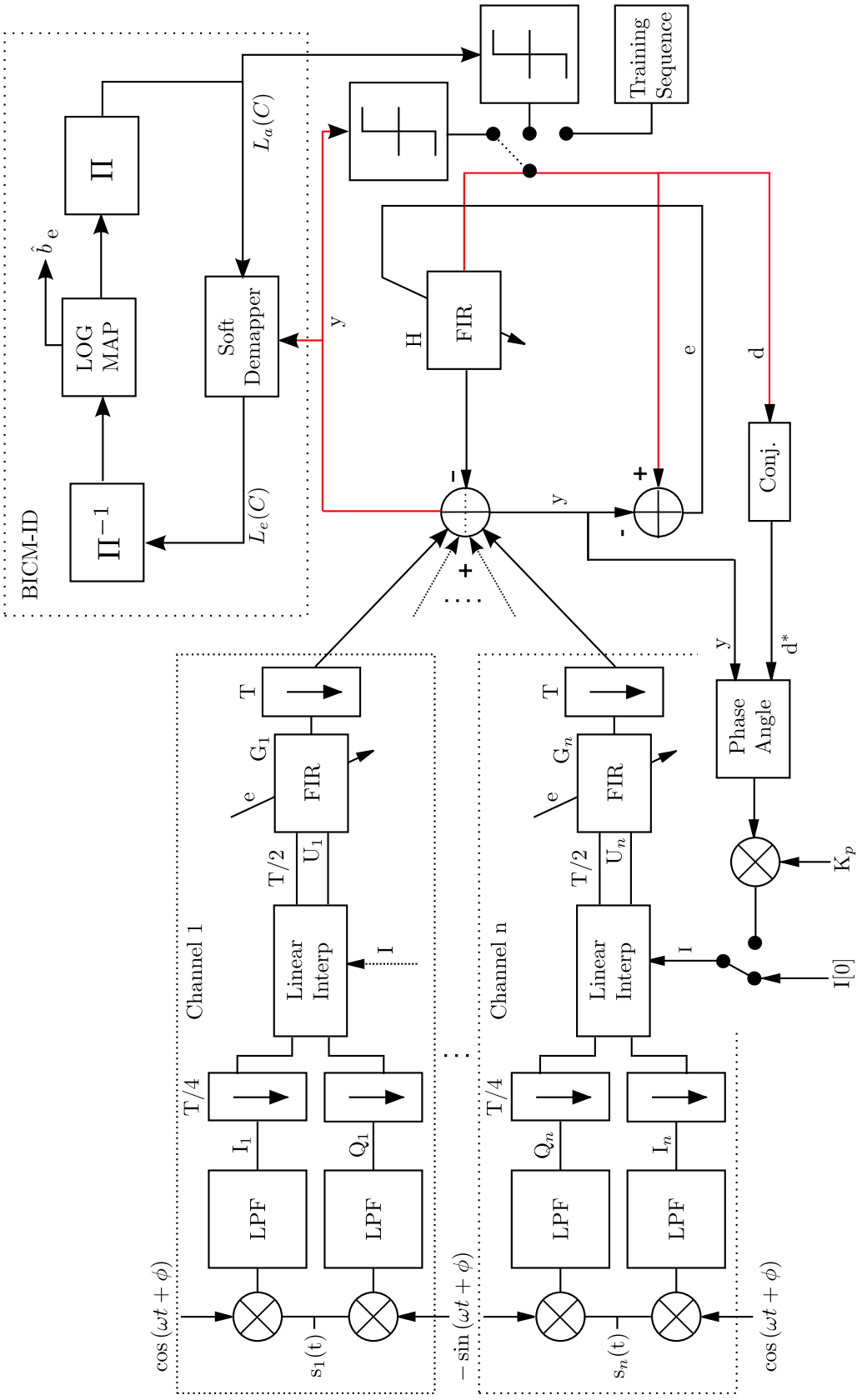


Figure 5.3: Proposed Multi-Channel DFE-BICM-ID Receiver Structure

| LFM | Training Sequence | Header | Data Payload |
|---|---|---|---|

(a) Single Packet Structure

| Code Rate | Mod Scheme | Re-Tx | Cont. | Packet No. | Header CRC |
|---|---|---|---|---|---|

(b) Packet Header Structure

Figure 5.4: Proposed Packet Structures:
(a) Single Packet Structure, (b) Packet Header Structure

- Modulation Scheme [3 Bits]:
  *The second field identifies the technique used to modulate the data stream onto the carrier signal. Again, 8 states can be represented using this structure, with only two being assigned in this work: QPSK and 16-QAM*

- Retransmit Flag [1 Bit]:
  *Indicates whether the packet is a requested retransmission. Within this work this field is unused and no protocol is implemented to enable the request for a retransmission. This field is solely included for use in future work.*

- Continuous Transmission Flag [1 Bit]:
  *Used to indicate whether the packet is part of a continuous stream or a singular transmission. Again, within this research all test transmissions were continuous streams.*

- Packet Number [8 Bits]:
  *Each transmitted packet is assigned a local packet number in order to identify the order of transmission and to indicate the loss of any packets. The assigned value of this field is between 0 and 255*

- CRC Checksum [16 Bits]:
  *A CRC-16 is used for error detection purposes. The checksum included in the header is computed based solely on the other header fields and not the rest of the data payload.*

In total, the packet header consists of 32 data bits, including the CRC checksum. The header is transmitted utilising the most robust communication scheme possible, in this case QPSK at 1/2 code rate. This ensures that the header will always be more resilient to low SNR levels and severe channel conditions than the payload data, reducing the possibility of a header failure. As with the main payload data, the header transmission is demodulated utilising a DFE-BICM-ID structure. Both

outer iterations and inner iterations are performed until the CRC detects no errors, or until a maximum number of iterations have been carried out.

Increased throughput can be achieved through: a reduction in coding overhead, resulting in less redundancy; or the use of a higher order modulation scheme, increasing the number of bits represented by each symbol i.e. 16 QAM. Table 5.2 presents a comparison of the various schemes tested within the scope of this research. For each: the total throughput and overall channel efficiency are presented, taking into account the coding redundancy and framing overhead. These values are calculated assuming a communication link with a bandwidth of 20kHz, around a centre frequency of 50kHz, and offering a symbol rate of 20kSym/s (i.e. 1Sym/Hz). Further information relating to the fundamental transmission parameters of the investigated acoustic link can be found in Chapter 4, Section 4.1.1.1.

| Scheme | Modulation | Code Rate | Effeciency | Throughput |
|---|---|---|---|---|
| (1) | QPSK | Uncoded | 81.4% | 32.56 kbps |
| (2) | QPSK | 1/2 | 40.65% | 16.26 kbps |
| (3) | QPSK | 2/3 | 54.2% | 21.68 kbps |
| (4) | QPSK | 5/6 | 67.8% | 27.11 kbps |
| (5) | QPSK | 9/10 | 73.2% | 29.28 kbps |
| (6) | QAM | Uncoded | 81.4% | 65.10 kbps |
| (7) | QAM | 1/2 | 40.68% | 32.54 kbps |
| (8) | QAM | 9/10 | 73.2% | 58.57 kbps |

Table 5.2: Comparison of the Channel Efficiency and Total Throughput for Various Implemented Communication Schemes

## 5.2 Receiver Implementation

This section focuses on the real-time implementation of a high data rate acoustic receiver structure. Both the hardware platform and software design are considered, indicating suitable component selection and optimisation techniques to ensure effective real-time operation.

### 5.2.1 Hardware Design

As highlighted by the results shown in Chapter 4, the shallow water operating environment of a $\mu$ROV present a wide range of communication challenges. One of the main limitations identified was the severity of the highly dynamic multipath channel

created by the compressed channel geometry. Results from field trials clearly demonstrated the limitations of a single element receiver structure to operate successfully under such channel conditions. A compromise was therefore presented, utilising an amalgamation of a small linear array receiver alongside high order equalisation and coding techniques.

To carry out preliminary field trials a linear four element beamforming array was constructed, combined with the interface hardware required to allow each channel to be independently filtered, amplified and digitally sampled. A basic block diagram of the receiver construction is shown in Fig. 5.5, indicating the four individual hardware components: the array receiver; the pre-amplifier circuitry; an analogue to digital interface; and a digital signal processing unit.

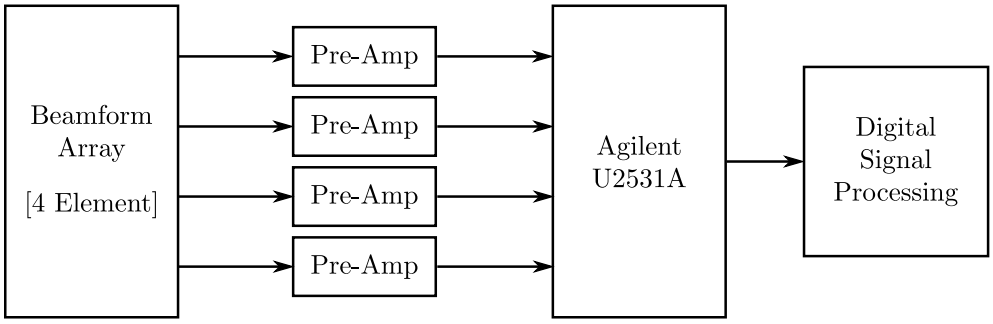


Figure 5.5: Multi-Element Receiver Hardware Structure

#### 5.2.1.1 Signal Processing Platform

In contrast to many traditional systems, where the processing is performed on a dedicated embedded platform, the receiver developed in this research is focussed around a standard Personal Computer (PC). With typical PCs now offering high levels of processing power, and a range of dedicated signal processing functionality, the requirement for bespoke hardware is considerably reduced. The proposed receiver utilises minimal hardware to amplify, filter and sample the received acoustic signal, with the PC used to perform the more complex synchronisation, equalisation and decoding algorithms.

The reduced complexity of the receive hardware, and the short bill of materials, enables the platform to be produced at a very low cost. Additionally, the simplicity of the hardware ensures minimal likelihood of mechanical failure and offers a wide variety of improvements to be made through simple firmware changes, rather than expensive and time consuming hardware re-designs. To enable easy relocation and deployment during periods of field work, a portable laptop computer was utilised.

The laptop selected is a Toshiba Satellite Pro, manufactured circa 2007, and built around an Intel® Centrino® 2 processor. This architecture is based on the Core 2 Duo platform, with several modifications specific to portable applications, i.e. improved power efficiency. A detailed break down of the systems specification is given in Table 5.3.

| Component | Attribute | Specification |
|---|---|---|
| Processor | Architecture | Intel® Centrino® 2 (Core 2 Duo) |
| | Clock Frequency | 2.53 GHz |
| | Front Side Bus | 1066 MHz |
| | Second Level Cache | 6 MB |
| Memory | Capacity | 3 GB (3,073 MB) |
| | Technology | DDR2 |
| | Frequency | 800 MHz |
| Hard Drive | Capacity | 320 GB |
| | Drive Rotation | 5,400 rpm |

Table 5.3: Real Time Receiver Laptop Specification
(Toshiba Satellite Pro U400-142)

The multi-core architecture offered by this platform is effectively used to enable several threads to be executed simultaneously. The acquisition, equalisation and output processes have been separated into individual threads to optimise the overall system performance. This method of operation ensures real-time processing, removing down-time while the system acquires new data or displays previously processed results.

In contrast to the majority of work presented by the research community, a key aspect of this investigation was to develop a real-time practical system. The majority of results presented in recent academic literature have been tested through the post processing of previously captured data sets. Typically in such cases, data is recorded during sea trials, but not processed until a later date. Utilising this form of processing, the complexity of the developed system is rarely considered.

#### 5.2.1.2 Data Acquisition and Conversion

A suitable Data AcQuisition (DAQ) unit was selected to enable the capture and conversion of the raw analogue input streams received by each of the hydrophone elements. The DAQ continuously samples each of the channels and streams the output information to the PC receiver for further stages of signal processing and

equalisation. Rather than developing a bespoke hardware platform, a Commercial Off-The-Shelf (COTS) Agilent U2500 data acquisition unit was selected. This device offers the ability to sample multiple analogue channels simultaneously, outputting the digitised stream to PC via Universal Serial Bus (USB). A more detailed specification for the chosen device, an Agilent U2531A, is given in Table 5.4.

| Parameter | Value |
|---|---|
| Resolution | 14-bit |
| No. Channels | 4 |
| Sample Rate | 200kHz |
| Input Range | ±1.25V, ±2.5V, ±5V, ±10V |

Table 5.4: Agilent U2531A Data AcQuisition (DAQ) Unit Configuration

A significant advantage of the U2500 range of devices is the multiple Analogue to Digital Converter (ADC) channels available. The majority of available DAQ units typically utilise a single ADC channel with multiplexers or switches to sample multiple channels. This unit offers a dedicated ADC for each of the four receive elements ensuring all channels can be sampled simultaneously and incur minimal phase offset. Additionally, the adjustable input range offered by each channel enables effective adaptive gain control to be applied.

#### 5.2.1.3 Buffered Operation

When sampling at higher frequencies, the PC software and relevant drivers struggle to support real time sample by sample transmissions through USB. The overhead required to process each individual arrival results in a significant processing delay and the possibility of a bus over-run. The outcome of this effect is a significant loss of information, with a large proportion of captured samples being lost during transmission to the PC.

To overcome this problem, the U2531A data acquisition unit utilises a First In First Out (FIFO) buffer to store multiple samples prior to USB transmission. Once several readings have been acquired, the data is relayed to the PC as a single block rather than as individual samples. This approach is demonstrated in Fig. 5.6, where samples are loaded from each of the independent ADC units into a dedicated FIFO buffer. Once the buffer is filled, the data is multiplexed and communicated via USB to the PC, meanwhile the DAQ unit continues to acquire new readings and loads them into the FIFO buffer.

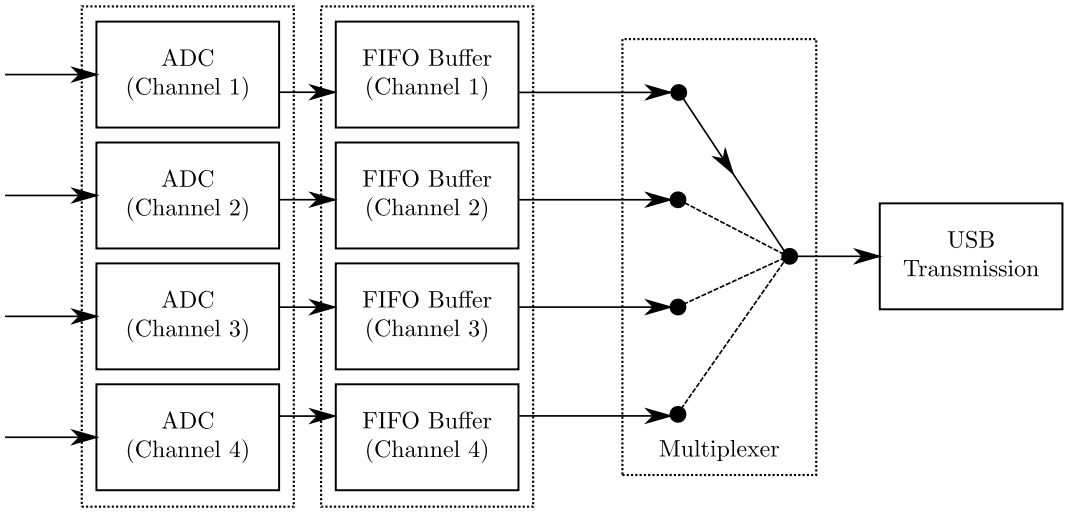


Figure 5.6: Operational Diagram of a Four Channel Agilent U2531A Data Acquisition Unit

The buffer on the U2531A enables a maximum of 8 MSamples to be stored, or in the case of a 4 element array receiver, 2 MSamples per channel. The number of points collected prior to transmission is configurable via the terminal connection, enabling much smaller buffers to be used as required. An important aspect to consider is the most appropriate length for the given application. In the case of a short buffer: the driver may be unable to cope with the regularity of the USB transmissions, possibly resulting in the over-run effect described previously. However, if a longer buffer is chosen, a significant latency may be observed while samples are accumulated in the FIFO. This can have a detrimental effect on the performance of the real-time system, resulting in a noticeable delay between the initial transmission and processing of the received packet.

#### 5.2.1.4 Beamformer Construction

As discussed previously, a bespoke four element beamform array was constructed in order to allow extensive testing and analysis of suitable receiver schemes. A cross sectional representation of the prototype array is shown in Fig. 5.7. The four elements are evenly spaced at $\lambda$ intervals, and are moulded in an acoustically matched polyurethane potting compound, Rho-C.

A summary of some of the design considerations made during production of the prototype receiver are given below, highlighting the reasoning behind the material selection and physical construction of the prototype unit:

**Transducer Elements:**
Four PZ-27 (Navy Type 2) soft piezoelectric ceramic tubes were used, positioned

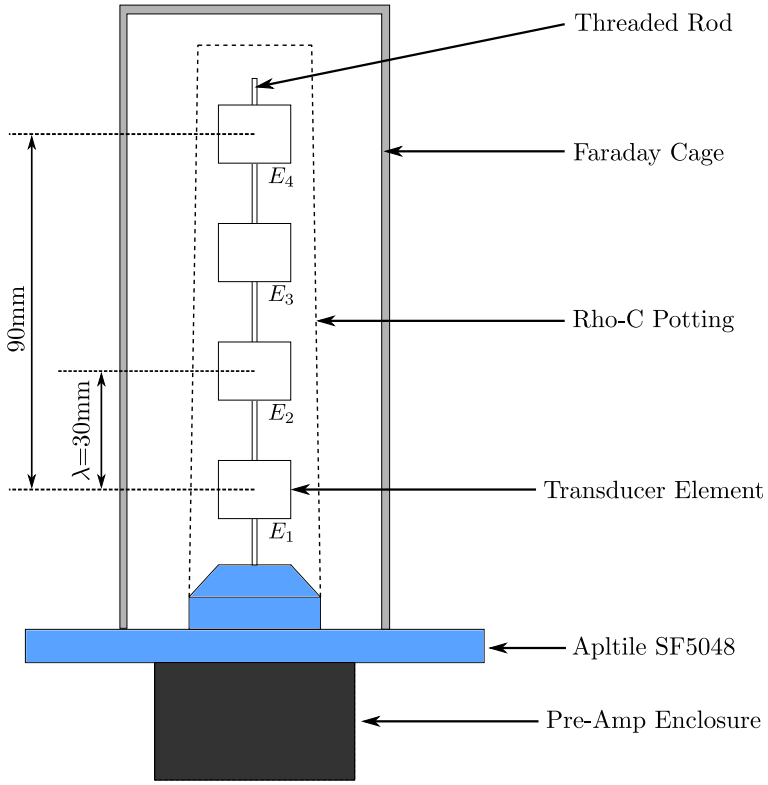


Figure 5.7: Cross Sectional Outline of the Proposed Four Element Beamform Receiver

in a linear $\lambda$-spaced array configuration. Each element had the dimensions of: $\varnothing_O$=11mm, $\varnothing_I$=9mm and thickness=10mm. For ease of construction, a thin threaded rod, 2mm in diameter, mounted through the base plate was used as a central support column. The threaded rod ensures maximum scattering of sound, minimising the formation of any significant multipath arrivals. Each transducer is mounted from the rod using a circular piece of closed cell foam forming an air backing, and improving the sensitivity of each element.

**Backing Plate:**
A backing plate, constructed from 'Apltile SF5048' acoustic absorbent material, was machined to form the base plate of the prototype beamformer. This plate was utilised to enable mechanical mounting of the array, during construction and deployment. The material used for construction was selected to minimise the generation of any internal reverberation paths, absorbing any back scatter from the array and shielding the transducers from any acute surface reflections. The backing plate was additionally machined into a conical shape to try and disperse any residual reverberation away from the array.

**Rho-C Potting:**
Post assembly, the transducer array was encapsulated in a material to protect the construction from mechanical strain and to electrically insulate the transducers from

the salt water medium. The 'Rho-C' material selected to enclose the assembly has specific properties such that it is optimally matched to the acoustic impedance of water. This serves to reduce the reflection and attenuation of sound within the material, ensuring the maximum amount of the transmitted sound waves arrives at the receive elements.

**Faraday Cage:**
A conductive cage was fixed around the outside of the hydrophone construction and connected to a common grounding point. The cage was used to suppress any Electro-Magnetic (EM) signals arising from either natural or application specific sources. Prior to use of the cage a significant source of EM interference was identified to be caused by the transmission of generated waveforms down the long lengths of tether to the vehicle mounted transmitter. In a 'real life' application this source of EM would not exist as the tether would be replaced with a solely acoustic link.

**Pre-Amplifier Enclosure:**
Once the pre-amplifier circuit had been fully tested, it was mounted on the back plane of the Apltile plate and potted into place using epoxy resin to form a watertight construction. The separation between the ceramic and the front end filters was kept to a minimum to ensure maximum SNR prior to transmission through the riser cable, thus avoiding any antenna effects coupling interference into the system.

#### 5.2.1.5 Physical Constraints

As a consequence of utilising a higher frequency band, $f_c = 50$kHz, and by constraining the element spacing to $\lambda$, the overall construction of the 4 element array is shown to be $< 150$mm in length. The reduced size and lightweight construction ensures the array is easy and quick to deploy from a small surface vessel. The array is found to be comparable in size to a typical single-element omni-directional receiver, such as the Reson TC4032 tested in Chapter 4. The photo shown in Fig. 5.8 demonstrates a comparison between the micro-array and the omni-directional single element hydrophone.

#### 5.2.1.6 Pre-amplification and Filtering

A pre-amplifier was applied to each of the beamformer channels, in order to maximise the received signal strength prior to being relayed to the surface unit. A differential amplifier with single ended output, as shown in Fig. 5.9, is used to give an initial amplification stage and supply broadband filtering to each of the four channels. The bandpass filters ensure any low frequency noise such as environmental or shipping noise and any high frequency out of band harmonics are suppressed.

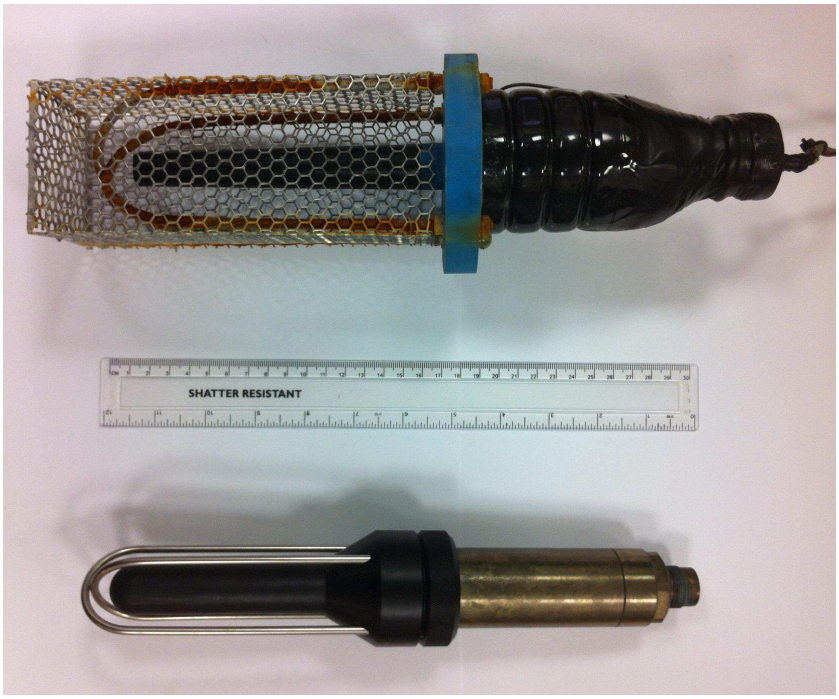


Figure 5.8: (Top): Prototype 4-Element $\lambda$-Spaced Beamform Array (Bottom): Single Element Omnidirectional Hydrophone (Reson TC4032)

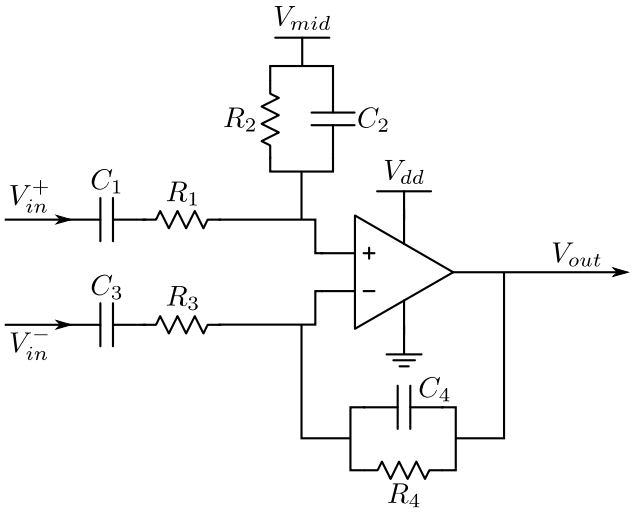


Figure 5.9: Active Differential Bandpass Filter Schematic: Implemented on Each Beamforming Channel for Pre-Amplification and Filtering Purposes

| Filter Pairing | Component Value | |
|---|---|---|
| | $R_n$ | $C_n$ |
| Highpass Filter *(n = 1 and 3)* | $1k\Omega$ | $4.7nF$ |
| Lowpass Filter *(n = 2 and 4)* | $150k\Omega$ | $15pF$ |

| Parameter | Value |
|---|---|
| Passband Gain ($A_d$) | 40dB |
| Highpass Cutoff | 17.5kHz |
| Lowpass Cutoff | 74.8kHz |

Table 5.5: Filter Parameters and Suitable Component Values for the Receiver Front End Pre-Amplifier Circuit

The chosen component values and theoretical filter parameters are given in Table 5.5. The selected component values supply a flat response across the proposed frequency band, 40 - 60kHz, offering approximately 40dB of gain at the centre frequency point. The 3dB down, half power, points are positioned at roughly 20kHz - 75kHz, allowing adequate clearance either side of the utilised transmission band and ensuring minimal phase distortion on the received signal. Fig. 5.10 demonstrates the frequency response, both simulated (P-Spice) and practical, for the component values given in Table 5.5.

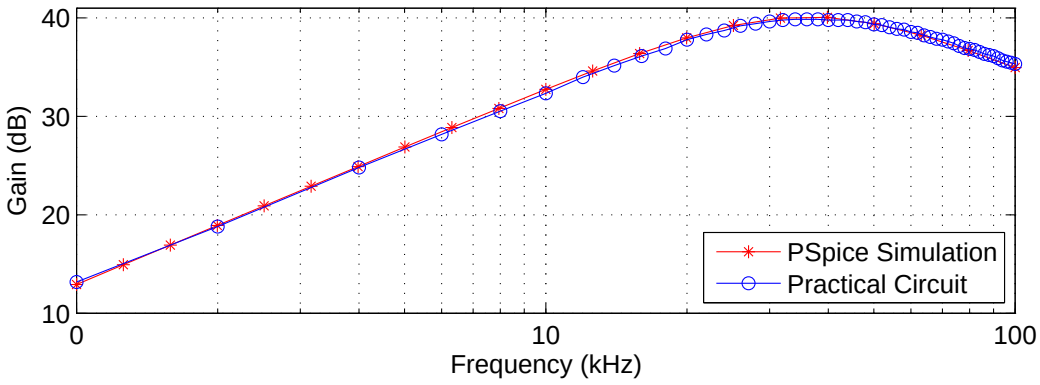


Figure 5.10: Frequency Response of the Receiver Front End Pre-Amplifier and Filter - Simulated (P-Spice) and Practical Response

### 5.2.2 Software Considerations

The acquisition and processing of the received signals is performed by a bespoke software package written in Microsoft Visual C++. This section presents an overview of the developed software infrastructure, highlighting optimisation techniques used to enable real-time demodulation and decoding.

#### 5.2.2.1 Coding Optimisation

To ensure the developed code is capable of operating in real-time several forms of coding optimisation are utilised. A selection of the techniques used are described below.

**Identify Parallelism:**
By identifying sections of code which can be performed simultaneously, the operation can be divided into multiple concurrent threads. The multi core architecture allows several threads to be scheduled in a given time period. Therefore the code should be rearranged to enable separate processes to operate simultaneously. When identifying parallel sections of code, careful consideration should be given about the dependency a routine may have on another. Situations where the output from one thread directly affects the operation of another can result in harmful race conditions, or at worse complete dead-locks.

**Compress the Content of Loops:**
Through reorganisation and restructuring of certain algorithms, time consuming operations can be removed from the long, regularly performed, loops. By reducing the number of calculations performed within a loop structure the overall complexity of the system can be significantly reduced. By moving operations which require higher numbers of clock cycles, i.e. divisions, to the outside of a long loop the overall speed of the system can be seen to vastly improve.

**Initialisation of Constant Look-Up Tables:**
A significant benefit of developing a PC based receiver is the increased memory availability. In a typical embedded platform, the reduced memory size can be seen to considerably limit the generation and storage of long look-up tables. The ability to initialise the system by calculating regularly used values at start-up, significantly reduces the time to repeatedly perform certain tasks. An example of this form of optimisation is during FIR filtering operations where the filter coefficients can be generated at initialisation rather than each time the filter is used.

#### 5.2.2.2 Intel® Integrated Performance Primitives (IPP)

The Intel® Integrated Performance Primitives (IPP) are a set of predefined routines developed to optimise the performance of the compiled code when operated on an x86 Intel processor [107]. The libraries offer an interface between the software developer and any dedicated hardware features, allowing high performance code to be constructed with minimal consideration for the processor structure. These libraries can therefore be seen to reduce the time required in generating platform specific code.

The library is constructed from a large collection of mathematical procedures suitable for use in a diverse range of signal processing applications. Of specific interest are the complex matrix and vector commands, offering noticeable performance gains when calculating multiplications or divisions of large arrays of values. Additionally, dedicated filtering routines have been developed which offer significant improvement during initial signal conditioning stages.

Although the libraries are developed to give improvement when operating on an Intel platform, some benefits, albeit significantly reduced, have been observed when tested on other processor architectures such as those produced by AMD. The ability to generate code which is ideally suited to the given platform infrastructure has shown performance improvements in excess of 300%, when compared to code generated by highly optimised compilers. The functions are developed to operate safely on a multi-threaded platform, ensuring division of tasks across both cores when not occupied with other tasks.

The IPP libraries were utilised throughout the receiver structure to improve the run-time performance of the software. Certain filtering and vector routines were utilised during initial signal processing stages, with additional mathematical routines used to reduce the time taken to perform the equalisation and decoding operations.

#### 5.2.2.3 Multi-Threaded Implementation

By identifying aspects of the code which can be performed in parallel, the receiver can be re-organised into a multi-threaded structure. The ability to perform several processes simultaneously enables a reduction in the time taken to process each packet. By examining the system's operation, 3 parallel sections of code can be identified. For simplicity, these 3 threads are referred to as: data capture; data processing; and visualisation and output storage. A summary of the threads is given below, with a brief description explaining the processing performed by each.

**Thread 1: Data Capture**

This thread focusses on the capture and storage of real time data received by the hydrophone array. Primarily this thread interfaces between the DAQ unit and the main processing stages. Because of the buffering performed by the DAQ unit, as described in Section 5.2.1.3, the receiver is forced to wait until a certain number of samples have been acquired. During this period the thread loops continuously, polling the DAQ unit at regular intervals until new data is available. Once the information has been transferred by USB, the thread reformats the data set and stores the samples into a temporary storage file.

The temporary file is utilised as a double buffer, allowing previous samples to be stored prior to being processed by the other threads. Additionally, when the receiver is terminated this file is saved to the hard drive, enabling the full data set to be re-processed at a later date if required. This structure enables the recorded information to be tested with a wide variety of receiver configurations. Through adjustments to the receiver structure and selection of coefficient values, i.e. equaliser forgetting factors and Doppler control gain, the system can be tuned until optimum performance is achieved.

A block diagram of the processing performed by this thread is shown in Fig. 5.11. Once started, the thread can be seen to continuously loop, accumulating new samples and loading them into the temporary buffer file. The thread is terminated by the user attempting to close the main program, in this situation the thread waits for the final set of samples to be collected prior to ending.

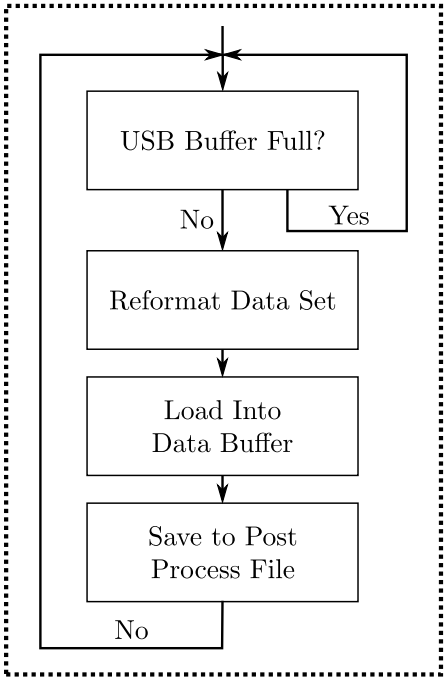


(1) Signal Capture
[Thread 1]

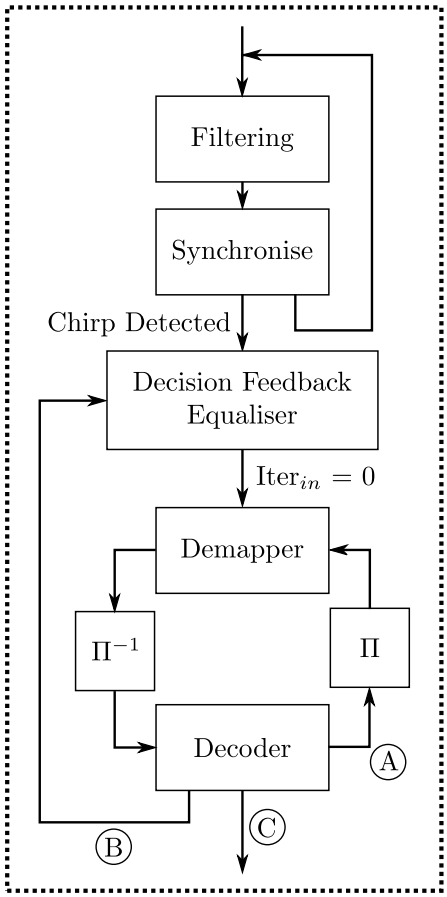


(2) Signal Processing
[Thread 2]

| Branch | Iter$_{in}$ | Iter$_{out}$ | BER |
|---|---|---|---|
| Ⓐ | $< 3$ | $\leq 3$ | $> 0$ |
| Ⓑ | $= 3$ | $< 3$ | $> 0$ |
| Ⓒ$_1$ | $= 3$ | $= 3$ | $> 0$ |
| Ⓒ$_2$ | - | - | $= 0$ |

Table A: Branch Criteria

Figure 5.11: Receiver Software Structure

**Thread 2: Data Processing:**
The second thread is utilised to perform the majority of the signal processing tasks, including the synchronisation, demodulation and decoding of the received packets. A detailed overview of each of the processing stages are given below:

1. *Synchronisation:* The first processing stage is used to identify and synchronise the receiver with the beginning of a new packet. The synchronisation process is continuously looped until a new packet is detected or until the user terminates the program.

2. *Filtering:* Once the start of the packet has been identified, the sampled data set is filtered using a 100 tap Finite Impulse Response (FIR) bandpass filter. The filter offers a tight response between 35kHz and 65kHz, ensuring any out of band noise or interference is suppressed.

3. *Equalisation - Training:* The equaliser is initially operated in a training mode, enabling the filter to identify the channel impulse response and configure the relevant filter coefficients. During this period a known sequence is transmitted, enabling the equaliser to accurately estimate the multipath channel response. During training an RLS algorithm is utilised to maximise the convergence rate and enable a shorter training period to be used.

4. *Header Processing:* Prior to any packet data being received, the header information is captured, equalised and decoded. If the header fails to be successfully decoded within the predefined number of iterations the receiver returns to the synchronisation state and waits for the next packet to be detected.

5. *Equalisation - Decision Directed Mode:* Utilising the received header information, the remainder of the packet is processed. Initially the equaliser structure is utilised to remove any channel reverberation effects. In comparison to the previous mode of operation, when receiving the payload data the DFE operates in decision directed mode utilising an LMS update algorithm.

6. *Iterative Decoding:* Once the full data set has been equalised, a SISO (Max-Log-MAP) decoder is utilised to decode the received data. If errors are still observed an iterative process is performed, passing soft information between the decoder and the de-mapper to improve the certainty of the decisions. If code rates of less than 1/2 are used, a puncturing and de-puncturing process is required.

7. *Equalisation - Outer Iteration:* If the inner iterations fail to remove all the errors incurred by the channel, an outer iteration is utilised. This process re-runs the equaliser structure, utilising feedback from the inner iterations as

the DFE decision values. Once this process has been carried out, the output from the DFE is passed back through the iterative decoding process, to further improve the certainty of the decoded decisions.

The processing performed by this thread is performed in a state machine structure, with multiple break statements to return to previous states for further equalisation or decoding iterations. During the processing of each packet a maximum of 2 outer and 3 inner iterations are performed. If the receiver detects zero errors prior to this the receiver will return to the synchronisation state and await the arrival of the next packet. As highlighted previously, the main processing tasks can be performed on either real-time data or previously recorded samples. In the second of these two cases data is read from an external file rather than from data received by the first thread.

In comparison to the other two threads, the processing performed within this thread are most computationally intense. Therefore, careful optimisation is required to ensure that the processing can be performed in real-time and not result in a accumulated delay. A block diagram of the processing performed by this thread is shown in Fig. 5.11. Table A, inset, shows the branch conditions during each of the iterative cycles. For simplicity purposes the diagram does not show the iterative processing of the header information.

**Thread 3: Visualisation and Output Storage**

The third thread is utilised for the regular processing and visualisation of receiver performance information. Fig. 5.12b, demonstrates a typical output from the receiver visualisation GUI. In this window five sets of axis are demonstrated, these are:

1. I-Q Plot *[Top Left]*: Demonstrates the signal space constellation plot for the most recently demodulated packet. The I-Q plot can be used as an indicator of any phase distortion and incurred SNR through observation of the spreading and location of the constellation points.

2. Bit Errors *[Top Right (a)]*: This plot displays the number of bit errors incurred over the last one hundred packets. When combined with the other four plots the historical information can be used to examine a correlation between the occurrence of errors and the vehicles operation / transmission characteristics.

3. Doppler Shift *[Top Right (b)]*: A historical plot of the induced Doppler shift observed on the last one hundred packets. The presented Doppler readings are taken from the initial block estimates and not the closed loop update values.

4. Mean Squared Error (MSE) *[Centre Middle]*: The fourth plot shows the mean squared error of the equaliser output for the most recently demodulated packet. This figure gives indication of the convergence time of the equaliser during training and the ability for the filter to continue tracking changes in channel conditions during operation in decision directed mode.

5. Channel Impulse Response (CIR) *[Bottom Middle]*: The final figure shows the estimated CIR, generated through cross correlation with the synchronisation header chirp appended to the start of the most recently received packet.

In continuous streaming mode the diagnostics GUI is only updated every five packets, i.e. not on a packet by packet basis. The code is organised in this manner to reduce the computational load incurred by the GUI thread, maximising the availability of both processor cores for data capture and processing and thus reducing the time taken to demodulate each packet.

### 5.2.3 Receiver Benchmarking

In order to evaluate the receivers performance and to ascertain the structures ability to operate in real-time, a selection of tests were carried out. An essential consideration during the construction of the receiver, was the ability to process each packet in real-time. The following results evaluate the performance of the proposed receiver structure when implemented on the PC platform described in Section 5.2.1.1

#### 5.2.3.1 Benchmarked Receiver Performance: Single Packet Processing

The first set of tests evaluate the duration taken to process an individual packet, assuming a certain number of inner and outer iterations are performed. Utilising a pre-recorded data set, the receiver is configured to post-process each packet, outputting to a intermediary file, the duration taken to perform a pre-defined number of processing iterations.

Accurate timings are calculated through the placement of the routine call, *'GetTickCount'*, at certain point in the code. This routine returns a value, given in milliseconds, since the PC was initially turned on. Unless the processor is put into a low power idle state, the 32-bit counter is incremented by a hardware interrupt that occurs once every millisecond. The minimum duration measurable utilising this command is therefore circa 1 millisecond, operations performed in a shorter time period are considered unmeasurable with this technique.

Although, alternative methods may offer improved timing precision, an important consideration is the effect on the operation of the code. Higher precision timers tend

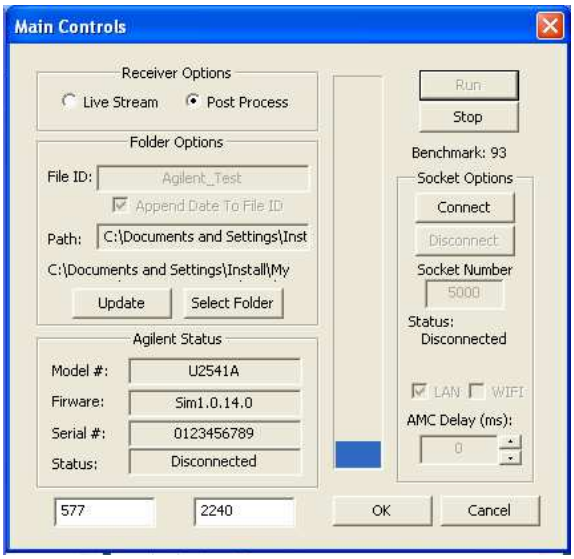


(a) Software Control Box

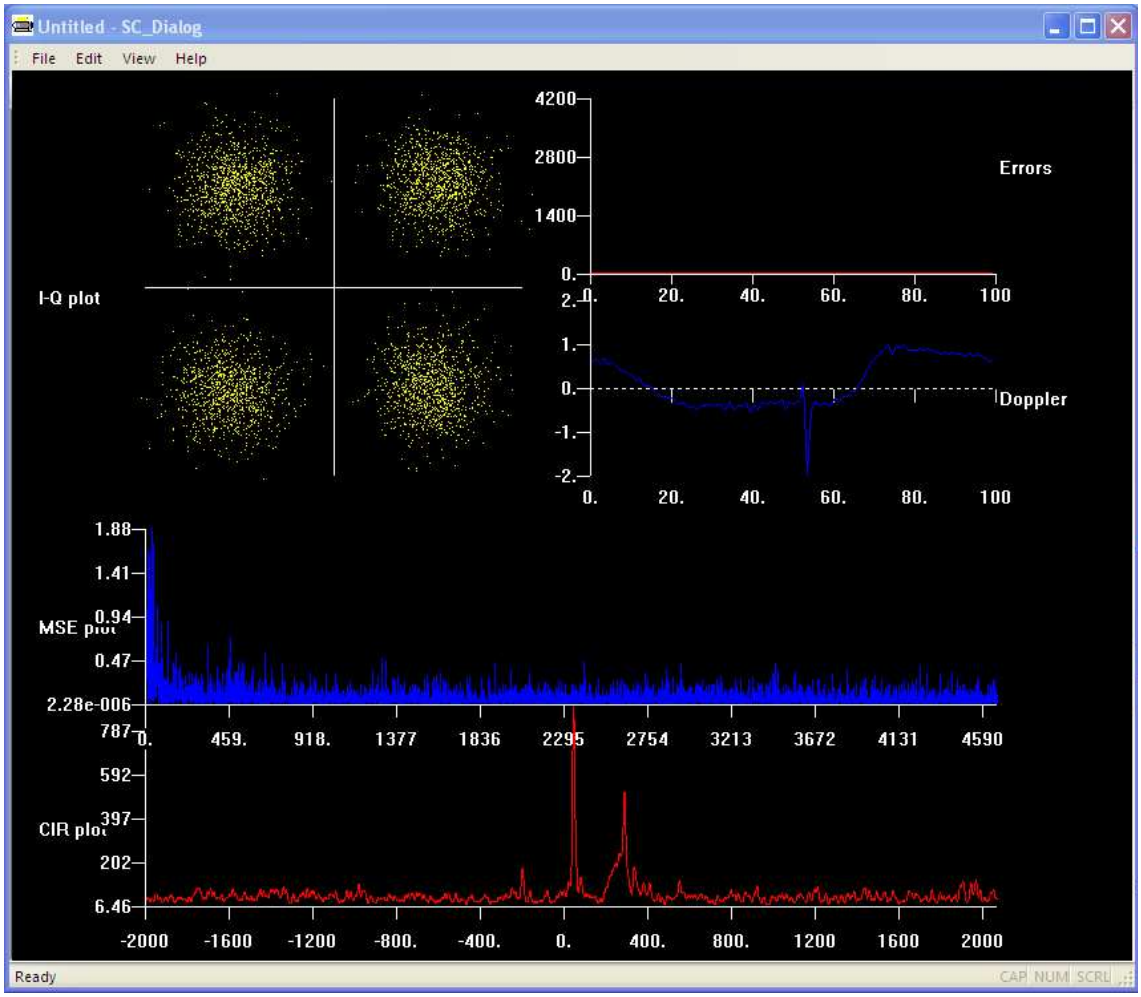


(b) Receiver Graphical Diagnostics Output

Figure 5.12: PC Based Real-Time Receiver Software Outputs:
(a) Software Control Interface, Enabling Setting of Various Control Parameters
(b) Graphical Diagnostics Output,

to utilise more computationally intense interrupts which will have a considerable impact on the performance of the code under test. Therefore, since the lower timing precision is considered acceptable, and to minimise the impact caused by the test methodology, higher resolution counters are avoided.

To examine the time taken to perform the processing of an individual packet, the global *'tick'* count is recorded: at the beginning of the packet, i.e. prior to synchronisation; and at the end of the packet, i.e. post the final decoding / de-mapping stage has been performed. By evaluating the difference between the two times, the duration taken to perform the full set of processing operations can be recorded.

Although the main processing tasks are typically allocated uninterrupted processor time, certain management tasks, which have a higher *'time critical'* priority, are scheduled use of the processor ahead of the main receiver thread. This form of scheduling can be seen to result in impulsive processing delay, forcing the receiver to wait while other house keeping operations are performed. It should be noted that some of these operations occur periodically, i.e. interrupt handling, while others are performed asynchronously, i.e. driver or GUI handling.

To take into account the additional scheduling delays, processing times are averaged across a large number of processed packets. Since, the scheduled tasks tend to occur infrequently, occupying a low duty cycle, and resulting in minimal accumulated delay, the averaged duration is considered accurate enough to conduct a valid evaluation of the receivers performance. For the results demonstrated, the mean average processing duration is calculated from a data set of 900 QPSK packets and 1200 QAM packets. Both schemes utilise a 1/2 rate RSC code. The first data set, as shown in Fig. 5.13, compares the mean processing duration of both QPSK and QAM data packets: for different numbers of inner and outer iterations. A dashed black line is used to highlight the maximum processing duration, such that feasible real-time operation may be possible.

It is immediately evident from these results that the system is more than capable of supporting QPSK 1/2 with any of the demonstrated combinations of inner and outer iterations. Utilising the arrangement typically presented within this thesis, i.e. 3 inner, 2 outer iterations, the receiver can successfully process an individual QPSK packet on average every 150ms.

In contrast, the performance of the receiver during 16-QAM transmissions is less clear cut, with higher numbers of iterations resulting in an average processing duration in excess of 250ms. Therefore, it can be assumed that lower numbers of iterations must be utilised to insure real-time operation, i.e. such that the processing time is less than the length of the packet. In the case of the proposed number of iterations, 3 inner and 2 outer, the receiver is shown to perform below the maximum threshold level, processing a packet on average every 240ms.

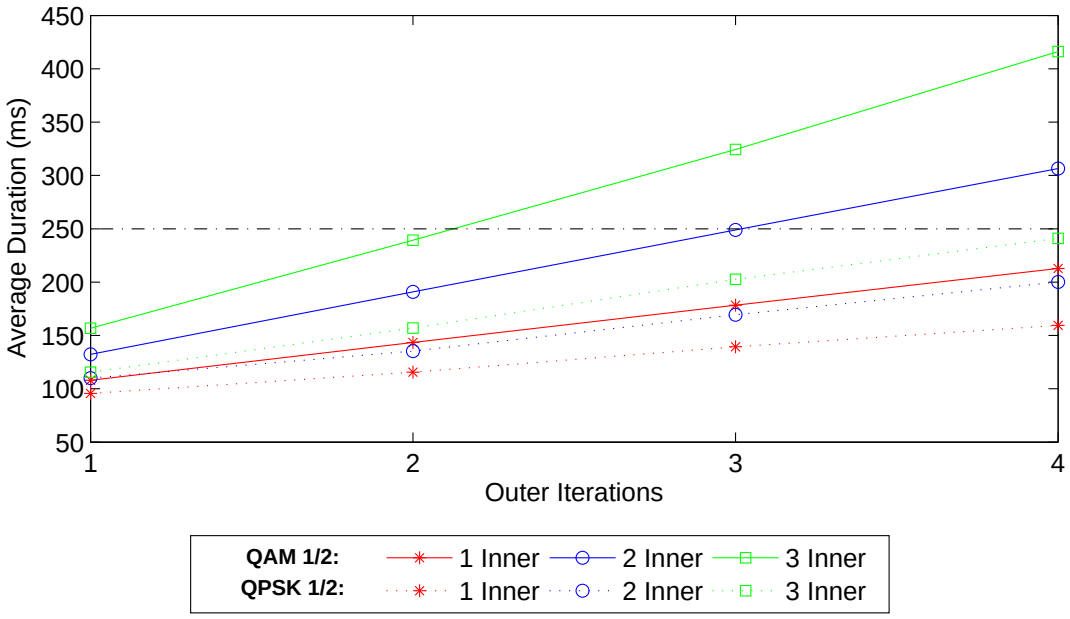


Figure 5.13: Mean Processing Duration of QPSK and QAM 1/2 Transmissions for a Varying Number of Outer Iterations

A secondary set of results are presented in Fig. 5.14, demonstrating the comparable processing duration for a single element and multi element receiver structure. As discussed previously, the multi element receiver utilises a similar DFE structure, with an additional $(L-1)$ feed-forward filters. In the discussed results a 4 element $\lambda$ spaced array is considered, i.e. $L = 4$. All results are presented for QPSK, rate 1/2, assuming 3 inner iterations and a variable number of outer iterations. As with the previous results a dashed black line is used to indicates the real-time operation level (250ms).

For both the single and multi element structures, the average processing duration is shown to be considerably less than the maximum operating threshold. The simplified single element receiver structure is shown to offer improved performance, with the majority of cases ($\text{iter}_{\text{out}} \geq 2$) requiring less than half the time of a multi-channel receiver to process a full packet. The increased complexity of the receiver can be seen to correspond to the additional filter coefficient updates performed on the extra forward filters. The additional forward filter calculations are only performed during the initial equaliser operation and further outer iteration stages.

#### 5.2.3.2 Benchmarked Receiver Performance: Packet Breakdown

A comparison of the computational time for different sections of the receiver are given in Fig. 5.15, where Table 5.6 itemises the individual processing stages. In contrast to the previous tests, where the overall time to process a single packet

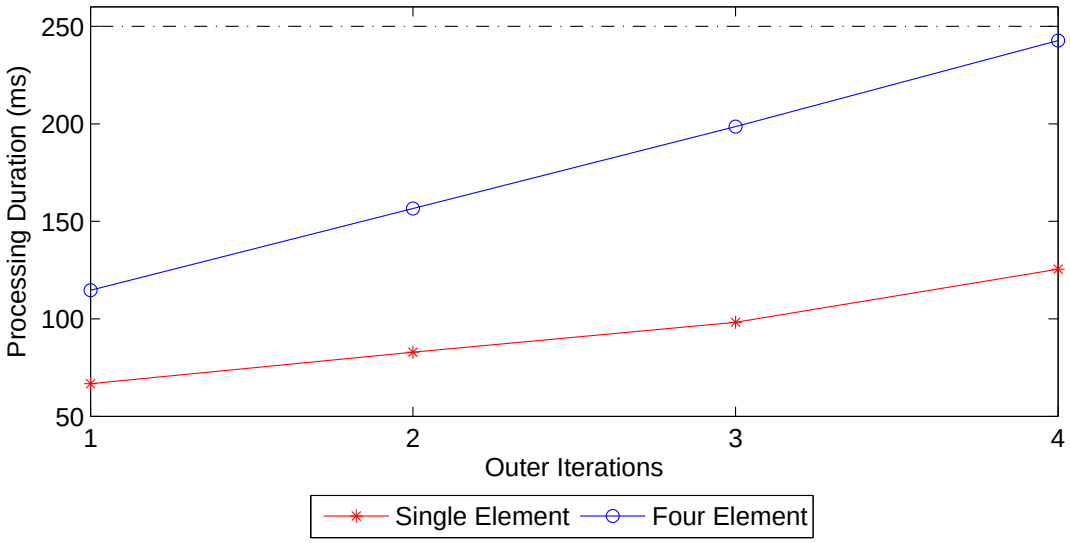


Figure 5.14: QPSK 1/2, 3 Inner Iterations. Comparison Between Processing Time of Single Element and Multi Element Receivers

is discussed, this form of evaluation allows a comparison to be made between the individual subsections of the receiver. This technique enables deeper understanding of the complexity of the receiver, highlighting which sections are computationally intense and which can be assumed to have minimal impact on the overall system performance.

| Label | Description |
|---|---|
| (a) | Packet Synchronisation |
| (b) | Initial Training, Header Demodulation and First Outer Iteration |
| (c) | First Set of Inner Iterations |
| (d) | Second Outer Iteration - Re-Run of DFE Equaliser Structure |
| (e) | Second Set of Inner Iterations |

Table 5.6: Summary of Benchmarked Processing Stages, for a 3 Inner 2 Outer DFE-BICM-ID Four Element Beamformer Receiver

As with the previous tests the results shown are an average taken over a long data capture, negating the effects of impulsive background tasks. Again the results indicate the capability of the implemented receiver to support real-time operation for a range of update algorithms and transmission schemes. It should be noted that in all cases an LMS algorithm is utilised during decision-directed mode and that the specified algorithm indicates the processing performed during training of the DFE. The results are presented for the processing of 2 outer and 3 inner iterations. In

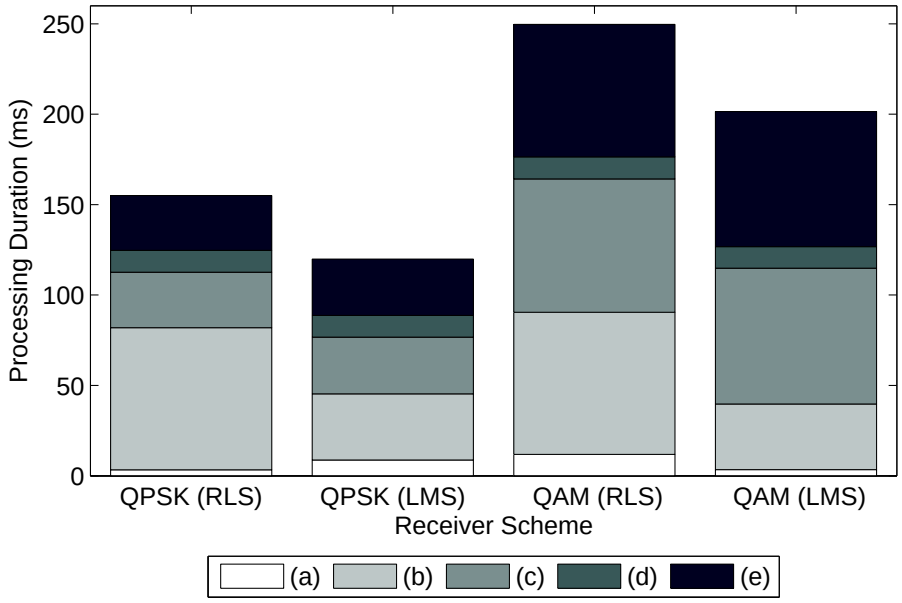


Figure 5.15: Itemised Processing Duration for Specific Aspects of the Real Time Implementation (Multi-Channel Receiver Structure)
Descriptions of the Individual Processing Stages, (a)-(e), Given in Table 5.6

the scenarios where an RLS algorithm is utilised to update the filter coefficients, it is evident that a considerable proportion of the processing time is occupied by the first outer iteration / training period.

## 5.3 Transmitter Structure

To fully test the proposed receiver structure, during sea trials and laboratory experimentation, a bespoke transmitter platform has been developed. The transmitter is again a PC based software implementation, operating on an independent PC from the previously described receiver structure. It should be noted that although the receiver is perceived to demonstrate a realistic 'final' design, that in a real implementation the transmitter would be miniaturised and implemented on a more efficient embedded platform, suitable for mounting on a $\mu$ROV. The implementation described in the following section is therefore solely designed for speed of construction and ease of testing.

### 5.3.1 Hardware Description: PC Interface Unit

Previous work carried out by the underwater communications group at Newcastle university has typically focussed on transmissions in much lower frequency bands, i.e. 8-16kHz or 7-15kHz. At these frequency ranges integrated sound cards can

be used to generate and record the relevant signals, with little if any loss in clarity. Sound cards are typically developed with high end 24-bit Analogue to Digital (ADC) and Digital to Analogue Converters (DAC), which are sampled at a frequencies of approximately 96kHz.

The limited ability to sample at higher frequencies, significantly restricts the ability to successfully generate or record transmissions in the 40-60kHz band. To ensure the Nyquist criteria is met, frequencies upto a maximum of 48kHz can typically be generated. In many cases this is further restricted by the upper cutoff frequency of the sound-cards input and output filters, often limiting the signal to upto 24kHz. Therefore, a bespoke hardware platform was developed to enable analogue waveforms to be streamed from a PC in real-time. The interface unit, offered continuous analogue signals to be generated and streamed at sample rates of upto 1MHz.

The interface unit consists of three sections of hardware: a USB interface; a microcontroller; a Digital to Analogue Converter (DAC); and an anti-imaging filter. A block diagram, demonstrating the interaction between each of the hardware stages is shown in Fig. 5.16.

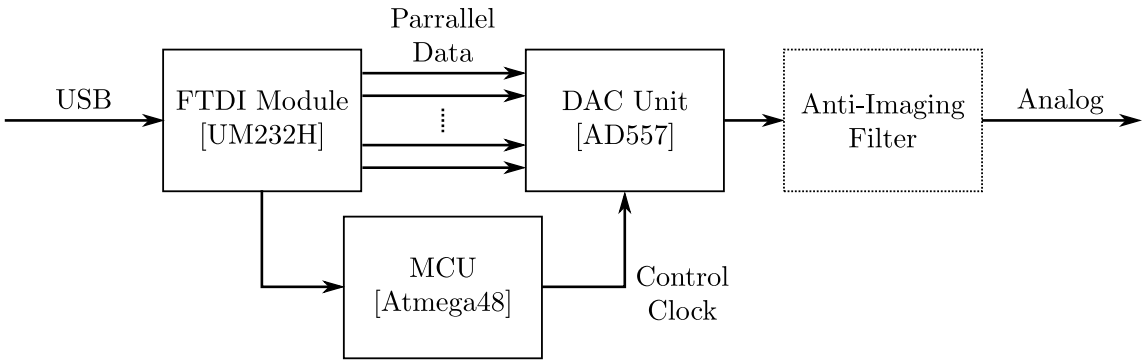


Figure 5.16: Hardware Block Diagram for Custom PC Transmission Interface Unit

New waveform data, generated by the PC, is streamed to the DAC unit via a USB 2.0 connection. The binary data is then converted into an analogue output level suitable for amplification and transmission through the underwater channel. Further information relating to each of the hardware components is given below:

1. USB Interface:
   The FTDI UM232H module is a USB development board offering hi-speed USB 2.0 to 8-bit parallel data bus at throughputs of upto 480Mbits/s [108]. Predefined drivers offer direct communication with the module at high throughputs, ensuring a transparent method of interfacing between the developed software and the rest of the hardware structure. A 1kByte First-In-First-Out (FIFO) buffer is used to queue incoming data streams, reducing the possibility of data being incorrectly transmitted during period of heavy processing.

2. Micro-Controller (MCU):
   A low power, 8-bit micro-controller was utilised to generate the required clock and control signals to the output DAC unit. Using this hardware configuration the firmware in the MCU could be adjusted to produce a range of output clock frequencies, enabling data to be transmitted from the DAC at rates of upto 1MHz. All transmissions shown in this work were generated at a 200kHz clock frequency.

3. Digital-to-Analogue Converter (DAC):
   An 8-bit DAC unit is utilised to convert the incoming binary data sequence, from the parallel data bus, into an analogue output waveform. The selected device, an Analogue Devices AD557, offered 8-bit resolution across a unipolar output range of 0 to 2.56V, when operating from a single ended 5V power supply. The component is accurately factory calibrated, removing the requirement for complex offset or trimming circuitry. Utilising 8-bit resolution the minimum precision was found to be approximately 10mV, ensuring minimal quantisation noise adequate for the transmissions of both QPSK and 16-QAM waveforms.

4. Anti-Imaging Filter:
   A low pass filter was utilised to suppress the affects of any high frequency harmonics generated by the sampling process. The 3dB half power cut-off frequency was selected at ≈67kHz, ensuring that any harmonics were successfully suppressed, while avoiding distortion of the in-band signal (40-60kHz). A schematic of the specified anti-imaging filter is presented in Fig. 5.19, combining: an input biasing circuit; a unity gain buffer; and a second order unity gain low pass filter. A Multiple Feedback (MFB) filter topology was selected over a Sallen-Key construction due to its low sensitivity to component variability.

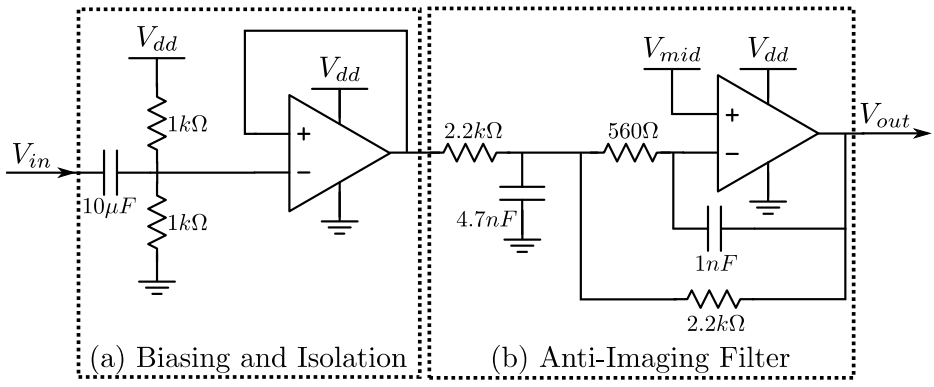


Figure 5.17: Transmit Anti-Imaging Filter

The overall hardware platform is developed to operate successfully from a single 5V power supply. This allows the system to be self powered from the USB port without the need for any external supplies. Additionally, the low current draw of the hardware meets the power budget of a single port ($< 500$mA), again minimising the complexity of the hardware design. An initial Printed Circuit Board (PCB) was developed, consisting of each of the hardware elements discussed. Each of the boards were enclosed in an IP67 enclosure to protect the electronics from any physical impact or water ingress during trials. An annotated photo of a prototype unit is shown in Fig. 5.18.

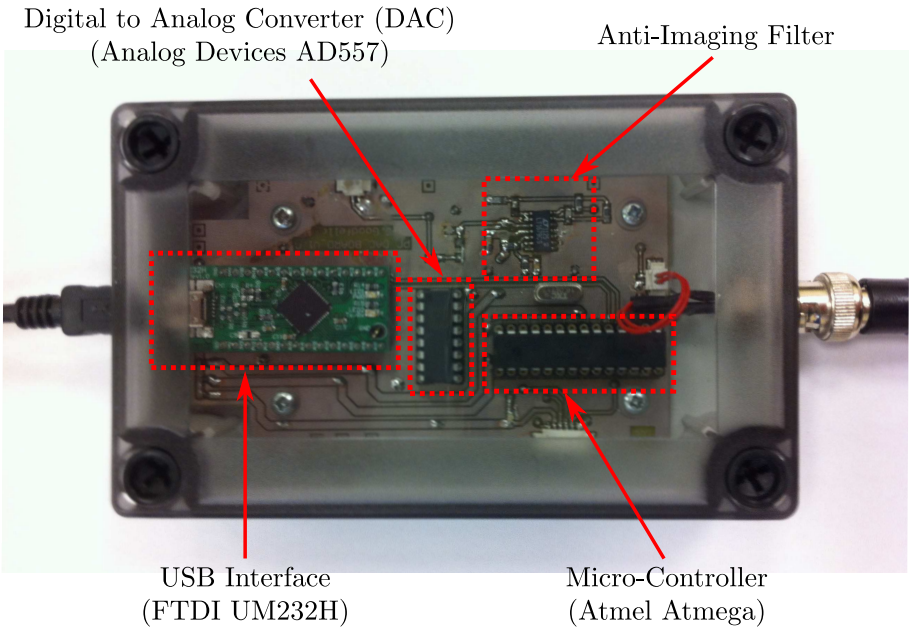


Figure 5.18: USB DAC Unit Hardware Construction

### 5.3.2 Software Requirements

In comparison to the receiver, the software used for generating and transmitting an acoustic packet is relatively simple. The transmitter is required to generate each packet in real-time based on the transmission parameters defined by the user, i.e. code rate, modulation scheme, etc. Once each packet has been constructed it is fed to the hardware interface unit, via USB, and converted into an analogue output signal. A polling process is required to ensure that data is not transmitted through USB at a rate which causes an overflow of the FIFO buffer.

In order to assess the performance of the proposed receiver, a Maximum-length Sequence (M-Sequence) was utilised as the packet payload. An M-sequence is a pseudo-random binary pattern, covering a periodic sequence of every $M$ length binary value. The statistical randomness of the sequence allows the performance

of the system to be examined for every given binary pattern. Through knowledge of the M-sequence at the receiver the number of incurred errors and the distribution across the length of the packet can be assessed.

An M-Sequence is typically generated using a Linear Feedback Shift Register (LFSR), with a known set of tap coefficients and an initial start criteria. The LFSR operates as a cyclic delay line, generating every possible sequence apart from a continuous zero vector. The simplicity of a LFSR is ideal in generating a basic transmitter structure, comprising of basic delay and addition blocks. In the discussed transmitter two separate LFSR are utilised: a 14 bit M-sequence for the packet payload; and a 9 bit M-sequence for the BPSK training sequence. Both of these binary patterns can be generated during initialisation, avoiding continuous re-calculation of the predetermined sequence for each packet.

In a practical scheme the binary test pattern would be replaced with information captured from an external sensor, such as a video camera or SONAR . In a typical communication scheme, this input stream is exclusively or'd (XOR) with a similar M-sequence to minimise the possibility of long runs of ones or zeros occurring. This technique is required to avoid the equaliser structure becoming unstable due to the lack of symbol state information conveyed.

To enable a continuous stream of packets to be generated a double buffering structure is proposed. This approach utilises one buffer to prepare the next packet, while the other buffer is used to store the data being streamed to the hardware unit. This approach ensures that neither buffer over-run, i.e. a packet being overwritten prior to transmission, or buffer under-run, i.e. the transmission ceases as no new data is available, occur. Two threads are utilised to replicate these operations: the first to prepare new packets, based on the instantaneous transmission parameters; and the second to control the interface with the hardware module. A flow diagram of the software structure is shown in Fig. 5.19, demonstrating the use of two separate threads for the generation and transmission of new packet data.

The overall system can be seen to be composed of three sections of code: the first operating once at start-up; and the other two operating continuously in separate threads during run-time. An overview of the different sections of code is given below, describing the operations performed by each.

#### 5.3.2.1 Initialisation

To reduce the computational complexity of the system during run time many of the repeatable mathematical operations are extracted and performed during initialisation, storing the values in lookup tables or predefined arrays. By removing such operations and performing them once at start-up considerably improves the

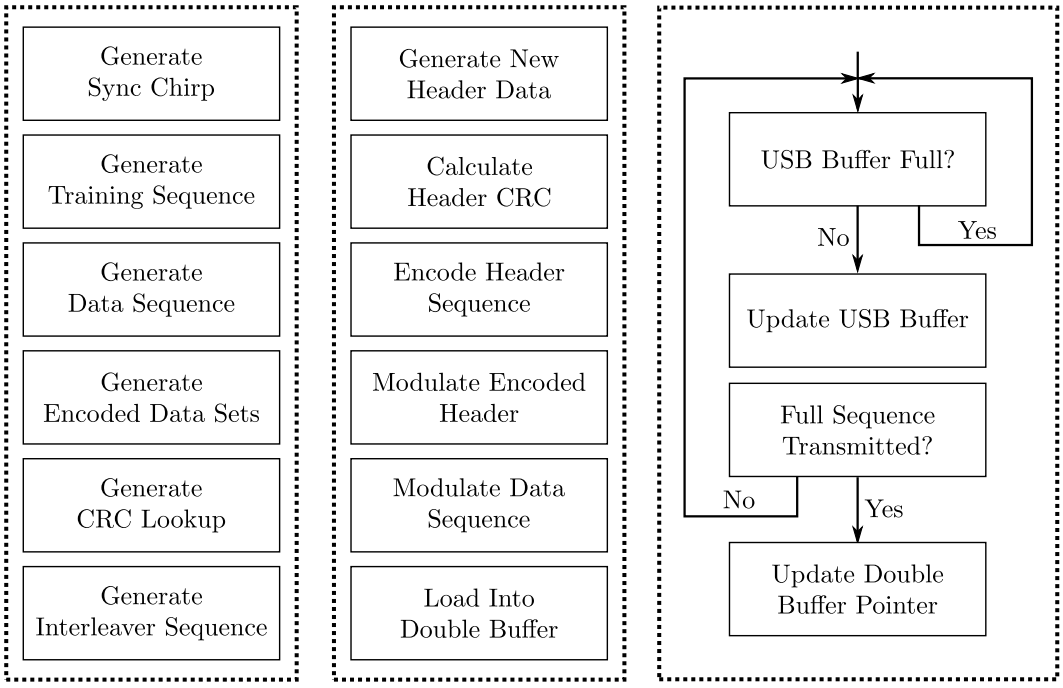


Figure 5.19: Real-Time Transmitter Software Structure

efficiency of the system. In the case of an embedded system, where the amount of memory is restricted, the generation of substantial lookup tables may not be feasible. However, in a PC based system where memory is more freely available, the generation of large numbers of constant variables results in limited compromise. The initialisation code generates sections of the packet which are static across all transmissions, including: the synchronisation chirp samples; the training sequence; the encoded data set; the interleaver vectors; and the CRC lookup tables.

#### 5.3.2.2 Thread 1: Signal Generation

The first thread is used to generate each individual packet prior to transmission through the UAC. Although some of the data is generated during initialisation, large proportions of the payload and header information are selected by the user during run-time. This thread encodes and modulates the payload data based on the parameters input by the user, or from feedback from the receiver. Additionally, information relating to the individual packet configuration is compacted and formatted such that it can be appended to the start of the packet. Once the packet has been fully constructed it is loaded into one of the double buffers and a flag is raised to indicate that new information is ready for transmission.

#### 5.3.2.3 Thread 2: Signal Transmission

The second thread controls the rate that new packet data is relayed to the hardware DAC unit. As discussed previously without monitoring the state of the FIFO buffer, the transmission of new binary data can result in a buffer over-run and the related loss of valuable sample information. Therefore, this thread monitors the state of the FIFO buffer, and where space is available loads new packet information to the hardware platform. The double buffer configuration is also primarily controlled by this thread: updating the pointer to the next packet transmission; and identifying the next buffer to be used by the signal generation thread.

#### 5.3.2.4 Thread Execution

To avoid the possibility of dead locks a message handling structure is implemented to indicate the completion of a packet being generated and transmitted. The message handling structure is used to avoid the same buffer location being accessed by both the generation and transmission threads simultaneously. Such an event could result in the overwriting of data or the transmission of an invalid packet. In the worst case scenario the system could end up in a dead-lock situation, with the system crashing or freezing due to simultaneous access of the same memory location.

The message handling structure utilises a pair of flags to indicate: when new data is available; and when the buffers content has been transmitted. New packet data will only be generated, and loaded into the specified buffer, if its 'packet transmitted' flag is raised. Once a new packet has been produced and the 'new data' flag raised, the second thread will begin to transmit the binary data sequence through the USB connection. Through careful monitoring and selection of the two status flags, dead locks and data loss can be avoided.

## 5.4 Summary

Based on the findings of experimental work presented previously, this chapter explores the design and implementation of a multi-channel receiver structure. An examination of suitable synchronisation, equalisation and soft decoding blocks is conducted, highlighting optimum techniques in terms of performance and computational complexity. A description is given of the receiver hardware, giving insight into the design considerations and construction techniques of a bespoke multi element receiver. An overview of the software implementation is given, demonstrating suitable optimisation and threading techniques to ensure real-time performance. Benchmarked timings demonstrate the ability to perform a maximum of 2 outer

and 3 inner iterations of both QPSK and 16-QAM transmissions. Finally the development of a software based transmitter is presented which enables continuous transmissions of real-time data for testing and validation purposes.

# Chapter 6

# Development of a Full Duplex Link

This chapter focuses on the development of a asymmetric full-duplex communication link, capable of supporting simultaneous transmissions of uplink sensor readings and downlink control information. A thorough analysis of the various communication challenges are highlighted, evaluating the complications faced in avoiding receiver saturation caused by the '*near-far*' problem. Results are presented demonstrating the performance of the full-duplex structure at simulated ranges of 150 and 250m.

## 6.1 Transmission Multiplexing

Various multiplexing techniques have previously been presented in order to enable bidirectional or multi-user transmissions across a shared communication channel. Each approach can typically be described as being capable of supporting either half-duplex or full-duplex transmissions.

### 6.1.1 Half Duplex Communications

The term half-duplex, refers to the ability to support the bi-directional transfer of information, without being able to support simultaneous transmission. A typical approach, in a bandwidth constrained channel, is to divide the total frame duration, $T_f$, into, $K$, non-overlapping time intervals of duration $T_f/K$. Each user, or communication link, is assigned a specific time slot within the frame, ensuring complete isolation between transmissions. This approach is typically referred to as Time Division Multiple Access (TDMA) [59].

Since time separation is used to isolate the independent streams, this technique is shown to be incapable of supporting long periods of continuous transmission. Additionally, silent guard periods are typically inserted between the time slots to minimise interference. In the case of long reverberant channels, such as the UAC,

the duration of the guard period, $T_g$, can far exceed the length of the transmission period, i.e. $T_g \gg T_f/K$, having a catastrophic effect on the overall throughput of the system and the incurred propagation delay.

### 6.1.2 Full Duplex Communications

A full-duplex approach enables bi-directional transmissions to occur simultaneously, i.e. without the incurred time separation observed with TDMA. When utilising a single common channel, a typical approach is to divide the available bandwidth into a number of non-overlapping sub-bands. In a similar way to TDMA, each user or communication link is assigned an individual frequency band, ensuring isolation from other concurrent transmissions. This method is generally known as Frequency Division Multiple Access (FDMA) [59].

### 6.1.3 Overview

An illustrative representation of the two multiplexing techniques, FDMA and TDMA, for a single user bidirectional communication network are shown in Fig. 6.1. The first sub-plot, (a), demonstrates a half-duplex TDMA protocol, utilising a single frequency band and separate time allocations to isolate the *'uplink'* and *'downlink'* transmissions. The second sub-plot, (b), demonstrates a full-duplex FDMA approach, where the full bandwidth is divided into two sub-bands, $f_{l1} - f_{h1}$ and $f_{l2} - f_{h2}$.

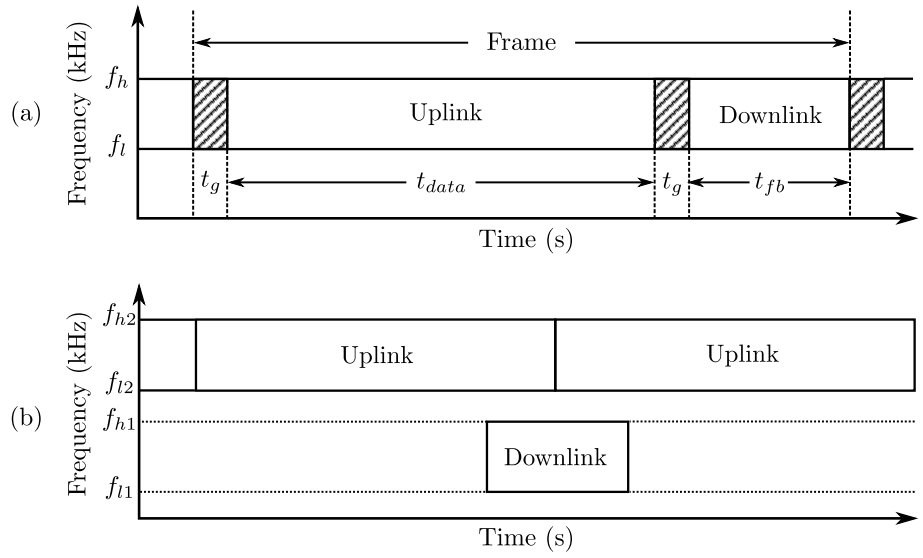


Figure 6.1: Comparison of (a) Half Duplex, Time Division Multiple Access (TDMA), and (b) Full Duplex, Frequency Division Multiple Access (FDMA)

TDMA can be used, along with powerful control protocols, to enable bi-directional transmissions of control data and video imagery. However, such schemes require pre-scheduled time slots, or adaptive schedulers, to avoid transmission within the same time period. Such scheduling will cause an increase in latency, resulting in a lag to the visual imagery, and more seriously, a delay in control, which could accumulate with unstable movement of the vehicle. The benefits of a full-duplex approach is therefore immediately evident: supporting increased data throughput, due to reduced packet overhead; and offering reduced transmission latency, caused by the TDMA scheduling process. In the discussed application, the limited ability to support continuous transmissions heavily affects the ability to stream video or SONAR images to the surface. Additionally, the scheduling delay incurred by TDMA, results in a degradation in the real-time control of the vehicle.

The use of FDMA is uncommon in the UAC, having been rarely discussed or presented in previous literature. The limited bandwidth available in the UAC considerably restricts the spacing of each independent sub-band, especially when operating over long transmission ranges, $>$ 1km. Although FDMA has been shown to be a reliable technique for the RF band, the reduced bandwidth of the acoustic spectrum has considerably restricted its mainstream use subsea. Some individual areas of niche research have shown preliminary results from FDMA experimentation [109] [110]. However, limited practical testing has been conducted, giving minimal indication of the systems realistic performance.

Although, the UAC is typically believed to be restricted to half duplex operations, the limited transmission range of the application and therefore the increase in usable bandwidth, has lead the author to believe the channel described would be capable of supporting reliable full duplex, FDMA communications. Previous results have indicated feasible high data uplink transmissions around a centre frequency of 50kHz, highlighting the availability of lower frequency bands for simultaneous downlink transmissions.

### 6.1.4 Full Duplex Message Analysis

Prior to investigating the performance of the proposed full-duplex scheme the requirements of the two transmission channels must be examined. To enable realistic tether-less operation of the $\mu$ROV two simultaneous links are proposed: the *'uplink'* between the vehicle and the surface; and the *'downlink'* for relaying information to the vehicle.

#### 6.1.4.1 Downlink Transmissions

The low data rate downlink is utilised for two primary functions:

1. **Transmission of Control Information:**
   *To enable the platform to be used in a semi-autonomous fashion, the downlink is used to relay new control data and task objectives during deployment. Unlike a typical ROV deployment, the data payload will specify the vehicles position or depth, rather than detailed 'fly-by-wire' commands. This approach reduces the duration and regularity of the downlink transmissions.*

2. **Signalling of Adaptive Communication State Information:**
   *To ensure reliable uplink transmissions the use of an adaptive communication protocol is proposed. In order to 'close the loop' and supply feedback information to the uplink transmitter a reliable return path is required. The transmitted state information, indicates the requirement for the communication parameters to change, and therefore is only relayed if significant changes to the channel conditions are observed.*

In both cases the generated data set can be seen to occupy a very short period, with effective compression techniques enabling the payload to typically occupy less than a couple of bytes. An important attribute of the downlink is its ability to operate with minimal packet errors across a very hostile channel. The content of the transmitted messages is critical to the reliable operation of the vehicle, therefore, the downlink must be capable of operating at very low signal levels and in the presence of high amounts of background noise and interference. The loss of downlink communications could result in catastrophic effects, with possible loss of vehicle control and in the worst case scenario the $\mu$ROV not returning to the surface or designated base station.

To ensure the tolerance of the communication link a low data rate Chirp Spread Spectrum (CSS) system is proposed. As discussed in Section 3.1.2, the reduced spectral diversity enables the proposed system to operate at very low SNR's, tolerating both severe multipath and Doppler effects. Additionally, when considering the constrained dimensions of the $\mu$ROV, a benefit of the CSS downlink is shown to be the ability to operate successfully utilising a small single element receiver.

#### 6.1.4.2 Uplink Transmissions

In the discussed application, the uplink is utilised to transfer data captured from the sensor payloads attached to the vehicle. This information typically comes in the form of a video stream, SONAR imagery, or environmental sensor data. The acquired information enables the surface operator to monitor the status of the vehicle, and unlike in a standard AUV, adjust the pre-defined operation plan to account for observations made during deployment.

To allow continuous visualisation of the surrounding area, a high data rate communication link is required. Even after the use of highly efficient video compression techniques, the generated data stream will require a throughput in excess of 20kbps in order to support real-time streaming [111] [41]. In contrast to the data relayed by the downlink, a loss in packet integrity may result in the video stream becoming distorted, or in the worst case unusable, but will not affect the vehicle's primary operation. Therefore, a slight reduction in link integrity is believed to be acceptable during periods of severe channel distortion, with the repercussions resulting in slight disturbance to the video feed, but no prolonged complications.

Based on the presented requirements and the results achieved previously, the single carrier scheme, developed in Chapter 3 and 4, is believed to be suitable for uplink transmission of video or SONAR data. The ability for the developed multi element DFE-BICM-ID to operate reliably through typical shallow water channels emphasises the selection, achieving data rates in the region of 30-40kbps.

#### 6.1.4.3 Overview

| | SNR* | Data Rate | Application |
|---|---|---|---|
| Downlink | 0dB | $\approx$ 100bps | • Vehicle Control Signals<br>• AMC Control Signals |
| Uplink | 10dB | $>$ 30kbps | • Video and Sonar Footage<br>• Sensor Readings |

Table 6.1: Comparison of the Uplink and Downlink Communication Requirements
(∗) SNR Denotes the Intended Worst Case Operating Environment

The asymmetric transmission scheme proposed for use within the discussed application reflects well within an FDMA transmission scheme: utilising a lower frequency band to ensure high integrity of the control messages transmitted through the downlink; and a higher frequency band for the high data rate uplink transmissions. The use of lower frequencies, 8-16kHz, ensures a reduced effect from absorption loss, and thus increased reliability over greater transmission ranges. Alternatively, the increased bandwidth of the 40-60kHz band enables greater data rates.

## 6.2 The *'Near-Far'* Problem

A considerable limitation on the ability to operate in a full-duplex manner is the saturation of the near end receiver. The minimal transmission loss between the near

end transducers results in the received input signal featuring a very high amplitude out of band component. The magnitude of the acoustic waveform causes the receiver hardware to become saturated, causing clipping and loss of information relating to the far end transmission.

When examining the geometry of the transmitter receiver pairings used in the $\mu$ROV application, the implications of near end saturation becomes even more apparent. Due to the physical constraints of the vehicles dimensions, minimal separation between the lower end transducers is possible. The limited spacing between the elements can be seen to exaggerate the problem constricting the ability to manually space the transducers in such a way as to reduce the *'near-far'* effect. The physical constraints of the envisaged acoustically operated ROV deployment is shown in Fig. 6.2. The diagram shows a $\mu$ROV, with two acoustic transducers positioned such that the maximum physical separation is achieved, $R_2$. The vehicle is operated over a range of $R_3$ metres from the surface craft or structure. The surface elements are spaced vertically in the water column, with a separation of $R_1$ metres.

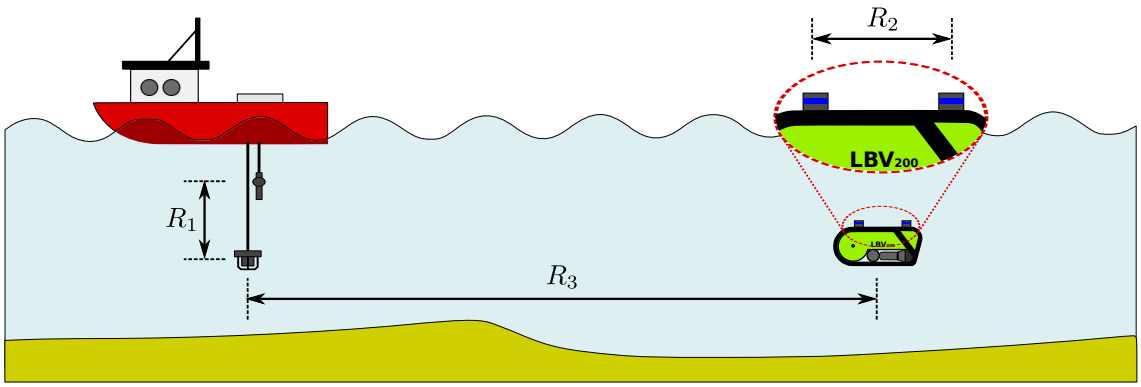


Figure 6.2: Illustration of the *'Near-Far'* Problem
$R_1$: Seperation Between Surface Transducers ($rx_{hf}$ and $tx_{lf}$)
$R_2$: Seperation Between Subsea Transducers ($rx_{lf}$ and $tx_{hf}$)
$R_3$: Operational Range

#### 6.2.0.4 Physical Channel Evaluation

It can be considered that the separation between the transducers is considerably less than the transmission range between the ROV and surface vessel, i.e. $R_1 < R_3$ and $R_2 < R_3$. In a typical application the following assumptions can be made:

- The typical operational range, $R_3$ of a standard $\mu$ROV is limited to a range of approximately 250m due to manageable tether deployment. Although most applications require shorter ranges, in the region of less than 50 to 100m, a

worst case scenario of 250m will be considered. The operating environment is also considered fully omnidirectional, as complete navigational freedom is vital to the vehicles operation.

- The physical dimensions of the vehicle considerably restrict the separation of the low frequency receiver, $rx_{lf}$, and the high frequency transmitter, $tx_{hf}$. Micro-ROV dimensions are typically of the order of $< 0.5$m, the separation, $R_2$, is therefore limited to approximately 0.3m. Positioning of transducers is further restricted by the location of other highly interfering noise sources, such as thrusters and imaging SONAR . Careful selection of suitable mounting positions is therefore essential to minimise interference from both out of band communications and self made noise.

- The positioning of the surface transducers, $rx_{hf}$ and $tx_{lf}$, is considerably less constrained, enabling increased separation and thus reduced cross band interference. Limitations on the spacing of the transducers is still restricted to an extent by the depth of the channel and the length of the surface vessel. In this research the configuration considered will be a vertical separation of approximately 1m. Such a separation will be practical in most typical applications, allowing for easy deployment while maximising transducer isolation.

A summary of the predicted channel separations for a typical $\mu$ROV application are presented in Table 6.2. For the remainder of the evaluation carried out in this chapter these channel characteristics will be assumed.

| | Maximum | Typical | Description | |
|---|---|---|---|---|
| $R_1$ | $\approx$ 5m | 1m | Surface Seperation | $rx_{hf}$ to $tx_{lf}$ |
| $R_2$ | $\approx$ 0.5m | 0.3m | Subsea Seperation | $rx_{lf}$ to $tx_{hf}$ |
| $R_3$ | 300m | 100m | Transmission Range | $rx_{lf}$ to $tx_{lf}$<br>$rx_{hf}$ to $tx_{hf}$ |

Table 6.2: Evaluation of Realistic $\mu$ROV Channel Separation

### 6.2.1 Acoustic Solutions

One of the proposed methods of isolating the two transmission paths is to acoustically shield the transducers or to use highly directional transducers. Through shielding or *'baffling'* of the hydrophone the unwanted transmission can be suppressed, reducing the possibility of saturation. However, this approach can be seen to be impractical due to the dynamic nature of the vehicle and the requirement

for the link to continue to operate in all directions and depths around the surface vessel. Omnidirectional transducers are therefore essential, to ensure uninterrupted operation.

An alternative approach is to utilise mechanical steering to focus a narrow beam in the direction of the far end receiver. In the discussed application, this technique is again seen to be impractical with the dynamic nature of the vehicle making it very hard to track the position of the $\mu$ROV in real time, thus making it difficult to accurately steer the beam. Additionally, the use of mechanical parts subsea presents a maintenance issue, due to the stresses and strains of working in such an environment often resulting in breakages and thus long periods of system downtime.

### 6.2.2 Passive Filtering

Passive filters are proposed to reduce the dynamic range of the input signal, suppressing the effects of any out of band *'near'* end transmissions and, in doing so, reduce the overall peak signal level. By attenuating the out of band interference, an ADC with a reduced voltage range can be used to acquire the incoming waveform, enabling higher sampling precision to be achieved.

Simple lowpass and highpass filters are utilised at the downlink and uplink receivers respectively, allowing the two frequency multiplexed streams to be isolated prior to being sampled and demodulated. To enable optimum performance it is preferable to insert the passive filters as close to the hydrophone as possible, ensuring any cross band interference is sufficiently suppressed prior to further stages of active filtering or amplification. To ensure minimal deviation from the ideal filter response, component values must be selected such that they are dominant to the internal parasitic values of the piezo-electric transducer element.

The use of simple Inductor-Capacitor (LC) filters are proposed in this work, due to the improved roll off when compared with an equivalent RC configuration. Additionally, an ideal LC filter has very little resistance, allowing circuits to be constructed with very low levels of attenuation across the operational pass band.

Utilising the approach described by Hagen [112], the values of the reactive filter components can be selected based on a scaling of the normalised filter values, found in the tables generated by Matthaei *et al.* [113]. The capacitor and inductor values for a lowpass filter are calculated utilising (6.1), where, $C_n$ and $L_n$ are the normalised prototype values, $R_L$ is the load resistance, and $f_{3dB}$ is the half power cut-off frequency. For a simple second order filter the normalised filter values are $C_n = L_n = \sqrt{2}$.

$$C_{lp} = \frac{C_n}{(2\pi f_{3dB})R_L} \qquad L_{lp} = \frac{L_n R_L}{(2\pi f_{3dB})} \tag{6.1}$$

A low pass filter can be easily amended into a high pass configuration by exchanging inductors with capacitors and vice-versa. In this case the values of the capacitors and inductors are calculated as their reciprocal values, as demonstrated in (6.2).

$$C_{hp} = \frac{1}{L_{lp}} \qquad L_{hp} = \frac{1}{C_{lp}} \tag{6.2}$$

#### 6.2.2.1 Filter Shape

A Butterworth filter was selected, exhibiting a maximally flat response and a linear phase response across the utilised passband. The response of the Butterworth filter configuration can be expressed in the form (6.3), where: $f_{3db}$ is the cutoff frequency of the filter; $f$ is the frequency of the input signal; $n$ is the order of the filter; and $V_{\text{in}}$ and $V_{\text{out}}$ are the input and output voltages respectively.

$$\left|\frac{V_{\text{out}}}{V_{\text{in}}}\right|^2 = \frac{1}{1 + (f/f_{3db})^{2n}} \tag{6.3}$$

In comparison to other forms of filter design, such as the Chebyshev Type I and Type II, the Butterworth filter is shown to have a significantly slower roll off, often requiring higher order filter configurations to meet the applications requirements. The Chebyshev filters are often favoured due to their similarity to an idealised filter, however, the incurred ripple across the passband can result in irregular performance. Although the Butterworth filter is seen to have a limited roll off, the benefits of a flat passband and linear phase response are thought to be essential, to ensure minimal distortion of the in-band transmission.

#### 6.2.2.2 Higher Order Filters

Ideally, to reduce the size of the guard band and to maximise the frequency bandwidth of each link , a filter with an idealised *'brick wall'* response would be favoured. Therefore the slow roll-off of a low order Butterworth filter can be seen to be a major constraint of the system. Using higher order filters, the roll off of the filter can be considerably improved.

A comparison of the simulated frequency response for a simple highpass Butterworth filter is shown in Fig. 6.3a. The plot demonstrates the response for varying orders of filter, from second order through to fifth. The improved roll off for higher order filters is apparent, with an $n^{\text{th}}$ order filter offering a roll off of $20n$ dB/decade.

However, the limitation of higher order filters is apparent through examination of the phase response shown in Fig. 6.3b. An increase in the filter order, results in a considerable increase in phase shift variation.

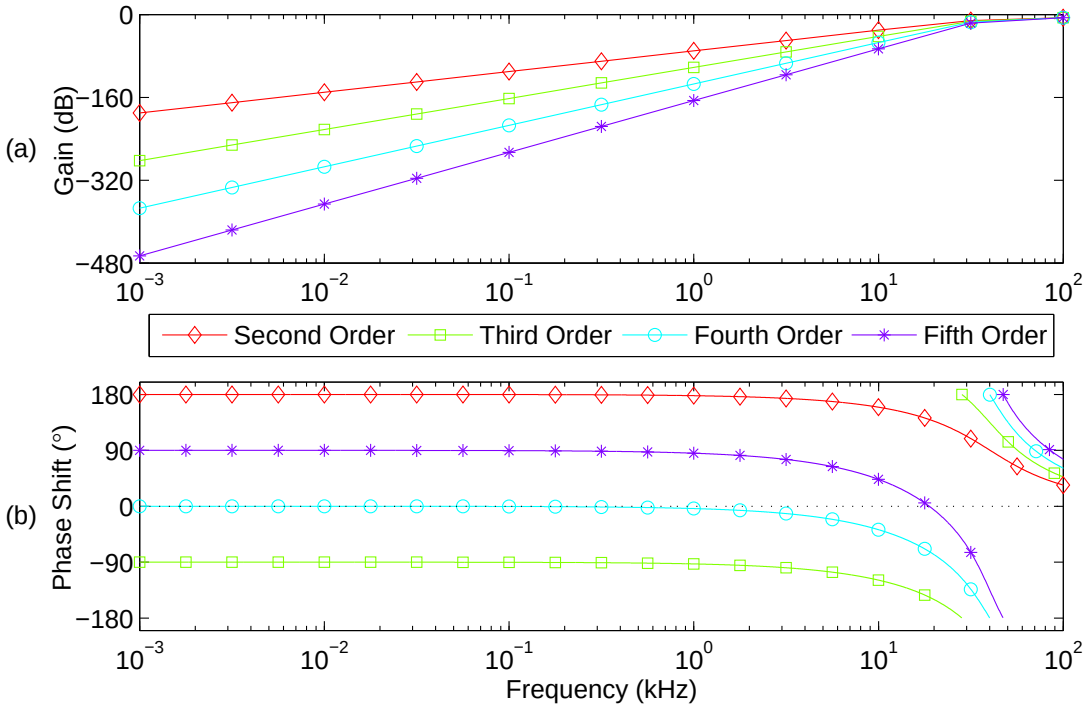


Figure 6.3: Comparison of High Order LC Passive Filters: (a) Gain and (b) Phase Distortion

Utilising the discussed communication schemes, information is typically portrayed through a variation in the phase of the signal. Therefore it is critical to minimise the phase distortion across the operational transmission band. The increased phase shift when utilising higher order filters, can be believed to have a severe detrimental effect on the performance of the system. Therefore, despite the reduction in available bandwidth, the remainder of this work will consider a $2^{nd}$ order single stage LC Butterworth filter.

### 6.2.3 Digital Filtering

Alongside passive filtering techniques, the use of digital filtering is proposed to further reduce the incurred cross band interference. Although digital techniques cannot be used to overcome the receiver saturation effects, they can be used to further improve the receivers performance by suppressing any out of band interference, whether self-made or naturally occurring.

#### 6.2.3.1 Finite Impulse Response (FIR)

High order digital Finite Impulse Response (FIR) filters can be designed to suppress the content of any out of band transmissions. Additionally, through careful selection of the bandpass cut-off frequencies, any other interference such as thruster noise or natural background noise may be rejected.

Although FIR filters can be shown to significantly improve the quality of the processed signal, it should be noted that due to the *'near-far'* problem they cannot be used in isolation. Therefore, the use of both passive filtering and digital FIR filters are shown to offer an ideal solution; the first stage reducing the dynamic range of the signal prior to sampling, and FIR filtering.

#### 6.2.3.2 Adaptive Noise Cancellation

Since the near end transmission is known *a priori* by the receiver, the use of adaptive noise cancellation has been proposed. Utilising a similar adaptive filter structure to the DFE and through knowledge of the near end interference signal, the out of band transmission can be adaptively isolated from the received signal. Such techniques have previously been explored for the removal of feedback or the isolation of a single artefact from within a digital recording [114] [115]. A block diagram of a typical adaptive noise cancellation structure is shown in Fig. 6.4, where, $s(t)$ is the original *'far'* end transmission and $n(t)$ is the local *'near'* end noise transmission.

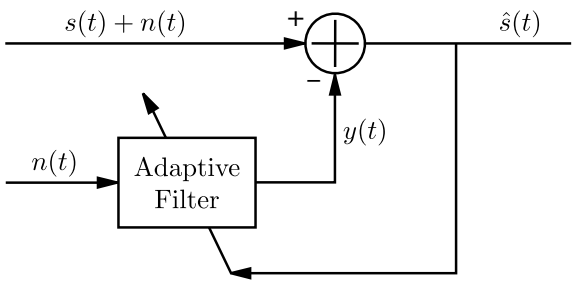


Figure 6.4: Adaptive Noise Cancellation Structure

A limiting factor on the use of noise cancellation techniques, is the duration of the delay spread exhibited by the shallow water channel. In order to successfully remove the effect of the near end transmission, the filter must be able to span the duration of all conflicting arrivals. Within the constrained shallow water environment, the time-spread of the local noise signal may span several thousands of consecutive symbol. Therefore, although this technique is capable of suppressing the initial local transmission, unrealistic filter lengths would be required to cancel the delayed replicas of the signal, created by the signal being internally reflected by the channel boundaries.

Additionally, although the reflected near end transmission will have incurred considerable transmission loss, in many cases the magnitude will still be far greater than that of the far end transmission. Therefore, if the full delay spread is not considered, the secondary reflections will cause considerable interference on the far-end signal. For this reason, the use of adaptive noise cancellation is considered unsuitable for isolating the two concurrent signal transmissions.

## 6.3 Controlled Experimentation

To practically examine the performance of a full-duplex system, a set of controlled experiments were conducted in the anechoic test tank at Newcastle University. The controlled environment ensured the repeatability of the tests and isolated the effects of multipath, Doppler and background ambient noise. The experiments examined the ability to overcome the *'near-far'* problem, utilising a combination of analogue LC filters and digital FIR filters to isolate the two concurrent transmission bands.

The experimental hardware structure for the high frequency uplink receiver is presented in Fig. 6.5. Although a 4-element beamformer has previously been recommended, due to the simplified channel conditions and to reduce the hardware complexity, the tests were conducted utilising a single element receiver. The hardware is presented in three stages: the hydrophone receiver, and pre-amplifier; a highpass passive filtering stage; and a final stage of filtering and amplification.

The single element receiver used for these tests was a Reson TC4032, offering a flat operational band between 5Hz and 120kHz. As previously discussed this hydrophone offers near omni-directional performance in both the horizontal and vertical plane. In an ideal scenario the LC passive filters would be connected as close to the ceramic element as possible. However, since the TC4032 incorporates an integral 10dB pre-amplifier within the hydrophone construction this was not feasible.

Post amplification, the signal is sampled at 200kHz utilising a 12-bit Handyscope HS4 ADC unit. Block captures of the sampled waveform are stored as a binary file and post processed in Matlab. The receiver code parses the recorded data set and applies further digital FIR filtering prior to demodulation and equalisation. A breakdown of the receiver parameters are given in Table 6.3.

Since spread spectrum schemes have previously been shown to be operational at very low SNR levels, i.e. SNR = 0dB, the system is believed to be restricted by the less reliable high data rate, single carrier, communication link. Therefore, the presented results predominately focus on the isolation and demodulation of the high frequency, uplink transmissions.

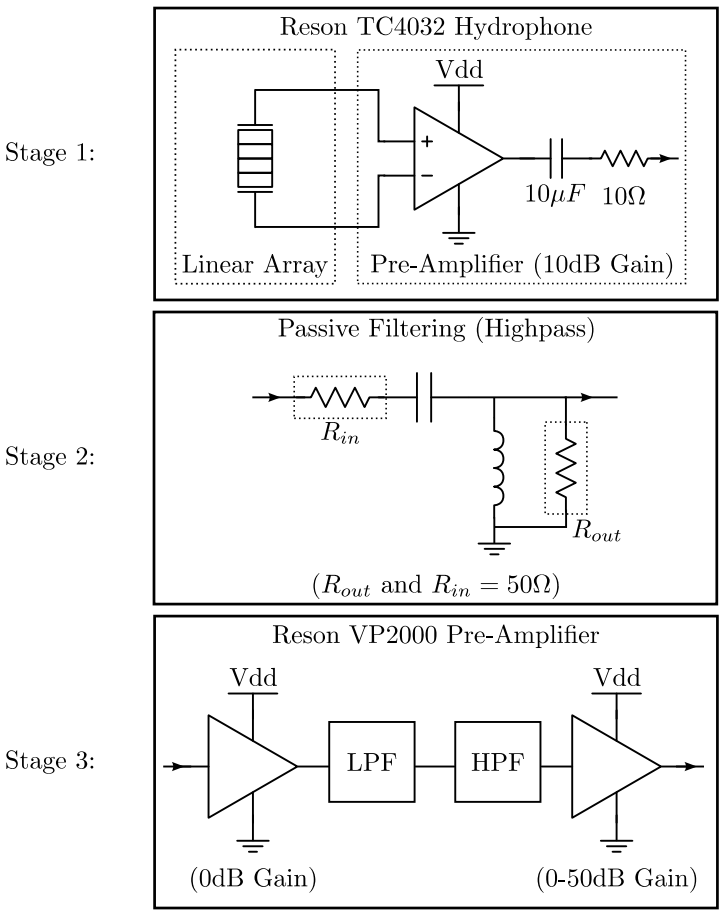


Figure 6.5: Experimental Hardware Configuration for Uplink Receiver
Stage 1: Reson Hydrophone with Amplifier (10dB)
Stage 2: Highpass LC Passive Filtering
Stage 3: Reson Bandpass Filter and Amplifier

| Stage | Characteristic | |
|---|---|---|
| 1 | Pre-Amp Gain | 10dB |
| 2 | Highpass Cutoff ($f_c$) | 40kHz |
| 3 | Amplifier Gain | 10dB |
| 3 | Highpass Cutoff ($f_{high}$) | 25kHz |
| 3 | Lowpass Cutoff ($f_{low}$) | 100kHz |
| ADC | Precision | 12-bit |
| ADC | Sampling Frequency ($f_s$) | 200kHz |
| ADC | Full Scale Range | 20V |

Table 6.3: High Frequency (Uplink) Receiver Characteristics

### 6.3.1 Channel Model

Due to the limited size of the anechoic test tank, the separation between the receiver and transmitter are severely constrained. Therefore, to replicate a realistic transmission loss the source level of the far end, high frequency, transmitter was reduced. By scaling the transmit power the experiment simulated the '*near-far*' effect of a much longer channel. To calculate the correct scaled transmit power we must consider the SONAR equations:

Assuming spherical spreading the estimated transmission loss, TL, through the channel can be calculated as (6.4), where, $\alpha$ defines the absorption coefficient and $R$ is the transmission range. Additionally, the source level, SL, of the generated acoustic wave can be calculated using (6.5), where, TVR expresses the transmit voltage response of the transducer, and $V_{\text{rms}}$ defines the RMS drive voltage applied to the element.

$$\text{TL} = 20\log_{10}(R) + \alpha R \tag{6.4}$$

$$\text{SL} = 20\log_{10}(V_{\text{rms}}) + \text{TVR} \tag{6.5}$$

Through rearrangement of the two SONAR equations, the scaled voltage output of the '*far*' end transmitter can be calculated, as given by (6.6). In this scenario, $R_{\text{sim}}$ refers to the simulated range, and $R_{\text{actual}}$ refers to the actual spacing between the receiver and the far end transducer. Similarly, $V_{\text{sim}}$ and $V_{\text{actual}}$ refer to the simulated and actual voltage applied to the far end transducer. In the case of the proposed tests the following values are applied: $V_{\text{sim}} = 10V_{\text{rms}}$ and $R_{\text{sim}} = 2\text{m}$.

$$V_{\text{actual}} = 10^{\frac{20\log_{10}(V_{\text{sim}}) - (20\log_{10}(R_{\text{sim}}) - 20\log_{10}(R_{\text{actual}})) + \alpha R_{\text{sim}}}{20}} \tag{6.6}$$

Table 6.4 presents a selection of suitable scaled voltage levels, for distances from 25m to the maximum operational range of a $\mu$ROV, i.e. 250m.

### 6.3.2 Full Duplex Results

Utilising the structure defined previously, testing was carried out utilising parallel QPSK uplink transmission and spread spectrum LFM downlink transmissions. The QPSK waveform occupied the 40-60kHz band and was tested with no Forward Error Correction (FEC). The uplink was therefore shown to be capable of supporting a continuous data rate of approximately 32kbps pre coding. The downlink transmission, in the 8 to 16kHz band, utilised Binary Orthogonal Keying. Each chirp

| Range $[R_{\text{sim}}]$ | Spreading Loss $[20\log_{10}(R_{\text{sim}})]$ | Absorption Loss $[\alpha R]$ | Output Voltage $[V_{\text{actual}}]$ |
|---|---|---|---|
| 25m | 27.96 dB | 0.3 dB | 772mV |
| 50m | 33.98 dB | 0.6 dB | 373mV |
| 100m | 40 dB | 1.25 dB | 173mV |
| 200m | 46.02 dB | 2.50 dB | 75mV |
| 250m | 47.95 dB | 3.12 dB | 56mV |

Table 6.4: Calculated Transmission Power to Simulate Different Operating Ranges [Far End Tx @ $10V_{pkpk}$], Absorption Loss Calculated Using Fisher and Simmons Estimation with the Following Parameters:
Temperature 10°C, Depth 50m, Salinity 35ppt, Acidity 8.

occupied a 10ms time slot enabling throughputs of approximately 100bps, prior to any overhead.

For the purposes of testing, each uplink packet was composed of a 4064 bit pseudo random PN-sequence. Each packet occupied a period of approximately 150ms including additional overheads, such as a 500 symbol BPSK training sequence and 20ms synchronisation chirp. The downlink transmission consisted of an alternating pattern of '1's and '0's, generating a sequence of alternating up and down chirps.

Two results are presented: the first, shown in Fig. 6.6, represents a simulated range of 150m; and the second, shown in Fig. 6.7, represents the maximum simulated range of 250m. For each data set, comparative results are shown for the performance of the system with and without passive filtering. At both 150m and 250m the system is shown to operate successfully when utilising passive filtering achieving 0 bit errors.

Although the output IQ plot for the unfiltered input signal, Fig. 6.6e, appears to converge on four distinct constellation points, this is in fact caused by the DFE structure going into limit cycles. This effect is caused by the saturation of the receive hardware, resulting in the system failing to converge, or diverging away from the correct output sequence while operating in decision directed mode.

Comparing the Power Spectrum Density (PSD) plot for the two signal inputs, filtered and unfiltered, the reduction in dynamic range caused by the passive filtering process is evident. In the unfiltered case, Fig. 6.7d, the spectrum shows minimal energy to be focused within the uplink band (40-60kHz), with the majority of the received signal appearing across the frequency band of the downlink transmission (8-16kHz). Any transmission made across the uplink is therefore seen to appear below the background noise level, making the packets impossible to accurately detect and demodulate.

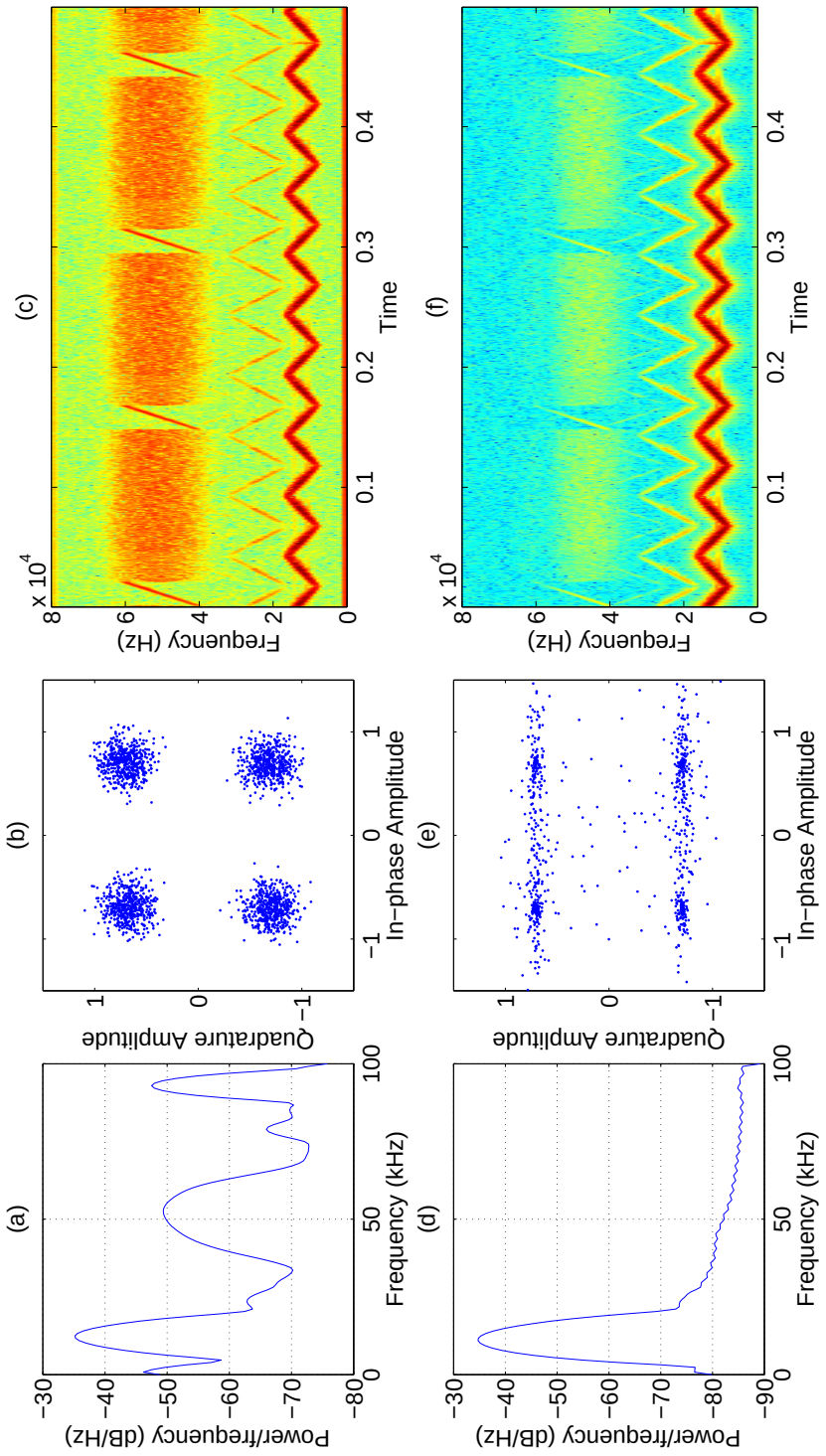


Figure 6.6: Single Carrier Demodulator Output for a Simulated 150m Channel Filtered Receive Signal: (a) PSD (b) I-Q Plot, (c) Spectrogram, (0 Errors / 4064 Bits, Pre. Correction), SINR = 14.68dB, Non-Filtered Receive Signal: (d) PSD (e) I-Q Plot, (f) Spectrogram, (1991 Errors / 4064 Bits, Pre. Correction)

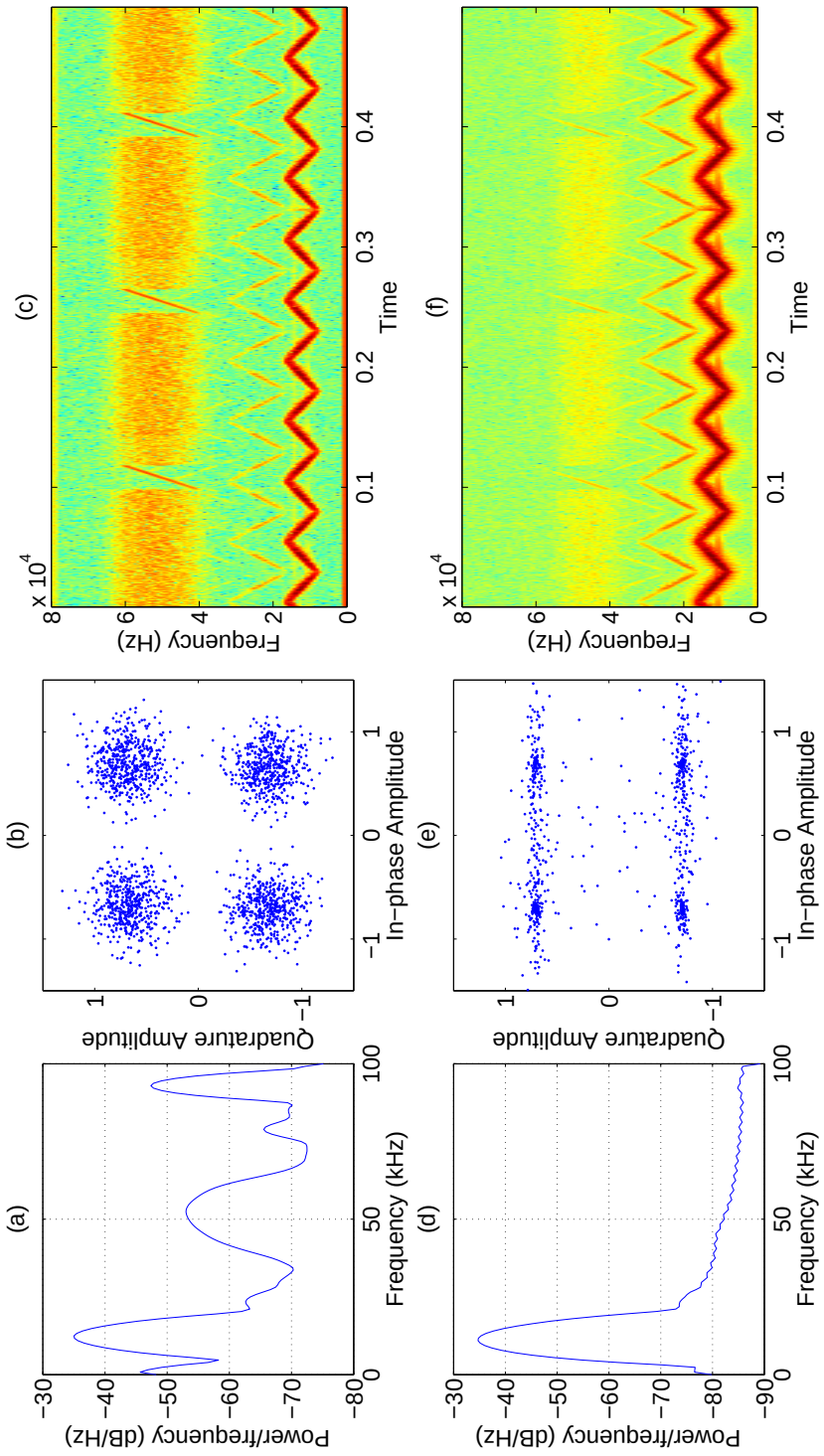


Figure 6.7: Single Carrier Demodulator Output for a Simulated 250m Channel Filtered Receive Signal: (a) PSD (b) I-Q Plot, (c) Spectrogram, (0 Errors / 4064 Bits, Pre. Correction), SINR = 11.17dB, Non-Filtered Receive Signal: (d) PSD (e) I-Q Plot, (f) Spectrogram, (2090 Errors / 4064 Bits, Pre. Correction)

The use of passive filtering is shown to significantly reduce the dynamic range of the received signal. By suppressing the out of band, near-end transmission, the sampling hardware is capable of converting the acoustic waveform with minimal distortion or loss of information caused by clipping. Additional digital FIR filtering again reduces the affect of any out of band interference, ensuring successful demodulation at simulated ranges of upto 250m. Through further testing, the repeatable performance of the system was demonstrated encountering minimal packet losses across a range of transmission ranges.

### 6.3.3 Summary

The presented results successfully indicate the feasibility of full duplex bidirectional communications for a $\mu$ROV application. Through controlled tank testing, practical experimentation has demonstrated the ability to relay two simultaneous frequency isolated transmissions at simulated ranges of upto 250m. Passive filtering has been used at the receiver to reduce the dynamic range of the received waveform, suppressing the effect of any near end transmissions. The use of second order LC filters can be seen to avoid the saturation of the analogue hardware, enabling the waveform to be sampled and digitally filtered to remove any remaining out of band artefacts.

# Chapter 7

# Investigation of Adaptive Modulation and Coding (AMC) Techniques

An AMC system is presented as a method of further improving the reliability and throughput of the high data rate uplink. The ability to support concurrent full-duplex transmissions between the surface and the vehicle is seen as an essential technological enabler for reliable AMC operations, offering the ability to relay real-time feedback information to the $\mu$ROV. Results are presented demonstrating the improved performance of a fully adaptive communication structure, comparing the performance across a range of noise profiles, channel conditions and simulated propagation delays.

In the majority of published research, transmissions through the UAC typically utilise fixed channel parameters, i.e. modulation depth and coding rate. An alternative approach, which has seen widespread use in the terrestrial communication band, is the real-time adaptation of the link parameters based on the instantaneous channel conditions. An Adaptive Modulation and Coding (AMC) structure works towards achieving maximum throughput and optimum link reliability for the instantaneous channel conditions.

## 7.1 Benefits of Adaptive Techniques

In the case of a Continuous Coding and Modulation (CCM) structure, all packets are generated utilising a static code rate and modulation scheme. To ensure that the system will operate with minimal outages, the parameters are typically selected based on the *'worse-case'* scenario, often achieving sub-optimal capacity through utilising excessive levels of redundancy. This shortfall in capacity can be seen to

directly correspond with a reduction in channel throughput, limiting the ability for the link to support high quality image or video transmissions.

The benefits of an adaptive system are therefore two fold: offering increased throughput; and ensuring maximum tolerance to the hostile channel conditions. Utilising reliable channel indicators, and through the selection of suitable adaptation criteria, AMC structures ensure optimal throughput is achieved for the given channel conditions. Additionally, neglecting propagation delay, and assuming an instantaneous change in packet parameters, an adaptive system can also add further levels of redundancy as the channel conditions deteriorate, reducing the number of packet errors incurred.

A well tuned system will ensure the link operates with optimum transmission parameters at any given period in time. However, the non ideal characteristics of the UAC result in long propagation delays causing feedback information to become dated and inaccurate. Such effects will cause the system to struggle to track rapid changes in channel conditions, resulting in an increase in packet errors. Alternatively, if an overly responsive system is utilised, changes to the transmission parameters will occur in advance of the channel deteriorating, resulting in fewer packet errors, but at a significant cost to the average throughput.

This work will investigate the effect of realistic propagation delays and non ideal channel conditions on the performance of an adaptive communication system. An examination of various channel indicators will be performed, assessing their ability to continuously select the ideal link parameters such that maximum throughput and optimum system reliability is achieved.

## 7.2 Past Research in the Field of Adaptive Subsea Communications

The ability to relay real-time feedback information between the transmitter and receiver is highly affected by the the severe propagation delay of the UAC. Therefore, minimal research has previously examined the use of true AMC techniques to improve the throughput of a high data rate acoustic links. In many cases, demonstrated both commercially and academically, multiple transmission schemes are implemented within a single modem design. However, the chosen transmission parameters are typically selected in advance of deployment, based on the conceived operating conditions.

A paper presented by Mani *et al.* in 2008, proposed the development of an AMC strategy to improve the throughput of an acoustic communication link, operating within a shallow water channel [116]. The paper evaluated a range of post-processed

trial data sets to demonstrate the performance of different modulation and coding schemes. Based on these results, a suitable AMC technique was tested through simulation. No further results were presented demonstrating the true performance of a practical system, particularly during periods of significant propagation delay.

To reduce the effect of long transmission delays, the work by Radosevic *et al.* investigated techniques to estimate the state of future channel conditions [117]. By interpolating trends in previous channel estimates, a prediction of future path coefficients could be achieved. The paper concluded that the use of the generated channel predictions offered significant improvement over the use of dated channel estimates. However, within the context of this research, the dynamic nature of the $\mu$ROV is believed to cause severe inaccuracies in future channel predictions.

An alternative approach, proposed by Qarabaqi and Stojanovic [118], is the adaptation of the transmit power level. The proposed structure dynamically adapts the transmission level based on the current channel conditions or predictions of the future channel state. Two adaptive techniques are presented to vastly improve the power efficiency and reliability of the overall system, these are; the reduction of the transmit power during favourable communication periods; and the termination of transmissions when the channel conditions deteriorate beyond a point where reliable communications becomes implausible. However, within the discussed $\mu$ROV application power minimisation is not seen to be of high priority, with the importance being on minimising the number of packet outages.

## 7.3 Adaptive System Overview

An adaptive communication system can be seen to consist of two key parts: a method of estimating the instantaneous channel conditions; and an adjustable set of transmission parameters. A suitable *'probe'* is required to give feedback relating to the communication conditions, highlighting the effect the channel may have on future transmissions. Selecting a suitable channel indicator is essential in order to identify when the conditions have deteriorated and for estimating periods when significant numbers of errors may occur. Additionally, the channel quality estimate may be used to identify when the channel is capable of supporting lower levels of redundancy or more efficient modulation schemes. A brief discussion of possible Channel Quality Indicators (CQI), is given, followed by a description of adaptable transmission parameters capable of offering a variation in system reliability and channel efficiency.

### 7.3.1 Channel Quality Indicators (CQI)

A selection of suitable Channel Quality Indicators (CQI) are presented, for estimating the instantaneous channel conditions in a highly dynamic underwater channel. An ideal method of monitoring the channel condition is through the insertion of a dedicated channel probe, but this has a direct impact on the packet overhead and thus the overall system throughput. Therefore, monitoring the performance of previously received data packets is proposed as an alternative real-time measure of the channel conditions. The most suitable indicators available at the output of the receiver are:

1. **Channel Impulse Response (CIR)**
   A typical impulse response is presented in Fig. 7.1, detailing a range of parameters which could be utilised to give an indication of the current channel condition. The three indicators presented are; the duration of the multipath spread, $T_{mp}$; the peak amplitude of the most significant multipath arrival, $A_{mp}$; and the number of multipath arrivals received. An alternative measure of the CIR is the total multipath energy received, $E_{mp}$, which can be efficiently estimated as the summation of the binary channel representation $b_{\text{mp}}$ (7.1).

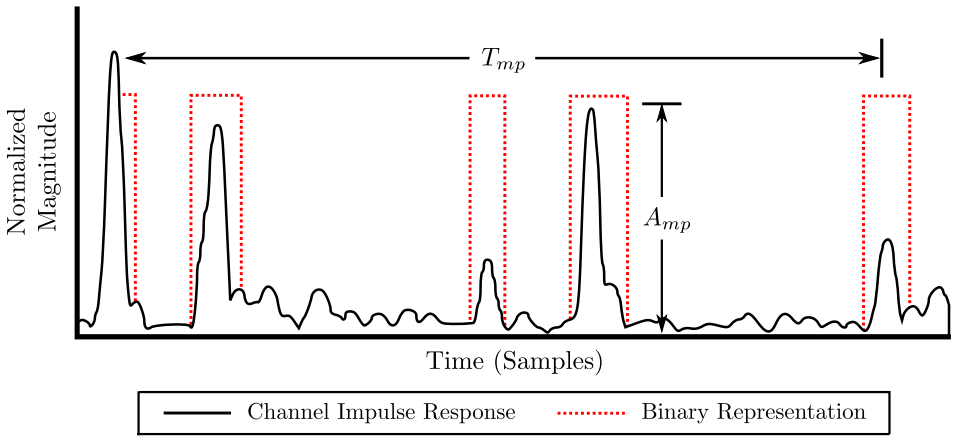


Figure 7.1: Multipath Response, Highlighting Various Parameters Suitable For Indicating the Quality of the Transmission Channel

$$\widehat{E_{mp}} = \sum_{t=0}^{T_{mp}} b_{mp}(t) \tag{7.1}$$

By monitoring the CIR an accurate indication of the incurred ISI can be achieved. Although this effect can be seen to have a severely detrimental effect on the receiver performance, this CQI does not indicate the effects of other parameters such as background noise or Doppler shift.

2. **Packet Errors**
   One of the simplest methods of estimating the quality of the channel is to monitor the number of packet errors incurred. In a realistic scenario, if an error is observed it can be presumed that the current transmission parameters are unsuitable for the given channel conditions. A negative aspect of this indicator is the requirement for an error to occur prior to a change in transmit state. In an idealised AMC scheme the indicator would identify a deterioration in channel conditions prior to the failure. In comparison with many of the other proposed CQIs the output given from this approach is very restricted, offering only a 'Pass' or 'Fail' indication.

3. **Number of Iterations**
   By monitoring the number of BICM-ID iterations, a decision can be made to change the transmission parameters prior to the link completely failing. If the receiver is operating with minimal to no iterations, the decision could be made to improve the throughput of the channel. This estimator enables a decision to be made in advance of a complete packet failure, supplying a gradual response, where the number of iterations can be used to indicate the size of the step required.

4. **Doppler Shift**
   The output of of the Doppler estimate gives a prediction of the vehicle's motion and thus the related degradation of the received packet. Suitable transmission parameters can be selected based on observations of the instantaneous velocity, or a prediction of future movement based on a historical data set. This indicator is severely limited, solely offering information corresponding to the vehicles movements in a direction perpendicular to the receiver. Additionally, although Doppler can be seen to have a severe impact at high velocities, or during periods of rapid acceleration, adjusting coding rates and modulation scheme offers limited benefit. In the majority of examples, severe Doppler shift is shown to result in the system struggling to synchronise, leading to total failure of the receiver structure.

5. **Signal to Noise Ratio (SNR)**
   The SNR gives an accurate indication of the signal amplitude, $A_{signal}$, compared with the ambient background noise level, $A_{noise}$ (7.2). Typically, to estimate the background noise amplitude, a silent period is appended at the start of each packet, allowing the noise level to be calculated without the effect of any self generated signals. In channels with a long delay spread, this silent period can be seen to represent a significant period of the overall transmission.

$$\mathrm{SNR}_{dB} = 20 \log_{10} \left( \frac{A_{signal}}{A_{noise}} \right) \tag{7.2}$$

6. **Signal to Interference and Noise Ratio (SINR)**
   An alternative approach is to estimate the SNR at the output of the equaliser structure, often referred to as post-equalisation SNR (7.3). The mean signal level can be perceived as the sum of the equaliser decisions, $d_i(n)$, and the standard deviation of the background noise can be estimated from the equalisation error signal, $e_i(n)$, which is also found to incorporate any residual ISI. In simple terms this estimate can be seen to describe the spread of constellation points from idealised IQ positions. It should be noted that the 'signal' level can actually be seen to be the product of both the transmit signal and any incurred channel interference. Therefore this estimate is often referred to as the Signal to Interference and Noise Ratio (SINR).

$$\text{SINR} = \frac{E\left|d_i(n)\right|^2}{E\left|e_i(n)\right|^2} \tag{7.3}$$

   Although the SINR calculation only acts as an indication of the true SNR, a distinct advantage is the ability to acquire continuous updates on a packet-by-packet basis, without the need for a predetermined silent period

### 7.3.2 Adaptive Parameters

A list of feasible adaptation parameters are given below, highlighting their suitability for improving the systems reliability or operational throughput:

1. **Code Rate**
   Varying levels of redundancy can be utilised to improve the reliability of the system in severe channels or increase the throughput in benign conditions. The optimal coding rate should be selected to ensure maximum throughput and maximum reliability for the given channel conditions.

2. **Modulation Scheme**
   Higher order modulation schemes enable an increased number of bits to be represented using a single symbol value. However, the increased minimum euclidean distance demonstrated by lower level schemes, reduces the possibility of false detection in low SNR or high Doppler conditions.

3. **Transmit Power**
   By adapting the transmit power level, maximum reliability can be ensured while minimising the power consumption. This criteria is used to increase the transmit power during intervals of low signal to noise, while ensuring conservation of energy and thus the extended lifetime of a battery powered modem.

4. **Symbol Rate**
   By reducing the symbol rate the equaliser structure can be shown to perform better in channels with high levels of interference or fading. The longer duration of the symbol increases the temporal span of the equaliser filter, but reduces the tracking rate of the adaptive algorithm.

5. **Packet Length**
   By reducing the length of the packet, the block Doppler estimate is found to be able to more effectively track the acceleration or deceleration of the vehicle. However, shorter packets are shown to be less accurate at estimating the incurred Doppler shift and increase the percentage of the transmission occupied by overheads, reducing the overall throughput of the system.

### 7.3.3 Summary of AMC Techniques

A wide range of suitable channel indicators have been examined, each demonstrating a varying ability to identify a deterioration in the channel conditions. The examination of the measured Doppler shift and the CIR are proposed as feasible CQI. However, both are felt to give limited information relating to the full extent of the channel conditions, negating the affect of other factors such as background noise or self induced interference. When used alone, neither CQI is believed to be suitable for identifying the overall degradation of the receiver performance. Therefore, this research will focus on the combined use of the output SINR and the occurrence of packet errors as suitable channel indicators.

Based on the findings in Chapter 4 the use of different code rates and modulation schemes are shown to offer variability in terms of throughput and reliability. To ensure simplification of the receiver structure, a static packet length and constant symbol rate are typically preferred. Additionally, adaptation of the transmit power is shown to have minimal merit, where the operational range of the $\mu$ROV is reasonably short and the conservation of transmission power is not shown to be of significant importance. Within the following experiments the code rate and modulation scheme will be selected as the primary adaptive transmission parameters.

## 7.4 Adaptive Protocol Structures

Within the scope of this work, four different adaptive protocol structures are presented. Each of these structures demonstrate varying benefits in terms of: implementation complexity; throughput maximisation; and response time to impulsive changes in channel conditions. An overview of each protocol is given below, highlighting the benefits and limitations of each.

### 7.4.1 Configuration 1: Linear Adaptation

The first approach is a basic linear adaptation technique, referred to in this work as the *'Step-by-Step'* configuration. Utilising this scheme, modulation and coding levels are adjusted by a single incremental or decremental step. A block diagram of the various state interactions is shown in Fig. 7.2. The number of stages is limited to four for illustration purposes only, in a practical system additional schemes may be utilised as required.

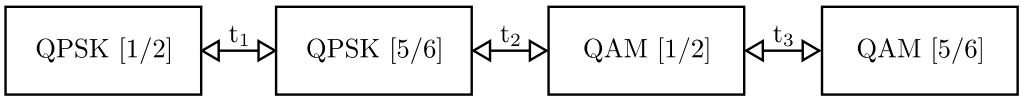


Figure 7.2: Adaptive Protocol: Linear *'Step-by-Step'* Approach

This protocol's ability to react to rapid changes in channel conditions is severely limited, due to the transmission scheme only adjusting by a single state per iteration. It is therefore only suitable in environments where slow changes in channel conditions are observed, or where the amount of feedback information is restricted. Utilising this approach, the maximum number of transition paths required is limited to a maximum of two per state, one higher and one lower. The number of threshold boundaries required can therefore be kept to a minimum, ensuring ease of configuration and reduced complexity in implementation.

### 7.4.2 Configuration 2: Fall Back

The second technique discussed is referred to as the 'Step Up: Fall Back' approach. In a similar way to the previous technique, transmission states which offer improved throughput can only be selected in single incremental steps. However, to overcome the problems addressed with the previous protocol, when a severe deterioration is observed, a transition is made directly to the state with the highest redundancy / reliability. A block diagram of this configuration is shown in Fig. 7.3.

This technique can be seen to vastly improve the tolerance to impulsive changes in channel conditions. When the channel degrades to a point where a change in signal parameters is required, the protocol recommends the transmitter returns to the *'worst case'* scenario. Once the channel has dropped back to this state, if it is believed to be capable of supporting a higher throughput scheme, the system will begin to step back up in incremental stages. In certain scenarios this scheme can be seen to be overly responsive, causing an over reaction to minor changes in the channel and a significant reduction in average throughput.

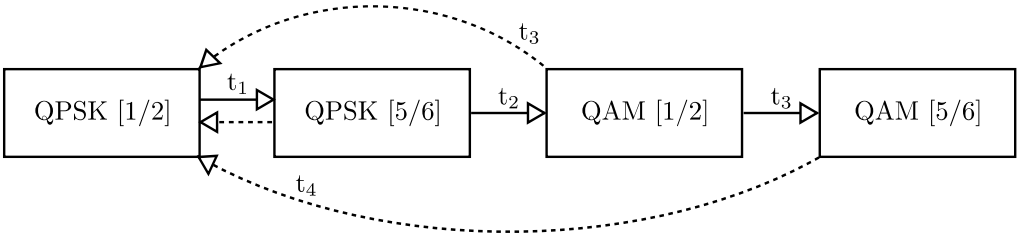


Figure 7.3: Adaptive Protocol: *'Step Up: Fall Back'* Approach

### 7.4.3 Configuration 3: Fully Adaptive

The third configuration presented is referred to as a *'Globally Adaptive'* approach. In contrast to the two linear techniques presented previously, this configuration enable transitions between all states at any given time period. This approach can therefore be seen to be more complex than the previous two structures, requiring additional transition thresholds to be defined such that the system can freely adapt between states. Fig. 7.4 illustrates the block diagram for a fully adaptive structure utilising four independent transmission schemes.

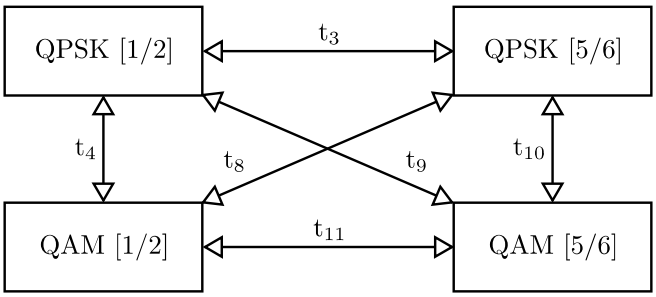


Figure 7.4: Adaptive Protocol: Fully Adaptive Approach

The key benefit of a fully adaptive scheme is clear, enabling the amount of redundancy and the modulation scheme used to be adjusted freely in a single iteration. In both of the previous structures limitations have been presented in terms of the ability to react quickly to changes in the channel conditions. The ability to instantly select the optimum transmission parameters can be seen to minimise the number of packet errors incurred during periods of impulsive channel degradation whilst also maximising the average system throughput.

The presented scheme can however be seen to incur increased complexity in terms of configuration and implementation. The requirement for additional transition states directly impacts on the number of detection stages utilised. To ensure ideal operation, each threshold level has to be carefully selected based on a schemes

performance under specific channel conditions. Additionally, this configuration is not suitable for use with indicators such as PER which supply very basic *'hard'* feedback decisions.

### 7.4.4 Configuration 4: Gated Fully Adaptive

The final configuration is a multi-layer adaptation scheme, referred to as the *'Gated Fully Adaptive'* approach. This configuration is very similar to the fully adaptive scheme, offering the ability to easily step between any of the communication schemes in a single iteration. The primary difference between the two is the gating operation on the fall-back transition paths. This protocol utilises a secondary *'hard'* feedback decision to indicate the need to drop down a state, prior to the primary CQI deciding the most suitable modulation scheme and level of redundancy. As with the basic fully adaptive configuration, an incremental change is based solely on the primary CQI.

Utilising this technique the transmission scheme is effectively forced to stay the same, or improve, unless the secondary CQI indicates a requirement to change. A block diagram of the final configuration is shown in Fig. 7.5, where, the dashed transitions indicate paths which are *gated* by the secondary CQI.

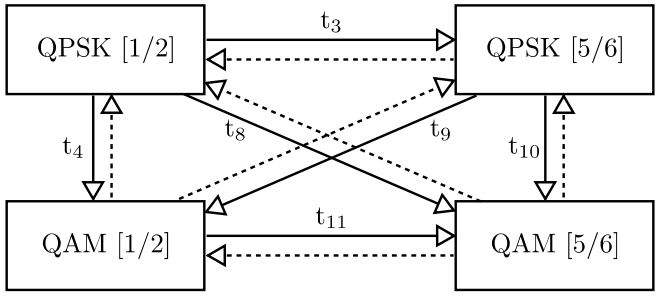


Figure 7.5: Adaptive Protocol: Gated Fully Adaptive Approach

Within this study, the SINR CQI is used as the primary indicator, and the PER as the secondary. Although this may appear counter intuitive, the main aim of this protocol is to ensure that the system operates at its maximum throughput for as long as possible. By utilising the occurrence of a packet error as the gate indicator the system will continue to transmit utilising the best possible scheme, even if the system falls below the predefined SINR threshold.

## 7.5 Experimental Results

To examine the benefits of an AMC system, a range of controlled practical experiments are conducted. Two sets of trials are presented: the first evaluating the performance of the structure with varying background noise profiles and increased transmission latency; and the second examining the effectiveness in overcoming varying motion and dynamic channel conditions.

### 7.5.1 Hardware Configuration

The real-time multi-element DFE-BICM-ID receiver structure discussed in Chapter 5 was modified to enable the performance of an adaptive system to be explored and benchmarked. Additional code was added to the receiver software, enabling the output of the iterative DFE structure to be analysed and examined against a set of proposed criteria. If the output CQI dropped below a predetermined threshold level, a message signal would be invoked by the receiver and relayed to the PC based transmitter. Based on this feedback the parameters of future packet transmissions would be modified to insert additional redundancy or drop the modulation complexity. A block diagram of the overall experimental setup is shown in Fig. 7.6.

To reduce the system complexity and isolate any possible effects from cross band interference, the acoustic downlink was removed and replaced with a tethered connection. An Ethernet based Transmission Control Protocol (TCP) socket was selected to connect the PC transmitter and receiver, as a direct replacement for the low data rate LFM link discussed previously. The additional code required to generate the feedback information, at the receiver, and monitor the return socket, at the transmitter, was inserted into a separate worker thread. By isolating the code into an independent thread the 'downlink' transmissions could be processed simultaneously, avoiding any impact on the main operation of the high data rate receiver and transmitter code.

To ensure repeatability, and to minimise the variability of the channel conditions, all tests were carried out in a controlled test tank environment. Due to the constrained dimensions of the tank, and to avoid saturation of the receive transducer, the linear amplifier was removed from the experimental setup, utilising a direct connection from the DAC unit as the input to the transmit transducer.

### 7.5.2 Measured Experimental Delay

A significant limitation on the performance of an AMC system is the latency between the transmission of data and the arrival of feedback information. This effect can be

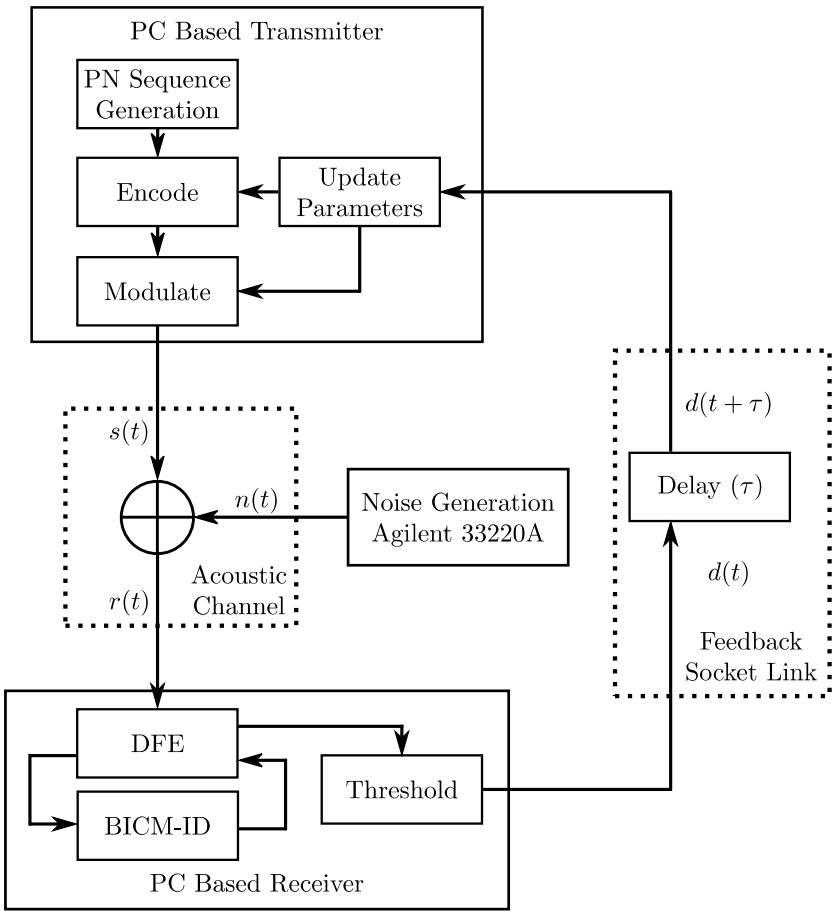


Figure 7.6: Adaptive Modulation and Coding Controlled Experimental Setup

seen to correspond with the inability to instantly adapt to the current state of the receiver output, often leading to decisions being made on dated channel estimates. The slow propagation speed of sound through the underwater channel is found to have a severe impact on the time taken to relay feedback information to the vehicle.

To thoroughly investigate the performance of a real-time AMC system, the causes of any system latency must be considered. Despite the experimental setup operating in a similar manner to a realistic practical system, due to the reduced propagation range and the simplification of the downlink structure, not all of the latency conditions are considered. Therefore to enable the simulation of varying round trip transmission delays, and to take into account the actual delay incurred when utilising a LFM downlink, a method of inserting a repeatable delay in the socket transmission was devised in software.

#### 7.5.2.1 Downlink Processing Delay

The ability to process each LFM downlink packet utilising a matched filter structure, ensures real-time operation i.e. minimal incurred latency. However, the limited throughput of the LFM link can be seen to correspond to a noticeable packet duration. Utilising a 50ms synchronisation chirp, followed by a combination of 10ms data chirps, consisting of 4 control bits, 4 state bits and an 8 bit CRC the duration of a single packet will exceed 210ms. Since a full packets worth of data is required prior to the calculation of the CRC and the updating of the transmission parameters, a noticeable delay is observed.

The Ethernet connection, used within the experimental setup, can be shown to offer significantly higher data throughput and minimal transmission delay, when compared with a realistic LFM acoustic transmission. However, since the TCP socket connection utilises a delayed acknowledgement technique, the feedback information relayed through the socket connection is delayed by ≈200ms until the acknowledgement timer expires. Therefore, within the context of this study the delay of the experimental setup is considered realistic to an optimal LFM transmission. The use of a simulated delay is therefore only required to simulate the time taken for the signal to propagate through channels of realistic distances.

#### 7.5.2.2 Round Trip Transmission Delay

Another source of system latency is the transmission delay observed when operating across increased ranges. Due to the low sound velocity through water, typically in the range of 1485-1500m/s, the time taken for an acoustic signal to propagate through the channel is relatively severe. Since the results presented were collected in an anechoic test tank, the transmission range was constrained to approximately

2.5m, exhibiting a propagation delay of approximately 1.6ms. Therefore, to evaluate the performance of an AMC system in a realistic communication channel a corresponding simulated delay must be inserted.

Table 7.1 presents a selection of transmission delays, for distances ranging from 40m upto 1km . In a realistic scenario the round trip delay must be considered, i.e. taking into account the propagation delay of both the uplink and downlink transmissions. Therefore, assuming the same operating environment as a tethered $\mu$ROV, a maximum transmission delay of 400ms (300m) is believed to be reasonable.

| Range | Delay (ms) | |
|---|---|---|
| | One Way | Round Trip |
| 40m | 26.6 | 53.2 |
| 100m | 66.6 | 133.3 |
| 300m | 200 | 400 |
| 500m | 333.3 | 666.6 |
| 1000m | 666.6 | 1333.3 |

Table 7.1: Estimated Round Trip Delay ($\tau_{rt}$) for Varying Transmission Ranges. [Assuming: $c = 1500$m/s]

Within this study increased transmission delays are presented, typically upto a maximum simulated range of 3km (4 seconds). Despite these delays being unrealistic to the operational environment of a $\mu$ROV the results are presented to show the inefficiency of the structure when the feedback information becomes dated or unreliable.

### 7.5.3 Data Set A: Varying Noise Profiles and Transmission Delays

During the first set of tests, the performance of the various AMC protocols were examined against varying background noise profiles and increased propagation delays.

#### 7.5.3.1 Noise Profiles

To vary the severity of the background noise an Additive White Gaussian Noise (AWGN) signal was projected into the tank, such that the received SNR could be severely degraded. The induced noise sequence, $n(t)$, was generated artificially using an Agilent 33220A arbitrary signal generator. The magnitude of the AWGN signal was controlled from a terminal PC, utilising a bespoke 'Matlab' script to generate a set of three repeatable *'background'* noise profiles.

The acoustic noise sequences were emitted into the water through a Chelsea Transducer Group (CTG) Broadband 030 omni-directional acoustic projector. Despite this transducer being resonant around 30kHz, the transmit sensitivity was found to be linear at approximately 144dB re 1$\mu$Pa/V at 1m ($\pm$ 1dB) across the operational transmission band of 40-60kHz. The three noise sequences used within this study are: a slowly varying sinusoid; a step response; and an impulsive noise profile. A representation of the three noise patterns utilised are shown in Fig. 7.7

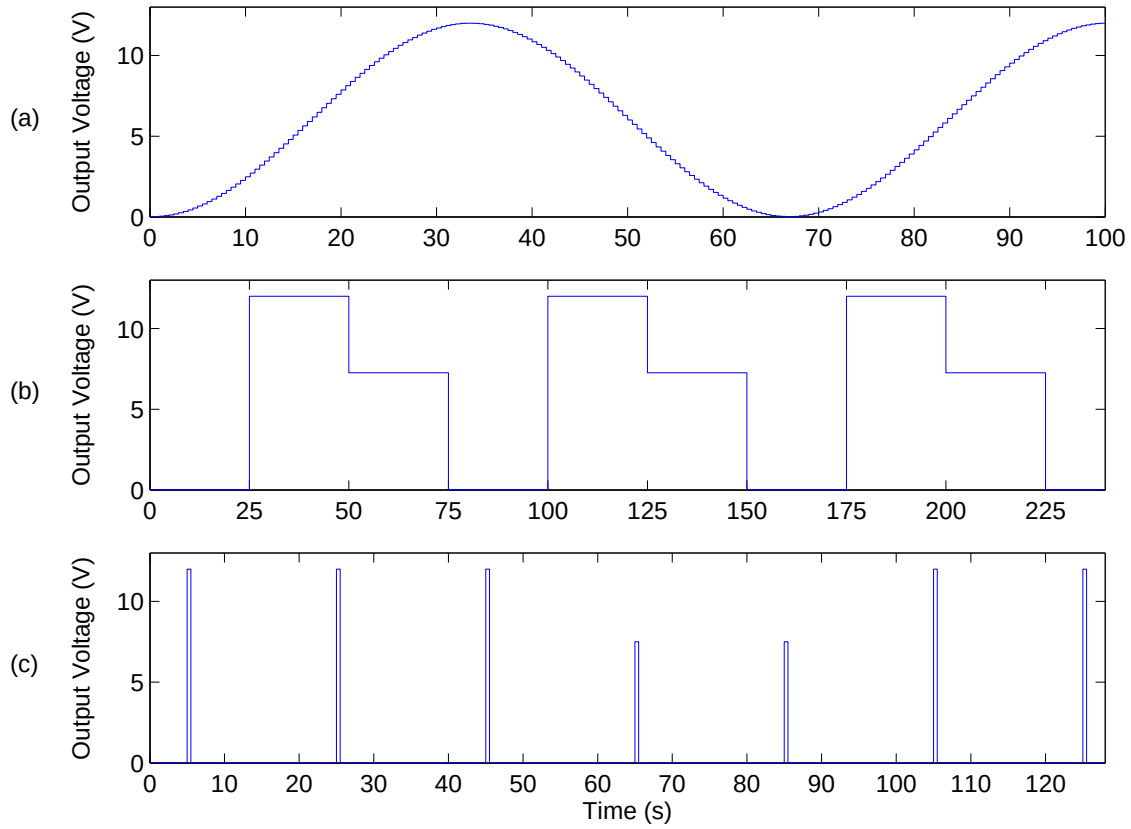


Figure 7.7: Amplitude of Generated Additive White Gaussian Noise Sequences: (a) Slowly Varying (Sinusoidal), (b) Step Response, (c) Impulsive Noise

Each of these reference signals represent different characteristics of the UAC channel, such as: slow varying changes similar to the effect of changing wind or sea state; and impulsive step responses typical of the noise from the vehicles thrusters or intermittent marine wildlife. It should also be noted that although these experiments demonstrate reduced SNR due to synthesised noise, the resulting effect is similar to a loss in signal power, i.e. transmission loss or channel fading. The three profiles are derived such that they test the capability of an AMC system in terms of reaction time, error reduction, and average throughput.

#### 7.5.3.2 Hydrophone Configuration

To maximise the severity of the channel, both the transmitter and the receiver were positioned at the maximum depth possible, slightly less than 2m, and with a separation of ≈3m. Prior to testing, the $\mu$ROV was panned horizontally at the range stated until the worst CIR, caused by the surface reflection, was observed. This stationary position was then used for the duration of the tests presented. In this configuration of maximum range and maximum depth, the longest delay spread feasible within the tank environment was observed.

The depth of the data transmitter; beamform receiver; and AWGN noise projector, were kept equal i.e. all elements were positioned on a level horizontal plane. By positioning both transmitters at approximately the same depth the suppression effect of the beamformer was significantly reduced, enabling the beam steering effect to be neglected. The noise projector was statically mounted approximately 1m from the beamformer, and not in the direct path of the main signal transmitter.

#### 7.5.3.3 Profile 1: Slowly Varying (Sinusoidal)

The first set of results examine the performance of an AMC system for data sets exhibiting a slowly varying noise profile. The results shown in Fig. 7.8 demonstrate the performance of each of the proposed AMC strategies for varying propagation delays, ranging from 0-4 seconds. In each case the AMC protocol selects the most suitable of four transmission states, based on the post equalisation SINR level. The four transmission states used in these experiments are: QPSK 1/2, QPSK 9/10, QAM 1/2 and QAM 5/6.

In this context of this work the average throughput is calculated as the number of successful transmissions divided by the duration of the overall capture. In all cases the additional delay is shown to result in an increase in packet errors and a reduction in overall throughput. On average, the drop back architecture can be seen to correspond with the lowest throughput, regularly returning to a lower transmission rate than necessary. This effect is further emphasised with increased delays causing the system to continue to operate in a sub-optimum state over a longer period of time.

Although the practical system is intended to operate within a maximum range of 250m, i.e. a propagation delay of less than 500ms, increased simulated delays are also presented. These results are included to further emphasise the loss in performance caused by the use of dated and inaccurate feedback decisions. The most evident demonstration of this effect is in the case of the linear adaptation approach, where increased delays are shown to correspond with an exponential rise in incurred packet errors.

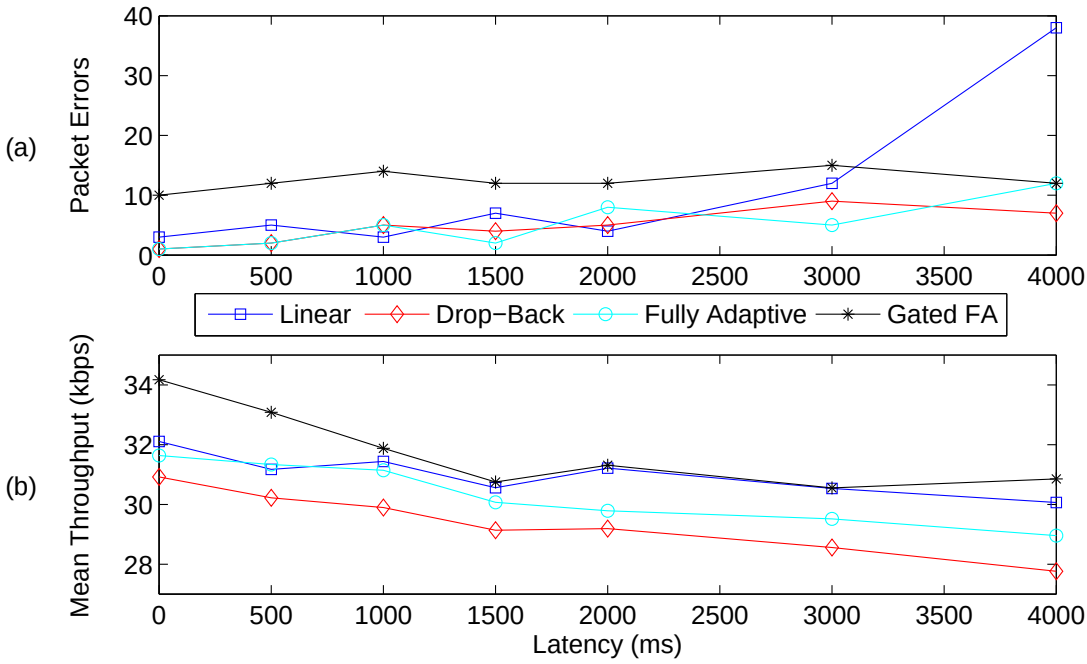


Figure 7.8: Sinusoidal Noise Profile: Comparison of AMC Techniques with Varying Simulated Latencies (a) Number of Packet Errors (b) Mean Throughput

The presented results indicate that the gated fully adaptive protocol offers superior performance over any alternative AMC technique. This approach typically exhibits higher numbers of packet errors, caused by the requirement for an error to occur prior to a change in state. However, at shorter ranges (i.e. $T_{\text{sim}} < 1$s) the overall throughput is consistently seen to increase by upto 2kbps when compared with other AMC approaches.

The performance of the receiver, when operating with a static set of transmission parameters, is presented in Table 7.2. As emphasised in the table, the QPSK 9/10 transmission scheme is shown to offer superior performance, demonstrating minimal packet errors and the maximum average throughput.

| | QPSK 1/2 | QPSK 9/10 | QAM 1/2 | QAM 5/6 |
|---|---|---|---|---|
| Throughput (kbps) | 16.30 | 28.45 | 14.89 | 22.72 |
| Packet Errors | 0 | 12 | 212 | 247 |

Table 7.2: Sinusoidal Noise Profile: Performance of Static Transmission Schemes

When compared with the most favourable AMC strategy, gated fully adaptive, the average throughput is shown to improve by approximately 5kbps (33.08kbps), for a realistic round trip propagation delay of 500ms. Additionally, 12 packet errors are

observed when operating under both an AMC and a CCM structure. This number of errors is felt to be acceptable, particularly when used in parallel with an appropriate video compression technique or retransmission request algorithm.

#### 7.5.3.4 Profile 2: Stepped Response

The second set of results demonstrate the capability of the four AMC schemes during a noise profile exhibiting multiple stepped variations across a transmission of approximately 1000 packets. The results shown in Fig. 7.9 again emphasise the variation in throughput and incurred packet errors for varying propagation delays.

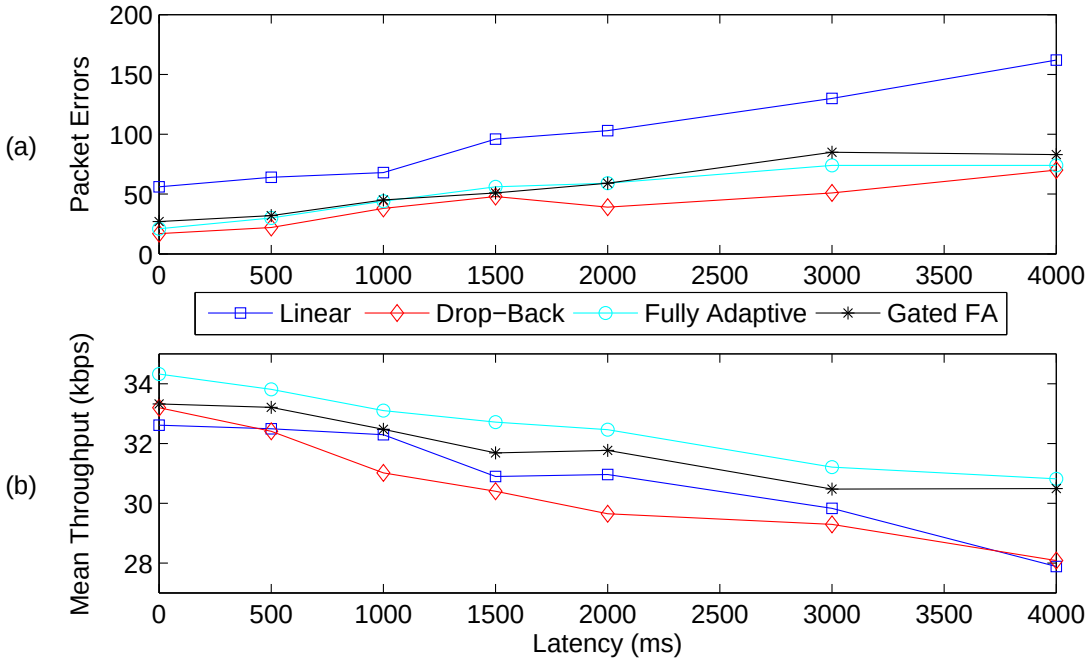


Figure 7.9: Stepped Noise Profile: Comparison of AMC Techniques with Varying Simulated Latencies (a) Number of Packet Errors (b) Mean Throughput

The results highlight the limitation of a linear adaptive algorithm, demonstrating a significant increase in the number of incurred packet errors and a reduction in the average throughput of the system. This effect is caused by the multiple steps taken to adapt from the 'best' transmission state through to the 'worst' and is further emphasised by an increase in simulated delay. Again the drop-back algorithm can be seen to yield a reduced throughput, in many cases utilising unnecessary levels of redundancy and sacrificing data symbols which could have been successfully decode.

Both the gated and none gated fully adaptive approaches offer similar performance, offering an average throughput of 33-34kbps and a similar number of packet errors, during a simulated latency <1 second. When compared with the performance of

the best static transmission scheme, shown in Table 7.3, an AMC approach can be seen offer a significant improvement in throughput, >20%, and an overall reduction in incurred packet errors ≈ 50%.

| | QPSK 1/2 | QPSK 9/10 | QAM 1/2 | QAM 5/6 |
|---|---|---|---|---|
| Throughput (kbps) | 16.19 | 26.59 | 11.98 | 20.08 |
| Packet Errors | 5 | 88 | 567 | 568 |

Table 7.3: Stepped Noise Profile: Performance of Static Transmission Schemes

#### 7.5.3.5 Profile 3: Impulsive Noise

The final set of results demonstrate the performance of an AMC approach during periods of impulsive noise. The results shown in Fig. 7.10 demonstrate the average performance of each scheme across a duration of approximately 500 packets, whilst experiencing a total of 7 impulsive events.

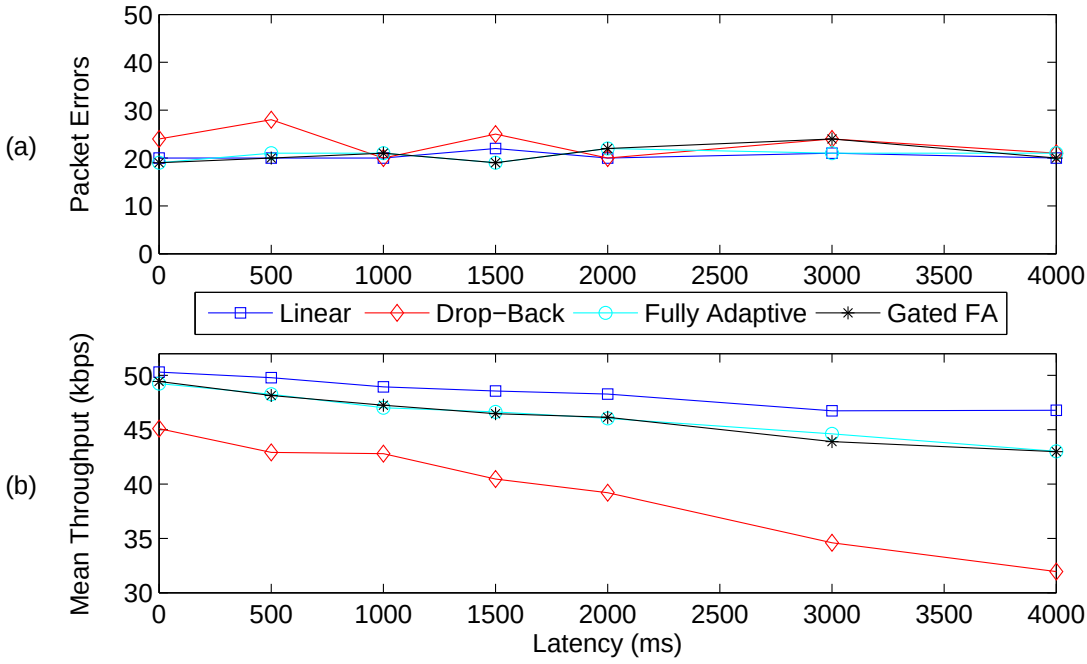


Figure 7.10: Impulsive Noise Profile: Comparison of AMC Techniques with Varying Simulated Latencies (a) Number of Packet Errors (b) Mean Throughput

In contrast to the previous two noise profiles, the results presented indicate the ineffectiveness of an AMC system. In all cases, the latency of the feedback channel is shown to be significantly longer than the length of the noise impulse. The reduction in throughput is therefore attributed to a two-fold effect: firstly, a loss of

packets during the impulsive noise period; and secondly, the system operating in a suboptimal state for a significant period after the channel returns to a benign state.

For all of the proposed AMC approaches the results demonstrate a significant loss in performance, particularly at increased propagation delays. For each scheme, the number of packet errors can be seen to be constant and relate to a complete failure of the receiver during the interval of impulsive noise. The linear approach is seen to offer the best performance, only stepping the transmission scheme down by a single state and minimising the loss in throughput once the impulsive noise has subsided.

When compared with the use of the best static transmission scheme, presented in Table 7.4, the AMC approach can be seen to demonstrate a reduction in throughput i.e. $< 51.65$kbps. This degradation in performance is attributed to the inability to predetermine such changes in the channel conditions.

| | QPSK 1/2 | QPSK 9/10 | QAM 1/2 | QAM 5/6 |
|---|---|---|---|---|
| Throughput (kbps) | 16.10 | 28.70 | 32.18 | 51.65 |
| Packet Errors | 5 | 10 | 21 | 24 |

Table 7.4: Impulsive Noise Profile: Performance of Static Transmission Schemes

### 7.5.4 Data Set B: Varying Channel Conditions and Vehicle Motion

The second data set examines the performance of the AMC system for varying channel conditions and relative movements. Unlike the previous results, these captures demonstrate a wide variety of transmission conditions, exhibiting a range of movement across the length, width and depth of the anechoic tank.

#### 7.5.4.1 Experimental Description

To examine the direct effect of vehicle motion and channel variability, these experiments were conducted with the vehicle able to freely operate within the tank environment. Although the lining of the tank significantly damped the multipath, the reflection from the surface boundary created a noticeable interference path. In contrast to the previous experiment, no additional 'background' noise was artificially introduced into the tank. Therefore, the incurred noise can be solely attributed to the self-induced noise of the vehicle, i.e. thruster noise. To limit the possibility of cavitation, the thruster gains were limited to half power.

During each capture, a vast selection of vehicle operations were performed, encompassing a range of motions at different depths and ranges. To ensure variability in the CIR, the vehicle was positioned at various points around the tank, including close to the surface and near to the bottom of the tank. A range of movement was demonstrated during the capture, including, but not limited to: slow speed panning; rapid accelerations; abrupt decelerations (due to collisions with the tank lining); continuous movement (at a fixed velocity), and stopped.

Although best attempts were made to ensure repeatability from one transmission to the next, it was unrealistic to assume that the operations performed during each capture were identical. For this reason a longer data capture was conducted ensuring, on average, an even distribution of operations were performed across the duration of the 2000 packet transmission.

#### 7.5.4.2 Comparative Results

Comparative results were collected for both the proposed AMC approaches and the four static transmission schemes. In each case, an additional transmission delay was not applied to the feedback channel, ensuring minimal latency between new parameters being proposed by the receiver and a change in the current transmission scheme. The performance of each approach is presented in Fig. 7.11, again evaluating both the number of incurred packet errors and the average throughput of the system.

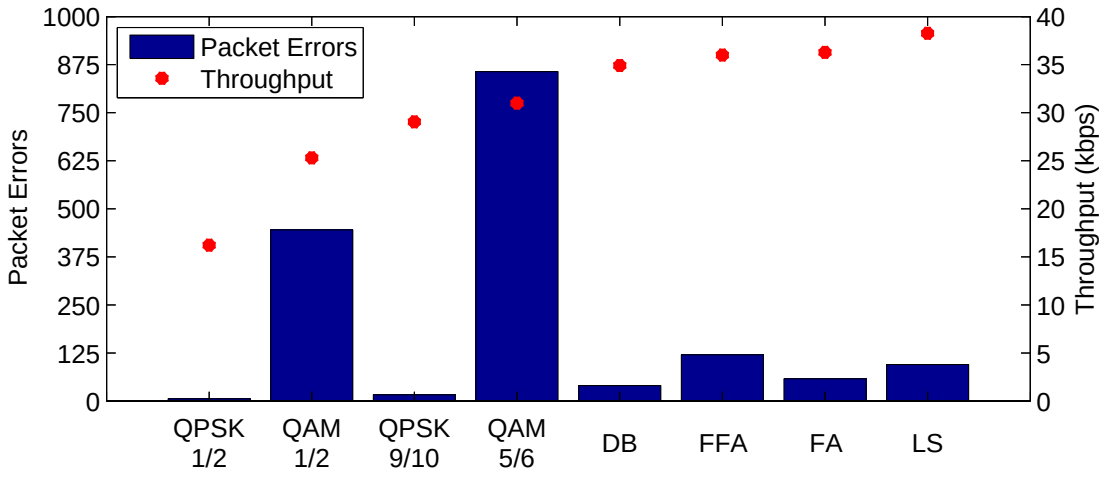


Figure 7.11: Comparative Performance of AMC and CCM Techniques During Varying Channel Conditions and Vehicle Motion (Data Set B)

The results shown in Fig. 7.11 clearly demonstrate the limitations of a CCM strategy. In the case of both QAM 1/2 and QAM 5/6, high numbers of packet errors were incurred, severely effecting the overall performance. If a static transmission scheme

were to be implemented, the most appropriate trade-off would be to utilise QPSK 9/10, offering reasonable throughput and minimal packet errors across the duration of the capture.

In contrast, an AMC strategy is shown to offer significantly improved performance, demonstrating a slight degradation in packet errors when compared with either QPSK scheme, but an overall improvement in throughput of 6-7kbps ($\approx$ 20%). All four AMC approaches are shown to offer comparable performance, with similar throughput, $\pm$1kbps, and a slight variation in the number of packet errors. In practice, either the drop-back or the fully adaptive structure would be selected as they demonstrate reduced numbers of packet errors but offer similar throughput to either of the alternative AMC approaches.

A 120 packet section of the data set recorded during testing of the drop-back protocol is shown in Fig. 7.12. During this period no packet errors were observed. In the presented plots, it can be seen that as the vehicle begins to move away from the receiver a reduction in SINR is observed. This reduction is detected by the AMC control algorithm, and a recommendation is made to revert to the 'base' transmission state. As the SINR begins to improve the AMC approach recommends a reduction in redundancy, improving the throughput of the system in stages until the maximum transmission scheme is reselected.

### 7.5.5 Summary

In general, the proposed AMC structures have demonstrated a significant improvement in performance when compared to a traditional CCM approach. In both experiments an adaptive technique has demonstrated improved throughput, of the order of 5-10kbps, with minimal degradation in the number of packet errors. In practice, if a fixed parameter system were to be utilised, the results have highlighted the benefits of a QPSK 9/10 transmission scheme, which offers optimal trade-off between throughput and packet errors. In all examples an AMC scheme was shown to offer improved throughput when compared to this form of static transmission.

During the first set of tests, where the system was tested against a range of different noise profiles, a reduction in AMC performance was observed during periods of impulsive noise. This effect can be linked to the inability to implement a fully predictive strategy, making it impossible to predetermine such rapid variations in channel conditions. Additionally, due to the latency of the channel, the communication structure was unable to instantly adapt the transmission parameters based on the current receiver output. Therefore, a loss in throughput is observed while feedback information is relayed between the surface and the $\mu$ROV.

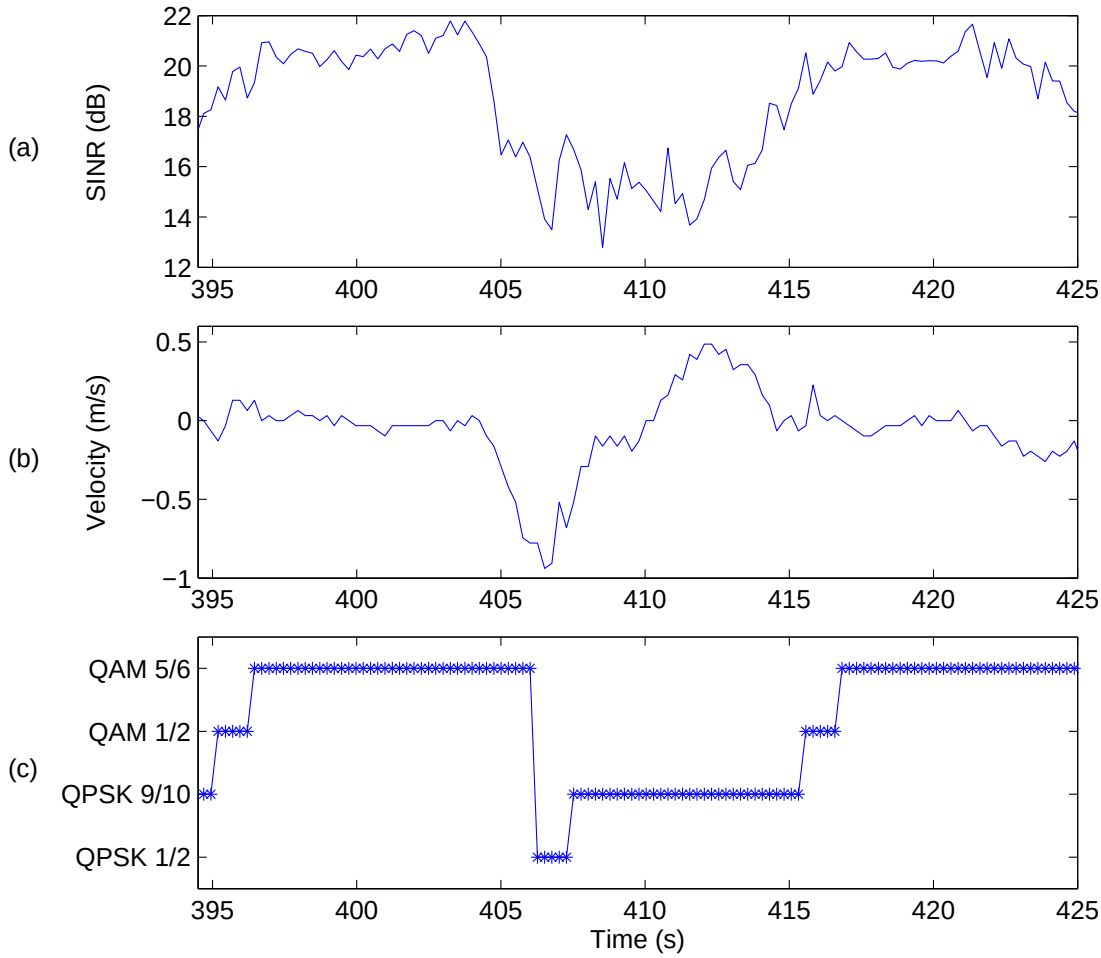


Figure 7.12: Variation in Transmission Scheme Utilising AMC Drop Back Protocol in Varying Channel Conditions. [0 Packet Errors / 120 Packets]

(a) Time Varying Signal and Interference to Noise Ratio (SINR)
(b) Estimated Velocity Profile (Calculated From Block Estimation)
(c) Current Transmission Parameters (Coding Rate and Modulation Scheme)

It should also be noted that during the first set of experiments a heavily simplified set of noise profiles were utilised. In a realistic scenario the noise signature would represent a combination of all three profiles, exhibiting a mix of slow variations, impulsive and stepped changes. The results from profile three are therefore shown to demonstrate an exaggerated scenario, returning each time from an impulsive occurrence to a completely benign background noise level.

The results captured during the second data set focus on the realistic operation of the vehicle, encapsulating a range of movements and varying channel conditions. Again, the capability of a practical AMC approach is demonstrated, offering an average improvement in throughput of $\approx 20\%$ when compared with the best CCM transmission scheme. Once again, he experiment is believed to demonstrate an exaggerated scenario, as minimal separation between the receiver and the vehicle thrusters cause greater fluctuations in the background noise level.

It is believed that improvements can be made through further tuning of the CQI threshold levels. The threshold levels utilised were selected based on preliminary test and examination of results captured during previous sea trials. By examining an increased data set it is believed that a more accurate estimation of suitable CQI threshold levels can be achieved. Alternatively, future work could investigate the development of an automated system, where the magnitude of each threshold level is based on the previous performance of the system.

# Chapter 8

# Conclusion

This chapter combines the key results and conclusions from the previous five chapters. A concise description of each chapter is given, focusing on the key contributions towards the development of a reliable low cost communication link for a $\mu$ROV platform. Furthermore, suggestions of future work are provided, highlighting areas where developments could be made to provide additional contribution to the academic field.

This thesis initially investigated the specific channel characteristics related to a $\mu$ROV deployment. An examination of the channel response revealed the considerable delay spread and the sparse separation between multipath arrivals caused by the low range to depth ratio and the lack of acoustic refraction inherent to the channel geometry. Additionally, despite having a low maximum velocity, i.e. <1-2kts, the high acceleration and deceleration of the vehicle is found to cause complications in the estimation and compensation of the incurred Doppler shift. Finally, despite the typical operating conditions demonstrating a high SNR, the noise generated by the vehicle's thrusters, and the fading caused by the cavitation effect, were shown to cause intermittent fluctuations in the received signal strength.

Based on an understanding of the specific channel conditions, Chapter 4 explored a selection of suitable receiver structures. The use of a single element receiver was initially proposed, which offers a reduction in size, cost and complexity of the required hydrophone. Initially, the adaptive equaliser structure was shown to be inadequate at combating sparse delay spreads, typical of the $\mu$ROV operating conditions. This was particularly emphasised when operating at higher symbol rates, >20kSym/s, where a large number of filter coefficients were required to span the extent of the delay spread. Despite iterative structures, such as BICM-ID or *Turbo* equalisation, having previously been shown to offer optimal performance for a single element receiver, such techniques were shown to be inadequate in overcoming such long delay spreads, even when utilising high levels of coding redundancy, >50%, and a significant number of processing iterations.

Due to the inherent limitations of a single element receiver, a multi-channel array was considered. Despite the component cost and the increased physical dimensions of such an array having previously discouraged their use, the ability to null multipath arrivals, through electronically steering the directional beam offered incomparable performance gains. Additionally, the low range to depth ratio resulted in wide angular separation between arrivals, reducing the specification of the required beam pattern and enabling it to be realised with the use of fewer transducer elements and reduced spatial separation. Therefore, the proposed array consisted of four $\lambda$ spaced elements, offering suitable performance with a low component count and an overall construction of $<$ 150mm. The physical dimensions of this array were therefore shown to be comparable with that of a high end omnidirectional receiver, such as a Reson TC4032.

The results shown in Chapter 4 demonstrate the combined performance of an adaptive DFE-BICM-ID structure and a small 4-element beamforming array. From extensive practical experimentation, the proposed receiver structure is found to be capable of supporting throughput in excess of 20kbps, whilst also demonstrating very few packet errors and utilising a very low coding overhead, $<$15%. The combination of an initial open loop Doppler estimate and a symbol by symbol closed loop tracking scheme were shown to be necessary to effectively compensate for the highly dynamic motion of the vehicle. The proposed structure was shown to achieve reliable performance while utilising a shorter training sequence, reducing the packet overhead and improving the overall throughput of the system.

Based on the performance of the proposed receiver, Chapter 5 examined the development of a low cost real-time implementation. The design was tailored to meet the specific requirements of the $\mu$ROV application, which included the implementation of: a robust synchronisation technique; a computationally efficient decoding structure; and an equaliser structure combining RLS training and LMS tracking algorithms. This structure ensured a good compromise between the performance of the system and the computational load of the real time implementation. To simplify the hardware structure, and to reduce the overall system cost, a PC was proposed as the signal processing platform, thereby limiting any external hardware to that of a data acquisition unit and a basic pre-amp and filter. A multi-threaded software architecture was utilised to enable new samples to be acquired uninterrupted, while processor intense operations, such as equalisation and iterative decoding, were performed simultaneously. Additionally, the use of a PC allowed captured data to be stored in memory and post-processed at a later date, utilising different receiver topologies and parameter values, such that incremental refinements could be made, ultimately resulting in a highly efficient receiver structure.

A series of benchmarking tests were conducted on a low specification PC, demonstrating the capability of the system to operate in true real-time. The system was shown to be able to support 2 outer and 3 inner iterations without the generation of any accumulated processing delays. The proposed implementation is felt to be a realistic representation of a final receiver design, with the exception of the commercial off-the-shelf (COTS) data acquisition unit, which could be replaced with a simplified custom built unit to further reduce the cost of the overall system.

The development of a bidirectional communication scheme is presented in Chapter 6 to enable simultaneous transmission of video and control information. The limitations of a half-duplex TDMA structure were discussed, namely reduced throughput and considerable scheduling latency. Therefore, this study examined the use of FDMA techniques to support full-duplex transmissions. The effect of the *'near-far'* problem was shown to give rise to the strong possibility of receiver saturation. Several solutions were discussed, including the use of adaptive cancellation, which was dismissed due to the long channel reverberation resulting in the inability to perform perfect cancellation of the near end transmission with a realistic length filter.

A combination of passive and digital filtering techniques were shown to offer acceptable isolation of the two simultaneous frequency transmissions. Experimental results demonstrated acceptable performance at simulated ranges of upto 250m. The results highlighted the requirement for passive filters to suppress the near end transmission, such that saturation of the receiver hardware was avoided. Assuming, the dynamic range was considerably reduced, the far end signal was shown to be successfully demodulated with minimal bit errors. Consequently, the proposed full-duplex structure was recommended as an enabler for the development of a realistic AMC communication scheme.

The final chapter investigated the development of an AMC communication scheme, capable of adapting the transmission parameters to maximise throughput and minimise packet errors during operation in a rapidly varying channel. Utilising the receiver structure described in Chapter 5 a set of controlled experiments were conducted to evaluate the performance of an AMC structure in the presence of varying noise and channel conditions. Four different AMC strategies were proposed and evaluated for varying channel delay; achieving peak data rates of 55kbps and average throughputs of 36kbps, post coding. Such practical results demonstrate a considerable improvement in average throughput of $\approx 20\%$ when compared with an optimum static transmission scheme.

A considerable limitation of the proposed AMC techniques at much longer ranges was the delay between a change in the channel conditions and the adaptation of the transmission parameters. This effect was attributed to the inherently slow propagation speed of acoustic waves in water, resulting in a considerable feedback delay.

This was shown to result in incorrect decisions due to outdated feedback information, and in many cases culminating in a reduction in throughput or an increase in packet errors. The use of an open-loop approach is recommended for such transmissions across longer ranges, $> 300m$, where increased channel latency is observed. The use of local feedback information, such as inertial sensor readings, downlink reliability indicators and thruster activity, could enable immediate decisions to be made by the uplink transmitter, negating the effects of feedback delay.

This thesis has presented a set of comprehensive recommendations for the design of a high data rate communication system suitable for a $\mu$ROV platform. Based on rigorous testing and a thorough evaluation of the typical operating conditions, a suitable multi-channel iterative receiver structure has been developed. Based on these findings a PC based receiver structure has been constructed, enabling real-time processing of packets with adaptive code rates and modulation schemes. The simplified hardware structure, has enabled the platform to be developed at a low cost, making it an ideal solution for the discussed application and significantly advancing the state-of-the-art.

## 8.1 Future Work

Based on the outcomes and findings of the presented research, several areas of further work are proposed:

A final engineering task could be conducted to fully integrate the presented 'building blocks' onto the Acoustically Controlled Tetherless ROV (ACTROV) platform, presented in Section 1. A full integration of the proposed high data rate communication scheme would enable a true demonstration of the proposed concept. Additionally, to enable simultaneous observation and control to be achievable, further research may wish to focus on the development of a suitable network protocol. Consequently, a more detailed examination of suitable video streaming techniques may be required, leading to further development of the presented acoustic transmission scheme, based on the requirements of the selected compression algorithm.

Based on the discussed recommendations, a communication scheme has been shown to reliably support throughputs in excess of 30kbps, post coding, utilising a mixture of QPSK and QAM transmissions. The author believes that given a suitable transmitter that the proposed structure would be capable of supporting much higher symbol rates, $>$ 40kSym/s. This assumption is further supported by the increase in available bandwidth when operating at ranges of $<$ 500m. Further research into the use of higher symbol rates would therefore be recommended, potentially offering the ability to yield throughputs of $>$ 50kbps.

The use of an AMC structure has improved the performance of the proposed link, in many cases increasing throughput by upto 20%. Further research could focus on the tuning of the adaptive threshold levels, through studying a larger data set to improve the certainty and precision of the selected values. Alternatively, a dynamic system could be developed, enabling the threshold to be increased or decreased based on the prior performance of the adaptive structure. The presented results have also highlighted the limitations of the AMC structure during periods of high latency, causing the author to propose the use of an open loop technique when operating at significant range. Further research could examine the use of local feedback information from inertial sensors, thruster controllers or downlink quality indicators to adapt the transmission parameters with reduced *'loop'* delay.

# Appendix A

# Sea Trials and Experimental Conditions

Throughout this investigation, three trials locations have been utilised to enable rigorous testing of the proposed receiver structure: an anechoic test tank; a shallow salt water marina; and a mid-depth fresh water lake. Additional information about the channel conditions associated with each is supplied below.

## A.1 Newcastle University Anechoic Tank

A specialised test tank was utilised within the Sensors, Electromagnetics and Acoustics laboratories (SEA Lab) at Newcastle University. The tank is lined with an anechoic matching material, 'Apltile SF5048'. This material ensures ideal matching to water, ensuring minimal internal reflections and thus limited multipath time-spread. The tank has the approximate dimensions of 3m long x 2m wide x 2m deep.

Fig. A.1 shows two photos taken of the anechoic test facilities. Within the context of this research, these facilities were used for the testing of initial hardware prototypes and for experimentation where controlled repeatable conditions were desirable.

## A.2 Royal Quays Marina

A large proportion of the results presented were collected during trials at Royal Quays Marina, North Shields [054° 59.75'N, 01° 26.75"W]. The salt water marina is considered an ideal location for trials, enabling longer range experiments to be

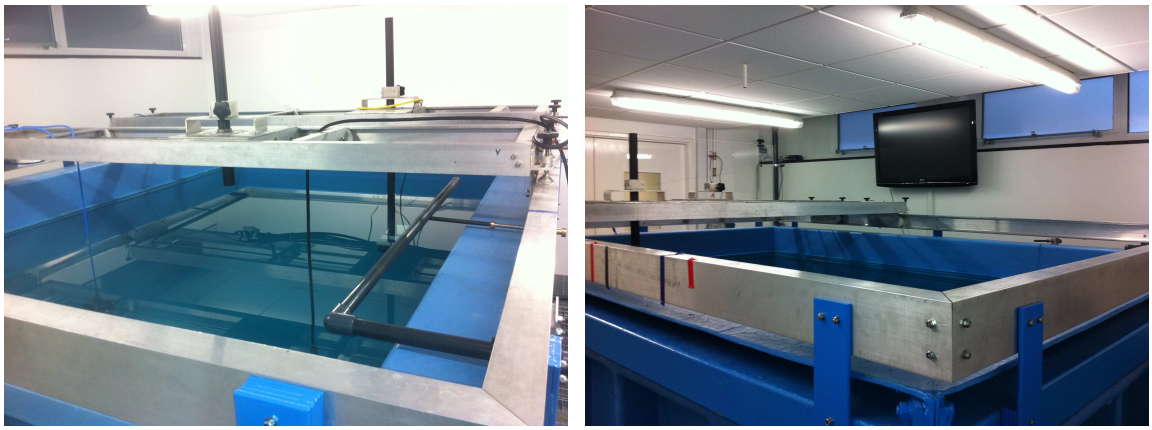

Figure A.1: Newcastle University Sensors Electromagnetics and Acoustics Laboratory (SEA Lab) Anechoic Testing Tank

carried out within a realistic shallow water channel. Fig. A.2 presents an aerial plan of the marina and highlights the location of the $\mu$ROV deployment with a dashed red circle.

The channel model for the marina environment can be defined by its enclosed dock walls and absorbent seabed. Additionally, the infrastructure required to locate the pontoon walkways and mooring points are constructed using an array of large metallic piles. These again contribute heavily to the time varying reverberant channel response for $\mu$ROV.

To enable unhindered operation over longer ranges, the end of the main pontoon was selected for the majority of tests. This location enabled access to areas of open water, for ranges of upto 250m in certain directions. High levels of background noise were regularly observed due to vessels passing nearby to the main test site. Additionally boats moored in nearby berths were often believed to be the cause of complex multipath arrivals. The depth across the majority of the marina is thought to be fairly constant around 10m. Testing was therefore typically carried out with the vehicle at a mid water column depth of 5-6m.

## A.3 Windermere

The final test location used within this research was Lake Windermere [054° 37.69'N, 02° 93.30"W]. With a maximum length of 18.09km and maximum with of 1.49km, Windermere is shown to be the largest natural lake in England. The majority of testing was performed in the North basin, from a motor vessel (Corvette 320)


Figure A.2: Plan View Of Royal Quays Marina Trials Site Highlighting The Area Of Operations. Photo Inlay Of A $\mu$ROV Deployment Conducted During Experiments In Early March 2012

anchored just south of Wansfell Boathouse, on the East shore of Windermere. The position is indicated in Fig. A.3a by a blue star.

A significant benefit in operating from this location was the deep ravine approximately 20m south of the anchorage position. This subsea land formation can be clearly seen on the depth soundings shown in Fig. A.3b. The steep gradient enables the $\mu$ROV to be deployed from the stern of the motor vessel and operated at depths of upto 50m. Additionally, the $\mu$ROV could be deployed closer to the boat enabling operation in shallower channels, typically 20m, where required. As with the trials in Royal Quays Marina the seabed was largely composed of highly absorbent material.

A limited selection of results were also collected in the centre of the North basin from a drifting motor vessel. Although the available depths were greater, i.e. circa 70m, the ability to collect repeatable results for different transmission schemes were limited. Therefore, to minimise the number of variables, results collected from the anchored position was favoured.


(a) Windermere North Basin Chart

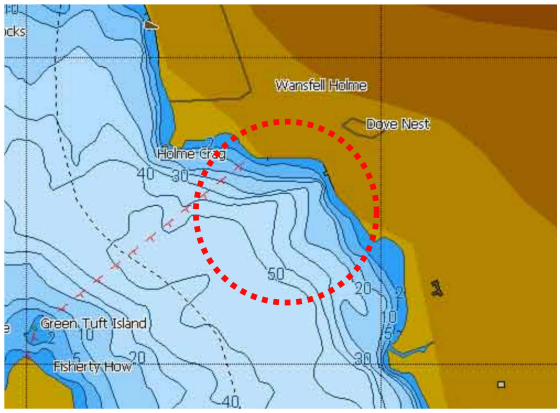


(b) Low Wood Bay Depth Soundings

Figure A.3: Windermere Location and Depth Soundings of Deployment Area (North Basin)

## A.4 Summary of Supporting Trial Work

A summary of the trials carried out in support of this research, at both Royal Quays Marina and lake Windermere, are given in Table A.1. Results collected from these trials form the basis of the rigorous evaluation carried out in the remainder of this chapter. It should be noted that this table solely includes information about trials and does not give reference to additional testing carried out in the controlled lab environment.

| Date | Location | Description |
|---|---|---|
| September 2010 | Initial Feasibility Study | Royal Quays Marina |
| March 2011 | Basic SC Transmissions | Royal Quays Marina |
| February 2012 | BICM-ID Receiver Testing | Royal Quays Marina |
| August 2012 | Beamformer Receiver Testing | Royal Quays Marina |
| December 2012 | High Order Code Rates | Royal Quays Marina |
| March 2012 | BICM-ID Receiver Testing | Lake Windermere |
| July 2012 | Initial Beamformer Testing | Lake Windermere |
| September 2012 | Final Beamformer Testing | Lake Windermere |

Table A.1: Summary Of Related Trials, Conducted Between 2010 and 2012

# References


[1] R. Moore, "Radio communication in the sea," *Spectrum, IEEE*, vol. 4, no. 11, pp. 42–51, 1967. [Cited on p. 6].

[2] J. Sojdehei, P. Wrathall, and D. Dinn, "Magneto-inductive (mi) communications," in *OCEANS, 2001. MTS/IEEE Conference and Exhibition*, vol. 1, 2001, pp. 513 –519 vol.1. [Cited on pp. 8, 9].

[3] M. Domingo, "Magnetic induction for underwater wireless communication networks," *Antennas and Propagation, IEEE Transactions on*, vol. 60, no. 6, pp. 2929 –2939, june 2012. [Cited on p. 8].

[4] S. Durrani, "Air to undersea communication with magnetic dipoles," *Antennas and Propagation, IEEE Transactions on*, vol. 12, no. 4, pp. 464–470, 1964. [Cited on p. 9].

[5] B. Cochenour, L. Mullen, and A. Laux, "Characterization of the beam-spread function for underwater wireless optical communications links," *Oceanic Engineering, IEEE Journal of*, vol. 33, no. 4, pp. 513–521, 2008. [Cited on p. 10].

[6] S. Tang, Y. Dong, and X. Zhang, "On link misalignment for underwater wireless optical communications," *Communications Letters, IEEE*, vol. 16, no. 10, pp. 1688–1690, 2012. [Cited on p. 10].

[7] S. Arnon and D. Kedar, "Non-line-of-sight underwater optical wireless communication network," *J. Opt. Soc. Am. A*, vol. 26, no. 3, pp. 530–539, Mar 2009. [Cited on p. 10].

[8] S. Tang, Y. Dong, and X. Zhang, "On path loss of nlos underwater wireless optical communication links," in *OCEANS - Bergen, 2013 MTS/IEEE*, 2013, pp. 1–3. [Cited on p. 10].

[9] M. Stojanovic, "Underwater acoustic communications: Design considerations on the physical layer," in *Wireless on Demand Network Systems and Services,*

*2008. WONS 2008. Fifth Annual Conference on*, 2008, pp. 1–10. [Cited on pp. 10, 12].

[10] T. C. Mark BOKENFOHR, "Underwater connector arrangement," Patent PCT/EP2012/052 873, 08 30, 2012. [Cited on p. 11].

[11] N. Farr, A. Bowen, J. Ware, C. Pontbriand, and M. Tivey, "An integrated, underwater optical /acoustic communications system," in *OCEANS 2010 IEEE - Sydney*, 2010, pp. 1–6. [Cited on p. 12].

[12] M. Rhodes, "Electromagnetic propagation in sea water and its value in military systems," in *SEAS DTC Technical Conference*, 2007. [Cited on p. 13].

[13] A. Palmeiro, M. Martin, I. Crowther, and M. Rhodes, "Underwater radio frequency communications," in *OCEANS, 2011 IEEE - Spain*, 2011, pp. 1–8. [Cited on p. 13].

[14] R. Coates, *Underwater acoustic systems*, ser. A Halstead Press book. John Wiley & Sons Canada, Limited, 1989. [Online]. Available: http://books.google.co.uk/books?id=0qUeAQAAIAAJ [Cited on pp. 14, 16, 101].

[15] C. van Moll, M. Ainslie, and R. van Vossen, "A simple and accurate formula for the absorption of sound in seawater," *Oceanic Engineering, IEEE Journal of*, vol. 34, no. 4, pp. 610–616, 2009. [Cited on p. 15].

[16] R. E. Francois and G. R. Garrison, "Sound absorption based on ocean measurements: Part i: Pure water and magnesium sulfate contributions," *The Journal of the Acoustical Society of America*, vol. 72, no. 3, pp. 896–907, 1982. [Cited on pp. 15, 16].

[17] ——, "Sound absorption based on ocean measurements. part ii: Boric acid contribution and equation for total absorption," *The Journal of the Acoustical Society of America*, vol. 72, no. 6, pp. 1879–1890, 1982. [Cited on pp. 15, 16].

[18] M. A. Ainslie and J. G. McColm, "A simplified formula for viscous and chemical absorption in sea water," *The Journal of the Acoustical Society of America*, vol. 103, no. 3, pp. 1671–1672, 1998. [Cited on p. 16].

[19] L. Brekhovskikh and I. Lysanov, *Fundamentals of ocean acoustics*, ser. Springer series in electrophysics. Springer-Verlag, 1982, no. v. 8. [Cited on pp. 17, 19].

[20] L. M. Brekhovskikh and Y. P. Lysanov, "Fundamentals of ocean acoustics (3rd edition)," *The Journal of the Acoustical Society of America*, vol. 116, no. 4, pp. 1863–1863, 2004. [Cited on pp. 17, 19].

[21] R. Urick, *Principles Of Underwater Sound*. McGraw-Hill Ryerson, Limited, 1983. [Cited on p. 17].

[22] E. LaCasce and P. Tamarkin, "Underwater sound reflection from a corrugated surface," *Journal of Applied Physics*, vol. 27, no. 2, pp. 138–148, 1956. [Cited on p. 17].

[23] A. Zielinski, Y.-H. Yoon, and L. Wu, "Performance analysis of digital acoustic communication in a shallow water channel," *Oceanic Engineering, IEEE Journal of*, vol. 20, no. 4, pp. 293–299, 1995. [Cited on p. 17].

[24] H. Poor and G. Wornell, *Wireless Communications: Signal Processing Perspectives*, ser. Prentice Hall Signal Processing Series. Pearson Education/Prentice Hall Professional Technical Reference, 1998. [Cited on p. 19].

[25] X. Lurton, *An Introduction to Underwater Acoustics: Principles and Applications*, ser. Geophysical Sciences Series. Springer Verlag, 2002. [Cited on p. 21].

[26] L. Kinsler, *Fundamentals of acoustics*, 4th ed. Wiley, 2000. [Cited on p. 21].

[27] G. M. Wenz, "Acoustic ambient noise in the ocean: Spectra and sources," *The Journal of the Acoustical Society of America*, vol. 34, no. 12, pp. 1936–1956, 1962. [Cited on p. 23].

[28] N. R. C. Committee on Potential Impacts of Ambient Noise in the Ocean on Marine Mammals, *Ocean Noise and Marine Mammals*. The National Academies Press, 2003. [Cited on p. 23].

[29] R. K. Andrew, B. M. Howe, J. A. Mercer, and M. A. Dzieciuch, "Ocean ambient sound: Comparing the 1960s with the 1990s for a receiver off the california coast," *Acoustics Research Letters Online*, vol. 3, no. 2, pp. 65–70, 2002. [Cited on p. 24].

[30] M. Stojanovic, "Recent advances in high-speed underwater acoustic communications," *Oceanic Engineering, IEEE Journal of*, vol. 21, no. 2, pp. 125–136, 1996. [Cited on pp. 26, 30].

[31] J. Proakis, *Digital Communications*, ser. McGraw-Hill Series in Electrical and Computer Engineering. McGraw-Hill Education, 2001. [Cited on pp. 26, 32, 38, 48, 52, 53].

[32] L. Olson, J. Backes, and J. Miller, "Communication, control, and data acquisition systems on the ishte lander," *Oceanic Engineering, IEEE Journal of*, vol. 10, no. 1, pp. 5–16, 1985. [Cited on p. 26].

[33] M. Suzuki, K. Nemoto, T. Tsuchiya, and T. Nakanishi, "Digital acoustic telemetry of color video information," vol. 3, pp. 893–896, 1989. [Cited on p. 27].

[34] A. Kaya and S. Yauchi, "An acoustic communication system for subsea robot," in *OCEANS '89. Proceedings*, vol. 3, 1989, pp. 765–770. [Cited on p. 27].

[35] M. Stojanovic, J. Catipovic, and J. G. Proakis, "Adaptive multichannel combining and equalization for underwater acoustic communications," *The Journal of the Acoustical Society of America*, vol. 94, no. 3, pp. 1621–1631, 1993. [Cited on p. 27].

[36] M. Stojanovic, J. Catipovic, and J. Proakis, "Phase-coherent digital communications for underwater acoustic channels," *Oceanic Engineering, IEEE Journal of*, vol. 19, no. 1, pp. 100–111, 1994. [Cited on pp. 27, 58].

[37] J. Neasham, D. Thompson, A. Tweedy, M. Lawlor, O. Hinton, A. Adams, and B. Sharif, "Combined equalisation and beamforming to achieve 20 kbits/s acoustic telemetry for rovs," vol. 2, pp. 988–993 vol.2, 1996. [Cited on pp. 27, 28].

[38] L. Freitag, M. Grund, S. Singh, S. Smith, R. Christenson, L. Marquis, and J. Catipovic, "A bidirectional coherent acoustic communication system for underwater vehicles," in *OCEANS '98 Conference Proceedings*, vol. 1, 1998, pp. 482–486 vol.1. [Cited on p. 28].

[39] A. Kaya and S. Yauchi, "An acoustic communication system for subsea robot," in *OCEANS '89. Proceedings*, vol. 3, 1989, pp. 765–770. [Cited on p. 28].

[40] J. Trubuil, T. Le Gall, G. Lapierre, and J. Labat, "Development of a real-time high data rate acoustic link," in *OCEANS, 2001. MTS/IEEE Conference and Exhibition*, vol. 4, 2001, pp. 2159–2164 vol.4. [Cited on p. 28].

[41] J. Kojima, T. Ura, H. Ando, and K. Asakawa, "High-speed acoustic data link transmitting moving pictures for autonomous underwater vehicles," in *Underwater Technology, 2002. Proceedings of the 2002 International Symposium on*, 2002, pp. 278–283. [Cited on pp. 28, 160].

[42] J. Kojima and Y. Shirasaki, "Acoustic video-signal transmission system for autonomous underwater vehicle," in *Autonomous Underwater Vehicle Technology, 1996. AUV '96., Proceedings of the 1996 Symposium on*, 1996, pp. 348–353. [Cited on p. 28].

[43] M. Suzuki, T. Sasaki, and T. Tsuchiya, "Digital acoustic image transmission system for deep-sea research submersible," in *OCEANS '92. Mastering the Oceans Through Technology. Proceedings.*, vol. 2, 1992, pp. 567–570. [Cited on p. 28].

[44] C. Pelekanakis, M. Stojanovic, and L. Freitag, "High rate acoustic link for underwater video transmission," in *OCEANS 2003. Proceedings*, vol. 2, 2003, pp. 1091–1097 Vol.2. [Cited on p. 28].

[45] S. Weinstein, "The history of orthogonal frequency-division multiplexing [history of communications]," *Communications Magazine, IEEE*, vol. 47, no. 11, pp. 26–35, 2009. [Cited on pp. 29, 69].

[46] B. Li, J. Huang, S. Zhou, K. Ball, M. Stojanovic, L. Freitag, and P. Willett, "Mimo-ofdm for high-rate underwater acoustic communications," *Oceanic Engineering, IEEE Journal of*, vol. 34, no. 4, pp. 634 –644, oct. 2009. [Cited on p. 29].

[47] M. Stojanovic, "Low complexity ofdm detector for underwater acoustic channels," in *OCEANS 2006*, 2006, pp. 1–6. [Cited on p. 29].

[48] J. Huang, S. Zhou, J. Huang, C. Berger, and P. Willett, "Progressive intercarrier interference equalization for ofdm transmission over time-varying underwater acoustic channels," *Selected Topics in Signal Processing, IEEE Journal of*, vol. 5, no. 8, pp. 1524–1536, 2011. [Cited on p. 29].

[49] B. Li, S. Zhou, M. Stojanovic, L. Freitag, and P. Willett, "Multicarrier communication over underwater acoustic channels with nonuniform doppler shifts," *Oceanic Engineering, IEEE Journal of*, vol. 33, no. 2, pp. 198 –209, april 2008. [Cited on pp. 29, 71].

[50] S. Mason, C. Berger, S. Zhou, and P. Willett, "Detection, synchronization, and doppler scale estimation with multicarrier waveforms in underwater acoustic communication," *Selected Areas in Communications, IEEE Journal on*, vol. 26, no. 9, pp. 1638 –1649, december 2008. [Cited on pp. 29, 71].

[51] C. Berrou, A. Glavieux, and P. Thitimajshima, "Near shannon limit error-correcting coding and decoding: Turbo-codes. 1," in *Communications, 1993. ICC '93 Geneva. Technical Program, Conference Record, IEEE International Conference on*, vol. 2, 1993, pp. 1064–1070 vol.2. [Cited on pp. 29, 73].

[52] C. Douillard, M. Jézéquel, C. Berrou, and Others, "Iterative correction of intersymbol interference: Turbo-equalization," *European Transactions on Telecommunications*, vol. 6, no. 5, 2008. [Cited on pp. 30, 76].

[53] J. Sifferlen, H. Song, W. Hodgkiss, W. Kuperman, and J. Stevenson, "An iterative equalization and decoding approach for underwater acoustic communication," *Oceanic Engineering, IEEE Journal of*, vol. 33, no. 2, pp. 182–197, 2008. [Cited on p. 30].

[54] E. Sozer, J. Proakis, and F. Blackmon, "Iterative equalization and decoding techniques for shallow water acoustic channels," in *OCEANS, 2001. MTS/IEEE Conference and Exhibition*, vol. 4, 2001, pp. 2201–2208 vol.4. [Cited on p. 30].

[55] R. Otnes and T. Eggen, "Underwater acoustic communications: Long-term test of turbo equalization in shallow water," *Oceanic Engineering, IEEE Journal of*, vol. 33, no. 3, pp. 321–334, 2008. [Cited on p. 30].

[56] C. Shah, C. Tsimenidis, B. Sharif, and J. Neasham, "Low-complexity iterative receiver structure for time-varying frequency-selective shallow underwater acoustic channels using bicm-id: Design and experimental results," *Oceanic Engineering, IEEE Journal of*, vol. 36, no. 3, pp. 406–421, 2011. [Cited on pp. 30, 79].

[57] D. Kilfoyle and A. Baggeroer, "The state of the art in underwater acoustic telemetry," *Oceanic Engineering, IEEE Journal of*, vol. 25, no. 1, pp. 4–27, 2000. [Cited on p. 30].

[58] C. R. Cahn, "Performance of digital phase-modulation communication systems," *Communications Systems, IRE Transactions on*, vol. 7, no. 1, pp. 3–6, 1959. [Cited on p. 35].

[59] S. Haykin and M. Mosher, *Communication Systems*. John Wiley & Sons, Limited, 2010. [Cited on pp. 37, 156, 157].

[60] R. Dixon, *Spread Spectrum Systems with Commercial Applications*, ser. Wiley-Interscience publication. Wiley, 1994. [Cited on pp. 38, 63].

[61] A. Sayed, *Fundamentals of Adaptive Filtering*. Wiley, 2003. [Cited on pp. 44, 53, 55].

[62] S. Haykin, *Adaptive filter theory*, ser. Prentice-Hall information and system sciences series. Prentice Hall, 2002. [Cited on pp. 46, 49, 50, 51, 53].

[63] G. Ungerboeck, "Fractional tap-spacing equalizer and consequences for clock recovery in data modems," *Communications, IEEE Transactions on*, vol. 24, no. 8, pp. 856–864, 1976. [Cited on p. 47].

[64] A. Benveniste and M. Goursat, "Blind equalizers," *Communications, IEEE Transactions on*, vol. 32, no. 8, pp. 871–883, 1984. [Cited on p. 49].

[65] B. Widrow and M. E. Hoff, "Adaptive Switching Circuits," in *1960 IRE WESCON Convention Record, Part 4*. New York: IRE, 1960, pp. 96–104. [Cited on p. 50].

[66] B. Widrow, J. McCool, and M. Ball, "The complex lms algorithm," *Proceedings of the IEEE*, vol. 63, no. 4, pp. 719–720, 1975. [Cited on p. 50].

[67] S. Qureshi, "Adaptive equalization," *Proceedings of the IEEE*, vol. 73, no. 9, pp. 1349–1387, 1985. [Cited on p. 53].

[68] M. Stojanovic, *Underwater Acoustic Communication*. John Wiley & Sons, Inc., 2001. [Cited on p. 54].

[69] J. Treichler, C. Johnson, and M. Larimore, *Theory and design of adaptive filters*, ser. Topics in digital signal processing. Wiley, 1987. [Cited on p. 54].

[70] C. Halkias, G. Carayannis, J. Dologlou, and D. Emmanoulopoulos, "A new generalized recursion for the fast computation of the kalman gain to solve the covariance equations," in *Acoustics, Speech, and Signal Processing, IEEE International Conference on ICASSP '82.*, vol. 7, 1982, pp. 1760–1763. [Cited on p. 54].

[71] D. Falconer and L. Ljung, "Application of fast kalman estimation to adaptive equalization," *Communications, IEEE Transactions on*, vol. 26, no. 10, pp. 1439–1446, 1978. [Cited on p. 54].

[72] G. Carayannis, N. Kalouptsidis, and D. Manolakis, "Fast recursive algorithms for a class of linear equations," *Acoustics, Speech and Signal Processing, IEEE Transactions on*, vol. 30, no. 2, pp. 227–239, 1982. [Cited on p. 54].

[73] J. Mathews and S. Douglas, *Adaptive Filters*. Prentice Hall PTR, 2001. [Cited on p. 55].

[74] F. Hsu, "Square root kalman filtering for high-speed data received over fading dispersive hf channels," *Information Theory, IEEE Transactions on*, vol. 28, no. 5, pp. 753–763, 1982. [Cited on p. 55].

[75] J. Neasham, D. Thompson, A. Tweedy, M. Lawlor, O. Hinton, A. Adams, and B. Sharif, "Combined equalisation and beamforming to achieve 20 kbits/s acoustic telemetry for rovs," in *OCEANS '96. MTS/IEEE. Prospects for the 21st Century. Conference Proceedings*, vol. 2, 1996, pp. 988–993 vol.2. [Cited on pp. 57, 58, 61, 98].

[76] M. Johnson, L. Freitag, and M. Stojanovic, "Improved doppler tracking and correction for underwater acoustic communications," in *Acoustics, Speech, and Signal Processing, 1997. ICASSP-97., 1997 IEEE International Conference on*, vol. 1, 1997, pp. 575–578 vol.1. [Cited on pp. 58, 59, 60, 61].

[77] B. Sharif, J. Neasham, O. Hinton, and A. Adams, "A computationally efficient doppler compensation system for underwater acoustic communications," *Oceanic Engineering, IEEE Journal of*, vol. 25, no. 1, pp. 52–61, 2000. [Cited on pp. 59, 61, 62, 63].

[78] B. Sharif, J. Neasham, O. Hinton, A. Adams, and J. Davies, "Adaptive doppler compensation for coherent acoustic communication," *Radar, Sonar and Navigation, IEE Proceedings* -, vol. 147, no. 5, pp. 239–246, 2000. [Cited on p. 61].

[79] S. Weinstein and P. Ebert, "Data transmission by frequency-division multiplexing using the discrete fourier transform," *Communication Technology, IEEE Transactions on*, vol. 19, no. 5, pp. 628–634, 1971. [Cited on p. 67].

[80] N. LaSorte, W. Barnes, and H. Refai, "The history of orthogonal frequency division multiplexing," in *Global Telecommunications Conference, 2008. IEEE GLOBECOM 2008. IEEE*, 2008, pp. 1–5. [Cited on p. 67].

[81] A. Peled and A. Ruiz, "Frequency domain data transmission using reduced computational complexity algorithms," in *Acoustics, Speech, and Signal Processing, IEEE International Conference on ICASSP '80.*, vol. 5, 1980, pp. 964–967. [Cited on p. 69].

[82] S. Coleri, M. Ergen, A. Puri, and A. Bahai, "Channel estimation techniques based on pilot arrangement in ofdm systems," *Broadcasting, IEEE Transactions on*, vol. 48, no. 3, pp. 223–229, 2002. [Cited on p. 69].

[83] S. H. Han and J. H. Lee, "An overview of peak-to-average power ratio reduction techniques for multicarrier transmission," *Wireless Communications, IEEE*, vol. 12, no. 2, pp. 56–65, 2005. [Cited on p. 71].

[84] A. Jones, T. Wilkinson, and S. Barton, "Block coding scheme for reduction of peak to mean envelope power ratio of multicarrier transmission schemes," *Electronics Letters*, vol. 30, no. 25, pp. 2098–2099, 1994. [Cited on p. 71].

[85] I. Capoglu, Y. Li, and A. Swami, "Effect of doppler spread in ofdm-based uwb systems," *Wireless Communications, IEEE Transactions on*, vol. 4, no. 5, pp. 2559 – 2567, sept. 2005. [Cited on p. 71].

[86] S. Yerramalli, M. Stojanovic, and U. Mitra, "Partial fft demodulation: A detection method for highly doppler distorted ofdm systems," *Signal Processing, IEEE Transactions on*, vol. 60, no. 11, pp. 5906 –5918, nov. 2012. [Cited on p. 71].

[87] R. Johannesson, K. Zigangirov, I. C. Society, I. I. T. Society, and V. T. Society, *Fundamentals of convolutional coding*, ser. IEEE series on mobile & digital communication. Institute of Electrical and Electronics Engineers, 1999. [Cited on p. 71].

[88] S. Benedetto and G. Montorsi, "Serial concatenation of block and convolutional codes," *Electronics Letters*, vol. 32, no. 10, pp. 887–888, 1996. [Cited on p. 72].

[89] G. Ungerboeck, "Channel coding with multilevel/phase signals," *Information Theory, IEEE Transactions on*, vol. 28, no. 1, pp. 55–67, 1982. [Cited on p. 75].

[90] ——, "Trellis-coded modulation with redundant signal sets part i: Introduction," *Communications Magazine, IEEE*, vol. 25, no. 2, pp. 5–11, 1987. [Cited on p. 75].

[91] ——, "Trellis-coded modulation with redundant signal sets part ii: State of the art," *Communications Magazine, IEEE*, vol. 25, no. 2, pp. 12–21, 1987. [Cited on p. 75].

[92] L.-F. Wei, "Coded m-dpsk with built-in time diversity for fading channels," *Information Theory, IEEE Transactions on*, vol. 39, no. 6, pp. 1820–1839, 1993. [Cited on p. 75].

[93] G. Caire, G. Taricco, and E. Biglieri, "Bit-interleaved coded modulation," *Information Theory, IEEE Transactions on*, vol. 44, no. 3, pp. 927–946, 1998. [Cited on p. 75].

[94] M. Tchler and A. Singer, "Turbo equalization: An overview," *Information Theory, IEEE Transactions on*, vol. 57, no. 2, pp. 920–952, 2011. [Cited on p. 76].

[95] G. Bauch, H. Khorram, and J. Hagenauer, "Iterative equalization and decoding in mobile communications systems," in *Second European Personal Mobile Communications Conference (2. EPMCC '97*, 1997, pp. 307–312. [Cited on p. 76].

[96] M. Tchler, A. Singer, and R. Koetter, "Minimum mean squared error equalization using a priori information," *Signal Processing, IEEE Transactions on*, vol. 50, no. 3, pp. 673–683, 2002. [Cited on p. 76].

[97] X. Li and J. Ritcey, "Bit-interleaved coded modulation with iterative decoding," *Communications Letters, IEEE*, vol. 1, no. 6, pp. 169–171, 1997. [Cited on p. 76].

[98] F. Schreckenbach, N. Gortz, J. Hagenauer, and G. Bauch, "Optimization of symbol mappings for bit-interleaved coded modulation with iterative decoding," *Communications Letters, IEEE*, vol. 7, no. 12, pp. 593–595, 2003. [Cited on p. 77].

[99] L. Bahl, J. Cocke, F. Jelinek, and J. Raviv, "Optimal decoding of linear codes for minimizing symbol error rate (corresp.)," *Information Theory, IEEE Transactions on*, vol. 20, no. 2, pp. 284–287, 1974. [Cited on pp. 123, 124].

[100] J. Tan and G. Stuber, "New siso decoding algorithms," *Communications, IEEE Transactions on*, vol. 51, no. 6, pp. 845–848, 2003. [Cited on p. 123].

[101] P. Robertson, E. Villebrun, and P. Hoeher, "A comparison of optimal and sub-optimal map decoding algorithms operating in the log domain," in *Communications, 1995. ICC '95 Seattle, 'Gateway to Globalization', 1995 IEEE International Conference on*, vol. 2, 1995, pp. 1009–1013 vol.2. [Cited on pp. 124, 125].

[102] S. Papaharalabos, P. Sweeney, and B. Evans, "Siso algorithms based on max-log-map and log-map turbo decoding," *Communications, IET*, vol. 1, no. 1, pp. 49–54, 2007. [Cited on p. 125].

[103] W. Gross and P. Gulak, "Simplified map algorithm suitable for implementation of turbo decoders," *Electronics Letters*, vol. 34, no. 16, pp. 1577–1578, 1998. [Cited on p. 125].

[104] A. Viterbi, "An intuitive justification and a simplified implementation of the map decoder for convolutional codes," *Selected Areas in Communications, IEEE Journal on*, vol. 16, no. 2, pp. 260–264, 1998. [Cited on p. 125].

[105] H. R. Sadjadpour, "Maximum a posteriori decoding algorithms for turbo codes," *Proc. SPIE*, vol. 4045, pp. 73–83, 2000. [Cited on p. 125].

[106] Iterative Solutions, "CML: Coded Modulation Library," http://www.iterativesolutions.com/Matlab.htm, 2007. [Cited on p. 126].

[107] Intel Corporation, *Intel Integrated Performance Primitives for Intel Architecture Reference Manual*, 8th ed., 2002–2013, http://software.intel.com/sites/products/documentation/doclib/ipp_sa/80/ipp_userguide.pdf. [Cited on p. 138].

[108] Future Technology Devices International Ltd., *UM232H Single Channel USB Hi-Speed FT232H Development Module Datasheet*, 1st ed., 2012, http://www.ftdichip.com/Support/Documents/DataSheets/Modules/DS_UM232H.pdf. [Cited on p. 149].

[109] K. Smith, A. Larraza, and B. Kayali, "Scale model analysis of full-duplex communications in an underwater acoustic channel," in *OCEANS, 2001. MTS/IEEE Conference and Exhibition*, vol. 4, 2001, pp. 2250–2255 vol.4. [Cited on p. 158].

[110] G. G. Xie, J. H. Gibson, and K. Bektas, "Evaluating the feasibility of establishing full-duplex underwater acoustic channels," DTIC Document, Tech. Rep., 2004. [Cited on p. 158].

[111] D. Hoag, V. Ingle, and R. Gaudette, "Low-bit-rate coding of underwater video using wavelet-based compression algorithms," *Oceanic Engineering, IEEE Journal of*, vol. 22, no. 2, pp. 393–400, 1997. [Cited on p. 160].

[112] J. Hagen, *Radio-Frequency Electronics: Circuits and Applications*. Cambridge University Press, 2009. [Cited on p. 163].

[113] G. Matthaei, L. Young, and E. Jones, *Microwave filters, impedance-matching networks, and coupling structures*, ser. Artech House microwave library. McGraw-Hill, 1964, no. v. 1. [Cited on p. 163].

[114] B. Widrow, J. Glover, J.R., J. McCool, J. Kaunitz, C. Williams, R. Hearn, J. Zeidler, J. Eugene Dong, and R. Goodlin, "Adaptive noise cancelling: Principles and applications," *Proceedings of the IEEE*, vol. 63, no. 12, pp. 1692–1716, 1975. [Cited on p. 166].

[115] S. Boll and D. Pulsipher, "Suppression of acoustic noise in speech using two microphone adaptive noise cancellation," *Acoustics, Speech and Signal Processing, IEEE Transactions on*, vol. 28, no. 6, pp. 752–753, 1980. [Cited on p. 166].

[116] S. Mani, T. M. Duman, and P. Hursky, "Adaptive coding-slash modulation for shallow-water uwa communications," *The Journal of the Acoustical Society of America*, vol. 123, no. 5, pp. 3749–3749, 2008. [Cited on p. 175].

[117] A. Radosevic, T. Duman, J. Proakis, and M. Stojanovic, "Channel prediction for adaptive modulation in underwater acoustic communications," in *OCEANS, 2011 IEEE - Spain*, 2011, pp. 1–5. [Cited on p. 176].

[118] P. Qarabaqi and M. Stojanovic, "Adaptive power control for underwater acoustic communications," in *OCEANS, 2011 IEEE - Spain*, 2011, pp. 1–7. [Cited on p. 176].